~~THE~~ CALCULATION OF GAS, OIL AND PULVERISED COAL-FIRED ELECTRIC POWER ~~STATION BOILERS~~ FURNACES

by

George Lazopoulos

Thesis submitted for the Degree of
Doctor of Philosophy
in the Faculty of Engineering
of University of London
and for the
Diploma of Membership
of Imperial College

Mechanical Engineering Department
Imperial College of Science Technology and Medicine
January 1995

BIBL. LONDIN. UNIV.

Στη Μητερα μου και
στη μνημη του πατερα μου

To my Mother and
to the Memory of my Father

ABSTRACT

The subject of the thesis is the development of mathematical models and their subsequent application to the prediction of Industrial Scale Electric Power Furnaces fired with gas, oil or pulverised coal.

The Eulerian formulation is used for the description of the gas phase time - averaged conservation equations. Turbulence is modelled along with the k - ε model. The partial differential equations are discretised in a finite volume framework. The set of simultaneous finite difference equations, namely u, v, w momentum, pressure correction, turbulence kinetic energy k and its dissipation rate ε , enthalpy h and mixture fraction f is solved iteratively following the SIMPLE algorithm and utilising a TDMA solver.

The discrete phase, i.e. coal particles or atomised oil droplets, is described following a Lagrangian approach and the two phases are coupled through the 'Particle Source in Cell' method.

For the pulverised coal combustion, models accounting for the calculation of the particle temperature, devolatilisation processes and heterogeneous combustion, whereas for the oil droplets models for the calculation of droplet temperature and droplet evaporation have been applied to assess the appropriate sources for the gas phase calculations.

Since the optical properties of oil flames change considerably due to the presence of soot, soot formation and destruction models have been employed to account for this phenomenon.

The radiative heat transfer is modelled along the 'Discrete Transfer' method appropriately modifying the absorption coefficient of the flame for each type of fuel, and coupled with the gas phase enthalpy equation through an additional source term.

The developed models have been incorporated into a three - dimensional generalised computer code and have been applied to the prediction of two industrial scale opposed-

fired furnaces. The obtained results in terms of flow field profiles, heat fluxes to the walls and particle trajectories where applicable are presented and discussed in the thesis, conclusions are driven and recommendations for future work are given.

For the gas and oil predictions, a 320 MWe opposed-fired furnace, equipped with 18 burners arranged in two opposing 3x3 arrays, has been modelled. The thermal loading has been kept the same for the two separate test cases. In the case of oil firing, a part of flue gases where recirculated through the hopper, and the code has proved versatile enough to cope with this additional operational variation.

Comparing the two cases, the flames appear to be shorter in the oil-fired case which is attributed to the swirling flows of the burners. Most importantly, it is found that the reduced emissivity of the gas flame, as compared with that of an oil flame, is compensated for by its higher temperature so that the total heat transfer due to the fuel conversion is not strongly affected.

For the pulverised fuel predictions, a 500 MWe opposed-fired furnace has been simulated. The furnace is equipped with 48 burners arranged as arrays of 4 rows of 6 burners each located in two opposite walls. The results obtained with the model proposed by this thesis are encouraging in terms of computer economy. Given the lack of experimental data for industrial furnaces, the results of the simulations performed do not conflict with the existing engineering knowledge and appear reasonable. For the design considered, the predictions give warning of the likely existence of wall hot spots. They reveal an unexpected level of flow activity in the hopper region, the engineering consequences of which are, however, probably small. And they reveal that the 'nose' which precedes the convective section perturbs the flow to an unexpected extent throughout the entirety of the combustion chamber.

ACKNOWLEDGEMENTS

First of all I would like to express my gratitude to my supervisor Prof. F.C.Lockwood who has been a constant source of inspiration, support and advice throughout the course of this work. His invaluable comments and guidance in technical as well as personal frustrations helped to overcome these difficulties.

I wish also to thank my colleagues and friends at the thermofluids section, Dr. C. Papadopoulos, Dr. P.G.Costen, Dr. T. Abbas, Dr. J. E van Nickerk and Messrs N. Kandamby, C. Pikoulas, M.D.Emami and M.A. Selim who have all helped with the sometimes endless discussions to solve difficult problems or to open my eyes when the solutions were obvious.

I would also like to thank ANSALDO GIE srl.and particularly Dr. M. Sala, Ing. M. Bonvini and Ing. A. Antifora for providing the data on which this study is based and for their critical comments and assistance. Here, I wish to mention separately Ing. L. Vigevano, former ANSALDO and now Politecnico di Milano, for his suggestions and valuable arguments.

In addition, I would like to acknowledge the moral support I have received from my family and friends who showed considerable patience during the frustrating periods and shared my joy when the progress of the project was fast.

I would also like to express my warm feelings for my former colleagues at the Physics and Meteorology section of the Agricultural University of Athens, led by Prof. N. Chryssochoidis, for their moral support.

Finally, I would like to thank the staff of the computer centre Messrs. N. James and J. Studnicka for their support when things on the computers where going wrong. I would like also to thank Mrs. C. Hopkins for her secretarial support.

TABLE OF CONTENTS

	page
ABSTRACT	3
ACKNOWLEDGEMENTS	5
TABLE OF CONTENTS	6
LIST OF TABLES	11
LIST OF FIGURES	13
NOMENCLATURE	21
CHAPTER 1 : INTRODUCTION	28
1.1 Preliminary Remarks	28
1.2 Description of the Combustor	30
1.3 Previous and Related Work	32
1.3.1 Two - Dimensional Furnace Predictions	33
1.3.2 Three - Dimensional Furnace Calculations	35
1.4 Objectives Of The Present Study	36
1.5 Outline Of The Thesis	38
CHAPTER 2 : MATHEMATICAL FORMULATION	40
Introduction	40
2.1 The Gas Phase	40
2.1.1 Continuity Equation.	41
2.1.2 Momentum Equation.	42
2.1.3 Energy Equation.	45
2.2 THE TURBULENCE MODEL	48
2.2.1 The Closure problem.	48
2.2.2 Classification of Turbulence Models.	49
2.2.3 The Choice of the Turbulence Model.	52

2.2.4 Transport Equation of Turb. Kinetic Energy. 52

2.2.5 Transport Equation of Dissipation Rate of Turb. Kin. Energy. 53

2.2.6 The Turbulence Model Constants. 53

2.3 THE DROPLET / PARTICULATE PHASE 54

2.3.1 Eulerian and Lagrangian Approaches 54

2.3.2 Mathematical Formulation 56

2.3.2a Particle/Droplet Mass Balance Equation 57

2.3.2b Equation of the Mean Motion 58

2.3.2c Energy balance Equation 61

2.3.2c.1. Coal Particle Energy Balance 61

2.3.2c.2 Oil Droplet Energy Balance Equation 63

2.4 THE COMBUSTION MODELS 64

2.4.1 Gas Combustion Modelling 65

2.4.2 Oil Combustion Model 68

2.4.2a. Expression of Droplet Diminution 68

2.4.2b. Soot Model 69

2.4.2b.1. Description of the Soot Model. 70

2.4.2c Gas-Phase Combustion Model. 72

2.4.3 Coal Combustion Model 73

2.4.3a. The Devolatilisation Model. 73

2.4.3b. The Char combustion model. 75

2.4.3c Gas - Phase Combustion Modelling 76

2.4.3c.1. The coupling of the Phases. 76

2.4.4 Thermodynamics. 81

2.5 THERMAL RADIATION MODELS 82

2.5.1 The Transport Equation. 82

2.5.2 Classification of Radiation Models. 85

2.5.3 The Discrete Transfer Model. 86

2.5.4 Optical Properties of Gaseous, Oil and Coal Flames. 89

CHAPTER 3 : THE SOLUTION PROCEDURE 99

3.1 Introduction 99

3.2 The Differential Equations 99

3.3 The Numerical Grid 100

3.4 The Disctretisation Scheme 103

3.5 The Solution Algorithm 106

3.5.1 The SIMPLE Algorithm 106

3.6 Boundary Conditions 109

3.6.1 Inlet Boundary Conditions 109

3.6.2 Outlet Boundary Conditions 111

3.6.3 The Wall Functions 111

3.7 Droplet / Particle Tracking Calculations 113

3.7.1 The Analytical Solution Equations 113

3.7.2 The Calculations for the Particle / Droplet Phase 114

3.7.3 The Calculation of Particle / Droplet Temperature 118

3.7.4 The Interaction Source Terms 120

3.7.5 The Solution Procedure 123

3.7.6 The Boundary Conditions 124

3.7.6a The Collision Model 128

3.8 Solution of Thermal Radiation Equation 130

3.9 Computational Details 133

3.9.1 Convergence Characteristics 133

3.9.2 Under - relaxation 133

3.9.3 Numerical Stability. 134

3.9.4 Accuracy of the Solution 134

CHAPTER 4: GAS COMBUSTION CALCULATIONS 135

4.1 Introduction 135

4.2 The Numerical Grid 135

4.3 Operating Conditions 138

4.4 Results and Discussion. 139

4.4.1 The Flow Field 141

4.4.2 The Temperature and Oxygen Concentration Fields 142

4.4.3 The Absorption Coefficient 144

4.4.4 The Heat Fluxes 144

4.5 Conclusions 144

CHAPTER 5: OIL COMBUSTION CALCULATIONS 176

5.1 Introduction 176

5.2 The Numerical Grid 176

5.3 The Operating Conditions 176

5.4 The Oil Characteristics 177

5.5 The Calculation Set-up 179

5.6 Results and Discussion. 182

5.6.1 The Flow Field 184

5.6.2 The Temperature and Oxygen Concentration Fields 185

5.6.3 The Absorption Coefficient 187

5.6.4 The Heat Fluxes 188

5.6 Conclusions 188

CHAPTER 6: COAL COMBUSTION CALCULATIONS 220

6.1 Introduction 220

6.2 The Furnace Operating Conditions 222

6.3 The Coal Characteristics 222

6.4 The Calculation Set-Up 223

6.5 Computational Details 224

6.6 Results And Discussion 224

6.6.1 The Flow Field 226

6.6.2 Particle Trajectories 227

6.6.3 The Temperature and Oxygen Concentration Fields. 228

6.6.4 Wall Heat Fluxes 230

6.7 Conclusions 231

CHAPTER 7 : CLOSURE 259

7.1 Introduction 259

7.2 Summary 259

7.2.1 Gas Combustion and Thermal Radiation 260

7.2.2 Oil Combustion 260

7.2.3 Coal Combustion 261

7.2.4 Applications 262

7.3 Recommendations for Future Work 265

REFERENCES 267

APPENDIX 282

NOMENCLATURE

a_i	Discretisation Coefficients
A	Area, Magnussen Model Constant
A_c	Pre-exponential Factor for Char Combustion
A_p	Particle/Droplet Surface Area
B	Dimensionless Transfer Number
c_{pj}	Specific Heat as Functions of Temperature
C	Diffusion Correction Coefficient
C_d	Drag Coefficient
C_f	Soot Formation Constant
C_{pj}	Specific Heat at Constant Pressure and at Temperature T
C_1, C_2, C_μ	Turbulence Model Constants
d_p	Particle/Droplet Diameter
D_0	Binary Diffusion Coefficient
Di	Diffusion Coefficient
E_{char}	Activation Energy for Char Combustion
E_{devol}	Activation Energy for Devolatilisation
E_f	Activation Energy for Soot Formation
f	Mixture Fraction, Composite Mixture Fraction
f_{st}	Stoichiometric Mixture Fraction for Gas and Oil Combustion
f_{st1}	Stoichiometric Composite Mixture Fraction for Volatile Combustion
f_{st2}	Stoichiometric Composite Mixture Fraction for Full Combustion

F	Force
G	Generation Term of Turbulent Kinetic Energy
h	Specific Enthalpy
H_{fu}	Calorific Value of Fuel
i	Internal Energy
I	Radiation Intensity
k	Turbulence Kinetic Energy
k_g	Thermal Conductivity
k_0	Pre-exponential Factor for Devolatilisation Model
K_a	Absorption Coefficient
K_s	Scattering Coefficient
K_c	Chemical Reaction Rate (Char Combustion)
K_d	Diffusion Reaction Rate (Char Combustion)
K_t	Overall Reaction Rate (Char Combustion)
l	Characteristic Length Scale
L_v	Latent Heat of Devolatilisation
$L( )$	Convection - Diffusion Operator
m_j	Mass Fraction of Species j in the Mixture
m_p	Particle/Droplet Mass
Nu	Nusselt Number
p	Pressure
p'	Pressure Correction
p_{fu}	Fuel Partial Pressure

Pe	Peclet Number
Pr	Prandtl Number
$\dot{q}$	Heat Flux
$\dot{Q}$	Heat Transfer Rate
Q_b, Q_c, Q_r	Heat Transfer Rate Due to Combustion, Convection and Radiation
R_j	Reaction Rate of Species j
Re_p	Particle/Droplet Reynolds Number
R	Universal Gas Constant
s_1	Stoichiometric Factor for Volatiles Combustion
s_2	Stoichiometric Factor for Heterogeneous Combustion
S	Source Term from the Particulate to the Gas Phase
S_{rad}	Radiation Source Term
S_U, S_P	Linearised Source Terms
t	Time
T	Temperature of the Gas Mixture
T_p	Particle/Droplet Temperature
T_{sat}	Liquid Fuel Saturation Temperature
T_w	Wall Temperature
u,v,w	Velocity Components in the x, y, z Directions Respectively
$\mathbf{u}$	Velocity Vector
$\mathbf{u}_s$	Fuel Vapour Velocity Vector at Particle/Droplet Surface
$\mathbf{u}_p$	Particle/Droplet Velocity Vector
u_i	Gas Velocity in the Direction i

u^+	Dimensionless Velocity
V	Volume
V,V*	Cumulative Amount of Volatiles, Potential Volatile Yield
$\dot{W}$	Work Rate
W_j	Molecular Mass of Species j
x_i	Co-ordinate Direction
x,y,z	Cartesian Co-ordinates
y^+	Dimensionless Normal Distance

Greek Symbols

α	Void Fraction, Under-relaxation Factor
γ	Ratio of Specific Heats (=1.4)
Γ	Exchange of Transport Coefficient
$\Delta x, \Delta y, \Delta z$	Control Volume Dimensions
Δt	Time Step
δ_{ij}	Kronecker Delta
ε	Turbulence Kinetic Energy Dissipation Rate, Emissivity
η	Fraction that Estimates the Heat Absorbed by the Particle During Combustion
κ	Von Karman Constant
λ	Wavelength of Radiation
μ	Laminar Viscosity
μ_{eff}	$\mu + \mu_t$ Effective Viscosity
μ_t	Turbulent Viscosity
ν	Kinematic Viscosity
ρ	Density
σ	Stefan-Boltzman Constant
σ_ε	Dissipation Rate Prandtl/Schmidt Number
σ_k	Turbulence Kinetic Energy Prandtl/Schmidt Number
σ_t	Turbulent Prandtl/Schmidt Number for the Mean Scalar
τ	Particle/Droplet Relaxation Time
τ_{ij}	Stress Tensor

τ_w	Wall Shear Stress
ϕ	Variable in Discretised Transport Equations, Equivalence Ratio
ϕ	Scalar Variable Defined as Linear Combination of Mass Fractions
Ω	Solid Angle

Subscripts

a	Absorption
air	Air Stream
c	Residue Carbon
CV	Control Volume
d	Destruction of Soot
D	Drag
eff	Effective Property
fu	Fuel Stream
g	Gas
h	Heat, Enthalpy
i,j	Component in Tensor Notation
iner	Inerts
inlet	Inlet Boundary Condition
j	Species j
m	Mass
mix	Mixture
oil	Oil Combustion

ox	Oxygen, Oxydant Stream
p	particle/droplet, Central Grid Node
pr	Products
r,rad	Radiation
s	Gas Control Volume, Soot, Scattering
s_p	Particle/Droplet Control Surface
st	Stoichiometric
t	Turbulent
vol	Volatiles
w	Wall
λ	Monochromatic Wave-length
ϕ	Any Dependent Variable

Superscripts

$\bar{}$	Time-Averaged Value
'	Fluctuating Component
+	Related to Couette Flow Analysis for Velocity Distribution Near the Wall

LIST OF TABLES

Table 2.1	Turbulence Model Constants	54
Table 2.2	Constants in the Grey Gas Model of a Gas/Soot Mixture Gas Combustion, p_w/p_c=2 (N_g=3, N_s=2)	92
Table 2.3	Constants in the Grey Gas Model of a Gas/Soot Mixture Oil combustion, p_w/p_c=1 (N_g=3, N_s=2)	93
Table 2.4	Constants in the Grey Gas Model of a Gas/Soot Mixture Gas Combustion, p_w/p_c = 2 (N_g=4, N_s=2)	94
Table 2.5	Constants in the Grey Gas Model of a Gas/Soot Mixture Oil Combustion, p_w/p_c = 1 (N_g=4, N_s=2)	95
Table 3.1	The Mixture Fraction Source Terms	122
Table 4.1	Inlet Velocities (Gas Combustion)	138
Table 4.2	The X - Z Visualisation Planes (Gas Combustion)	139
Table 4.3	The Y -Z Visualisation Planes (Gas Combustion)	140
Table 4.4	The X - Y Visualisation Planes (Gas Combustion)	140
Table 5.1	The Furnace Operating Conditions (Air)	177
Table 5.2	The Furnace Operating Conditions (Oil)	177
Table 5.3	The Oil Characteristics	178
Table 5.4	The Primary Air	179
Table 5.5	The Secondary Air	180
Table 5.6	The Flue Gas Recirculation Conditions	181

Table 5.7	The Oil Inlet Conditions	182
Table 5.8	The X - Z Visualisation Planes (Oil Combustion)	182
Table 5.9	The Y -Z Visualisation Planes (Oil Combustion)	183
Table 5.10	The X - Y Visualisation Planes (Oil Combustion)	183
Table 6.1	The Operating Conditions (Coal Combustion)	222
Table 6.2	The Coal Composition (Proximate Analysis)	223
Table 6.3	The Coal Composition (Ultimate Analysis)	223
Table 6.4	The Coal Characteristics	223
Table 6.5	The X - Z Visualisation Planes (Coal Combustion)	225
Table 6.6	The Y -Z Visualisation Planes (Coal Combustion)	225
Table 6.7	The X - Y Visualisation Planes (Coal Combustion)	225
Table 6.8	The Overall Mass Balance for the Particulate Phase	228

LIST OF FIGURES

1.1	Frontwall-Fired Furnace Configuration	31
1.2	Opposed-Fired Furnace Configuration	31
1.3	Tangentially-Fired Furnace Configuration	32
2.1	The Control Surfaces	41
2.2	Control Surface for Particle/Droplet	43
2.3	Mass Fractions of Species as a Function of the Mixture Fraction for Gas and Oil Combustion	66
2.4	Mass Fractions of Species as a Function of the Composite Mixture Fraction for Preferential Fast Reaction of Volatiles in Coal Combustion	79
2.5	Typical Rays and Control Volumes for the Discrete Transfer Radiation Model	88
3.1	Field variable value Placement about a computational cell	101
3.2	Numerical Interpolation	102
3.3	Central Differencing Scheme	104
3.4	Upwind Differencing Scheme	105
3.5	Scalar and Velocity Control Volumes	115
3.6	Subdivision of a Scalar Control Volume	117
3.7	Flow-Chart of operations for calculating the particle trajectory and the source terms for a single time-step	123
3.8	The four dimensional space utilised in the calculation of the time-step when particle impinges a solid boundary	127
3.9	Description of the Collision Geometry and Associated Notation	129

4.1	The Gas and Oil- Fired Combustion Chamber Geometry	136
4.2	The X-Z numerical grid (Gas and Oil Combustion)	146
4.3	The Y-Z numerical grid (Gas and Oil Combustion)	146
4.4	The X-Y numerical grid (Gas and Oil Combustion)	147
4.5	The Burner Geometry	137
4.6	The Burner Representation in Cartesian Co-ordinates	138
4.7	Velocity Vectors for Y = 1 (Gas Combustion)	148
4.8	Velocity Vectors for Y = 5 (Gas Combustion)	148
4.9	Velocity Vectors for Y = 8 (Gas Combustion)	149
4.10	Velocity Vectors for Y = 10 (Gas Combustion)	149
4.11	Velocity Vectors for Y = 12 (Gas Combustion)	150
4.12	Velocity Vectors for Y = 15 (Gas Combustion)	150
4.13	Velocity Vectors for Y = 19 (Gas Combustion)	151
4.14	Velocity Vectors for Z = 5 (Gas Combustion)	152
4.15	Velocity Vectors for Z = 10 (Gas Combustion)	152
4.16	Velocity Vectors for Z = 12 (Gas Combustion)	153
4.17	Velocity Vectors for Z = 17 (Gas Combustion)	153
4.18	Velocity Vectors for Z = 22 (Gas Combustion)	154
4.19	Velocity Vectors for Z = 32 (Gas Combustion)	154
4.20	Velocity Vectors for Z = 38 (Gas Combustion)	155
4.21	Velocity Vectors for X = 1 (Gas Combustion)	155
4.22	Velocity Vectors for X = 4 (Gas Combustion)	156
4.23	Velocity Vectors for X = 8 (Gas Combustion)	156
4.24	Velocity Vectors for X = 12 (Gas Combustion)	157
4.25	Velocity Vectors for X = 15 (Gas Combustion)	157
4.26	Temperature Contours (°C) for Y = 1 (Gas Combustion)	158
4.27	Temperature Contours (°C) for Y = 5 (Gas Combustion)	158
4.28	Temperature Contours (°C) for Y = 8 (Gas Combustion)	159

4.29	Temperature Contours (°C) for Y = 10 (Gas Combustion)	159
4.30	Temperature Contours (°C) for Y = 12 (Gas Combustion)	160
4.31	Temperature Contours (°C) for Y = 15 (Gas Combustion)	160
4.32	Temperature Contours (°C) for Y = 19 (Gas Combustion)	160
4.33	Temperature Contours (°C) for Z = 5 (Gas Combustion)	161
4.34	Temperature Contours (°C) for Z = 10 (Gas Combustion)	161
4.35	Temperature Contours (°C) for Z = 12 (Gas Combustion)	162
4.36	Temperature Contours (°C) for Z = 17 (Gas Combustion)	162
4.37	Temperature Contours (°C) for Z = 22 (Gas Combustion)	163
4.38	Temperature Contours (°C) for Z = 38 (Gas Combustion)	163
4.39	Temperature Contours (°C) for X = 1 (Gas Combustion)	164
4.40	Temperature Contours (°C) for X = 4 (Gas Combustion)	164
4.41	Temperature Contours (°C) for X = 8 (Gas Combustion)	165
4.42	Temperature Contours (°C) for X = 12 (Gas Combustion)	165
4.43	Temperature Contours (°C) for X = 15 (Gas Combustion)	166
4.44	Oxygen Concentration Contours (%) for Y = 3 (Gas Combustion)	167
4.45	Oxygen Concentration Contours (%) for Y = 6 (Gas Combustion)	167
4.46	Oxygen Concentration Contours (%) for Y = 8 (Gas Combustion)	167
4.47	Oxygen Concentration Contours (%) for Y = 10 (Gas Combustion)	168
4.48	Oxygen Concentration Contours (%) for Y = 12 (Gas Combustion)	168
4.49	Oxygen Concentration Contours (%) for Y = 16 (Gas Combustion)	168
4.50	Oxygen Concentration Contours (%) for Y = 18 (Gas Combustion)	169
4.51	Oxygen Concentration Contours (%) for Z = 10 (Gas Combustion)	169
4.52	Oxygen Concentration Contours (%) for Z = 16 (Gas Combustion)	170
4.53	Oxygen Concentration Contours (%) for Z = 22 (Gas Combustion)	170
4.54	Oxygen Concentration Contours (%) for X = 1 (Gas Combustion)	171
4.55	Oxygen Concentration Contours (%) for X = 4 (Gas Combustion)	171
4.56	Oxygen Concentration Contours (%) for X = 8 (Gas Combustion)	171

4.57	Oxygen Concentration Contours (%) for X = 12 (Gas Combustion)	172
4.58	Oxygen Concentration Contours (%) for X = 15 (Gas Combustion)	172
4.59	Absorption Coefficient Contours (m^{-1}) for Z = 11 (Gas Combustion)	173
4.60	Absorption Coefficient Contours (m^{-1}) for Z = 16 (Gas Combustion)	173
4.61	Absorption Coefficient Contours (m^{-1}) for Z = 22 (Gas Combustion)	174
4.62	Heat Fluxes to the Lateral Wall (kW/m^2) (Gas Combustion)	175
5.1	Sense of Swirl of Adjacent Burners	180
5.2	The Flue Gas Recirculation through the Bottom of the Hopper	181
5.3	Velocity Vectors for Y = 1 (Oil Combustion)	189
5.4	Velocity Vectors for Y = 5 (Oil Combustion)	189
5.5	Velocity Vectors for Y = 8 (Oil Combustion)	190
5.6	Velocity Vectors for Y = 10 (Oil Combustion)	190
5.7	Velocity Vectors for Y = 12 (Oil Combustion)	191
5.8	Velocity Vectors for Y = 15 (Oil Combustion)	191
5.9	Velocity Vectors for Y = 19 (Oil Combustion)	192
5.10	Velocity Vectors for X = 1 (Oil Combustion)	192
5.11	Velocity Vectors for X = 4 (Oil Combustion)	193
5.12	Velocity Vectors for X = 8 (Oil Combustion)	193
5.13	Velocity Vectors for X = 12 (Oil Combustion)	194
5.14	Velocity Vectors for X = 16 (Oil Combustion)	194
5.15	Velocity Vectors for Z = 5 (Oil Combustion)	195
5.16	Velocity Vectors for Z = 9 (Oil Combustion)	195
5.17	Velocity Vectors for Z = 12 (Oil Combustion)	196
5.18	Velocity Vectors for Z = 19 (Oil Combustion)	196
5.19	Velocity Vectors for Z = 33 (Oil Combustion)	197
5.20	Velocity Vectors for Z = 38 (Oil Combustion)	197
5.21	Temperature Contours (°C) for Y = 1 (Oil Combustion)	198
5.22	Temperature Contours (°C) for Y = 4 (Oil Combustion)	198

5.23	Temperature Contours (°C) for Y = 6 (Oil Combustion)	199
5.24	Temperature Contours (°C) for Y = 8 (Oil Combustion)	199
5.25	Temperature Contours (°C) for Y = 10 (Oil Combustion)	200
5.26	Temperature Contours (°C) for Y = 12 (Oil Combustion)	200
5.27	Temperature Contours (°C) for Y = 14 (Oil Combustion)	201
5.28	Temperature Contours (°C) for Y = 16 (Oil Combustion)	201
5.29	Temperature Contours (°C) for Y = 19 (Oil Combustion)	202
5.30	Temperature Contours (°C) for X = 1 (Oil Combustion)	202
5.31	Temperature Contours (°C) for X = 4 (Oil Combustion)	203
5.32	Temperature Contours (°C) for X = 8 (Oil Combustion)	203
5.33	Temperature Contours (°C) for X = 12 (Oil Combustion)	204
5.34	Temperature Contours (°C) for X = 14 (Oil Combustion)	204
5.35	Temperature Contours (°C) for X = 16 (Oil Combustion)	204
5.36	Temperature Contours (°C) for Z = 5 (Oil Combustion)	205
5.37	Temperature Contours (°C) for Z = 8 (Oil Combustion)	205
5.38	Temperature Contours (°C) for Z = 10 (Oil Combustion)	206
5.39	Temperature Contours (°C) for Z = 12 (Oil Combustion)	206
5.40	Temperature Contours (°C) for Z = 20 (Oil Combustion)	207
5.41	Temperature Contours (°C) for Z = 28 (Oil Combustion)	207
5.42	Temperature Contours (°C) for Z = 35 (Oil Combustion)	208
5.43	Temperature Contours (°C) for Z = 38 (Oil Combustion)	208
5.44	Oxygen Concentration Contours (%) for Y = 1 (Oil Combustion)	209
5.45	Oxygen Concentration Contours (%) for Y = 3 (Oil Combustion)	209
5.46	Oxygen Concentration Contours (%) for Y = 6 (Oil Combustion)	210
5.47	Oxygen Concentration Contours (%) for Y = 8 (Oil Combustion)	210
5.48	Oxygen Concentration Contours (%) for Y = 10 (Oil Combustion)	211
5.49	Oxygen Concentration Contours (%) for Y = 12 (Oil Combustion)	211
5.50	Oxygen Concentration Contours (%) for Y = 16 (Oil Combustion)	212

5.51	Oxygen Concentration Contours (%) for X = 1 (Oil Combustion)	212
5.52	Oxygen Concentration Contours (%) for X = 4 (Oil Combustion)	213
5.53	Oxygen Concentration Contours (%) for X = 8 (Oil Combustion)	213
5.54	Oxygen Concentration Contours (%) for X = 15 (Oil Combustion)	214
5.55	Oxygen Concentration Contours (%) for Z = 10 (Oil Combustion)	214
5.56	Oxygen Concentration Contours (%) for Z = 16 (Oil Combustion)	215
5.57	Oxygen Concentration Contours (%) for Z = 22 (Oil Combustion)	215
5.58	Absorption Coefficient Contours (m^{-1}) for X = 4 (Oil Combustion)	216
5.59	Absorption Coefficient Contours (m^{-1}) for Z = 11 (Oil Combustion)	216
5.60	Absorption Coefficient Contours (m^{-1}) for Z = 12 (Oil Combustion)	217
5.61	Absorption Coefficient Contours (m^{-1}) for Z = 14 (Oil Combustion)	217
5.62	Absorption Coefficient Contours (m^{-1}) for Z = 18 (Oil Combustion)	218
5.66	Absorption Coefficient Contours (m^{-1}) for Z = 25 (Oil Combustion)	218
5.67	Heat Fluxes to the Lateral Wall (kW/m^2) (Oil Combustion)	219
6.1	The Coal-Fired Combustion Chamber Geometry	221
6.2	The Arrangement of the Burners (Coal Combustion)	221
6.3	The X-Z numerical grid (Coal Combustion)	233
6.4	The Y-Z numerical grid (Coal Combustion)	233
6.5	The X-Y numerical grid (Coal Combustion)	234
6.6	Velocity Vectors for Y = 2 (Coal Combustion)	235
6.7	Velocity Vectors for Y = 8 (Coal Combustion)	235
6.8	Velocity Vectors for Y = 12 (Coal Combustion)	236
6.9	Velocity Vectors for Y = 16 (Coal Combustion)	236
6.10	Velocity Vectors for Y = 20 (Coal Combustion)	237
6.11	Velocity Vectors for Y = 27 (Coal Combustion)	237
6.12	Velocity Vectors for Y = 1 (Gas Combustion)	238
6.13	Velocity Vectors for Y = 21 (Gas Combustion)	238
6.14	Velocity Vectors for X = 2 (Coal Combustion)	239

6.15	Velocity Vectors for X = 6 (Coal Combustion)	239
6.16	Velocity Vectors for X = 10 (Coal Combustion)	240
6.17	Velocity Vectors for X = 15 (Coal Combustion)	240
6.18	Velocity Vectors for X = 24 (Coal Combustion)	241
6.19	Velocity Vectors for Z = 7 (Coal Combustion)	241
6.20	Velocity Vectors for Z = 18 (Coal Combustion)	242
6.21	Velocity Vectors for Z = 30 (Coal Combustion)	242
6.22	Velocity Vectors for Z = 38 (Coal Combustion)	243
6.23	3-D Particle Trajectories	244
6.24	Projection of the Particle Trajectories in the X-Z Plane	245
6.25	Char Burnout Against Residence Time for a Front Wall Burner in the Bottom Row	227
6.26	Temperature Contours (°C) for Y = 2 (Coal Combustion)	246
6.27	Temperature Contours (°C) for Y = 8 (Coal Combustion)	246
6.28	Temperature Contours (°C) for Y = 12 (Coal Combustion)	247
6.29	Temperature Contours (°C) for Y = 16 (Coal Combustion)	247
6.30	Temperature Contours (°C) for Y = 20 (Coal Combustion)	248
6.31	Temperature Contours (°C) for Y = 27 (Coal Combustion)	248
6.32	Temperature Contours (°C) for X = 2 (Coal Combustion)	249
6.33	Temperature Contours (°C) for X = 6 (Coal Combustion)249	
6.34	Temperature Contours (°C) for X = 10 (Coal Combustion)	249
6.35	Temperature Contours (°C) for X = 15 (Coal Combustion)	250
6.36	Temperature Contours (°C) for X = 24 (Coal Combustion)	250
6.37	Temperature Contours (°C) for Z =1 8 (Coal Combustion)	251
6.38	Oxygen Concentration Contours (%) for Y = 2 (Coal Combustion)	252
6.39	Oxygen Concentration Contours (%) for Y = 8 (Coal Combustion)	252
6.40	Oxygen Concentration Contours (%) for Y = 12 (Coal Combustion)	253
6.41	Oxygen Concentration Contours (%) for Y = 16 (Coal Combustion)	253

6.42	Oxygen Concentration Contours (%) for Y = 20 (Coal Combustion)	254
6.43	Oxygen Concentration Contours (%) for Y = 27 (Coal Combustion)	254
6.44	Oxygen Concentration Contours (%) for X = 2 (Coal Combustion)	255
6.45	Oxygen Concentration Contours (%) for X = 6 (Coal Combustion)	255
6.46	Oxygen Concentration Contours (%) for X = 10 (Coal Combustion)	256
6.47	Oxygen Concentration Contours (%) for X = 15 (Coal Combustion)	256
6.48	Oxygen Concentration Contours (%) for X = 24 (Coal Combustion)	257
6.49	Oxygen Concentration Contours (%) for Z = 18 (Coal Combustion)	257
6.50	Heat Fluxes to the Lateral Wall (kW/m^2) (Coal Combustion)	258

CHAPTER 1

INTRODUCTION

1.1 Preliminary Remarks

For the past century, the combustion of fossil fuels, i.e. natural gas, coal and oil, has been the main source of the global energy production. The awareness of the limitation of energy resources, and environmental considerations such as pollutant emissions and global warming have made the improvement of combustion equipment design and the development of new techniques absolutely necessary.

Major classes of combustion systems for energy production involve liquid rocket engines, gas turbines, internal combustion engines, and industrial furnaces such as power plant boilers, cement kilns, steel reheating furnaces and glass furnaces. These varied applications have lead to numerous studies concerning the complicated phenomena that take place in the combustion chambers. The ultimate task is to establish design criteria for efficient and stable combustors producing minimal pollutant emissions. Some of the problems to be addressed are :

- the evaluation of the heat transfer rates to the combustion chamber surfaces;

- the determination of the optimum operating conditions for increased efficiency for a given type of fuel;

- the formation of pollutants such as soot and nitrogen oxides.

Until very recently the design and development of combustion chambers has generally been based on very costly experimentation and on the invaluable experience of the combustion engineers. Due to the revolutionary development of the computer technology in the past twenty years, both in terms of speed and storage space, it has been possible to develop mathematical models for the simulation of the phenomena occurring in combustors, opening a new branch of fluid mechanics : Computational Fluid Dynamics (CFD). These models must be validated against experimental data to ensure their reliability is known and therefore become a design tool. It is only very recently that the combustion equipment manufacturers and users have been persuaded to use such mathematical models.

The development of a computer simulator of complex phenomena such as those occurring in a combustion chamber must take into account the scale of the combustor itself. Several detailed models describing these phenomena have been developed and reported in the literature. Their employment, however, is not always feasible for various reasons. Among these reasons are computer limitations and inaccuracies inherent to the design of the simulator in part or as a whole. In the latter case, it would be pointless to employ a very detailed and supposedly more accurate sub-model when the overall procedure is less precise. Simplifications and assumptions, however, must be made with increased caution so that they can be physically realistic and of engineering viable. It is, therefore, in the ability and dexterity of the developer of a CFD simulator to choose and incorporate the appropriate sub-models into a computer code that will be not only accurate but practically applicable for the prediction of the performance of industrial combustors.

The present study deals with the prediction of the flow field and heat transfer within industrial scale power plant boiler combustors, fired with all three types of fossil fuels (gas, pulverised coal and heavy fuel oil). There is currently a considerable activity on the development of combustion modifications to address the problems mentioned at the beginning of this section , such as air staging, fuel staging (reburn) and the recirculation

of the flue gases either at the burner or at furnace level. Due to the nature, the size and the operating conditions of the utility furnaces the in situ experiments are very costly and unreliable and data are generally unavailable. Therefore it is even more essential to develop reliable mathematical models for the prediction of their performance in order to assist combustion engineers in their basic design and design improvement tasks.

1.2 Description of the Combustor

A typical boiler combustor can be considered as comprising a box mounted on an ash collection hopper with the hot combustion gases exiting through the top section and directed to the superheaters. At the top part of the furnace a protrusion, called the 'nose', is formed in order to accelerate the flue gases. The furnace walls are typically made up of panels with metal tube circuits for the circulating water. The firing of the furnace is accomplished through the burners which generally consist of a set of co - axial pipes and vanes directly connected to a feeder manifold. Detailed description of the burners simulated in the present study will be given in chapter 4.

A boiler furnace can be characterised by the location of the burners and the direction of the firing (incoming air and fuel flow). The combustors to be classified fall into three categories:

1. FrontWall - Fired Furnaces

In this category the location of the burners is in the front wall of the furnace which is perpendicular to the inclined walls of the hopper usually arranged as in array of rows and columns, the number of which depends on the design. The firing pattern of this category of furnaces can be seen in Fig. 1.1.

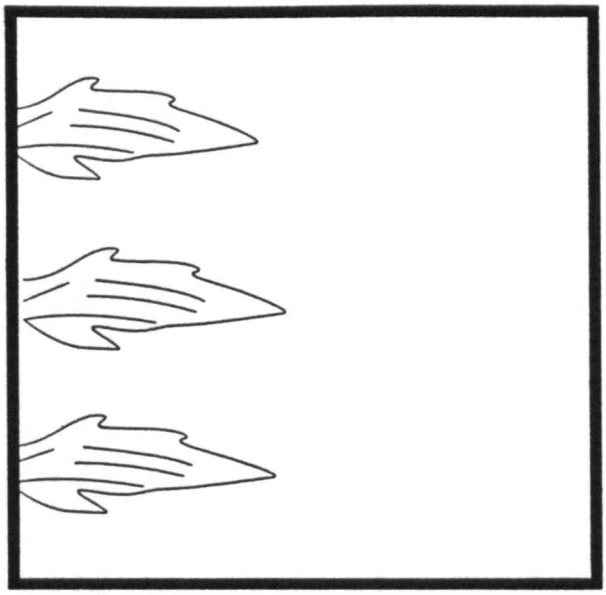


Fig. 1.1 Frontwall-Fired Furnace Configuration

2. Opposed - Fired Furnaces

In this type boiler furnaces the burners are located again as two identical arrays on the opposing walls. The firing pattern is shown in Fig. 1.2.

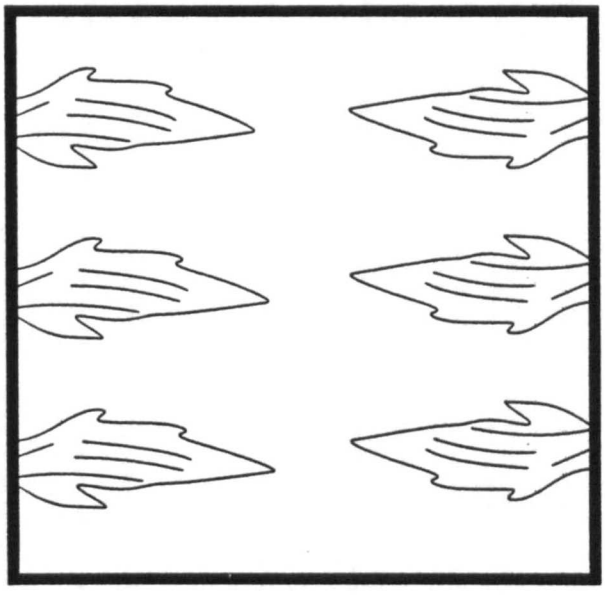


Fig. 1.2 Opposed-Fired Furnace Configuration

3. Tangentially - Fired Furnaces.

In this category of furnaces the incoming fuel and oxidising air enters the chamber from vertical sets of burners located at the corners of the chamber. The burners can be tilted with respect to an horizontal plane. This firing pattern is depicted in Fig. 1.3.

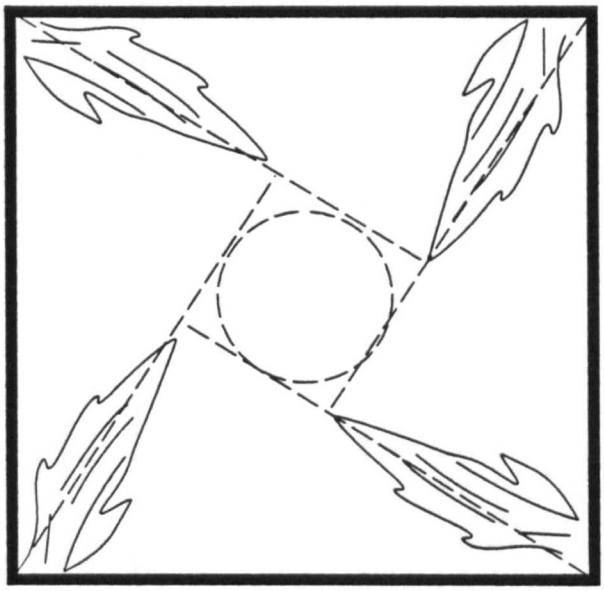


Fig. 1.3 Tangentially-Fired Furnace Configuration

1.3 Previous And Related Work

In this section existing predictive procedures are reviewed and previous applications to furnace calculations are reported. The individual phenomena that occur during turbulent combustion in a utility boiler and their modelling attempts are reviewed in chapters 2 and 3. This review is divided into two parts :

The first part deals with a review of the work related to the simulation of turbulent combustion and associated phenomena in two - dimensional axisymmetric furnaces. In this case the computer requirements to predict this class of furnaces in terms of storage

space, memory requirements and speed are less intensive. Additionally, experiments can be carried out cost effectively and reliably resulting in the availability of detailed data to validate the mathematical models. Therefore this field has been adopted as a benchmark for the development and validation of mathematical models.

The second part deals with the prediction of fully three - dimensional combustors and it is evident that the progress achieved in this research field is directly related to the advance of computer technology.

1.3.1 Two - Dimensional Furnace Predictions

The development of computational procedures for the calculation of turbulent combusting flows and the models that they employ can be found in various review papers such as, Jones and Whitelaw (1984) and Pope (1990).

The prediction procedures can be divided into two main groups : those which are the subject of this thesis and which solve the governing - time averaged partial differential transport equations and those which do not, see for example the stirred reactor model of Swithenbank et al (1973). Models of the second group are generally simpler and require less computational resources than the former one. The first group, however, procedures have superior predictive abilities which have been recognised by many investigators, see for example Bray (1975). In this category the second order Navier-Stokes type non-linear partial differential equations describing the processes of mass, momentum and heat transfer are discretised to form a set of finite - difference equations solved by iterative procedures.

The earlier studies dealt with the prediction of gaseous diffusion flames and adopted a 'Simple Chemically Reacting System' (SCRS) which assumes that a fast one - step global reaction to carbon dioxide and water is rate controlled by the turbulent mixing. Such a method can be found in Gosman et al (1978). To account for the turbulent fluctuations of a passive scalar such as the mixture fraction the presumed-shape probability density function approach can be used. This can be a clipped Gaussian,

proposed by Lockwood and Naguib (1975) or a β-function, see for example Malalasekera (1988). Its distribution characteristics are obtained by the mean and the variance field of the mixture fraction determined from their modelled transport equations. Jones and Whitelaw (1978) made comparisons between the predictions assuming each of these two types of pdf's and reported that the results are very similar.

For pulverised coal combustion the additional difficulty of modelling two - phase flows appears. Abbas et al (1981) consider the two approaches for treating the particulate phase, namely the Lagrangian Particle Source In Cell (PSIC) method, Migdal and Agosta (1967), and the Eulerian Continuum Method, Neilson and Gilchrist (1968), and reported that the PSIC method is superior. Furthermore, Lockwood et al (1984) and Risvi (1985) developed a two dimensional computer code for the prediction of swirling bituminous coal flames in a cylindrical experimental furnace. The devolatilisation process was simulated and a study of different models was carried out, namely constant evaporation model, Baum and Street (1967), single reaction model, reported in Badzioch et al (1970), two competing reaction scheme, Kobayashi et al (1977) and a multiple parallel reactions model proposed by Anthony et al (1977) and the latter was preferred.

Other works in this field are reported by, Truelove and Williams (1988), Lockwood and Mahmud (1988), Costa et al (1990), Visser et al (1990), Truelove and Holcombe (1990) with the use of varying sub - models and numerical techniques such as the PISO numerical algorithm, Issa (1982) and second order numerical schemes such as the QUICK scheme, Leonard (1979). Recent developments include the incorporation of Reynolds Stresses Turbulence Models for the more accurate prediction of the near burner aerodynamics, Lockwood and Shen (1992). The various sub-model and their merits are presented and discussed in chapters 2 and 3.

For the simulation of oil combustion two approaches can be assumed :

a. Instant evaporation of the atomised oil droplets as soon as they emerge into the combustion chamber and subsequent treatment as a gaseous diffusion flame, Carvalho (1983).

b. Treatment of the oil droplets as a second phase and therefore apply particle tracking techniques as in the case of PF combustion, Abbas, et al (1982) and Abbas et al (1984). The aforementioned researcher adopted a Lagrangian approach for the particle tracking incorporating models for the calculation of droplet temperature and particle diameter diminution.

An additional aspect when oil spray flames are considered is the presence of soot whose concentration affects strongly the optical properties of the combustion mixture within chamber and therefore the radiative heat transfer from the mixture to the surrounding walls. Therefore, soot formation and oxidation models need to be incorporated to calculate the soot concentration especially in the near burner region. The investigators cited have used a one step model, Khan and Greeves (1974), for the soot formation and a modified eddy break-up model for the soot destruction, Magnusen and Hjertager (1976).

A more recent study, Barreiros et al (1990), has incorporated the discrete transfer method for the calculation of the thermal radiation, Lockwood and Shah (1979), with the use of the emissivity constants obtained from Truelove (1976) with satisfactory results.

1.3.2 Three - Dimensional Furnace Calculations

Because of the extensive computer resources requirements full three-dimensional industrial scale furnace combustion calculations are relatively recent.

One of the first numerical simulations, using a CFD model, was of a gas-fired tangential furnace, Robinson (1985), who analysed the influence of excess air and burner configuration on the gas temperature and heat transfer distributions. Other

simulations of industrial scale gas-fired furnaces were carried out by Abbas and Lockwood (1986) concerning the simulation of one wall fired and a corner-fired furnace and by Lockwood et al (1990) concerning the simulation of a steel reheating furnace and a glass melting furnace.

Two - phase flow simulations have been performed by Lockwood et al (1988) in which particle trajectories for a corner-fired furnace were presented. Pulverised fuel (PF)-fired furnace predictions can be found in Boyd and Kent (1986) who presented oxygen and temperature profiles within the furnace and Goener and Zinser (1986) and Fiveland and Wessel (1988).

Calculations of oil - fired combustors were presented by Carvalho and Coelho (1990), and De Michele et al (1989), the latter including the simulation of the boiler convective section, but allowing only a loose coupling between flow field and heat transfer predictions.

Finally gas combustion calculations and thermal NO_x prediction can be found in Bonvini et al (1992).

1.4 Objectives Of The Present Study

Until very recently the design of a power plant boiler furnace has been subject of the experience and genius of the combustion and design engineers, based on experiment and overall balance calculations. The reason for this is twofold:

Detailed experiments can be carried out in small or large scale experimental furnaces or in scale models, and whose contribution towards insight into the various complicated phenomena is invaluable. In the case of the scale model measurements, and because different phenomena scale differently, the similarity problem arises. It is therefore questionable whether the results obtained during the experiments and the trends established about the effect that the various operational and design parameters have on

the overall performance of the combustor can be scaled up. As a result even these, and in some cases detailed measurements, are not being fully utilised for design purposes.

The mass, momentum and heat transfer in a turbulent reacting flow are described by a set of instantaneous non - linear partial differential equations which even with the present status of computer technology cannot be solved numerically without time - averaging and turbulence modelling. In addition to this the combustion related processes are arguably extremely complicated necessitating a certain number of assumptions and modelling, which depend on the scale and the engineering importance of the problem considered.

This apparent need for mathematical modelling requires careful consideration and assessment of the models available. The sub - models used must be well validated and reliable and at the same time be sufficiently computationally economical so that they can be of practical use.

The main objective of the present study is to contribute significantly to the development of a computer code that can be used as a design tool for industrial combustion chambers and that will be scientifically accurate, numerically robust , validated and user - friendly. In order to achieve this objective, several sub-models have been either adopted or developed and subsequently incorporated into the existing CINAR code already developed by co - workers. The code, before this study commenced, accounted for isothermal or gas-combustion (for diffusion flames) flows as well as the thermal radiation heat transfer modelling for any shape of confinements. An existing particle tracking procedure has been modified and consequently adapted into the code. Coal devolatilisation and heterogeneous combustion models have been adopted and incorporated into the computer code. For the case of pulverised coal firing, a new model has been developed to account for the combustion in the gas-phase. Subsequently, oil evaporation, combustion and soot formation and oxidation models have been adopted and introduced into the simulator. The work just described was accomplished with the emphasis on maintaining the user-friendliness of the computer

code. The whole simulator comprises a pre - processor, a solver CFD code and a post processor for the graphical representation of the acquired results.

1.5 Outline Of The Thesis

The thesis is presented in seven chapters, the present one included.

Chapter 2 is concerned with the mathematical formulation of the problems considered. It commences with the derivation of the gas field conservation equations in the presence of a second phase described by a Lagrangian approach. This is done so that when isothermal or gas combustion one-phase flows are considered, only the extra source terms have to be omitted resulting in the appropriate conservation equations. In the next section the turbulence closure problem is described and a brief review of turbulence modelling is presented with some emphasis in the k - ε model used. The derivation of the discrete phase balance equations is subsequently presented. The next section deals with the combustion modelling and is divided into sub - sections concerning gas -, oil - and coal - combustion. Finally in chapter 2, the thermal radiation equation is determined, the existing models for solving it are briefly reviewed and the adopted one is described in details.

Chapter 3 describes the numerical procedure employed to solve the coupled set of governing equations. After a generalised form of the partial differential equation for the continuum phase is determined, the numerical grid arrangement is presented and the discretised equations are derived. The subsequent section deals with the definition of the boundary condition for each conservation equation. Next the numerical treatment of the particulate phase is described together with the calculation of the interaction source terms between the phases. In the penultimate section of this chapter the numerical aspects of the radiation model are presented and the boundary conditions are defined. In the last section the overall computational sequence is described and additional computational details are given.

The following three chapters 4 to 6 present three case studies of opposed fired utility boilers. Their layouts are similar so they are outlined here in common. After the description of the furnace and burner geometries are introduced, the operating conditions are given followed by the computational set-up information. Finally in each of these chapters the results obtained are presented, discussed and criticised.

The final chapter concludes the thesis, summarises the work performed during this study and outlines the main findings and contributions in relation to the problem considered. The following section delineates the essential conclusions and lists the main conclusions and implications which have emerged. Finally, section 7.3 outlines some recommendations for future work.

CHAPTER 2

MATHEMATICAL FORMULATION

Introduction

The mathematical formulation of the phenomena that are the involved in this study are the subject of this chapter. It is divided into five sub-section dealing with the formulation of the gas-phase conservation equations, turbulence modelling, discrete-phase balance equations, combustion modelling and the thermal radiation heat transfer.

2.1 The Gas Phase

Derivation of the equations describing the conservation of mass, momentum and energy of two - phase inert or reacting flows have been performed using the Reynolds Transport Theorem. The Reynolds Transport Theorem , see Crowe (1976) and Fox and McDonald (1978), relates the rate of change of any arbitrary extensive property, E, of a system and the time variations of this property associated with a control volume. This is mathematically expressed as :

$$\left(\frac{dE}{dt}\right)_{system} = \frac{\partial}{\partial t}\int_{V_c} I\rho dV + \int_{S_s} I\rho \mathbf{u} d\mathbf{A} \qquad (2.1.1)$$

where I stands for the respective intensive property defined as the extensive property per unit mass, ρ for the density of the system, V_C for the inertial control volume, S_S for the system surface, **u** for the velocity vector whose direction is that of the outward normal to the element of the control surface, see Fig. (2.1), d**A** the differential area outward and normal to the control surface and t for time.

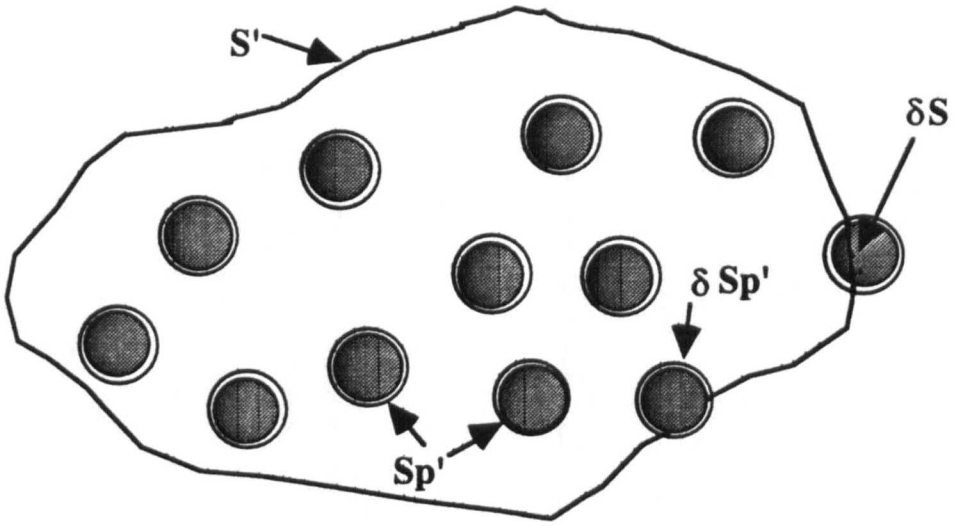


Fig 2.1 The Control Surfaces.

Equation (2.1.1) states that the rate of change of an extensive property of a system is equal to the rate of change of the property in a control volume plus the net efflux of the property across the system surface at the instant the system coincides with the control volume.

2.1.1 Continuity Equation

The gas density with the presence of the second phase is a function of the void fraction α defined as the volume occupied by the gas per unit volume of the composite mixture. Thus

$$\rho_{mix} = \alpha \rho \qquad (2.1.2)$$

where ρ_{mix} is the gas density of the mixture and ρ is the actual gas density. The void fraction in typical sprays and pulverised fuel flames is usually greater than 0.99, Smoot and Pratt (1979), so the bulk density ρ_{mix} may be to a great extent assumed equal to the actual gas density ρ.

Applying the Reynolds Transport Theorem yields :

$$\frac{\partial}{\partial t}\int_{V_c}\rho_{mix}\,dV + \int_{S_s}\rho_{mix}\,\mathbf{u}\,dA + \int_{S_p}\rho_p\mathbf{u}_p dA = 0 \qquad (2.1.3)$$

where S_p stands for the surface of each member of the particulate phase, ρ_p for the particle /droplet density and $\mathbf{u}_p$ for the particle velocity relative to the control volume. The continuity at the particle / droplet surface can be written as :

$$\int_{S_p}\rho_p\mathbf{u}_p dA = -S_{p,m} \qquad (2.1.4)$$

where $S_{p,m}$ is the rate of released mass flow from the second phase. Then Eq. (2.1.3) becomes :

$$\frac{\partial}{\partial t}\int_{V_c}\rho_{mix}\,dV + \int_{S_s}\rho_{mix}\,\mathbf{u}\,dA = S_{p,m} \qquad (2.1.5)$$

which means that the rate of increase of the mass inside the control volume plus the net efflux of gas through the control surface is equal to the released mass flow rate from the second phase. The differential form of Eq. (2.1.5) is obtained using Gauss' theorem to relate the surface and volume integrals. Using Cartesian tensor notation for steady flows, is written as:

$$\frac{\partial(\rho u_i)}{\partial x_i} = S_{p,m} \qquad (2.1.6)$$

2.1.2 Momentum Equations.

The momentum equation for the gas-phase in the composite mixture is obtained by applying the Reynolds Transport Theorem on the control volume Fig (2.2). The contribution of the discrete phase to the gas phase momentum will be provided by the exchange of mass and momentum between the phases.

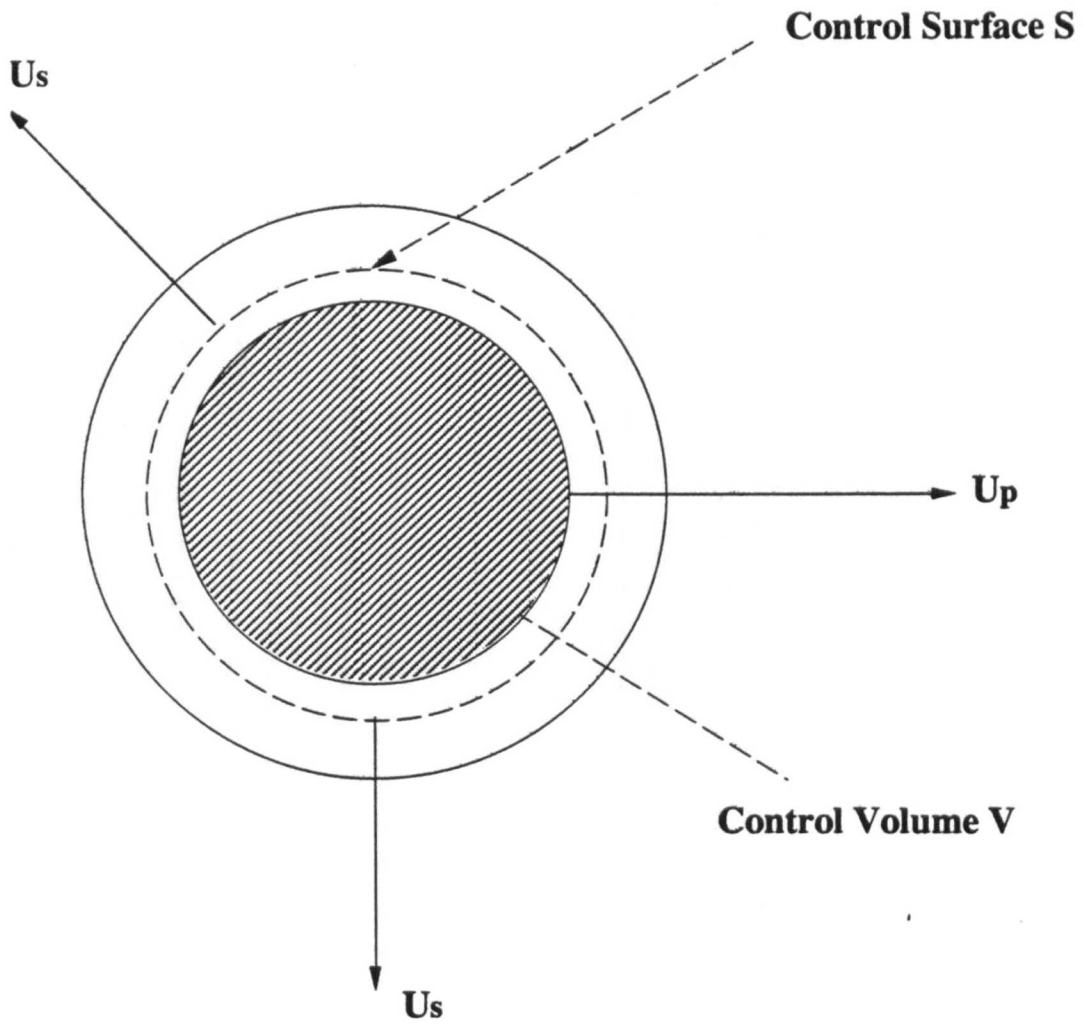


Fig. 2.2 Control surface for particle/droplet

Newton's second law states that the sum of the forces acting on each member of a group of particles that form a system is equal to the net rate of change of momentum of the system, mathematically expressed as:

$$\mathbf{F}tot = \sum_i \frac{d(m_i \mathbf{u}_i)}{dt} \qquad (2.1.7)$$

where i is to identify the individual members, $\mathbf{F}_{tot}$ is the total force acting on the system, surface and body forces are included.

By applying the Reynolds Transport Theorem for a single member of the system and summing over all the members the rate of change of the momentum is expressed, Crowe (1976), as :

$$\sum_i \frac{d(m_i \mathbf{u}_i)}{dt} = \sum_i \left(\frac{\partial}{\partial t} \int_{V_c} \mathbf{u}_i \rho_p dV + \int_{S_s} \mathbf{u}_i \rho_p \mathbf{u}_i dA + \int_{S_p} \rho_p (\mathbf{u}_p + \mathbf{u}_s) \mathbf{u}_s \, dA \right)$$

(2.1.8)

where $\mathbf{u}_s$ is the system velocity and ρ_p stands for the density of the particle.

Eq. (2.1.8) states that the sum of forces acting on the control volume is equal to the sum of the rate of change of momentum within the control volume and the net efflux of momentum through the control surface. Since $\mathbf{u}_p$ is constant over the surface of the individual droplets, and considering the Eq. (2.1.4), the momentum efflux through the particle/droplet surface, (the third term on the right hand side), may be rewritten as:

$$\int_{S_p} \rho_p (\mathbf{u}_p + \mathbf{u}_s) \mathbf{u}_s \, dA = - \mathbf{u}_p \, S_{p,m} + \int_{S_p} \rho_s \mathbf{u}_s (\mathbf{u}_s . dA) \qquad (2.1.9)$$

By assuming that the mass flux over the surface of the droplet to be uniform, which is a reasonably good assumption for most applications, the last term in Eq. (2.1.9) reduces to zero, i.e.

$$\int_{S_p} \rho_s \mathbf{u}_s (\mathbf{u}_s . dA) = 0 \qquad (2.1.10)$$

The total force, $\mathbf{F}_{tot}$, on the gas phase can be considered that is consisted by :

(i). Forces, $\mathbf{F}_s$, acting on the surface S (pressure and shear forces), which, assuming that the void fraction α is 1, can be expressed as:

$$\mathbf{Fs} = - \int_{S_s} p dA + \int_{S_s} \tau dA \qquad (2.1.11)$$

where p is the gas pressure and τ is the shear stress tensor representing the diffusive fluxes.

(ii). Forces, $\mathbf{F}_{Sp}$, acting on the surface S_p (aerodynamic forces) which are expressed as:

$$\mathbf{F}_{Sp} = -\mathbf{F}_d \tag{2.1.12}$$

where $\mathbf{F}_d$ is the cumulative drag force acting on the particles / droplets per unit volume.

(iii). Body forces, such as gravitational and buoyant. The buoyancy being negligible, only the gravitational contribution is taken into account given by

$$\mathbf{F}_{grav} = \Sigma\, m_i\, \mathbf{g} \tag{2.1.13}$$

The resulting final momentum conservation equation is:

$$\mathbf{F}_{pressure+shear+aerodynamic+grav} = \left(\frac{\partial}{\partial t}\int_{V_c}\mathbf{u}\rho_p dV + \int_{S_s}\mathbf{u}\rho_p\mathbf{u}d\mathbf{A} - \mathbf{u}_p\, S_{p,m}\right) \tag{2.1.14}$$

and the corresponding differential equation,in cartesian tensor notation and for steady state flows, is :

$$\frac{\partial}{\partial x_i}(\rho u_i u_j) = -\frac{\partial p}{\partial x_i} + \frac{\partial \tau_{ij}}{\partial x_i} + S_{pi} \tag{2.1.15}$$

where S_{pi} is the overall momentum exchange between the two phases per unit volume

$$S_{di} = u_{pi}\, S_{p,m} - F_{di} \tag{2.1.16}$$

2.1.3 Energy Equation.

For a reacting flow the most useful form of the energy equation is that having the total (stagnation) enthalpy as the dependent variable. The energy of the gas phase consists of thermal and mechanical energies. The energy equation is obtained by the combination of the First Law of Thermodynamics with the Reynolds Transport Theorem. The energy per unit mass (i.e. the intensive property) is :

$$e = (i_g + u_g^2/2) \tag{2.1.17}$$

where i_g is the internal energy of the gas per unit mass and u_g the gas velocity magnitude.

Writing the First law of Thermodynamics for the control volume in Fig (2.1) we get:

$$Q - W = \frac{d(me)}{dt} \tag{2.1.18}$$

The rate of energy exchange, following the Transport Theorem, can be formulated as:

$$Q - W = \frac{\partial}{\partial t}\int_{V_c}\rho e dV + \int_{S}\rho e \mathbf{u}.d\mathbf{A} + \int_{S_p}\rho_s e_s \mathbf{u}_s.d\mathbf{A} \tag{2.1.19}$$

a. The work rate term, W, involving the rate of work done against the pressure and the shear stresses, can be written as:

$$W = \int_{S_s}(p\mathbf{u} - \tau.\mathbf{u}).d\mathbf{A} + \int_{S_p}(p_s(\mathbf{u}_p+\mathbf{u}_s) - \tau_s(\mathbf{u}_p + \mathbf{u}_s)).d\mathbf{A} \tag{2.1.20}$$

where p is the gas pressure and τ the shear stress tensor.

Assuming that the velocity of the vapour from the second phase at the droplet/particle surface is uniform and that the droplet/particle velocity $\mathbf{u}_p$ is constant over its surface, the work that is done against the pressure force over the droplet/particle surface can be cast as:

$$\int_{S_p}(p_s(\mathbf{u}_p+\mathbf{u}_s).d\mathbf{A}) = \mathbf{u}_p\int_{S_p}p_s d\mathbf{A} + \int_{S_p}p_s\mathbf{u}_s.d\mathbf{A} \tag{2.1.21}$$

Since the shear stress at the droplet/particle surface is normal to the vapour velocity vector, the work done against the shear stress over the droplet/particle surface reduces to:

$$\int_{S_p}\tau_s(\mathbf{u}_p + \mathbf{u}_s).d\mathbf{A}) = \mathbf{u}_p\int_{S_p}\tau_s d\mathbf{A} \tag{2.1.22}$$

and therefore the total work done over the droplet/particle surfaces can then be written as:

$$\int_{S_p}(p_s(\mathbf{u}_p+\mathbf{u}_s) - \tau_s(\mathbf{u}_p + \mathbf{u}_s)).d\mathbf{A} = \mathbf{u}_p\int_{S_p}p_s d\mathbf{A} - \mathbf{u}_p\int_{S_p}\tau_s d\mathbf{A} + \int_{S_p}(\frac{p_s}{\rho_s})\rho_s \mathbf{u}_s.d\mathbf{A}$$

(2.1.23)

The first two terms on the right hand side represent the aerodynamic forces on the droplet surface and can be reduced to:

$$\mathbf{u}_p\int_{S_p}p_s d\mathbf{A} - \mathbf{u}_p\int_{S_p}\tau_s d\mathbf{A} = \mathbf{u}_p \mathbf{F}_d \qquad (2.1.24)$$

b. Heat transfer to the gas takes place by conduction / convection across the surfaces S and S_p as well as by radiation absorbed by the gas. Thus :

$$Q = \int_{V_c} q_r dV - \int_S q d\mathbf{A} - \int_{S_p} q_p d\mathbf{A} \qquad (2.1.25)$$

where q_r is the radiation contribution, and q and q_p the convective contributions through the surfaces S and S_p respectively.

Finally, substituting the above expressions for heat transfer and work and taking into account the definition of the stagnation enthalpy, $h \equiv e + p/\rho$, into the energy equation (Eq. 2.1.19) yields

$$\frac{\partial}{\partial t}\int_{V_c}\rho e dV + \int_S \rho h \mathbf{u} d\mathbf{A} =$$

$$-\int_S q d\mathbf{A} - \int_{S_p} q_p d\mathbf{A} + \int_{V_c} q_r dV + \int_{S_p}\rho_s(\frac{p_s}{\rho_s}+e_s)\mathbf{u}_s d\mathbf{A} - \mathbf{u}_p F_d + \int_S \tau \mathbf{u}.d\mathbf{A} \qquad (2.1.26)$$

The corresponding differential form, in Cartesian tensor notation and for steady flows, is :

$$\frac{\partial}{\partial x_i}(\rho h u_i) = \frac{\partial}{\partial x_j}(\tau_{ij} u_i) - \frac{\partial q_i}{\partial x_i} + S_{p,h} + S_{rad} \qquad (2.1.27)$$

where $S_{p,h}$ is the energy exchange between the two phases given by :

$$S_{p,h} = S_{p,m} h_s - q_p - u_{pi} F_{di} \qquad (2.1.28)$$

where $S_{rad} = \int_{V_c} q_r dV$ is the radiation energy absorbed by the gas.

The first term on the right hand side of Eq. (2.1.27) is the work rate due to shear stresses, which , for the low Mach number flows typical in the combustion chambers, can be neglected (Kays, (1975).

The second term in eq (2.1.27) represents the heat transfer through the gas due to the local temperature gradient. This heat transfer term can be expressed in terms of the gas phase enthalpy, h, as:

$$q = -\frac{\mu}{\sigma_h}\frac{\partial h_i}{\partial x_i} \qquad (2.1.29)$$

Therefore, the final form of the energy equation can be cast as:

$$\frac{\partial}{\partial x_i}(\rho h u_i) = -\frac{\mu}{\sigma_h}\frac{\partial h_i}{\partial x_i} + +S_{p,h} + S_{rad} \qquad (2.1.30)$$

2.2 The Turbulence Model

2.2.1 The Closure Problem.

The instantaneous conservation equations (2.1.15) form a closed set of time dependent, non-linear, simultaneous partial differential equations which together with the appropriate boundary conditions are suitable for describing both laminar and turbulent flows. In the case of turbulent flows, accurate numerical solution, since analytical solution is not feasible, of these equations is only possible if the time and spatial discretisation is fine enough to account for all time and length scales (i.e. all eddies present in the flow). Tennekes and Lumley (1972) have shown that the ratio of the length and time scales of the smallest eddies to the large ones is inversely proportional to some power of the Reynolds number and thus the numerical solution would require prohibitive number of grid nodes and time steps to resolve the detailed structure of the turbulent flow.

Fortunately, for most engineering applications, it is sufficient to know the time-averaged properties of the turbulent flow rather than its details, so the problem may be circumvented by solving the time-averaged conservation equations describing the flow.

In order to obtain the time-averaged conservation equations a statistical approach is taken, Hinze (1959). The instantaneous values of any property, ϕ, is decomposed into a mean value, ϕ, and a fluctuating component ϕ'. After the time-averaging process statistical correlation such as, $\rho u_i' u_j'$ named 'Reynolds stresses and $\rho u_j' h'$ called turbulent fluxes, Bradshaw (1971), whose the magnitude is not known. In an attempt to obtain information about these correlations, by deriving additional equations, higher order correlations appear thus constituting the so called 'closure problem'. The obvious way out of the closure problem is by approximating these correlations in terms of quantities that can be evaluated. This task is called 'turbulence modelling'.

2.2.2 Classification of Turbulence Models.

Since late nineteenth century many attempts have been made to model turbulence varying in both form and complexity. The several types of turbulence models are usually classified in three main categories (Launder & Spalding , 1972) :

a. Algebraic turbulent-viscosity models

b. Differential turbulent-viscosity models

c. Models employing differential equations for the Reynolds stresses/scalar fluxes directly (second moment closure).

The first two employ Boussinesq's (1877), suggestion that "the stress-strain law for time-averaged turbulent flows could be represented in the same form as that for a Newtonian fluid in laminar motion". These models make use of an algebraic formula to estimate of the turbulent viscosity or solution of differential equations for one or more properties of the turbulent motion and are called 'eddy viscosity models'. The third category of models involves the solution of transport equations for the relevant

BIBL. LONDIN. UNIV.

Reynolds stresses. Reviews of the different turbulence models have appeared in recent bibliography. Among these, works by Bradshaw (1977), Rodi (1980), and Gibson et al (1987) offer an insight into the concepts that these models follow along with the advantages or disadvantages they carry.

2.2.2.1 Eddy Viscosity Models

Eddy viscosity models are based on an analogy of the Reynolds stresses to the viscous stresses in laminar flows.

The Reynolds stresses can then be written as :

$$-\overline{u_i u_j} = \frac{\mu_t}{\rho}\left(\frac{\partial U_i}{\partial x_j} + \frac{\partial U_j}{\partial x_i}\right) - \frac{2}{3}\delta_{ij}k \qquad (2.2.1)$$

and the scalar flux as

$$-\overline{u_i \phi} = -\frac{\mu_t}{\rho \sigma_t}\frac{\partial \Phi}{\partial x_i} \qquad (2.2.2)$$

where μ_t is the turbulent viscosity, σ_t is the turbulent Prandtl/Schmidt number, k the turbulent kinetic energy and δ_{ij} is the Kronecker delta. Turbulent viscosity, in contrast to the molecular viscosity, is not a fluid property but depends on the state of turbulence and may vary in space and time and depend on the nature of the flow. The above expressions do not form a closure to the turbulence problem since another unknown term, the turbulent viscosity μ_t has been introduced.

Eddy viscosity models are further classified by means of the number of additional transport equations that need to be solved. Thus we have zero-equation, one-equation and two-equation models. Example of models are belonging to these classes are cited below:

i. Zero-Equation Model.

Prandtl's (1925) mixing length model.

ii. One-Equation Models.

Prandtl (1945).

Bradshaw, Ferris and Atwell (1967).

Nee and Kovansznay (1968).

iii. Two-Equation Models.

Kolmogorov (1942).

Harlow and Nakayama (1968).

Spalding (1969).

Jones and Launder (1972).

2.2.2.2 The Reynolds stress models.

The Reynolds stress / scalar flux models do not use the eddy viscosity concept outlined above, but evaluate the statistical correlations by solving the differential equations derived directly from the instantaneous equations (see Hinze, 1959). This is necessary in circumstances leading to high levels of turbulence anisotropy, or where body force effects due to, e.g., streamline curvature, are observed to exert a strain influence in the turbulence field, for which cases eddy viscosity models do not perform well. In these circumstances it is necessary to extend the turbulence closure level to the

one where individual transport equations are solved for all the non-zero Reynolds stresses and scalar turbulent fluxes. The use of such a model, however, may require the solution of up to ten additional transport equations for three - dimensional flows, or even more if scalar variables are included. This becomes extremely uneconomical, if not impossible, for real engineering calculations given the capabilities of present-day computers.

2.2.3 The Choice of the Turbulence Model.

The two equation model of Jones and Launder (1972), known as the k - ε model, has been adopted for the present study. The choice is based on the fact that zero - and one - equation models require a length scale distribution to be prescribed and this is not feasible for the complex reacting flows of this study. On the other hand, as aforementioned, the use of multi - equation Reynolds stress models for three - dimensional two - phase reacting flows is unacceptable on economic grounds.

The k - ε model has been tested extensively for the calculation of turbulent reacting flows, see for example Hutchinson et al (1976), Gosman et al (1976), Salooja (1978), Megahed (1979), El - Banhawy (1980), and the results yielded are satisfactory.

2.2.4 The Transport Equation for the Turbulence Kinetic Energy.

The k - ε model utilises the concept of the effective viscosity defined as:

$$\mu_{eff} = \mu + \mu_t \qquad (2.2.3)$$

where μ stands for the molecular viscosity and μ_t for the turbulent viscosity. The latter is obtained from:

$$\mu_t = C_\mu \rho \frac{k^2}{\varepsilon} \qquad (2.2.4)$$

where C_μ is a model constant given in section (2.2.5). This relation follows from dimensional considerations, Emmons (1954), and specifies the turbulent viscosity in a

unique manner by the local values of density, turbulence kinetic energy and a turbulence length scale related to the dissipation rate of the turbulence kinetic energy, Hanjalic (1970).

The transport equation for the turbulence kinetic energy, the detailed derivation of which may be found in Rodi (1970), takes the form:

$$\frac{\partial(\rho k)}{\partial t} + \frac{\partial(\rho u_i k)}{\partial x_i} = \frac{\partial}{\partial x_i}\left(\frac{\mu_{eff}}{\sigma_k}\frac{\partial k}{\partial x_i}\right) + G - \rho\varepsilon \qquad (2.2.5)$$

where $k = 1/2\ u_i'u_i'$, is the turbulence kinetic energy, $\varepsilon = \nu\left[\frac{\partial ui'\partial ui'}{\partial xj\ \partial xi}\right]$ is the dissipation rate of turbulence kinetic energy, C_d is a model constant the value of which is given in section (2.2.6) and G is the generation term given by :

$$G = -\rho ui'uj'\frac{\partial ui}{\partial xj} \qquad (2.2.6)$$

where the Reynolds stresses τ_{ij} are modelled according to the equations (2.2.1)

2.2.5 The Transport Equation for the Dissipation Rate of the Turbulence Kinetic Energy.

The transport equation for the dissipation rate, ε, of the turbulence kinetic energy is given by, Harlow and Nakayama (1968);

$$\frac{\partial(\rho\varepsilon)}{\partial t} + \frac{\partial(\rho u_i \varepsilon)}{\partial x_i} = \frac{\partial}{\partial x_i}\left(\frac{\mu_{eff}}{\sigma_\varepsilon}\frac{\partial \varepsilon}{\partial x_i}\right) + C_1\frac{\varepsilon}{k}G - C_2\frac{\varepsilon^2}{k} \qquad (2.2.7)$$

where σ_ε , C_1, and C_2 are model constants given in section (2.2.6).

2.2.6 The Turbulence Model Constants.

The values of the turbulence model constants and turbulent Prandtl numbers, as recommended by Launder et al(1972) and Launder and Spalding (1974), are given in table (2.2.1).

C_μ	C_1	C_2	σ_k	σ_ε	σ_ϕ
0.09	1.44	1.92	0.9	1.22	0.7-0.9

Table 2.1. Constants for the k-ε Model

2.3 The Droplet/Particulate Phase

2.3.1 Eulerian and Lagrangian Approaches.

Two fundamentally different mathematical approaches may describe the transport processes in two -phase flows, namely the Eulerian and the Lagrangian.

In the Eulerian approach the transport equations are cast in such a way that they represent the balance of some property at a fixed "station" in space with time.

In the Lagrangian approach a material element (fluid particle, droplet or solid particle) is traced and the flow field is described as a function of its dynamical history and time.

As aforementioned the Eulerian approach has been adopted to describe the carrier-phase treating it thus as a continuum and the transport equations have been derived in section 2.1. One of the two approaches has to be applied for the description of the discrete phase and the treatment of the phase coupling.

2.3.1.1 The Choice of the Approach.

The Eulerian or Continuum approach for describing two-phase flows treats the discrete phase as a kind of a continuum i.e. in the manner as the carrier-phase and solves for the appropriately modified transport equations for both the phases simultaneously. This formulation has proved to be preferable in cases where the discrete phase concentration

is high enough so that the densities of the gas and the mixture can be discriminated according to the values of the void fraction. The modelling that supports this approach is mainly limited by the closure of the turbulence equations which has to take into account the interaction between the phases, Pouramahdi and Humphrey (1983), and the imposition of appropriate boundary conditions for the particulate phase, Looney et al (1985). Assuming the two phases to be interspersed and due to the large value of the void fraction , the derivation of the transport equations is extremely complicated when it comes to averaging over the control volume, Drew and Segel (1971). The Eulerian approach necessitates the solution of a transport equation for each size group of particles thus the computer memory requirements increase considerably whenever the particulate phase is polysized. In order to take care of the numerical diffusion, which is related to the fineness of the numerical grid, Leschziner (1980), more grid nodes should be employed for simulating the flow but this quickly becomes prohibitively expensive in the Eulerian formulation because of the transport equations needed to be solved.

In the Lagrangian approach, formulated by Migdal and Agosta (1967), the flights of statistically representative particles are tracked from the point of entry to the exit of the domain under consideration. The coupling between the phases is achieved by means of explicit source terms of mass, momentum and energy.

Comparison studies between the discrete and continuum models by Lockwood and Syed (1977) and by Abbas et al (1981) favour on balance the Lagrangian approach against the Eulerian treatment. The following are considered to be the principal advantages which weigh in favour of the Lagrangian treatment:

(i) Particle slip is easily accounted for.

(ii) The computer storage requirement does not increase with the number of size groups in contrast with the Eulerian formulation. This could well be the single deciding factor for three-dimensional combustion computations.

(iii) Particle phenomena like drag, heat transfer, devolatilisation and evaporation, heterogeneous combustion and other physical phenomena are conveniently modelled.

(iv) The Lagrangian approach is computationally economical, Abbas (1982).

(v) The turbulent dispersion of particles, which is not so easily handled through the Lagrangian formulation, has been addressed, Papadopoulos (1989), with satisfactory results.

Opposing the choice of the Lagrangian approach is the fact that it may prove less stable due to the explicit source terms imposed on the mean flow calculations for the coupling of the two phases.

On the basis of the above arguments, the Lagrangian formulation has been adopted to describe the discrete phase for the present study.

2.3.2 Mathematical Formulation.

In the present study certain assumption are made for the derivation of the Lagrangian form of the discrete phase conservation equations of mass, momentum and energy. These assumptions are:

(i) The droplets/particles comprising the discrete phase are considered to be spherical. Their deformation may be taken into account in an implicit manner, if necessary, through the use of appropriate formulae for the drag coefficient and Nusselt number although the shape of the particles/droplets is assumed spherical for the calculations, Yuen and Chen (1976) and (1978).

(ii) The particle-particle or droplet-droplet interaction is neglected, assuming that the particle/droplet - gas coupling is more important than the collisions taking part between the particles/droplets. This can be assessed by the ratio of the time between collisions, τ_c, and the aerodynamic response time, τ_r, Crowe (1976), through the relationship:

$$\frac{\tau_r}{\tau_c} = Z \frac{Re_p}{10} \qquad (2.3.1)$$

where Z stands for the loading ratio, i.e. the ratio of the particle/droplet mass to the gas mass per unit volume, and Re_p is the particle/droplet Reynolds number expressed as a function of the particle/droplet - gas relative velocity, Crowe (1976). This ratio is much less than unity for most two - phase flows of engineering importance, which implies that aerodynamic forces dominate between the collisions and therefore the collisions between the particles/droplets can be neglected.

(iii) The particles/droplets do not agglomerate, coalesce nor break up to form smaller ones, although in reality they do.

(iv) The effect of the presence of the particles/droplets on the gas turbulence is accounted for in an implicit manner through the momentum and mass exchange and the k - ε turbulence model. It is assumed that the turbulence characteristics are not affected due to the presence of the second phase.

(v) The motion of the gas around the particle/droplet is considered to be quasi - steady, that is the flow adjusts immediately to the local boundary conditions for each instant of time, Faeth (1983), Sirignano (1983).

2.3.2a. Particle/Droplet Mass Balance Equation.

When the coal particle or oil droplet enters the combustion chamber it undergoes certain physical and chemical changes due to the convective and radiative heat exchange with the surrounding hot environment. Even though the phenomena that are taking place are completely different for the pulverised coal particles and the atomised oil droplets they both result in a mass efflux from the particle or droplet surface. During their flights the coal particles inside the combustion chamber undergo rapid heating, pyrolysis and char combustion. They exchange matter and heat with the surroundings by diffusion and convection and they experience further energy transfer due to thermal radiation. On the

other hand, the oil droplets evaporate due the rapid heating. The modelling of these processes will be discussed in sections (2.4.2) and (2.4.3) respectively.

The total rate of change of the particle or droplet mass, ignoring agglomeration or disintegration can be written as:

$$-\frac{dm_p}{dt} = r_{e,p} \qquad (2.3.2)$$

where $r_{e,p}$ is the rate of mass efflux from the particle or droplet surface due to the aforementioned processes.

2.3.2b. Equation of the Mean Motion.

The equation of motion for a non - rotating particle can be fully described by Newton's second law of motion written as:

$$\frac{d(m_p \mathbf{u}_p)}{dt} = \mathbf{F}_{tot} \qquad (2.3.3)$$

where m_p stands for the particle/droplet mass, $\mathbf{u}_p$ for the particle/droplet mean velocity in vector form, t for time and $\mathbf{F}_{tot}$ is the resultant of the forces acting on the particle/droplet in vectorial form.

The total force is composed of the following contributions:

(i) The drag force, which is a function of the particle/droplet relative velocity with respect to the gas, may be expressed as:

$$\mathbf{F}_{drag} = \frac{\rho_g A_p C_d}{2} | \mathbf{u}_g - \mathbf{u}_p | (\mathbf{u}_g - \mathbf{u}_p) \qquad (2.3.4)$$

where $\mathbf{F}_{drag}$ is the drag force in vectorial form, ρ_g is the gas density, A_p for the particle/droplet cross sectional area, and C_d is the drag coefficient.

(ii) Any particle that accelerates relative to the surrounding fluid induces a gas flow around it. This flow gives birth to an induced mass that requires an additional force in order for it to be accelerated, Wallis (1969), thus giving rise to an apparent force that is called apparent mass force. When the ratio of the gas to the particle density is much smaller than unity, then the inertial apparent force is negligible, Zubar (1964) .

(iii) The pressure gradient force due to the static pressure gradients in the flow across the particle in the direction of the motion.

(iv) The gravitational force that accounts for buoyancy effects is defined as :

$$\mathbf{F}_{grav} = m_p \mathbf{g} \frac{\rho_p - \rho_g}{\rho_p} \qquad (2.3.5)$$

where **g** stands for the acceleration of gravity. When the density of the gas is significantly smaller than the density of the particle, which is assumed to be the case for the present study, the buoyancy effect is neglected.

(v) Though the Magnus force, due to the rotation of the particle or the shear rate in the gas or both, is not taken into consideration for the present study since the particle is assumed to be a non-rotating. It is of significance only when the particles are large, Boothroyd (1971).

(vi) The Basset force, which constitutes an instantaneous flow resistance, becomes substantial only when the particle is accelerated at high rates and is also neglected.

(vii) The particle-particle interaction cannot be included as an explicit contribution to the total force but it can be modelled if necessary in a rather ambiguous manner through the use of an appropriately modified drag coefficient, McGarvey (1983) .

(viii) The particle-solid boundary interaction is modelled through the use of semi-analytic expressions, see section (3.7.3).

Due to the aforementioned contributions equation (2.3.2.1) is recast as :

$$\frac{d\mathbf{u}_p}{dt} = \frac{\rho_g A_p C_d}{2 m_p} |\mathbf{u}_g - \mathbf{u}_p| (\mathbf{u}_g - \mathbf{u}_p) + \mathbf{g} \qquad (2.3.6)$$

The drag coefficient Cd for a single particle moving in free, infinite flow depends primarily on the particle Reynolds number which is based on the mean relative velocity of the particle with respect to the gas.

$$Re_p = \frac{\rho_g |\mathbf{u}_g - \mathbf{u}_p| d_p}{\mu} \qquad (2.3.7)$$

where Re_p stands for the particle Reynolds number, d_p for the particle diameter and μ for the laminar viscosity of the gas. For the present study the drag law due to Wallis (1969) has been employed, and is expressed as:

$$C_d = \frac{24}{Re_p} (1.0 + 0.15\, Re_p^{0.687}) \qquad (2.3.8)$$

By combination of Eq (2.3.7) and (2.3.8) and substitution into Eq. (2.3.6) we obtain:

$$\frac{d\mathbf{u}_p}{dt} = W (\mathbf{u}_g - \mathbf{u}_p) + \mathbf{g} \qquad (2.3.9)$$

where W is equal to $18\mu C_d Re_p / 24 \rho_p d_p^2$ and τ_p, the particle dynamic characteristic time, is equal to W^{-1}.

For a given timestep Δt the analytical integration of Eq. (2.3.9) provides the mean final particle velocity as a function of the initial mean particle velocity at the initial spatial position, the timestep and the characteristic time. The mean final particle velocity may be expressed in vector form as :

$$\mathbf{u}_{p,f}(t) = \mathbf{u}_{g,i}(t) + \tau_p \mathbf{g} + (\mathbf{u}_{p,i}(t) - \mathbf{u}_{g,i}(t) - \tau_p \mathbf{g}) \exp (-\frac{\Delta t}{\tau_p}) \qquad (2.3.10)$$

where subscripts i and f stand for the initial and final position of the particle/droplet.

As can be seen both Eqs. (2.3.9) and (2.3.10) are in vectorial form and therefore they can easily be decomposed into the three components for the Cartesian co-ordinate system in use at this present study.

2.3.2c. Energy balance Equation.

Due to the different processes the coal particles and the oil droplets undergo the equation for the energy balance of the discrete phase will be written separately for each case.

2.3.2c.1. Coal Particle Energy Balance.

The total rate of heat gains or losses by the particle per unit mass, Q_t, comprises the contributions due to convection, Q_c, combustion, Q_b, and thermal radiation, Q_r. It may be written :

$$Q_t = Q_c + Q_b + Q_r \qquad (2.3.11)$$

A heat balance for the particle gives:

$$\frac{d}{dt}(m_p c_p T_p) = m_p Q_t - c_p T_p \left(-\frac{dm_p}{dt}\right) - L_v \frac{dm_p}{dt} \qquad (2.3.12)$$

where c_p is the particle specific heat , T_p the particle temperature, and L_v the latent heat of devolatilisation which is zero on the completion of devolatilisation.

Assuming that $\frac{dc_p}{dt} = 0$, equation (2.3.12) reduces to :

$$c_p \left(\frac{dT_p}{dt}\right) = Qt - \frac{L_v}{m_p}\left(\frac{dm_p}{dt}\right) \qquad (2.3.13)$$

This equation, integrated over discrete time intervals, is used for the calculation of the particle temperature in the combustion chamber, see section (3.7.2b).

Convective Heat (Q_c).

The rate of heat transfer per unit mass to or from the particle by convection is, see also Baum and Street (1971) :

$$Q_c = \pi d_p^2 h (T_g - T_p) / m_p \qquad (2.3.14)$$

where T_g is the gas temperature and h stands for the heat transfer coefficient given by,Ingebo (1962) :

$$h = Nu \frac{K_g}{d_p} \tag{2.3.15}$$

where Nu is the Nusselt number and K_g is the thermal conductivity of the gas. It must be noted here that the particle temperature is presumed to be uniform across the particle surface. The particle Nusselt number is given, see Kuo (1986) for example, through the expression :

$$Nu = 2.0 + 0.6\, Re_p^{1/2}\, Pr^{1/3} \tag{2.3.16}$$

where Pr is the Prandtl number. The thermal conductivity is evaluated through the following empirical expression proposed by Baum and Street (1971) :

$$K_g = 6.739 \times 10^{-5}\, T_g + 6.446 \times 10^{-3} \tag{2.3.17}$$

Heat Transfer due to Combustion (Q_b)

The rate of heat released on or near the particle surface per unit mass due to burning is obtained by assuming that the reaction of carbon dioxide and water with char carbon are negligible. The rate of heat gain per unit mass by the particle is given by :

$$Q_b = \frac{\eta\, H_c}{m_p} \left(- \frac{dm_p}{dt} \right) \tag{2.3.18}$$

where H_c is the char calorific value for complete combustion and η is the fraction of the heat released that is absorbed by the particle during combustion, arbitrarily taken as unity in the present study. However, if intermediate reaction is considered, for example oxidation of the char carbon to carbon monoxide and subsequent oxidation of the carbon monoxide to carbon dioxide in the gaseous phase, this fraction is less than unity, see Risvi, (1985) and Truelove and Williams, (1988).

Heat Transfer due to Radiation (Q_r).

The rate of radiative heat exchange per unit mass between the particle and the surroundings, assuming that the particles are spherical and behave as a grey body, may be expressed as :

$$Q_r = \pi \sigma \varepsilon_p \frac{d_p^2}{m_p} (T_R^4 - T_p^4) \qquad (2.3.19)$$

where σ is the Stefan-Boltzmann constant (5.67×10^{-8} J / m^2 s K^4), T_R is the ' radiation temperature ' and ε_p is the particle emissivity, see section (2.5) for further explanation.

2.3.2c.2 Oil Droplet Energy Balance Equation.

The heat transfer rate, Q_p, to the oil droplet can be written, see Abbas, (1982), :

$$Q_p = m_p \frac{di_p}{dt} - (h_s - i_p + \frac{u_s^2}{2}) \frac{dm_p}{dt} \qquad (2.3.20)$$

where m_p is the droplet mass, i_p is the internal energy per unit mass, h_s is the specific enthalpy of the evaporated mass, and $u_s^2/2$ is the droplet kinetic energy per unit mass. The value of $u_s^2/2$ is small compared to h_s so that it can be neglected, while the value of i_p can be evaluated as :

$$i_p = c_p T_p \qquad (2.3.21)$$

where c_p stands for the droplet specific heat, and T_p for its temperature.

Assuming that the prevailing mechanism of heat transfer to the droplet is by convection, Qp may be estimated as :

$$Q_p = \pi d_p^2 h (T_g - T_p) \qquad (2.3.22)$$

where Dp stands for the particle diameter, Tg is the gas temperature and h stands for the heat transfer coefficient, given in Eq. (2.3.15). The values of the Nusselt number are obtained from Chigier and Yule, (1977), as :

$$Nu = 2.0 + \frac{0.55\ (Re_p^{1/2}\ Pr^{1/3})}{(1.0 + 1.237/Re_p Pr^{4/3})^{1/2}} \qquad (2.3.23)$$

Finally the thermal balance equation can be cast as :

$$\frac{dTp}{dt} = \frac{6k_g}{\rho_p c_p D_p} Nu\ (T_g - T_p) - \frac{3L}{c_p d_p} \left|\frac{Dd_p}{dt}\right| \qquad (2.3.24)$$

where $L = h_s - i_p$ stands for the latent heat of vaporisation. This equation, integrated over discrete time steps, is used for the calculation of the droplet temperature. The droplet diameter diminution, $\frac{Dd_p}{dt}$, is dealt with in section (2.4.2).

2.4 The Combustion Models

A practical combustion system contains many complexities : The fuel may be gaseous or atomised liquid droplets or solid particles. The reaction mechanism vary with the type of fuel and may involve literally hundreds of intermediate and resultant species including radicals, soot formation and significant heat transfer by radiation. For different type of fuels different physical phenomena are present and different mechanisms are dominant. In addition, the reaction rate are subject to large uncertainties. The problem is further complicated, since turbulence determines the mixing of the reactants and products and through that the reaction rates.

Since the scope of this study extends to all three major types of fuels, i.e. gas, oil and coal, the combustion modelling will be dealt with separately for each type of fuel in the following sections. An effort has been made, though, to maintain similar approaches to secure a more unified formulation.

2.4.1 Gas Combustion Modelling.

A global one step reaction between fuel and oxidant is assumed, see for example Pun and Spalding, (1967), and Lockwood and Syed (1976). This procedure is termed 'The Simple Chemical Reacting System', (SCRS). This reaction is assumed to be instantaneous. A consequence of this assumption is that chemical equilibrium prevails everywhere in the flame. The fuel and oxidant combine in stoichiometric proportions such as :

$$1\text{kg fuel} + s\text{ kg oxidant} \rightarrow (1+s)\text{ kg products} \qquad (2.4.1)$$

This assumption reduces the number of species present to only three, namely the fuel, oxidant and products. The further conventional assumption made is that the turbulent exchange coefficients, Γ_{eff}, for all species are equal. The quantity :

$$\phi = sm_{fu} - m_{ox} \qquad (2.4.2)$$

becomes a passive scalar of the flow, i.e. a conserved quantity. It is convenient to define the mixture fraction, f, which is a normalised ϕ, as :

$$f = \frac{\phi - \phi_0}{\phi_1 - \phi_0} \qquad (2.4.3)$$

where subscripts 0 and 1 designate the oxidant and fuel bearing streams respectively. The value of f in the fuel stream is 1 whereas in the oxidant stream is 0.

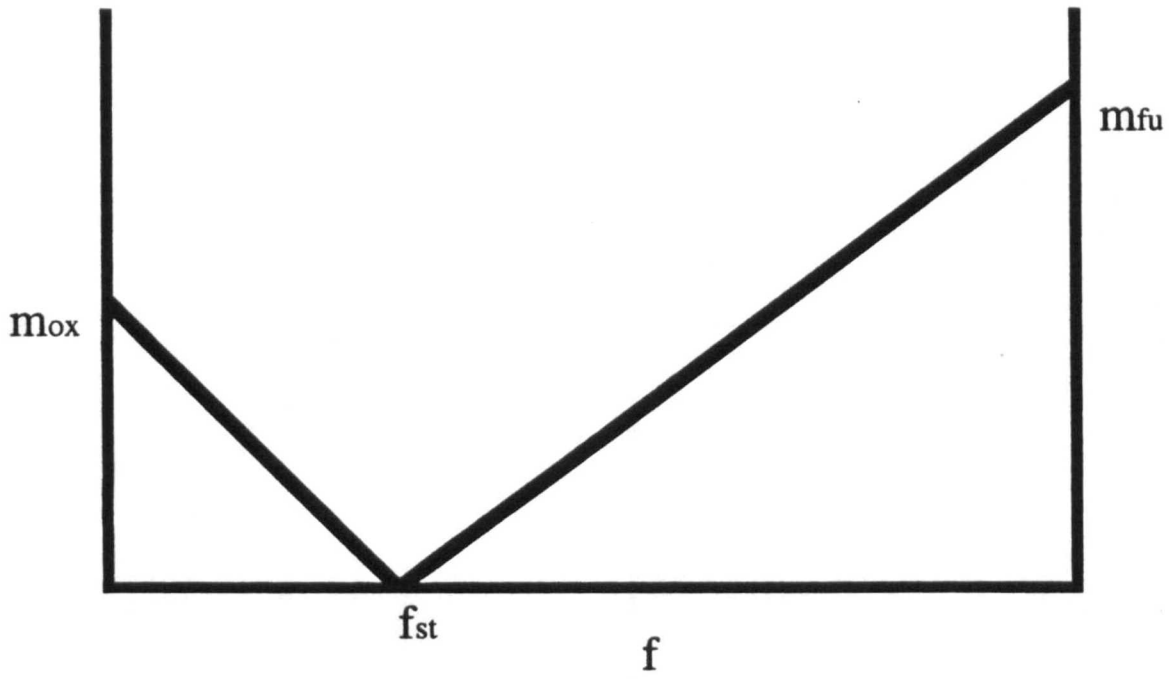


Fig. 2.3 Mass Fraction of Species as a Function of the Mixture Fraction

The stoichiometric mixture fraction, f_{st}, is obtained by substituting the values of the mass fractions of fuel and oxygen in Eq. (2.4.3) and is given by:

$$f_{st} = \frac{m_{ox0}}{s m_{fu1} + m_{ox0}} \qquad (2.4.4)$$

The instantaneous chemical reaction assumption implies a much faster chemical kinetic compared with the turbulent mixing rate. As a result fuel and oxidant cannot co-exist and accordingly, the fuel and oxidant mass fractions are linearly related to the mixture fraction, f, see Fig. (2.3), through the following expressions:

for $0 \le f \le f_{st}$ $\quad m_{fu} = 0$

$$m_{ox} = m_{ox0}\,(f_{st} - f)/f_{st} \qquad (2.4.5)$$

for $f_{st} \le f \le 1$ $\quad m_{fu} = m_{fu1}\,(f - f_{st})/((1 - f_{st})$

$$m_{ox} = 0 \qquad (2.4.6)$$

The mass fraction of an inert species m_{in}, is given by :

$$m_{in} = m_{in0}\,(1 - f) + m_{in1} \qquad (2.4.7)$$

The products mass fraction is obtained by subtraction, since the sum of the mass fractions of the species present in the mixture must be equal to 1. Therefore the mass fraction of the products is written as :

$$m_{pr} = 1 - (m_{ox} + m_{fu} + m_{in}) \qquad (2.4.8)$$

The mixture fraction is also a passive scalar since it is a linear combination of conserved quantities and therefore it obeys a similar transport equation :

$$\frac{\partial}{\partial x_i}(\rho \upsilon \varepsilon_i f) - \frac{\partial}{\partial x_i}\left[\Gamma_{f,eff}\frac{\partial f}{\partial x_i}\right] = 0 \qquad (2.4.9)$$

By solving this scalar transport equation simulataneously with the other equations describing for the flow field and enthalpy, one can obtain the values of the mixture fraction at any point in the combustion chamber. The mass fractions of the species present in the combustion mixture are subsequently calculated through the model described above, Eq. (2.4.5 and 6). In section (2.4.4) the thermodynamics of this model will be considered.

2.4.2 Oil Combustion model

This section deals with the droplet evaporation, soot formation and oxidation and gas-phase combustion modelling in oil flames.

2.4.2a. Expression of Droplet Diminution

The chemical reaction process in spray flames is one of the most complicated phenomena. However, it has been experimentally found, Chigier et al, (1973,1974), Onuma et al (1975,1977), Tuttle et al (1976), Komiyama et al (1977) and Styles et al (1977) that the chemical reaction process in spray flames of volatile fuels is similar to that of turbulent gaseous diffusion flames. An implication of this is that the vaporisation time is short. This conclusion has been extended, Onuma (1977), in the case of combustion of heavy oils. Therefore, the spray combustion model used herein is based on the assumption that the liquid droplets act as distributed sources of fuel vapour within the flame.

The combustion of heavy - fuel droplets is mainly characterised by the formation of cenospheres directly after the early stages of the combustion of the medium fuels, Williams (1973) and Williams (1976). Two theoretical models for the combustion of heavy oil fuel droplets the Ideal - Mixture Model and the Shell Model were derived by Law (1976). In the first model, the droplet is assumed to comprise an ideal mixture of the different fuel components, as the name implies, whilst in the second one, a shell - like distribution of fuel components is assumed such that quasi - steady single component combustion prevails for each shell.

For reasons of simplicity, an expression based on single component droplets evaporation is used herein. The droplets are assumed to comprise a fuel mixture having properties with averaged values. Furthermore, the influence of droplet interaction is neglected.

A typical and widely used rate of droplet diameter diminution of a single droplet, Spalding, (1953), is given by :

$$\frac{dD_p}{dt} = -\frac{4K_g}{\rho_p C_{pg} D_p} C \ln(1+B) \qquad (2.4.10)$$

where B is the transfer number for evaporating droplet in the absence of chemical reaction around it, given by, Spalding,(1953) :

$$B = C_{pg} (T_g - T_{sat}) / L \qquad (2.4.11)$$

and C is an empirical correction factor, Faeth and Lazer (1971), to account for the effect of convection on the evaporation rate. This constant is expressed as :

$$C = 1 + \frac{0.278 \, (Re_p^{1/2} \, . \, Pr^{1/3})}{(1 + 1.237/Re_p \, Pr^{4/3})^{1/2}} \qquad (2.4.12)$$

2.4.2b. Soot Model.

Soot formation is considerable in oil combustion and the presence of soot at high temperatures will enhance radiation from the flame to the walls of the combustion chamber. Furthermore, incomplete oxidation due to, for example, unsatisfactory aerodynamic design may prevent complete oxidation of the soot resulting thus in the emisssion of undesirable solids. These considerations have become accentuated as a result of the increasing use of lower grade and alternative fuels which frequently exhibit an augmented tendency to soot, Blazowski, (1978). A comprehensive review of literature dealing with soot can be found in Wagner , (1979) and Edelman et al (1979).

Several soot models which are suitable for furnace calculations have been reported, for example, Cozzi et al (1972), Khan and Greeves (1974), Magnussen et al (1976) and (1978) and Leung et al (1991). Some of the models consider the chemical aspects of soot formation and combustion and some are computationally expensive to incorporate into a three dimensional combustion model. The model used in this study is that of Lockwood and Abbas, (1985). This model has been used with some success in a

number of previous applications, Abbas(1978), Lockwood and Abbas (1985), Carvalho (1983), Malalasekera, (1988).

2.4.2b.1. Description of the Soot Model.

Soot is assumed to a single chemical species in the solid phase and the transport equations for the soot mass fraction, m_s, can be written :

$$\frac{\partial}{\partial x_i}(\rho u_i m_s) - \frac{\partial}{\partial x_i}\left[\Gamma_{f,eff}\frac{\partial m_s}{\partial x_i}\right] = S_s \qquad (2.4.13)$$

The distribution of soot can be obtained by solving the above equation which is coupled to the flow field. The source term S_s in equation (2.4.11) is given as

$$S_s = S_f - S_d \qquad (2.4.14)$$

where S_f stands for the soot formation and S_d for soot destruction (soot combustion).

(i) Soot Formation Model.

Two step models have been used by Tesner et al (1971) and Magnussen et al (1976), (1978) for the calculation of soot concentrations. In spite of the potentially greater generality of a two step formulation, an one step reaction for soot formation rate S_f of the kind used by Khan and Greeves (1974) is used in the present study.

$$S_f = C_f P_{fu} \phi^n \exp(-E_f/.RT) \qquad (2.4.15)$$

where p_{fu} is the partial pressure of the fuel, ϕ is the local equivalence ratio deduced from the mixture fraction and C_f, n and E_f are model constants. Following Lockwood and Abbas, (1985), the values used here are $n = 3$, $E_f/R = 20000$. The value of C_f is a function of an easily defined fuel property such as C/H ratio and is assigned a value of 0.01, Barreiros et al (1992).

The equivalence ratio, ϕ, and the fuel partial pressure, P_{fu} ,are calculated from the following relations :

$$\phi = \frac{f}{1-f} s_{fu} \qquad (2.4.16)$$

$$P_{fu} = x_{fu} P_0 \qquad (2.4.17)$$

where x_{fu} is the fuel volume fraction and s_{fu} is the stoichiometric oxygen requirement.

Experimental work by Glassman (1979) and Blazowski (1980) has shown that soot formation is absent for values of ϕ less than that corresponding to the incipient sooting limit and for ϕ in excess of a value corresponding roughly to the upper flammability limit. Following Khan and Greeves, (1974), these limits have been set to 2 and 8 respectively.

The calculated mixed mean mixture fraction is not appropriate for the calculation of soot since soot is produced in the immediate vicinity of the droplet. Early calculations showed that the calculated mean mixture fraction was almost everywhere less than that corresponding to the lower sooting limit. A linear variation was presumed between the value taken as unity at the droplet surface and the far field mean value. A satisfactory near droplet mean value is then simply :

$$f_d = \frac{1 + f}{2} \qquad (2.4.18)$$

(ii) Soot Combustion Model.

A simple method of estimating the soot burning rate has been proposed by Magnussen et al (1977) which presumes that the turbulence decay of the mixing rate is proportional to the magnitude of the soot concentration m_s, and the time scale of the large scale turbulence motion ε/k. Accordingly the rate of soot combustion can be expressed as :

$$S_d = A\, m_s \frac{\varepsilon}{k} \qquad (2.4.19)$$

for regions where the local soot concentration is low compared with the oxygen concentration. The model constant is assigned the value of 4, Magnussen et al ,(1977). In regions where the oxygen concentration is low, the rate of soot combustion will be limited by the lack of O_2. However, it must compete for oxygen with the unburnt fuel. This leads to the following expression, Magnussen et al , (1977) :

$$S_d = A \left[\frac{m_{ox}}{m_s s_s + m_{fu} s}\right] m_s \left(\frac{\varepsilon}{k}\right) \qquad (2.4.20)$$

where s_s is the stoichiometric oxygen requirement to burn 1kg of soot. Since either of the two expression describe a rate limiting process, the one that takes the smaller value will control leading to

$$S_d = \min \left\{A\, m_s \frac{\varepsilon}{k}, A \left[\frac{m_{ox}}{m_s s_s + m_{fu} s}\right] m_s \left(\frac{\varepsilon}{k}\right)\right\} \qquad (2.4.21)$$

2.4.2c Gas-Phase Combustion Model.

For the case of oil combustion a similar approach, as in the case of gas combustion, has been followed. Using the definitions of the passive scalar, ϕ, and the mixture fraction, f, and by algebraic manipulation of the transport equations for m_{fu} and m_{ox}, a transport equation for the time - averaged mixture fraction can be obtained. This equation in the presence of fuel droplets is given by :

$$\frac{\partial}{\partial x_i}(\rho \overline{u_i f}) - \frac{\partial}{\partial x_i}\left[\Gamma_{f,eff} \frac{\partial \overline{f}}{\partial x_i}\right] = S_{p,f} \qquad (2.4.22)$$

The generation term, $S_{p,f}$, in the f equation accounts for the release of fuel vapour due to droplet evaporation, calculated in section (2.3.2a). Details of the derivation of this equation are given in Appendix A.

2.4.3 Coal Combustion Model.

The processes of devolatilisation and heterogeneous combustion of pulverised coal as well as the gas-phase combustion are considered in this section.

2.4.3a. The Devolatilisation Model.

The purpose of a devolatilisation model is to describe the complex decomposition and transport phenomena occurring during fast pyrolysis. A complete pyrolysis model should be able to describe, at all stages of devolatilisation, the composition and physical state of the coal dust as well as the composition and evolution rate of the volatiles. Different proposals have been made to simulate this complicated physical process, see the review by Anthony and Howard (1976). The usable existing models are basically the ' single reaction model', Badzioch and Hawksley (1970), the ' two-competing reaction scheme', Kobayashi et al, (1976), and the 'multiple parallel reaction model', Anthony and Howard, (1976). The formulations vary in their degree of complexity, but depend strongly on empirical correlations so their application is restricted to certain types of coal. In reality it is restricted to coals very similar to those for which the model constants have been defined through experiments. These models have been used and assessed, Risvi, (1985), Lockwood and Mahmud, (1988), Levy, (1991), and none of them gave completely satisfactory predictions.

The 'single reaction model' has been favoured for use in this study. The main advantage of this model is that only two parameters for the two Arrhenius constants have to be prescribed in contrast with the six for the two-competing reaction scheme and further and largely statistical parameters for the multiple parallel reactions model.

The adopted model assumes that the volatiles are released by a single reaction (chemical decomposition). The cumulative amount of volatiles yield V up to time t as a weight fraction of the initial coal follows the equation :

$$\frac{dV}{dt} = k\,(V^* - V) \qquad (2.4.23)$$

where V^* is a prescribed maximum amount of volatiles release given by proximate analysis.

The rate constant k is given by an Arrhenius expression :

$$k = k_0 \exp\,(-E_{devol} / RT) \qquad (2.4.24)$$

Integration of eq. 3.2.1 over a time step Δt, gives

$$V = V^* \{1 - \exp[\, -k_0 \exp(\, -E_{devol} / RT\,)\,\Delta t\,]\,\} \qquad (2.4.25)$$

A simple model, is used to link the extent of particle swelling to the progress of volatile evolution. The particle diameter $d_{p,}$ at any degree of pyrolysis is may be expressed as

$$d_p = d\,[1 + (s_{WV} - 1)\,(1 - x_V)] \qquad (2.4.26)$$

where, x_V is the fraction of the total volatiles not yet evolved and s_{WV} is the swelling factor.

2.4.3b. The Char combustion model.

The reaction rate in heterogeneous combustion is controlled by two rate limiting processes, see, Risvi (1985), Smoot and Pratt, (1979), and Field et al (1967), which are:

•Chemical kinetics

•Diffusion of oxygen to the particle surface

and therefore two different rate constants k_c and k_d are involved in the modelling of this phenomenon. There is also pore diffusion which is usually considered into the chemistry expressions.

(i) The chemical rate coefficient k_c is given by a first order Arrhenius expression

$$k_c = A \exp (-E_{char} /RT) \qquad (2.4.27)$$

where E_{char} is the activation energy for the char combustion and A is the rate constant.

(ii) The diffusion coefficient is given by

$$k_d = D_c M_c /[R d_p/2 (T_p + T_g) /2)] \qquad (2.4.28)$$

where

$$D_c = D_0 \left(\frac{P_0}{P}\right) \left(\frac{T_g}{T_0}\right)^{1.75} \qquad (2.4.29)$$

D_0 is the binary diffusion coefficient, P_0 is the atmospheric pressure, P is the gas pressure, R is the universal gas constant and M_c is the molecular weight of carbon.

Finally the two separate coefficients, assuming first order reactions, can be combined in an overall reaction rate coefficient

$$k_t = \frac{k_c k_d}{k_c + k_d} \qquad (2.4.30)$$

which ensures that the actual controlling process is the slowest of the two.

The rate of the particle mass change due to heterogeneous combustion is

$$\frac{dm_p}{dt} = -k_t \pi d_p^2 P (FO_2)_\infty \qquad (2.4.31)$$

and therefore the final particle density can be calculated as

$$\rho_{p,f} = \rho_{p,i} - 6k_t P (FO_2)_\infty \Delta t \frac{d_{pf}^2}{d_{pi}^3} \qquad (2.4.32)$$

where $(FO_2)_\infty$ is the molar fraction of oxygen in the surrounding gas.

2.4.3c Gas - Phase Combustion Modelling

2.4.3c.1. The coupling of the Phases.

A definition different to the well-known one for the mixture fraction concept is proposed in order to couple the volatile release and char combustion modelling (Lagrangian approach) with the solution of the gas phase transport equations (Eulerian approach).

The transport equations for the mass fractions: m_{ox}, m_{vol}, m_c, of oxygen, volatiles and residue carbon respectively, can be written

$$L(m_{ox}) = R_{ox,1} + R_{ox,2} \qquad (2.4.33)$$

$$L(m_{vol}) = R_{vol} + S_{vol} \qquad (2.4.34)$$

$$L(m_c) = R_c + S_c \qquad (2.4.35)$$

where L( ) stands for the convection - diffusion operator on the left hand side of the transport equation, $R_{ox,1}$ and $R_{ox,2}$ are the consumption rates of oxygen due to volatile and char combustion respectively, R_{vol} and R_c are the consumption rates of volatiles and char carbon and finally S_{vol}, S_c are the production rates (source terms) of volatiles and char carbon.

If the stoichiometric factors for the aforementioned reactions are s_1 and s_2, respectively, the reaction rates are related through the expressions :

$$R_{ox,1} = s_1 R_{vol} \tag{2.4.36}$$

$$R_{ox,2} = s_2 R_c \tag{2.4.37}$$

assuming that the fuels react as soon as they are mixed ,which is a valid assumption for the volatiles, (especially given the necessary coarseness of a 3-D grid). In the case of char combustion, the rate limiting processes are taken into account in the Lagrangian formulation of the heterogeneous combustion model and therefore m_c and all the other related quantities may be considered as concepts to enable the consumption of oxygen due to the presence of the char particles to be calculated.

Combination of Eqs. (2.4.33), (2.4.34) and (2.4.35) leads to

$$L(s_1 m_{vol}+s_2 m_c-m_{ox}) = s_1 R_{vol} + s_1 S_{vol} + s_2 R_c + s_2 S_c - R_{ox,1} - R_{ox,2} \tag{2.4.38}$$

and taking into account Eqs. (2.4.36) and (2.4.37)

$$L(s_1 m_{vol}+s_2 m_c-m_{ox}) = s_1 S_{vol} + s_2 S_c \tag{2.4.39}$$

Let the scalar quantity $(s_1 m_{vol}+s_2 m_c-m_{ox})$, ϕ and introduce a mixture fraction related quantity f defined as

$$f = \frac{\phi-\phi_0}{\phi_1-\phi_0} \tag{2.4.40}$$

where ϕ_0 and ϕ_1 are the values of ϕ in the oxidant and 'fuel' streams respectively. The quantities ϕ_0 and ϕ_1 can be evaluated as follows :

$$\phi_0 = -m_{ox,air} = -0.232 \tag{2.4.41}$$

$$\phi_1 = s_1 m_{vol,fu} + s_2 m_{c,fu} \tag{2.4.42}$$

where $m_{vol,fu}$ and $m_{c,fu}$ are given by

$$m_{vol,fu} = \frac{\text{Volatiles source}}{\text{Volatiles source + Char source}} \qquad (2.4.43)$$

$$m_{c,fu} = \frac{\text{Char source}}{\text{Volatiles source + Char source}} \qquad (2.4.44)$$

Thus Eq. (2.4.39) becomes:

$$L(f) = (s_1 S_{vol} + s_2 S_c) (\phi_1 - \phi_0) \qquad (2.4.45)$$

The scalar quantity f, which as already mentioned, can be related to the mixture fraction concept of the Single Chemically Reacting System (SCRS), is here termed the "Composite Mixture Fraction". However, it is obvious that there are certain differences between the conventional and composite mixture fractions. Some further aspects of the present approach require clarification :

1. The presence of two types of "fuel" in the gas phase.

Since the two reactions (i.e. the volatile and char combustion) have different stoichiometric factors s_1 and s_2 and because at this point we are confining attention to the gas phase, the " local fuel stream " is assumed to consist of two fuels. These are the volatiles and the char carbon, represented by the mass fractions $m_{vol\ fu}$ and $m_{c\ fu}$ respectively, which compete for the same oxygen.

2. The Composite Mixture Fraction is not a conserved quantity.

Due to the nature of the coal combustion phenomenon, the volatiles and the fixed carbon cannot be considered as forming a fuel jet emerging at the inlet with an f value of 1. Rather, they react locally according to the thermal history of the coal particles. Therefore, instead the boundary conditions for f are everywhere 0. The fuel is locally released wherever the coal particles reside which mixes and reacts with the surrounding

oxidant stream thus providing a source term for the f equation. This is evident in the deduced composite mixture fraction transport equation (2.4.45), where the right-hand side is not zero but comprises the fuel source terms, thus forming a source term for the mixture fraction itself.

3. Priority in the consumption of oxygen.

Since the volatiles reaction rate is much faster than the heterogeneous combustion rate it is assumed that, in the absence of an excess of oxidant, only the volatiles reaction will take place. This is summarised by Fig. (2.4) where f_{st1} and f_{st2} are the stoichiometric values of the composite mixture fraction for which volatiles and complete combustion can take place. The values of f_{st1} and f_{st2} are given in the following subsection.

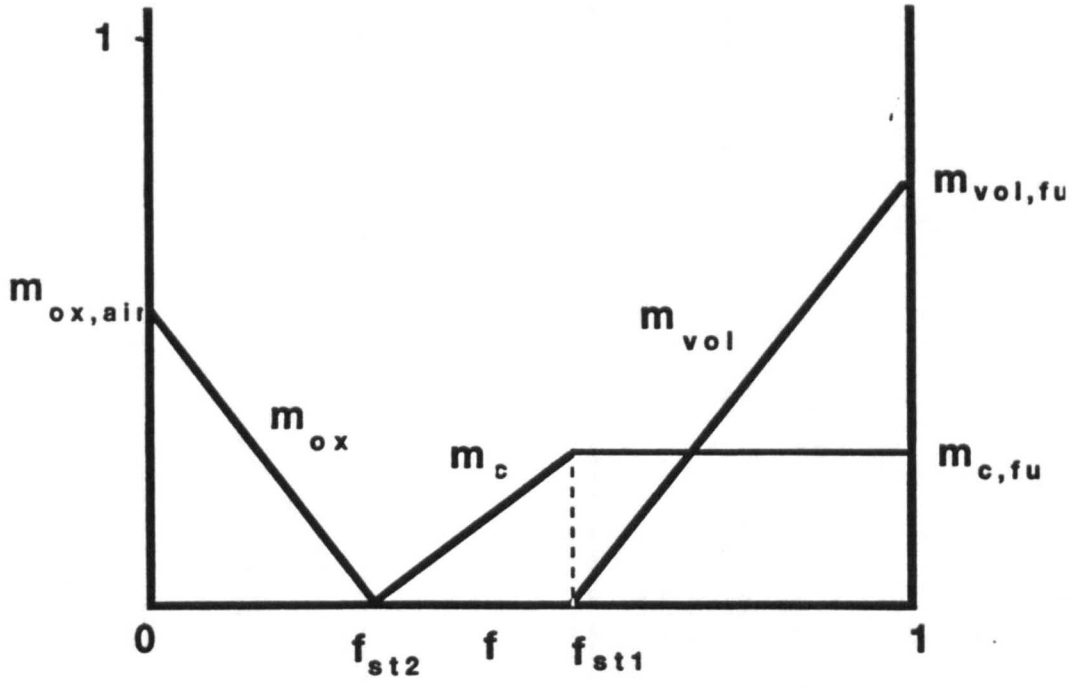


Fig.2.4 Mass fractions of species as a function of composite mixture fraction for preferential fast reaction of volatiles

4. Stoichiometric Composite Mixture Fractions.

A direct consequence of the "two local fuels" treatment is the requirement for two separate stoichiometric values of the composite mixture fraction f_{st1} and f_{st2}, that are not constant but depend on the values of $m_{vol,fu}$ and $m_{c,fu}$, which in turn are associated with the flight history of the particles. These two values are determined from the definition of the composite mixture fraction combined with the Fig. (2.4) and are :

$$f_{st1} = \frac{s_2 m_{c\,fu} + m_{ox\,air}}{s_1 m_{vol\,fu} + s_2 m_{c\,fu} + m_{ox\,air}} \qquad (2.4.46)$$

$$f_{st2} = \frac{m_{ox\,air}}{s_1 m_{vol\,fu} + s_2 m_{c\,fu} + m_{ox\,air}} \qquad (2.4.47)$$

5. Calculation of the mass fractions of the species.

From the value of the composite mixture fraction f, derived from the solution of the relative transport equation, and its position relative to f_{st1} and f_{st2} in the diagram presented in Fig. (2.4), the mass fractions of the present species can be worked out

When

- $f_{st1} \le f \le 1$, then

$$m_{ox} = 0$$

$$m_c = m_{c,fu} \qquad (2.4.48)$$

$$m_{vol} = m_{vol,fu} \left(\frac{f - f_{st1}}{1 - f_{st1}} \right)$$

When

- $f_{st1} \le f \le f_{st2}$, then

$$m_{ox} = 0$$

$$m_c = m_{c,fu} \left(\frac{f - f_{st2}}{f_{st1} - f_{st2}} \right) \qquad (2.4.49)$$

$$m_{vol} = 0$$

When

- $f_{st2} \leq f \leq 0$ then $\quad m_{ox} = \left(\frac{f_{st2} - f}{f_{st2}}\right)$

$$m_c = 0 \qquad (2.4.50)$$

$$m_{vol} = 0$$

The mass fractions of inerts and products are given by

- any f, then $\quad m_{iner} = m_{iner,air}\,(1 - f) \qquad (2.4.51)$

$$m_{pr} = 1 - \left(\sum m_i\right)$$

where $\sum m_i$ is the sum of the mass fractions of the species considered above.

2.4.4 Thermodynamics.

Ignoring kinetic heating since the velocities are relatively small (low Mach number flows), the specific enthalpy may be defined as :

$$h = \Sigma_j\, m_j \int_0^T C_{pj}(T)\, dT + m_{fu}\, H_{fu} \qquad (2.4.52)$$

where H_{fu} is the calorific value of the fuel, m_j and C_{pj} are, respectively, the mass fraction and the specific heat at constant pressure at temperature T of species j present in the mixture . The latter is defined as:

$$C_{pj} = \frac{1}{T} \int_0^T c_{pj}(T)\, dT \qquad (2.4.53)$$

The individual species specific heats $c_{pj}(T)$ are functions of temperature and are determined from third order polynomials given by Tribus (1961).

The temperature of the mixture is then given by :

$$T = \frac{h - m_{fu} H_{fu}}{\sum_j m_j C_{pj}} \qquad (2.4.54)$$

and the density of the mixture calculated from the equation of state is then:

$$\rho = \frac{p}{RT\sum_j m_j/W_j} \qquad (2.4.55)$$

where p is the pressure, R is the universal gas constant and W_j is the molecular weight of species j.

2.5 The Thermal Radiation Models

Thermal radiation is the most dominant mechanism of heat transfer in industrial furnaces whose role is augmented by the dimensions of these furnaces, Lockwood, (1987). The problem of determining the radiative heat transfer at a surface located either on a furnace wall or within the combustion chamber is a complex one. The energy emitted by the hot gases depends on their composition and temperature and it is not a very difficult task. The problem arises when the radiative heat flux arriving at the surface under consideration is to be estimated. The reason for this is that the radiant energy received is attenuated by absorption in the intervening medium, or by scattering away from the line of travel, and it is enhanced by scattering into this direction. Therefore the radiative heat flux arriving at a given surface in the combustion chamber is strongly influenced by the combustor geometry and the properties of the absorbing medium.

2.5.1 The Transport Equation

Let us consider a pencil of rays of wavelength λ, enclosed within an elemental solid angle travelling in a specified direction through a small volume element in an emitting - absorbing - scattering medium.

An energy balance gives :

$$(\mathbf{n}\,\nabla)I_\lambda = -(K_{\lambda,a} + K_{\lambda,s})\,I_\lambda + K_{\lambda,a}\,I_{b,\lambda} + \frac{K_{\lambda s}}{4p}\int_0^{4\pi} I_\lambda(\omega)d\omega \qquad (2.5.1)$$

(1) (2) (3) (4)

where **n** the unit vector in the specified direction

l wavelength of monochromatic radiant energy

$K_{\lambda,a}$ monochromatic absorption coefficient

$K_{\lambda,s}$ monochromatic scattering coefficient

I_λ intensity of radiation

$I_{b,\lambda}$ intensity of blackbody radiation

ω solid angle

in the above equation $I_{b,\lambda} = \sigma T^4/\pi$.

In the balance equation (2.5.1) term (1) represents the gradient of intensity in the specified direction; term (2) represents the energy loss due to absorption and scattering into other directions; term (3) is the increase due to emission from the medium within the volume; term (4) the increase of intensity due to scattering of rays into the considered direction from all the other directions with the scattering assumed to be isotropic.

Since flames and hot gases show an emission spectrum in discrete bands, a complete energy balance can be obtained by integrating equation (2.5.1) in all possible directions n and wavelengths λ:

$$\int_0^{\infty}\int_0^{4\pi}(n.\nabla)I_\lambda d\Omega d\lambda = \int_0^{\infty}\int_0^{4\pi}(K_{\lambda a} + K_{\lambda s})I_\lambda d\Omega d\lambda +$$

$$\int_0^{\infty}\int_0^{4\pi}K_{\lambda a}\, I_{b\lambda} d\Omega d\lambda + \int_0^{\infty}\int_0^{4\pi}\frac{K_{\lambda s}}{4\pi}\left(\int_0^{4\pi}I(\omega)d\omega\right)d\Omega d\lambda \qquad (2.5.2)$$

Equation (2.5.2) must be solved for the control volumes around the grid nodes in the chamber along with a similar equation for the surface control volumes where the spatial integration is limited to 2π steradians. The numerical solution of this set of integro-differential equations is extremely complicated even for very simple geometries resulting thus to the need for radiation modelling.

2.5.2 Classification of Radiation Models.

There are three main classes of models for radiation calculations, namely, zone method, Monte Carlo methods, and flux methods.

The Zone Method (Hottel and Cohen,1958).

The walls and the interior of the chamber are divided into zones of finite size. All the view factors between each pair of zones have to be evaluated. The exchange between each zone is calculated using the view factors which results in a set of simultaneous equations for the n zones. The method demands excessive storage and calculation of view factors can be difficult in some situations. See Hottel and Sarofim, (1967), for more details.

Monte Carlo Method (Harwell, (1964), Stewart et al, (1971)).

This a statistical method which employs a random number generator to establish directions and emissive powers. Representative rays are fired in random directions. The required quantities are then evaluated as each ray crosses the enclosure. The degree of accuracy of the calculations following this method depends on the number of chosen rays, but it is always subject to statistical errors associated with machine random number generation.

Flux Methods.

Flux models are based on solid angle discretisation and assumptions about the intensity as a function of temperature. The use of such a function reduces the integro - differential equations to a set of simultaneous first order partial differential equations, Bagnaro, (1982), that can be solved by the numerical algorithm employed for the flow field calculations. Details for the formulation of flux models can be found in Lockwood and Marco, (1975), and Lockwood and Shah (1979).

Shah (1979) and Lockwood and Shah (1980) proposed a precise and computationally economical model termed the Discrete Transfer Method (DTM) specially developed for incorporation into general combustion prediction procedures, which essentially combines the strong features of the zone, Monte Carlo and flux methods.. Its advantages include easy adaptability to complex geometries, ability to return any desired accuracy by the use of sufficient number of rays and easy accommodation of the boundary conditions. The method has been successfully applied and validated in various combustion predictions, see Lockwood et al, (1982 and 1987), Carvalho, (1983), Chakravarty, (1984), Abbas et al, (1984), and it has become popular in various other applications. For these reasons the Discrete Transfer Method has been applied in this study and is described in the next section.

2.5.3 The Discrete Transfer Method.

Equation (2.5.1) for monochromatic thermal radiation of wavelength λ may be expressed as, see for example Lockwood and Shah (1980) :

$$\frac{dI}{ds} = -(K_a + K_s)I + K_a\frac{E_g}{\pi} + \frac{E_s}{4\pi}\int_{4\pi}P(\Omega\Omega')I(\Omega')d\Omega' \qquad (2.5.3)$$

where I stands for the radiant intensity in the Ω direction, s is the distance in the Ω direction, and K_a and K_s are the absorption and scattering coefficients respectively.

$E_g = \sigma T^4$ is the black body emissive power of the gas at temperature T and $P(\Omega\Omega')$ is the probability that incident radiation in the direction Ω' will be scattered into the incremental solid angle $d\Omega$ about Ω. In the absence of scattering equation (2.5.3) reduces to :

$$\frac{dI}{ds} = -K_a I + \frac{K_a\sigma T^4}{\pi} \qquad (2.5.4)$$

When scattering is considered, as in the case of coal combustion , Eq. (2.5.3) reduces to the same form as Eq. (2.5.4) using the following transformations:

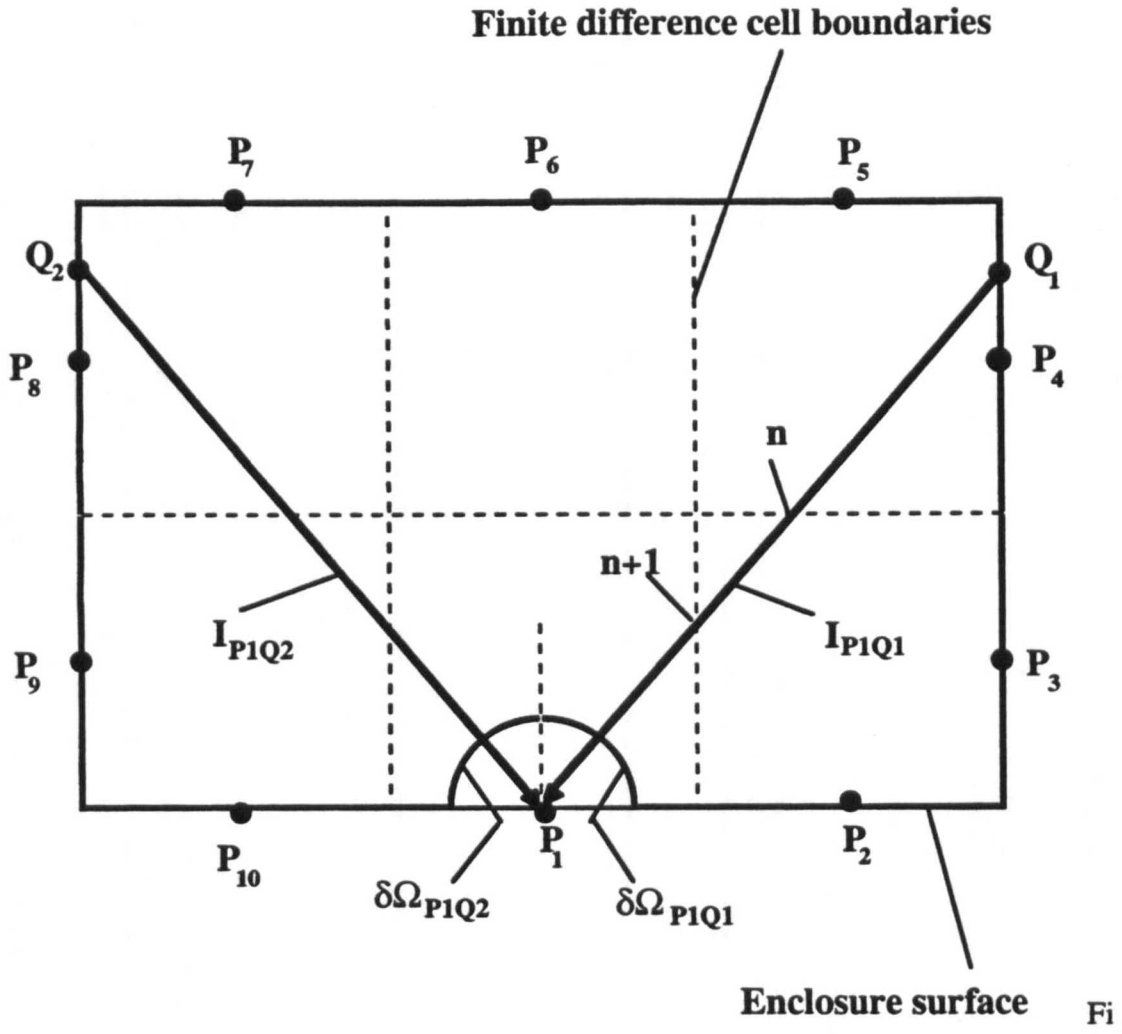
$$ds^* \equiv (K_g + K_p + K_s)ds \tag{2.5.5}$$

and

$$E^* \equiv [(\frac{K_g \sigma T_g^4}{\pi}) + (\frac{K_p \sigma T_p^4}{\pi}) + \frac{K_s}{4\pi}\int_{4\pi} P(\Omega\Omega')I(\Omega')d\Omega'](K_g + K_p + K_s)^{-1} \tag{2.5.6}$$

Equation (2.5.4) gives the rate of change in the intensity dI of a ray travelling a distance ds through a medium at temperature T and absorption coefficient K_a and is the one that is employed in this study. The first and second terms on the right hand side of this equation account for the absorption and emission respectively.

Consider a hemisphere about point P_1, on the surface of an enclosure, Fig. (2.5). This hemisphere is arbitrarily subdivided into four segments within which the intensities are considered constant. Four representative rays may be visualised impinging on the point P, and passing through the centroid of each segment. Two of the four rays are shown, $I(\Omega_{P1,Q1})$ and $I(\Omega_{P2,Q2})$, travelling to P_1 from points Q_1 and Q_2 on the far walls of the enclosure. The other two may be imagined entering from behind and in the front of the page.



g. 2.5 Typical Rays and Control Volumes

The two rays travel from Q_1 to P_1 and their respective intensities $I(\Omega_{1,1})$ and $I(\Omega_{1,2})$ are presumed constant over the solid angles $\delta\Omega_{P1Q1}$ and $\delta\Omega_{P1Q2}$. The intensities along the directions Ω_{P1Q1} and Ω_{P1Q2} are determined from the solution of equation (2.5.4) knowing the initial conditions of Q_1 and Q_2. Analogous pairs of rays, not shown in the figure, impinging on points P_2,.....,P_{10} and the intensities in these directions are similarly solved for.

The whole enclosure is subdivided into computational cells, which may, but not necessarily, coincide with the grid for the flow field calculations. The net gain or loss of radiation energy in a control volume is accounted for in the energy transport equation

as a source or sink term. The evaluation of these source terms together with the solution procedure is given in section (3.8).

2.5.4 Optical Properties of Gaseous, Oil and Coal Flames.

Equations (2.5.1) to (2.5.4) have been cast for monochromatic radiation of wavelength λ, and the corresponding absorption coefficients $K_{a,\lambda}$ has been assumed to be constant K_a. In real flames though the gases exhibit a wavelength variation in the absorption coefficient. Ideally to evaluate the radiation heat sources it is necessary to integrate over all possible wavelengths, which proves to be computationally very expensive. A first approximation would be to discretise the wavelengths into a finite number of intervals and solve the radiation equation in every interval where K_λ is supposed to be constant. Even this approach tends to be computationally expensive as well. A more practical approach will be to calculate a global absorption coefficient as a function of temperature and mixture composition. The cost of this approach is some loss of accuracy which is normally acceptable for engineering calculations. For simplicity it is assumed that a real gas can be represented by a mixture of grey gases, Hottel and Sarofim (1967).

(i) Gas Combustion

In gas - fired combustors two species are responsible for the majority of the radiation, namely, carbon dioxide and water vapour. These gases radiate in several bands of wavelengths. Following Hottel (1967), Truelove (1976) represented the emittance of a real gas by one clear and two grey gases. The clear component corresponds to the non - emitting regions of the spectrum between strong bands.

The spectral emittance for a path length, L for an isothermal grey gas at temperature, T, is given by:

$$\varepsilon_\lambda (T,L) = 1 - \exp (- K_\lambda L) \qquad (2.5.7)$$

where K_λ is the absorption coefficient at wavelength λ.

The total emittance of the mixture for a path length L, using the mixed grey representation, is given by :

$$\varepsilon_m = \sum \alpha_n(T) [1 - \exp (- K_n L)] \qquad (2.5.8)$$

with

$$\sum \alpha_n(T) = 1$$

and α_n is given by $\alpha_n(T) = \beta_{1,n} + \beta_{2,n} T$

where α_n is the weighting coefficient representing the fraction of black body energy in the wavelength region where the absorption coefficient K_n is given by :

$$\alpha_n(T) = \frac{1}{\sigma T^4} \int_{K=K_n} E_{b\lambda}(T) \, d\lambda \qquad (2.5.9)$$

where $E_{b\lambda}(T)$ is the Plank spectral distribution of the emissive power.

(ii) Oil Combustion

For oil - fired combustors the presence of soot plays a considerable role in the determination of the optical properties of the flame. For soot radiation, it has been found experimentally that the attenuation of the radiation passing through a cloud of soot particles follows the same exponential law, and hence the spectral emittance of an isothermal soot cloud may be expressed as:

$$\varepsilon_{s,\lambda} (T,L) = 1 - \exp (- K_{s,\lambda} CL) \qquad (2.5.10)$$

where $K_{s,\lambda}$ is the soot specific absorption coefficient, and C is the soot concentration in kg/m^3.

The soot total emittance can be determined in the same manner using the spectral absorption coefficient given by Truelove (1976) and a grey gas expansion of the form :

$$\varepsilon_s = \sum \alpha_{s,n'} (T) \{ 1 - \exp(- K_{s,n} CL)] \qquad (2.5.11)$$

with the weighting factor, $\alpha_{s,n'}(T)$, being a linear function of temperature.

The grey gas expansions for gas and soot can be combined to yield a grey gas representation of a gas - soot mixture. If $K_{g,n}$ and $K_{s,n'}$ are the gas and soot grey gas absorption coefficients, then it is reasonable to conclude that a grey gas expansion containing absorption coefficients

$$K_{m,n,n'} = K_{g,n} + K_{s,n'} \qquad (2.5.12)$$

will provide a good representation of the gas - soot mixture. By using the definition of $K_{m,n,n'}$ the total emittance of the gas - soot mixture may be expressed as:

$$\varepsilon_m = \sum \alpha_{m,n,n'}(T) [\, 1 - \exp(- K_{g,n} - K_{s,n'} C) L\} \qquad (2.5.13)$$

The mixture weighting factors, $\alpha_{m,n,n'}(T)$, must satisfy the sum conditions :

$$\sum_{n'} \alpha_{m,n,n'}(T) = \alpha_{g,n}(T)$$

$$\sum_{n} \alpha_{m,n,n'}(T) = \alpha_{s,n'}(T) \qquad (2.5.14)$$

The summation over n and n' are for all the grey gases assumed, that is three for gas, n, and two for soot, n'. The values of $\beta_{1,n,n'}$, $\beta_{1,n,n'}$, $K_{g,n}$ and $K_{s,n'}$ are reported by Truelove (1976) and they are shown in Tables (2.5.1 - 4).

n	n'	b_1	$b_2 x 10^3$	$k_{g,n}$	$k_{s,n'}$	$k^*_{s,n'}$
1	1	0.632	-0.2619	0.0	350	1130
1	2	-0.195	0.3332	0.0	1780	5720
2	1	0.488	-0.1896	1.88	350	1130
2	2	-0.098	0.1844	1.88	1780	5720
3	1	0.176	-0.0735	68.8	350	1130
3	2	0.003	-0.0074	68.8	1780	5720

Table 2.2 Constants in the Grey Gas Model of a Gas/Soot Mixture
Gas Combustion, $p_w/p_c=2$
($N_g=3$, $N_s=2$)

n	n'	b_1	$b_2 x 10^3$	$k_{g,n}$	$k_{s,n'}$	$k^*_{s,n'}$
1	1	0.717	-0.2964	0.0	350	925
1	2	-0.231	0.3861	0.0	1780	4710
2	1	0.459	-0.1787	2.50	350	925
2	2	-0.078	0.1391	2.50	1780	4710
3	1	0.120	-0.0499	109.00	350	925
3	2	0.013	-0.0002	109.00	1780	4710

Table 2.3 Constants in the Grey Gas Model of a Gas/Soot Mixture
Oil combustion, $p_w/p_c=1$
($N_g=3$, $N_s=2$)

n	n'	b_1	$b_2 x 10^3$	$k_{g,n}$	$k_{s,n'}$	$k^*_{s,n'}$
1	1	0.588	-0.2401	0.0	350	1130
1	2	-0.165	0.2834	0.0	1780	5720
2	1	0.412	-0.1665	0.89	350	1130
2	2	-0.127	0.2178	0.89	1780	5720
3	1	0.2375	-0.0941	15.5	350	1130
3	2	-0.0105	0.0265	15.5	1780	5720
4	1	0.0585	-0.0243	240.0	350	1130
4	2	0.0065	-0.0027	240.0	1780	5720

Table 2.4 Constants in the Grey Gas Model of a Gas/Soot Mixture
Gas Combustion, $p_w/p_c = 2$
(N_g=4, N_s=2)

n	n'	b_1	$b_2 x 10^3$	$k_{g,n}$	$k_{s,n'}$	$k^*_{s,n'}$
1	1	0.654	-0.2674	0.0	350	925
1	2	-0.201	0.3429	0.0	1780	4710
2	1	0.424	-0.1718	1.21	350	925
2	2	-0.097	0.1689	1.21	1780	4710
3	1	0.1785	-0.0694	27.1	350	925
3	2	-0.0045	0.0159	27.1	1780	4710
4	1	0.0395	-0.0164	454.0	350	925
4	2	0.0065	-0.0027	454.0	1780	4710

Table 2.5 Constants in the Grey Gas Model of a Gas/Soot Mixture
Oil Combustion, $p_w/p_c = 1$
(N_g=4, N_s=2)

(iii) Coal Combustion

For pulverised fuel flames the total absorption coefficient is calculated following the global expression due to Gibb and Joyner (1973) Eq. (2.5.18). The main materials participating in radiation exchange in a pf-fired furnace chamber are:

(i) soot

(ii) larger particulates (char, ash)

(ii) the triatomic gases water vapour and carbon dioxide.

A single equivalent grey component has been used for the gas absorption coefficient. The soot and larger particulates were assumed grey and the latter were treated as geometric absorbers/scatterers.

The Gas Absorption Coefficient

Gibb and Joyner (1973) correlated the Hottel emissivity data for a mean beam length intermediate between that for a single zone and for the chamber as a whole and derived a mean equivalent 'grey' gas coefficient k_g given by:

$$k_g = 0.28\exp(-T/1135)\ m^{-1} \qquad (2.5.12)$$

The Soot Absorption Coefficient

No reliable data appears to be available on soot absorption coefficients in PF flames. Measurements in oil flames indicate peak values of about $1m^{-1}$ tailing off to zero within about ten burner diameters. A typical volume mean value for vapour phase cracking products from this source would appear to be approximately $0.4m^{-1}$. Soot absorption was thus represented by adding a contribution, Eq (2.5.13) :

$$k_{soot} = 0.4m^{-1} \qquad (2.5.13)$$

to the gas absorption coefficient in the burner belt.

Larger Particulate Absorption

Again, reliable data are scarce and the absorption and scattering coefficients for this material were estimated from geometrical optics. Treating the material as opaque spheres with surface emissivity ε_p (reflectivity $1-\varepsilon_p$). The estimation of particulate emissivity is needed. Laboratory data (Street and Tawmley, 1971) indicate the ε_p varies beteewn 1 for unburnt char and 0.6 for residual ash, suggesting the approximation

$$\varepsilon_p = u + 0.6(1-u) \qquad (2.5.14)$$

where u is the fraction of the original char mass remaining unburnt at any point in the chamber.

The absorption and scattering coefficients would then be:

$$k_p = (0.6 + 0.4)\,(3/4\bar{r_{32}}\chi_f)\,(\rho_g/\rho_p) \qquad (2.5.15)$$

$$ks = 0.4\,(1-u)\,(3/4\bar{r_{32}}\chi_f)\,(\rho_g/\rho_p) \qquad (2.5.16)$$

where χ_f is the air/fuel ratio, ρ_g and ρ_p are the gas and particle densities respectively and

$$\bar{r_{32}} = \frac{\int_0^\infty r^3 n(r)dr}{\int_0^\infty r^2 n(r)dr} \qquad (2.5.17)$$

where n(r) is the number of particles per unit chamber volume with radii in the range r to r+dr. $\bar{r_{32}}$ is estimated from the original pf size distribution.

The volume mean absorption coefficient from the larger particles can be estimated, however, to be equal to $0.32m^{-1}$, see Gibb and Joyner (1973).

Finally, the total absorption coefficient would be

$$k_t = [0.32 + 0.28 \exp(-T/1135) + 0.4] \text{ m}^{-1} \qquad (2.5.18)$$

for the burner belt.

CHAPTER 3

THE SOLUTION PROCEDURE

3.1 Introduction

This chapter describes the numerical methods employed in this study. The set of governing partial differential transport equations for the for all the depended variables are discretised, and then consequently solved. The solution procedures for the discrete phase and thermal radiation are described. Finally, the prevailing boundary treatment for each of the above techniques is specified.

3.2 The Differential Equations

The set of differential transport equations, derived in chapter 2, can be written in the following general form :

$$\frac{\partial}{\partial x_i}(\rho \overline{u_i}\,\overline{\phi}) = \frac{\partial}{\partial x_i}(\Gamma_{eff,\phi}\frac{\partial \bar{\phi}}{\partial x_i}) + S_\phi + S_{p,\phi} \qquad (3.2.1)$$

where $\bar{\phi}$ stands for the time-averaged value of any transported property, $\Gamma_{eff,\phi}$ is the corresponding exchange coefficient of the diffusion term defined in equation (2.2). The source term, S_ϕ, includes all terms of the equation in question that do not belong to either the convection or the diffusion contributions. The source term Sp is the gas-droplet/particle interaction source term. These source terms are given in Table (3.1).

3.3 The Numerical Grid

The numerical grid comprises a set of Cartesian orthogonal intersecting lines which covers the whole computation domain. The grid spacing does not necessarily have to be uniform. All the scalar dependent variables are stored at the nodal points of the mesh, defined as the points of intersection of the grid lines. The velocity components are located at midway positions between the nodes, each component being displaced forwardly in its own direction. This grid arrangement is known as the 'staggered grid', see Patankar (1980), and offers two major advantages :

(i) the velocities lie between the pressures that drive them. This ensures that continuity may be satisfied avoiding the occurrence of wavy pressure fields, thus assisting in the convergence of the algorithm to a physically realistic solution.

(ii) the velocities are directly available to compute the fluxes across the cell interfaces.

A perspective view of a control volume is illustrated in Fig. (3.1). The scalar nodes are depicted as solid spheres while the velocities are indicated by arrows located at the cell faces. The neighbouring points of a node P are denoted as N,S,E,W,U or D, the former four being borrowed from the compass directions and the latter two standing for upstream and downstream respectively. The cell boundaries, i.e. the planes midway neighbouring nodes, are labelled, following the same convention, with lower case letters.

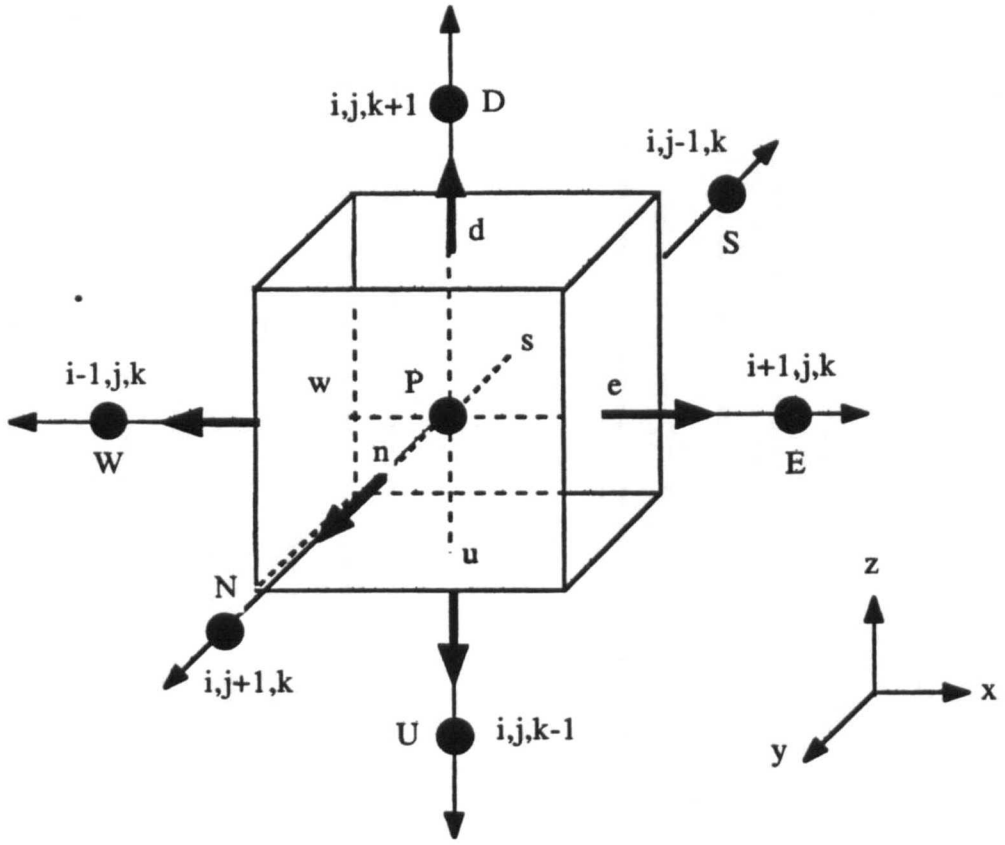


Fig. 3.1 Field variable value placement about a computational cell.

Very often due to the staggering of the grid the value of a velocity component is needed at a grid position where it has not been calculated. To ensure consistency and uniformity the following interpolating procedure is used to calculate unknown velocity components in three-dimensional domains. Fig. 3.2 shows a typical example where the velocity components u_s and u_n are needed for the calculation of the turbulence kinetic energy.

The first step is to interpolate for the velocity components u_{ne}, u_{nw}, u_{se} and u_{sw} at the apexes of the control volume. Subsequently, a second linear interpolations in the east-west direction gives the unknown velocities.

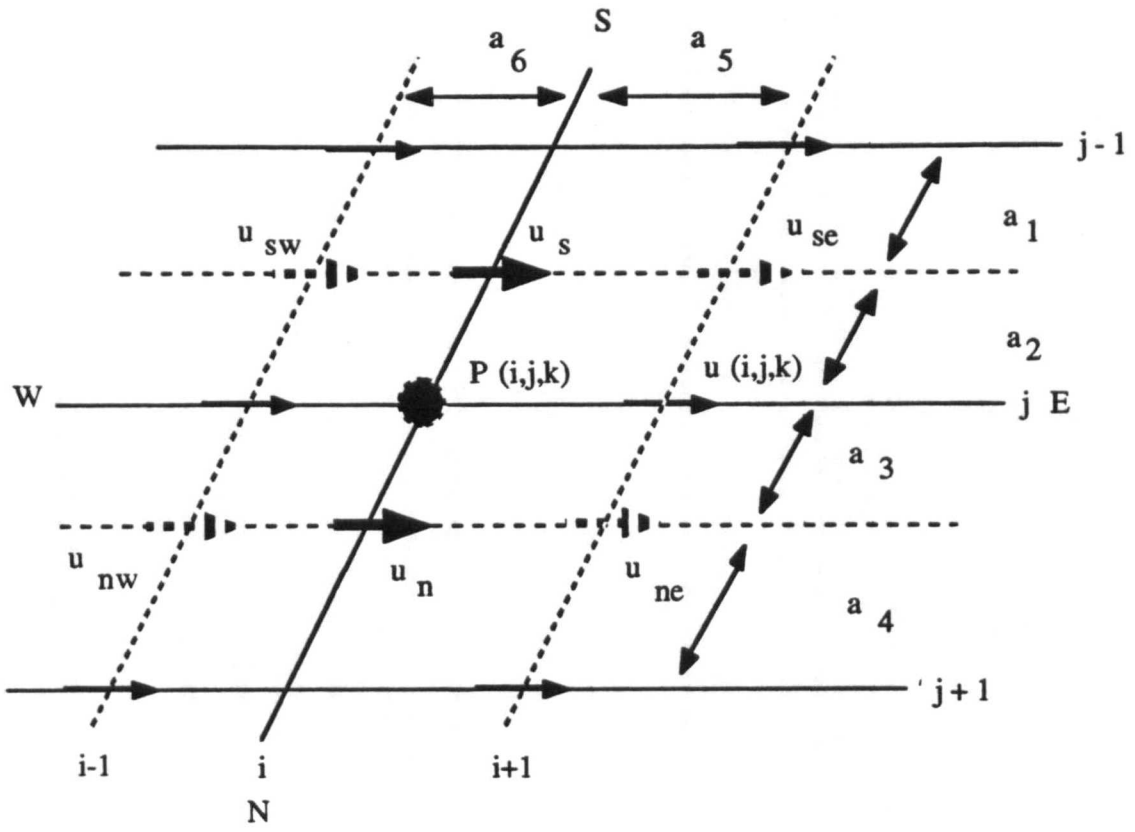


Fig. 3.2 Numerical interpolation. The thick arrows show the unknown velocities, the dashed ones show the interpolated velocities and the normal ones show the known velocities. The solid lines represent scalar planes while the dashed lines stand for velocity planes.

3.4 The Discretisation Scheme

The finite-difference equations are obtained by integrating the respective differential equations over the control volume element (cell) containing each grid node (Patankar (1980) , Roache (1982)). The following assumptions are made :

a. Φ is constant over a cell face.

b. The source terms that appear in the conservation equations are constant over the control volume at the value given by the cell centre point.

c. An implicit formulation is adopted, with all values assumed to exist at the same (next) iteration level.

The integration of Eq.(3.2.1) over the volume V_c of a typical cell (see fig. (3.1)) yields:

$$\sum_i [\int_{A_i} (\rho u_i \phi - \Gamma_{eff}\, \phi \frac{\partial \phi}{\partial x_i} dA)] + \int_{V_c} S_g dV + \int_{V_c} S_p\, dV = 0 \qquad (3.4.1)$$

where the summation is over all the cell boundaries, and A_i is the area of the cell boundary in question. The gas - droplet/particle source term S_p is added directly to the finite - difference equation as explained in section (3.7). Taking for example the cell west face, the integrals over the cell face can be approximated as follows :

a. For the convection terms.

$$\int_{A_w} (\rho u_i \phi)\, dA_w = \rho u_w\, [f_w \phi_p + (1-f_w)\phi_w] \int_{A_w} dA = \rho u A)_w\, [f_w \phi_p + (1-f_w)\phi_w] \qquad (3.4.2)$$

b. For the diffusion terms.

$$\int_{A_w} \Gamma_{\phi w} \frac{\partial \phi}{\partial x} dA = \Gamma_{\phi w} \frac{\phi_p - \phi_w}{x_p - x_w} \int_{A_w} dA = D_w (\phi_p - \phi_w) \qquad (3.4.3)$$

where ϕ_p and ϕ_w are the values of the variable ϕ at the central point P and the neighbouring node W. The weighting factor fw, for the west face, is related to the local Peclet number, $Pe = \frac{\rho u \, dx}{\mu_{eff}}$, which is the local convection to diffusion ratio, by :

$$f_w = \begin{cases} \dfrac{(1 + 2Pe^{-1})}{2} & \text{when} \quad |Pe| \leq 2 \\ 1 & \text{when} \quad Pe > 2 \\ 0 & \text{when} \quad Pe < 2 \end{cases} \qquad (3.4.4)$$

The above way of calculating the weighting factors is termed the 'hybrid scheme' and is a combination of the 'upwind scheme', see Raithby and Torence (1974), and the 'central difference scheme', see Spalding (1972). Figures (3.3) and (3.4) provide a visual presentation of the above:

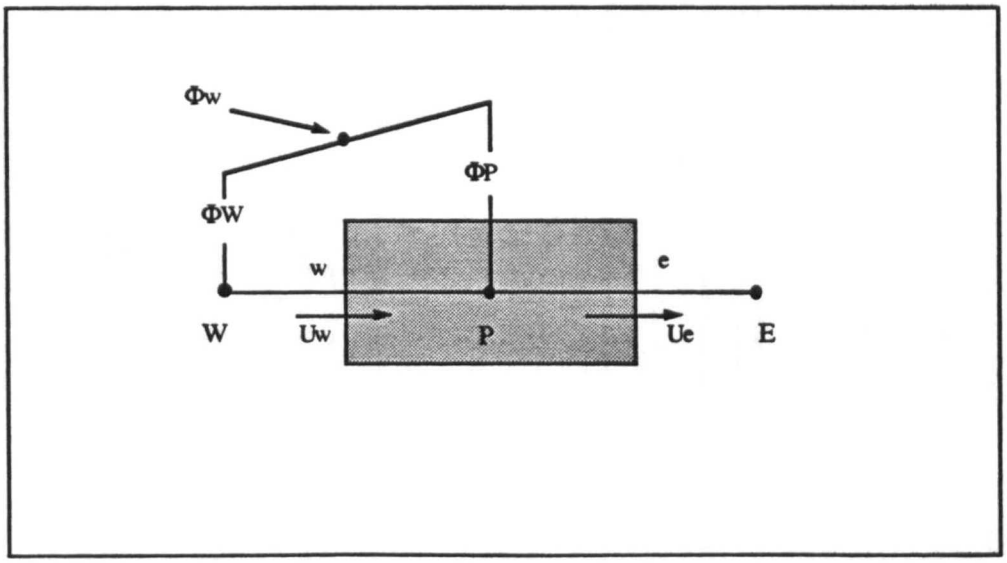


Figure 3.3 Central Differencing Scheme

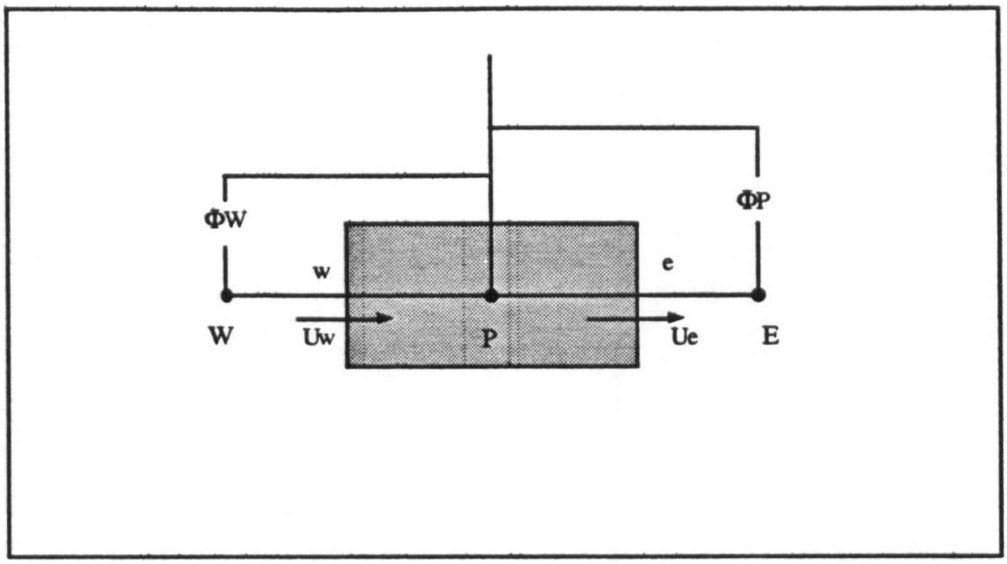


Figure 3.4 Upwind Differencing Scheme

The gas phase source terms are linearised as follows:

$$\int_{V_c} S_{g\phi}\, dV = S_A + S_B\, \phi \tag{3.4.5}$$

where S_A stands for all the contributions that are not functions of ϕ and S_B for the contributions that are functions of ϕ. The value of S_B must be non positive whereas a positive S_A improves stability, see Patankar (1980).

The resultant form of the finite difference equation (3.2.2) is :

$$a_P\, \phi_P = \sum_i a_i \phi_i + S_A + S_B\, \phi + S_P \tag{3.4.6}$$

where a_i are the finite - difference coefficients at the control volume interfaces and the summation is over the e,w,n.s,u and d interfaces.

The a_e coefficient , for example, is expressed as :

$$a_e = D_e - f_e C_e \tag{3.4.7}$$

where

$$C_e = (\rho u A)_e \tag{3.4.8}$$

$$D_e = \max [D_e , -(1-f_e)C_e , f_e C_e] \tag{3.4.9}$$

and

$$a_P = \sum_i a_i \tag{3.4.10}$$

Equation (3.4.6) is the finite - difference formula that is applied at every grid node for all the scalar variables as well as for the velocities, the only difference being that the velocities are stored at the cell interfaces, as explained in section (3.3). Therefore when the finite difference equations for the three momenta are determined appropriate modifications to the calculation of the coefficients and the source terms are applied.

3.5 The Solution Algorithm.

In order to obtain the desired flow field description the set of the simultaneous finite - difference equations (3.4.6) must be solved for each grid point in the flow field, assuming that the pressure field is known. Under these circumstances they form a closed set of algebraic equations. These equations are solved using the well known Tri - Diagonal Matrix Algorithm (TDMA) in an iterative procedure, see Patankar and Spalding (1972). The iterative procedure employed is known as 'SIMPLE' (Semi - Implicit Method for Pressure Linked Equation) , Caretto et al (1972). The procedure iterates from guessed initial fields for all the dependent variables until a converged solution is achieved.

3.5.1 The SIMPLE Algorithm

The set of algebraic equations (3.4.6) is solved by a semi - implicit procedure, wherein the velocities are calculated from the momentum equations for a guessed pressure field (or for the values from a previous cycle) p*. Intermediate velocity fields u*,v* and w*

are obtained which do not satisfy continuity unless convergence has been achieved. The velocity field is then corrected by linking it to a pressure correction p' in order to satisfy both continuity and the momentum conservation. The pressure correction p' is derived by combining the continuity and momenta equations as follows.

Assuming that the correct pressure is given by :

$$p = p^* + p' \tag{3.5.1}$$

and subsequently the correct velocities by :

$$u = u^* + u' \tag{3.5.2}$$

$$v = v^* + v' \tag{3.5.3}$$

$$w = w^* + w' \tag{3.5.4}$$

Combining equations (3.11) -(3.14) with equation (3.6) expressed for the correct and guessed values we get :

$$u = u^* + D^u_e(p'_P - p'_E) \tag{3.5.5}$$

where $D^u_e = \frac{A_e}{a_e}$, Ae is the area of the cell boundary normal to the velocity in question. Similarly :

$$v_p = v_p^* + D^v_s (p'_P - p'_N) \tag{3.5.6}$$

$$w_p = w_p^* + D^w_d (p'_P - p'_U) \tag{3.5.7}$$

In the last set of equations in order to calculate the correct velocities the pressure correction value at each grid point is needed, which is obtained as follows :

The finite - difference form of the continuity equation can be written as :

$$\sum_i C_i = S_{p,m} \tag{3.5.8}$$

where Ci stands for the convective fluxes and $S_{p,m}$ for the droplet / particle interaction mass source term. Substituting equations (3.15) - (3.17) into (3.18) results in the following equation for p' at each grid node :

$$a_p p'_p = \sum_i a_i p'_i + S_o \tag{3.5.9}$$

where the summation is over all the neighbouring points, and

$$a_i = \rho A D_i \tag{3.5.10}$$

$$ap = \sum_i ai \tag{3.5.11}$$

$$S_o = -\sum_i C_i + S_{p,m} \tag{3.5.12}$$

Incorporating the pressure correction equation (3.5.9) the SIMPLE Algorithm can be summarised into the following iterative sequence of calculations :

a. Guess a pressure field; this is usually taken as that of the previous iteration except from the first one.

b. Solve the momentum equations, Eqs. (3.5.6) and hence obtain an intermediate velocity field.

c. Solve the pressure - correction equation, Eq. (3.5.9), correct the pressure field, then correct the velocities accordingly.

d. Solve the finite - difference equations for the remaining scalar variables.

e. Treat the calculated velocity and pressure field as guessed values and return to step **(a)** until convergence is reached.

The updating of the thermodynamic properties is embedded into the above sequence, but are not necessarily invoked in every cycle. For example, in the case of the enthalpy equation the thermal radiation contribution is often not calculated in every iteration because it can prove time-consuming. The frequency of the update of the radiation

contribution to the overall heat transfer depend on the grid fineness and the convergence history.

An initial single-phase calculation solution is obtained with a certain degree of convergence, prior to invoking the discrete phase numerical procedure. The particle/droplet phase calculations precede each calculation sequence of an iteration in order to have the discrete phase sources available. This sequence of the solution is followed because the velocities and temperatures are needed as an initial field so that the second phase calculation can prove stable enough, otherwise the solution would oscillate strongly .

3.6 The Boundary Conditions

The specification of the boundary conditions in addition to the conservation equations define a well posed problem. The general principle concerning the boundary conditions for any variable is to break the link between the boundary value and its neighbouring point by setting the appropriate coefficient to zero. The contribution from the boundary cell then is introduced explicitly through the linearised source term.

3.6.1 The Inlet Boundary Conditions.

a. The Velocity Inlet Conditions.

The arrangement of the numerical mesh is such that the boundaries coincide with the scalar cell faces. Thus the velocity normal to the inlet plane is then easily introduced since its storage location coincides with the inlet plane. If velocities parallel to the inlet plane are desired to be introduced (e.g. for swirling flows) these are introduced explicitly in the value of the first node (note that no staggering occurs in this direction) through the appropriate source terms.

b. The Turbulence Inlet Conditions.

The turbulence kinetic energy at the inlet is calculated from the equation:

$$k_{inlet} = \text{turbulence intensity} \times u^2_{inlet} \qquad (3.6.1)$$

where u_{inlet} stands for the velocity normal to the inlet plane. The dissipation rate ε at the inlet is calculated through the relation, Gosman and Ideriah (1976) :

$$\varepsilon_{inlet} = \frac{k^{1.5}_{inlet} C^{0.75}_{\mu}}{L} \qquad (3.6.2)$$

where L stands for a characteristic length scale representing the size of the turbulent eddies.

c. The Pressure Correction Inlet Conditions.

Due to the prescription of the normal velocities at the inlet planes no pressure adjustments may influence these velocities leading to a zero gradient condition for the pressure correction equation.

d. The Enthalpy Inlet Conditions.

At the air inlet ports the value of the enthalpy is calculated through the expression:

$$h_{inlet} = h_{ref} + \int_{T_{ref}}^{T} C_p\,(T)\,dT \qquad (3.6.3)$$

where href is the specific enthalpy at the reference temperature Tref, and Cp is the air specific heat as a function of temperature given by a third order polynomial, Tribus (1971).

At the fuel inlet port and for gas combustion modelling a similar expression is applied having an additional term to account for the calorific value of the gaseous fuel. For the case of coal or oil combustion only the air enthalpy inlet conditions are prespecified, the

fuel heating value being taken into account locally within the domain through the explicit source terms.

3.6.2 The Outlet Boundary Conditions.

Usually the condition at the outlets are not known, but in the most of the cases the outlets are located in a region where the flow can be considered to be parabolic. Therefore parabolic outlet boundary conditions are applied. The velocity component normal to the outlet plane is corrected in every iteration in order to ensure overall mass conservation.

3.6.3 The Wall Functions.

The present form of the turbulence model is appropriate only for fully - turbulent flows. However, close to the walls the local Reynolds number of turbulence ($Re_t = k^{1/2} l/\nu$) is low so that viscous effects are dominant and the present turbulence model is not valid. To overcome this problem, boundary layer turbulence models (e.g. Jones and Launder (1973)) can be used in the near wall regions. However, these models require a fine grid near the walls in order to obtain an accurate solution which for three - dimensional reacting flows becomes impractical. Patankar and Spalding (1970) proposed the use of wall - functions in the near wall regions.

The wall - function formulation is based on the assumption that the flow near the solid boundary is one - dimensional Couette flow. The assumed wall layer is then one of constant shear stress, which in reality is true only for impermeable boundaries with zero stream-wise pressure gradients.

The main result of the wall function analysis is an algebraic expression that relates the values of the dependent variables at the wall to those at the near wall grid nodes. The presumed one - dimensional near wall layer is divided into two buffer zones, a viscous one and a turbulent one, Hinze (1959). The spatial position of the velocities is classified

as 'viscous' or 'turbulent' according to the value of y^+ which represents a critical distance from the wall and is defined as :

$$y^+ \equiv \frac{\rho\, C\mu^{0.25}\, k_p^{0.5}\, y_p}{\mu} \tag{3.6.5}$$

where ρ is the density, C_μ is a turbulence model constant, k_p is the turbulent kinetic energy, y_p is the actual distance of the point P from the wall and μ is the laminar viscosity. According to the values of y+ the dimensionless velocity component parallel to the wall is evaluated as :

$$\frac{u}{u_\tau} \equiv u^+ = \begin{cases} y^+ & \text{for } y^+ \leq 11.63 \\ \frac{1}{K} \ln (Ey^+) & \text{for } y^+ > 11.63 \end{cases} \tag{3.6.6}$$

where u_τ is the friction velocity ($u_\tau = \tau_w^{1/2}/\rho$), τ_w is the wall shear stress, K is the von Karman constant (K = 0.4187) and E is the quantitative measure of the wall roughness function and is obtained from measurements (E = 9.793 for smooth walls, see Patel (1965)). Equation (3.28) is used as the velocity distribution near the wall to obtain the source term for the cell next to the wall, see Gosman and Ideriah (1976).

For the value of the turbulent kinetic energy at the grid node adjacent to a solid wall is modelled through the expression :

$$k = C_\mu^{-1/2} \frac{\tau_w}{\rho} \tag{3.6.7}$$

The following expression for ε, the rate of dissipation of k may be obtained by balancing the generation and the dissipation of the turbulence energy in the regions close to the wall, see Salooja (1978) :

$$\varepsilon = \frac{C_\mu^{0.75}\ k^{1.5}}{K\ y} \tag{3.6.8}$$

The incorporation of enthalpy boundary conditions can be done in a similar manner with the result that the heat flux to the wall may be represented by :

$$q_w = \frac{\rho\ (\frac{\tau_w}{\rho})^{1/2}\ (h_p - h_w)}{\sigma_{ht}\ (u+ + p_j)} \tag{3.6.9}$$

where σ_{ht} is the Prandtl number and p_j is a function which accounts for the 'extra resistance' of the near wall layer and which depends on the ratio of the laminar to turbulent Prandtl numbers, given by the expression, see Spalding and Jayatillaka (1966) :

$$p_j = 9.24\ [(\sigma/\sigma_t)^{3/4} - 1\ ]\ [\ 1 + 0.28\exp(-0.007\sigma/\sigma_t) \tag{3.6.10}$$

The scale of the most industrial furnaces is so great that the convective wall heat transfer is found to be small compared with that due to the thermal radiation so this relation is assumed to be sufficient to account for convection.

3.7 Droplet / Particle Tracking Calculations

3.7.1 The Analytical Solution Equations

The analytical integration of equation (2.3.9) over a given timestep Δt expresses the mean final particle velocity as a function of the initial mean particle velocity at the initial spatial position. The timestep and the characteristic time are expressed in vector form as:

$$\mathbf{u}_{p_f}(t) = \mathbf{u}_{g_i}(t) + \tau_p\mathbf{g} + [\ \mathbf{u}_{p_i}(t) - \mathbf{u}_{g_i}(t) - \tau_p\mathbf{g}\ ] \exp\left(\frac{\Delta t}{\tau_p}\right) \tag{3.7.1}$$

Since the algebraic equation that describes the particle motion as well as its analytic solution is given in vectorial form, the particle velocity can be easily decomposed into

the appropriate components for the co-ordinate system in use. The three components for the particle velocity expressed in Cartesian co-ordinates are given by :

$$u_{p_f} = u_g + \tau_p g_x - (u_g + \tau_p g_x - u_{p_i}) \exp(-\Delta t/\tau_p) \qquad (3.7.2)$$

$$v_{p_f} = v_g + \tau_p g_y - (v_g + \tau_p g_y - v_{p_i}) \exp(-\Delta t/\tau_p) \qquad (3.7.3)$$

$$w_{p_f} = w_g + \tau_p g_z - (w_g + \tau_p g_z - w_{p_i}) \exp(-\Delta t/\tau_p) \qquad (3.7.4)$$

3.7.2 The Calculations for the Particle / Droplet Phase

The three-dimensional domain is discretised into scalar and velocity control volumes the later being staggered in a forward manner with respect to the scalar ones, Fig. (3.5). The numerical computation of the particle trajectories is based on the indexing of the scalar control volumes so the same numerical procedure is used for non staggered numerical grids. The chosen indexing and the staggered grid guarantee that the magnitude of the source terms due to the exchange of momentum between the two phases is properly weighted. Therefore, the appropriate percentage of the total contribution due to the presence of the particulate phase is accounted for by the traversed velocity control volumes.

In order to achieve the required accuracy when calculating the local gas velocity the scalar control volume is logically divided into eight sub-control volumes numbered one to eight, where the indexing is anti - clockwise starting from the north-west subdivision, Fig. (3.6). The four divisions that lie upstream are identified as 1, 2, 3 and 4 while the ones downstream are 5, 6, 7 and 8. This manner of subdividing the scalar control volume is achieved automatically because of the staggered grid. Note that the logical partitions, Fig. (3.6) dashed lines, that lie within the scalar control volume are the faces of the staggered velocity control volumes.

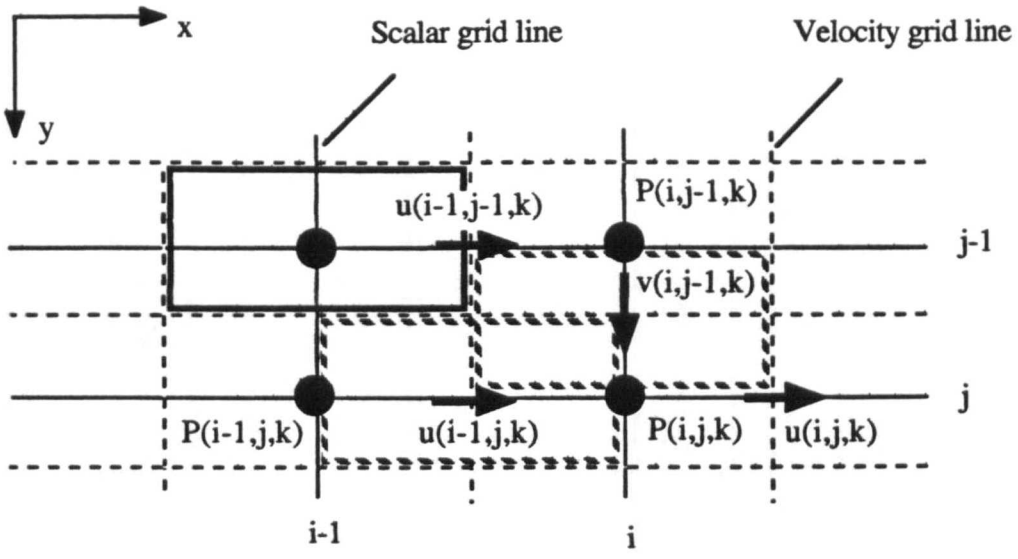


Fig. 3.5 Scalar and velocity control volumes.

In Fig. (3.5) X-Y plane is shown. The solid lined rectangles represent scalar control volumes while the dashed ones represent velocity control volumes. The symbols of u and v stand for the velocity in the X and Y direction respectively. The symbol P identifies the position of a scalar control volume.

Cross referencing figures (3.5) and (3.6) reveals that the sub-control volumes 1, 4, 5 and 8 belong to the u(i-1,j,k) velocity cell while 2, 3, 6 and 7 relate to the u(i,j,k) velocity cell. In the y direction the same reasoning leads to the conclusion that 3, 4, 7 and 8 belong to the v(i,j-1,k) cell while subdivisions 1, 2, 6 and 5 belong to the v(i,j,k). The same system is applied into the third coordinate direction.

Knowledge of the particle initial vector position $\mathbf{x}_i$ with reference to the inertial Cartesian co-ordinate system leads to the numerical identification of the scalar control volume at first and then to the choice of the sub-control volume within which the particle is enclosed. The numerical identification of the subdivision permits the calculation of the local gas velocity by appropriate linear interpolation from the prevailing neighbour values. The velocity gradient for each scalar control volume is thought to be varying linearly. Although this assumption is not always true, especially in areas of high strain, it is directly related to the fineness of the grid, thus it is legitimate

to say that the assumption of linearity holds on the grounds that the numerical grid has been carefully specified. The local gas velocity is the only information related to the gas phase that is needed for calculating the analytical solution (3.7.2) - (3.7.4) for the particle velocity components. The gas velocity field values needed for the calculation of the local particle Reynolds number (Eq. 2.3.7) as well as for the analytical solution of the equation of particle motion (Eq. 3.7.2 - 4) become available to the tracking routine from the calculations of the gas flow. The prevailing gas velocity is assumed constant over the time of integration and no gas velocity gradients are taken into account during that time step. The initial particle velocity vector $\mathbf{u}_{p,i}$, is known either from the calculation of the previous timestep or as a specified inlet condition. The physical parameters identifying the particle are also known so the particle relaxation time is calculated. The timestep is chosen as the minimum of the times that the particle needs to cross the scalar control volume if it moved along one of the co-ordinate directions only. This well verified condition for estimating the timestep ensures that the particle traverses at most a single scalar control volume. The criterion has been used by many researchers, Amsden and Ruppel (1981), Lockwood et al (1984), Gaffen et al (1985). The mathematical reasoning for doing so may be found in Roache (1972) and Anderson et al (1985). It can be expressed as :

$$\Delta t = \min \{ \frac{\Delta x}{u_{p_i}} , \frac{\Delta y}{v_{p_i}} , \frac{\Delta z}{w_{p_i}} \} \tag{3.7.5}$$

where Δx, Δy, Δz are the dimensions of the control volume within which the particle resides initially. The final particle position is calculated from

$$x_{p_f} = x_{pi} + \frac{(u_{p_i}+u_{p_f})}{2} \Delta t \tag{3.7.6}$$

$$y_{p_f} = y_{p_i} + \frac{(v_{p_i}+v_{p_f})}{2} \Delta t \tag{3.7.7}$$

$$z_{p_f} = z_{p_i} + \frac{(w_{p_i}+w_{p_f})}{2} \Delta t \tag{3.7.8}$$

The direction cosines for the particle trajectory during this particular time step are given by:

$$\text{cosl} = \frac{(x_{p_f} - x_{p_i})}{s} \tag{3.7.9}$$

$$\text{cosm} = \frac{(y_{p_f} - y_{p_i})}{s} \tag{3.7.10}$$

$$\text{cosn} = \frac{(z_{p_f} - z_{p_i})}{s} \tag{3.7.11}$$

where s stands for the length of the trajectory segment. An algorithm checks,based on analytical geometry, calculate the distances of the particle location from the control volume interfaces that lie in the direction of flight. The interface to be crossed first by the particle is then identified and through that the weighting factors for the source term distribution.

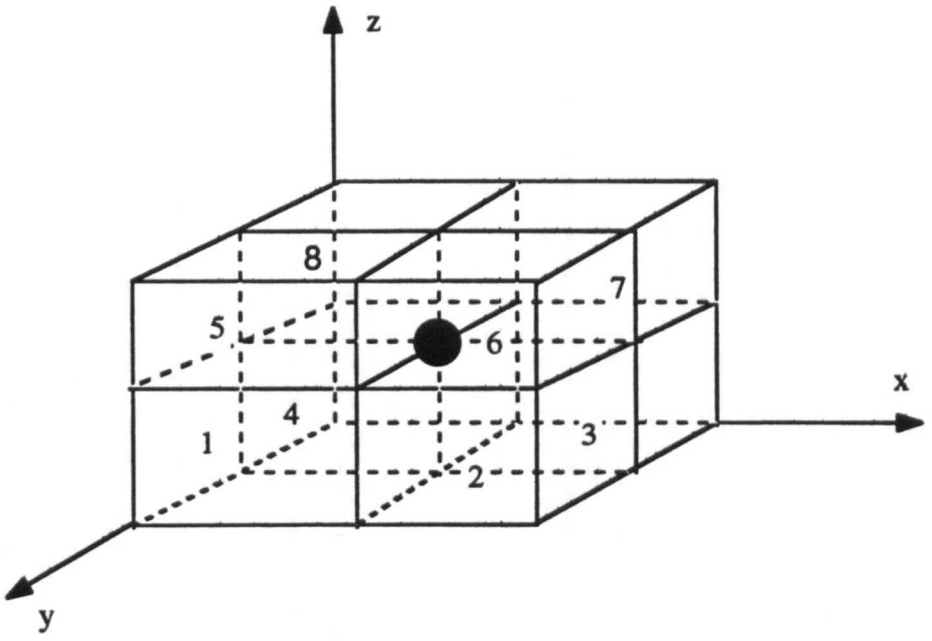


Fig. 3.6 Subdivision of the scalar control volume. The black sphere denotes the position of the scalar grid node.

Use of the analytical solution, Eqs. (3.7.2) - (3.7.4), gives the final particle velocity $\mathbf{u}_{p,f}$. There is a unique straight line connecting the initial and final particle position which crosses both the faces and the logical partitions of the scalar control volume. The orientation in space of this segment of the particle trajectory being expressed by the direction cosines, is calculated with reference to the inertial system in use. The crossing points of the particle trajectory and the logical partitions of the control volume are identified using formulae from analytic geometry. The fractions of the timestep needed for the particle to move from one partition to the next are estimated after weighting the total time of flight.

3.7.3 The Calculation of Particle / Droplet Temperature

a. Coal Particle Temperature Calculation.

The coal particle temperature is calculated by the analytical integration of equation (2.3.13). The differential equation 3.1 can be written in the form

$$\frac{dT_p}{dt} = A - BT_p \qquad (3.7.12)$$

which after the integration over a time Δt leads to a recurrence formula

$$T_{p,f} = T_{p,i} \exp(-B\Delta t) + \left(\frac{A}{B}\right)(1 - \exp(-B\Delta t)) \qquad (3.7.13)$$

The coefficients A and B are given by the expressions

$$A = k_1 T_g + k_2 + k_3 T_R^4 \tag{3.7.14}$$

$$B = k_1 + k_3 T_p^3 \tag{3.7.15}$$

where

$$k_1 = \pi \, Nu \, k_G \, d_p / (c_p m_p) \tag{3.7.16}$$

$$k_2 = [- \eta \, \mu \, H_c + (1 - \eta) \, L_v] / (c_p m_p) \frac{dm_p}{dt} \tag{3.7.17}$$

$$k_3 = \pi \, \sigma \, \varepsilon_p \, d_p^2 / (c_p m_p) \tag{3.7.18}$$

η has values either 1 or 0. This implies that during the devolatilisation process no char combustion occurs. If $\eta = 1$ signifies that devolatilisation is complete then all the volatiles have been released from the particle, thus the coal particle undergoing heterogeneous combustion processes. If η is 0 then the particle releases volatiles at that stage.

b. *Oil Droplet temperature Calculation*

Similarly the oil droplet temperature is calculated through the analytical integration of equation (2.3.25) which can be written in the form

$$\frac{dT_p}{dt} = -A_1 T_p + A_1 T_g - B1 \tag{3.7.19}$$

where Tp stands for the droplet temperature, Tg for the gas temperature and

$$A_1 = \frac{6 \, k_g \, Nu}{\rho_p \, c_p \, d_{pi}^2} \tag{3.7.20}$$

$$B1 = \frac{12 L k_g \, C}{c_p \, \rho_p \, Cpg \, d_{pi}^2} \ln (1+B) \tag{3.7.21}$$

All the parameters introduced in equations (3.7.19) and (3.7.20) have been defined in sections(2.3.2c) and (2.4.2). Integration of the equation (3.7.18) over the chosen time step yields the recurrence formula :

$$T_{pf} = \left(T_g - \frac{B_1}{A_1} \right) + \left(T_{pi} - T_g + \frac{B_1}{A_1} \right) \exp\left(- A_1 \Delta t \right) \qquad (3.7.22)$$

which gives the droplet temperature at the end of each time step.

3.7.4 The Interaction Source Terms

The procedure used herein, see Migdal and Agosta (1967) and Crowe (1976), for handling the gas-particle interaction is termed the particle source in cell (P.S.I.C) method. The presence of the particle in the finite-difference control volume is made known to the gas-phase through the introduction of extra source terms in the transport equations. The particulate-phase and the gas-phase are coupled through the frequent updating of the Eulerian source terms in the gas-phase equations with the local rates of mass, momentum, energy and mixture fraction exchange been deduced from the Lagrangian calculations for the particulate phase.

a. <u>The momentum source terms</u>.

The momentum source terms are expressed as follows :

$$S_{p,u} = [m_{pi}\, U_{p,i} - m_{pf}\, U_{p,f}]\, N \frac{\delta t}{\Delta t} \qquad (3.7.23)$$

where U_p stands for the particle velocities u_p,v_p and w_p in the x,y, and z directions respectively, m_p for the mass of the particle, i and f are indices that identify the initial and final particle positions for the chosen time step Δt, $\delta t/\Delta t$ is the weighting factor that

represents the fraction of the time step during which the particle belongs to the specific control volume, and N is the number of particles traced per second .

b. The mass source term

The mass source term is given by :

$$S_{p,m} = (m_{pi} - m_{pf}) N \frac{\delta t}{\Delta t} \qquad (3.7.24)$$

c. The enthalpy source term

(i) Coal Particles

During the flight of a coal particle heat exchange takes place between the particle and the surrounding gas, which is the enthalpy source. There are several contributions to this term related to the mechanism through which this exchange happens. Formulation of this source leads to :

$$S_h = H_{conv} + H_{rad} + H_{vcomb} + H_{devol} \qquad (3.7.25)$$

where each term on the right-hand side of eq.(3.7.25) represents the contribution of each mechanism.

• H_{conv} is the heat rate transferred to or from the particle due to convection

$$H_{conv} = \pi d_p Nu k_G (T_p - T_g) \qquad (3.7.26)$$

where Nu is t he Nusselt number, k_G is the thermal conductivity of the gas mixture given already in section 2.3.2b.

• H_{rad} is the radiative heat exchange rate between the particles and the gas

$$H_{rad} = -N \sigma \pi d_p^2 \varepsilon_p (T_r^4 - T_p^4) \qquad (3.7.27)$$

where N is the number of particles, with all the rest variables defined back in section 2.3.2b

• H_{vcomb} is the heat released to the gas phase due to volatiles combustion

$$H_{vcomb} = M_{vol,rel} H_{cal} \qquad (3.7.28)$$

where $M_{vol,rel}$ is the mass of volatiles burnt and Calval is the calorific value of the volatiles.

• H_{devol} is the heat intake rate due to devolatilisation

$$H_{devol} = - M_{vol,rel} H_{vol} \qquad (3.7.29)$$

where H_{vol} is the latent heat for devolatilisation.

(ii) Oil Droplets

For the oil droplet the source term is given by :

$$S_{p,h} = (m_{p,f} - m_{p,i}) N (H_{fu} - L) \qquad (3.7.30)$$

where Hfu is the calorific value of the fuel and L is the latent heat of evaporation.

d. <u>The mixture fraction source term</u>

The mixture fraction source terms, depending on the type of the fired fuel, are presented in Table 3.1:

Type of Fuel	$S_{p,f}$
Gas	0
Oil	$S_{p,m} (\frac{1 - \phi_0}{\phi_1 - \phi_0})$
Coal	$(s_1 S_{vol} + s_2 S_c) (\phi_1 - \phi_0)$

Table 3.1 The Mixture Fraction Source Terms

3.7.5 The Solution Procedure

The sequence followed for the Lagrangian phase calculations may be summarised by the following flow chart:

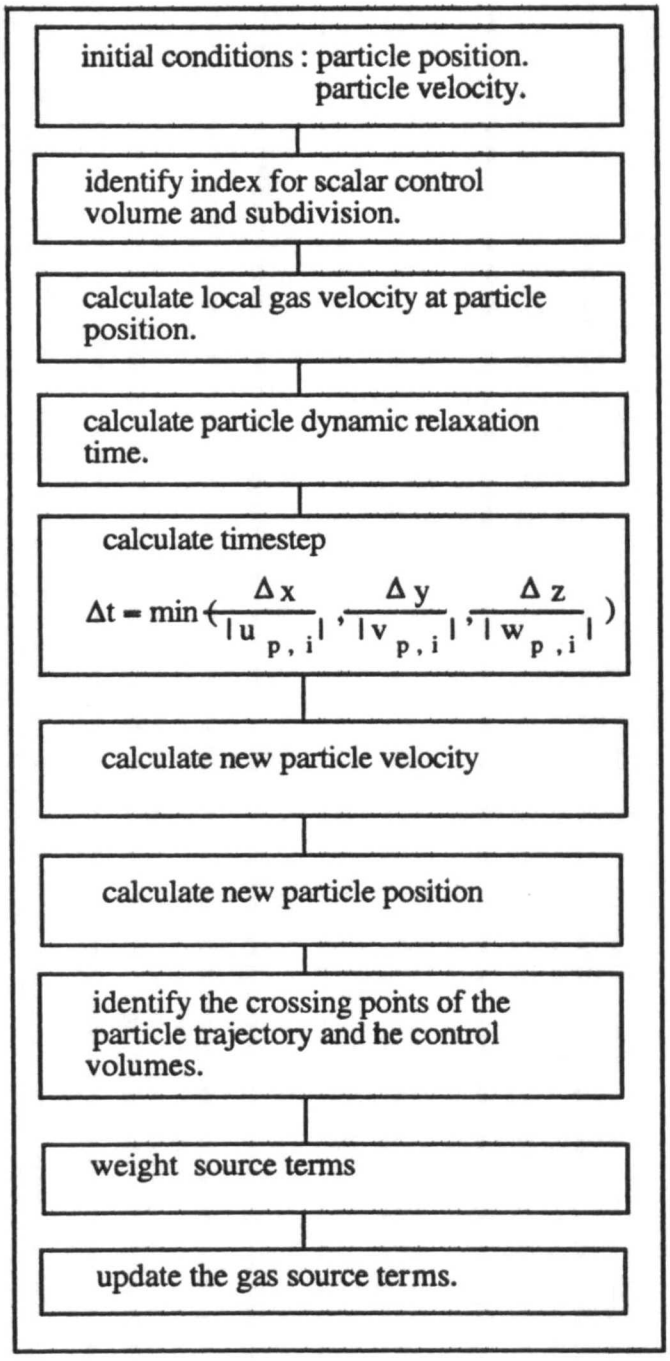


Fig. 3.7 Flowchart of operations for calculating the particle trajectory and the source terms for a single timestep.

3.7.6 The Boundary Conditions

The Lagrangian formulation for the particulate phase necessitates the detailed definition of the initial conditions for each timestep both when the particle just enters the solution domain or is in the free flow.

For each inlet position the spatial position of the incoming monosized particles and their velocity in vectorial form must be specified. The total number of characteristic trajectories of particles with the same physical properties tracked from each single inlet position depends on the area covered by the port and the prevailing gas conditions. When the velocity profile at the inlet is of the plug flow type then there is no need to track more than a couple of particles, otherwise a greater number of particles should be initiated from different positions within the area covered by the inlet port in order to simulate the velocity profile. The total number of monosized particles entering the numerical domain for each inlet position is then calculated from the mass flow rate of the particulate phase and the diameter of the particles. The definition of the initial conditions for every new timestep is straightforward by utilising the final particle position, velocity and temperature calculated analytically for the previous timestep.

When there is interaction with solid surfaces the boundary conditions are different for a particle that impinges the solid boundary from those for a rebounding particle. At first consider a particle which moves in an arbitrary orientation relative to a solid boundary. The analytic solution for the particle velocities (3.7.2) - (3.7.4) are not applicable when the particle traverses the control volume adjacent to a solid boundary because the timestep Δt is chosen on purely geometrical reasoning. In those cases the final spatial position for the particle would be true only if the solid boundary was permeable. The necessity to specify a timestep that would be adequate for the particle to traverse the control volume adjacent to a solid boundary and land on the boundary has been calculated by other investigators by the Runge-Kutta iterative method where the appropriate timestep was chosen by trial and error: Abbas et al (1981a), Lockwood et al (1984). In another attempt a numerical method was formulated for estimating the

timestep where the analytical solution for the particle velocity was substituted into the equation that gives the spatial particle position. The roots of the resulting transcendental equation for time were numerically calculated using the iterative methods of Newton-Raphson and Regula-Falsi. Although the last iterative method proved to be superior, both were numerically inefficient for the purposes of this study. The main shortcomings being that the region of values for the root had to be specified in advance with some accuracy, a difficult task on its own; the number of iterations needed to achieve the predefined accuracy, namely that of the particle diameter in question, sometimes exceeded all expectations. To avoid the aforementioned complications a new method for calculating the timestep was formulated and tested with good results.

The Lagrangian formulation predicts the final particle position and velocity if the initial conditions are specified in addition to the body and field forces acting on the particle during its flight but it does not give any detailed information about the shape of the particle trajectory that joins the two points. Suppose that the particle moves in a four dimensional space where the three dimensions are the spatial co-ordinates while the fourth is time. There is a unique straight line AC that connects the final positions with the initial ones, Fig. 3.7.4 . The letter B identifies the unknown spatial position, which is the point of the AC, where the particle impinges the arbitrary orientated solid boundary SB. Assume that the particle trajectory during a timestep is along the X-direction and then along the Y- and Z- directions before it reaches position B, see the bold arrows. At first the timestep Δt is chosen by the numerical criterion, defined in previously. If utilised then the final particle position would be at point C which lies outside the physical domain. The required flight time for the particle to land on the arbitrarily defined solid boundary SB is t_b. The direction of AC and the orientation of the surface of the solid boundary SB are computed so the exact position of point B is calculated by using formulae from the analytic geometry that give the intersection of a line and a surface. Comparison of the triangles $\Delta(At_bx_b)$ and $\Delta(At_cx_c)$, where t_c defines the ordinate for the timestep Δt on the axis for time, note that both triangles are on the same plane and that their sides t_bx_b and t_cx_c are drawn parallel to each other, gives :

$$\frac{At_b}{At_c} = \frac{Ax_b}{Ax_c} \tag{3.7.31}$$

Since the point A signifies the initial particle position equation (3.7.33) is recast as :

$$t_b = \frac{x_b - xpi}{x_f - x_{pi}} \Delta t \tag{3.7.32}$$

where $x_{p,i}$ stands for the particle initial position in the x direction, x_b is for the coordinate position of the point B in the x direction and x_f is for the final particle position as calculated from (3.7.2 -4). Equation (3.7.33) calculates the timestep as a function of the numericaly chosen timestep and the geometrical dimensions. It can be used for any orthogonal curvilinear co-ordinate system. Using the calculated timestep from (3.7.33) in (3.7.2 - 4) the final particle velocity is calculated which is used as the initial condition for the further prediction of the particle trajectory.

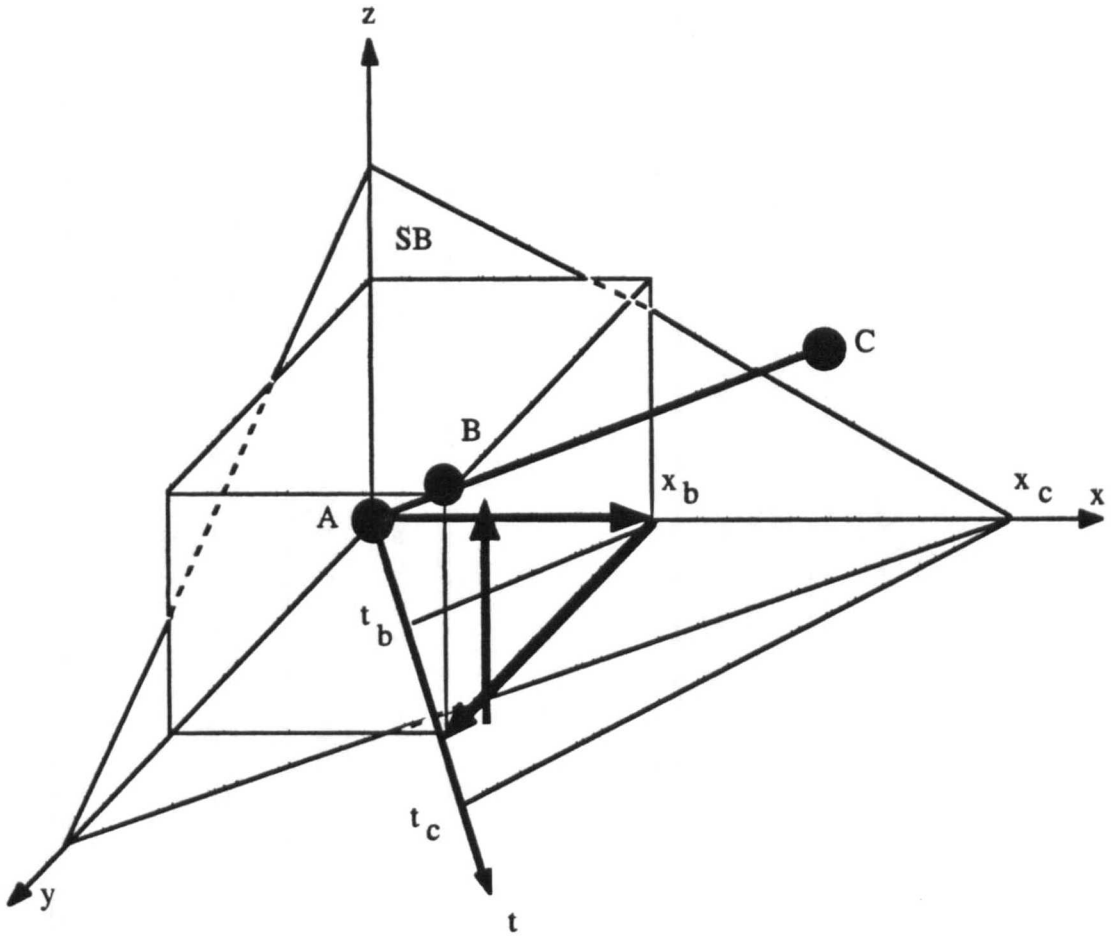


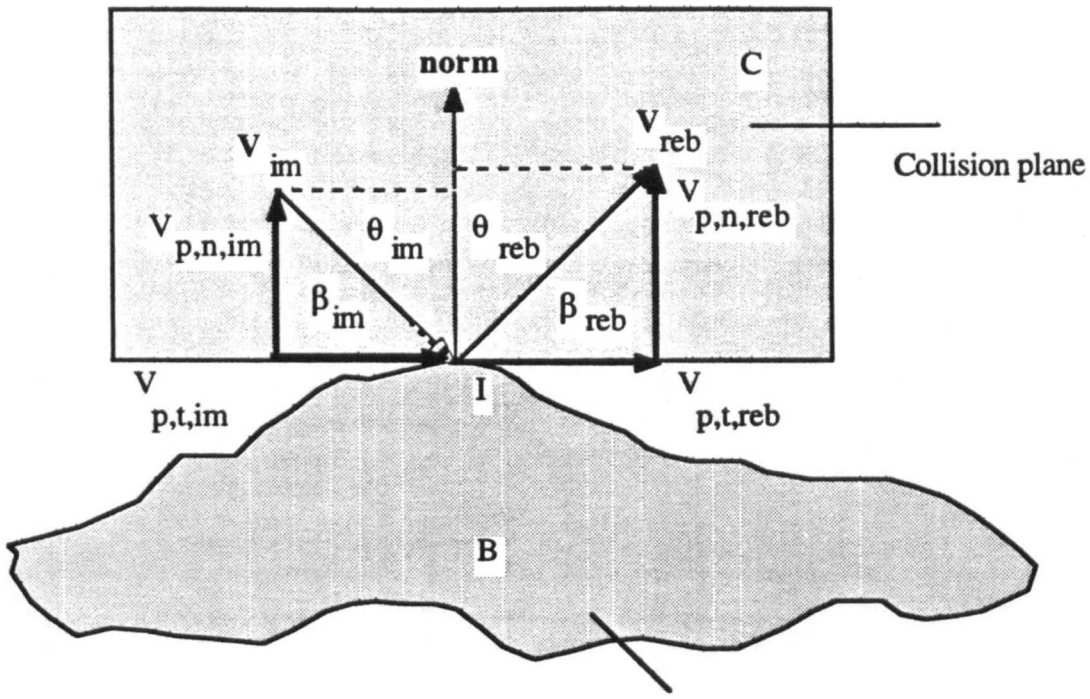
Fig. 3.8 The four dimensional space utilised in the calculation of the timestep when the particle impinges a solid boundary. The control volume adjacent to the physical boundary SB is sketched as a cube.

There is provision in the code to abandon the calculation of the particle trajectory when a particle is stagnant within the solution domain. This would be true only when the collision model specifies rebound conditions such that the particle is not capable of overcoming the aerodynamic resistance of the boundary layer. The phenomena of slagging and fouling in the combustor could be simulated in this manner.

3.7.6a The Collision Model

Tracking the particulate phase in enclosed geometries necessitates an accurate model for predicting velocity characteristics for the rebounding particles from the solid boundaries so that the solution of the equation of motion can be continued beyond the points of impact. The collision model used herein comprises a set of semi-analytic relations that are solved in a non-iterative manner. The equation of motion for a single particle is solved until the particle impacts the solid boundary then the rebounding velocity, direction and standard deviation are calculated from experimentally derived polynomial expressions that relate the rebounding quantities to those prior to the collision. These empirical correlations for the restitution coefficient measure the kinetic energy exchange between two objects upon impact.

The restitution ratios are only applicable to the collision plane C, Fig.(3.9). The absolute orientation of the solid boundary surface B is irrelevant although its relative position with respect to the collision plane, defined by the normal vector to the boundary surface at the point of impact and the impinging velocity vector of the particle, provides the essential information for calculating the rebounding particle velocity and its orientation in a three-dimensional domain.



cross section of the boundary surface

Subscripts

B	boundary surface	im	impingement
C	collision plane	n	normal component
I	point of impact	p	particle
norm	normal vector	reb	rebound
V	velocity component	t	tangential component
V	velocity vector		
b	angle		
q	complementary angle		

Fig. 3.9 Description of the collision geometry and associated notation.

A thorough investigation on collision models can be found in Papadopoulos (1989). The model adopted for this study is that of Beacher et al (1987), which can be described as follows :

$$\frac{U_{reb}^{n}}{U_{im}^{n}} = 1.0 - 0.4159\beta_{im} - 0.4994\,\beta_{im}^{2} + 0.292\,b_{im}^{3} \qquad (3.7.33)$$

$$\frac{U_{reb}^{t}}{U_{im}^{t}} = 1.0 - 2.12\,\beta_{im} + 3.0775\beta_{im}^{2} - 1.1\beta_{im}^{3} \qquad (3.7.34)$$

The collision geometry is shown in fig 3.7.5. U_{reb}^{n}, U_{reb}^{t} stand for the normal and tangential components of the particle rebounding velocity while U_{im}^{n}, U_{im}^{t} stand for the components of the impinging velocity, and β_{im} is the angle of impingement. The particle rebounding angle can then be calculated from :

$$\beta_{reb} = \arctan\left(\frac{U_{reb}^{n}}{U_{reb}^{t}}\right) \qquad (3.7.35)$$

The components of the rebounding particle velocity in the three - coordinate directions are determined by solving the simultaneous equation set :

$$\mathbf{norm} \cdot \frac{\mathbf{U}_{reb}}{|\mathbf{U}_{reb}|} = \sin(\beta_{reb})$$

$$\frac{\mathbf{U}_{im} \cdot \mathbf{U}_{reb}}{|\mathbf{U}_{im}|\,|\mathbf{U}_{reb}|} = \cos(\beta_{im} + \beta_{reb}) \qquad (3.7.36)$$

$$(\mathbf{norm} \times \mathbf{U}_{im}) \cdot \mathbf{U}_{reb} = 0$$

where **norm** stands for the normal unity vector that characterises the orientation of the plane of impingement.

3.8 Solution Of The Thermal Radiation Equation

The change in the intensity dI of a ray travelling a distance ds through a medium at temperature T_g and absorption coefficient K is given by equation (2.5.4) repeated here :

$$\frac{dI}{ds} = -K_a I + \frac{K_a \sigma T^4}{\pi} \qquad (3.8.1)$$

The first term in the right hand side accounts for absorption and the second one for emission. Considering a 'pencil of rays' along a representative direction that crosses a finite - difference cell of presumed uniform temperature and absorption coefficient then equation (3.8.1) may be integrated analytically yielding the following recurrence formula :

$$I_{n+1} = \frac{\sigma T_g^4}{\pi}(1 - \exp(-K s)) + I_n \exp(-K s) \qquad (3.8.2)$$

where I_n and I_{n+1} is the radiation intensity on the grid cell entry and exit respectively and s is the distance travelled by the ray (optical length) within the control volume. Referring to Fig (2.5.1) the relation (3.8.2) is successively applied from point Q_1 to P_1until the intensity I_m at the point P_1 is known. The flux arriving at the point P_1 is the sum of all the I_m in the hemisphere :

$$q_{+,p} = \int_{\pi} I\Omega d\Omega = \sum_{m} I_m \Omega_m \, d\Omega_m \qquad (3.8.3)$$

Applying the boundary condition for a prescribed temperature we obtain :

$$q_{-,p} = (1 - \varepsilon_w) q_{+,p} + \sigma \varepsilon_w T_w^4 \qquad (3.8.4)$$

where $q_{-,p}$ is the outgoing flux away from the wall, $q_{+,p}$ is the wall arriving flux, ε_w is the wall emissivity and T_w is the wall temperature.

If the representative direction characterises a small solid angle $d\Omega$ covering an area dA in the direction Ω , then the radiation source term for the cell under consideration is :

$$S_n = (I_{n+1} - I_n)\, \Omega \, d\Omega dA \qquad (3.8.5)$$

To obtain the flux arriving at point P_1 on the wall surface with cell area dA, the hemisphere at P_1 is subdivided into a number of smaller solid angles. The angle

measured with the normal is called θ and the azimuthal angle ϕ . These angles are divided into a specified number of equal solid angles. Each solid angle subdivision $d\Omega$ is about the representative direction Ω_m . Each representative direction is traced through the cells until the far wall is reached at point Q_1.

There the intensity leaving the wall cell Q_1 is taken to be the intensity leaving it at an adjacent point, the two values of the intensity are arbitrarily considered to be the same. Because the intensity is attenuated exponentially the solution along a representative direction is be very sensitive to the initial value.

This process is repeated for each wall control volume until the difference between the old negative flux and the new one is within some pre - specified error.

The net flux is given by :

$$q_p = q_{+,p} - q_{-,p} \tag{3.8.6}$$

Equation (3.8.6) is used as a boundary condition if the wall flux is prescribed. In this case the temperature of the wall is then calculated from equation (3.8.4).

The total radiative source for each control volume is the sum of the sources due to each 'pencil' of rays crossing a particular cell, i.e.

$$S_n = \sum_1 S_{ni} \tag{3.8.7}$$

Finally the radiative source term is introduced into the enthalpy equation explicitly in a similar way as the particulate source terms.

3.9 Computational Details

3.9.1 Convergence Characteristics

During the course of iterations, the imbalance in equation (3.4.1) is calculated and is called the residual. The sum of the absolute values of the residuals for all the control volumes is calculated and normalised by a representative value at the inlet(e.g. mass inflow rate for the mass residual or inlet momentum for the momentum residual). The calculations will be stopped when the residuals for all the dependent variables are less than 10^{-3} . A clearer picture of the convergence sequence is obtained by monitoring the values of the different ϕ's at a chosen location within the calculation domain, to ascertain whether these values become stable (converge to a certain value). The choice of this monitoring location is arbitrary, but it is recommended that should reside within a region where steep gradients occur.

3.9.2 Under - relaxation

Under - relaxation is used to suppress any sudden undesirable change in any of the dependent variables being solved. The effect of this is to increase the stability of the solution. The following relation is applied to any dependent variable :

$$\phi_{new} = (1\text{-}a\,\phi_{old}) + a\,\phi_{calculated} \qquad (3.9.1)$$

This means that the newly calculated values of ϕ are weighted between their old values and the newly calculated ones, with a weighting factor a. The values of under - relaxation factors used herein are cited separately for each test case.

3.9.3 Numerical Stability

The non - linear character of the partial differential equations and the strong coupling between them are the main reasons for numerical instability. The non - linearity is accommodated through the introduction of under - relaxation previously mentioned. The number of applications of the TDMA solver effected for each variable greatly affects the stability of the solution. Numerical experimentation showed that the pressure correction equation usually needs more iterations before updating the coefficients.

3.9.4 Accuracy of the Solution

The accuracy of the solution is mainly dependent on the extend to which the solution has converged and the distribution of the numerical grid.

CHAPTER 4

GAS COMBUSTION CALCULATIONS

4.1 Introduction

The combustion chamber of the simulated boiler of 320 MWe, which has the shape of a parallelepiped mounted on a hopper has overall dimensions of 10 x 10 x 30 m approximately, see Fig (4.1). The furnace is of the opposed - fired type and is equipped with 18 burners in total arranged as 3 x 3 arrays in the front and rear wall of the furnace respectively. The description of the furnace geometry used for the numerical simulation is restricted to the combustion chamber up to the height corresponding to the 'nose'.

4.2 The Numerical Grid

The simulation was carried out on a Cartesian orthogonal framework and utilised a numerical grid composed of 16 x 19 x 40 = 12160 volume elements in the three X, Y, and Z directions respectively. In Figs. (4.2), (4.3) and (4.4), the X - Z (parallel to the axis of the burners), Y - Z (perpendicular to the axis of the burners) and X -Y (horizontal) grids are shown. The inclined walls constituting the hopper and the nose are represented in a step-wise manner in order to pair the real geometry of the furnace off.

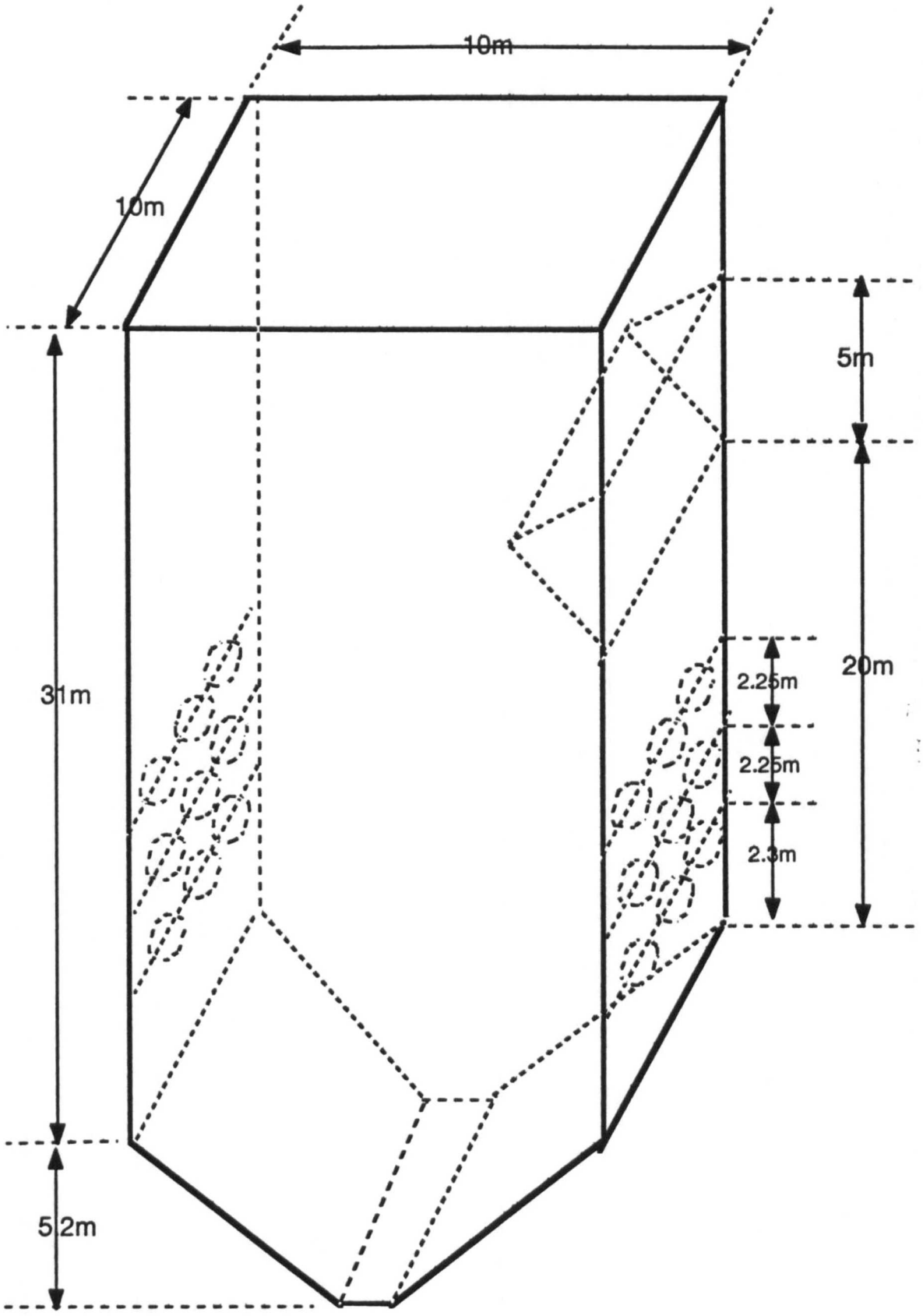


Fig. 4.1 The Gas and Oil-Fired Furnace Geometry

The burners are represented by nine grid cells forming a square. The central cell is allocated to the fuel port whereas the surrounding eight cells are for the air inlets. Care has been taken to ensure that the areas of the burner pipes are kept the same as those for the axisymmetric actual burner. The reader is referred to Fig (4.5) and (4.6). where the real burner design and the grid arrangement assigned for the simulation of each burner is depicted.

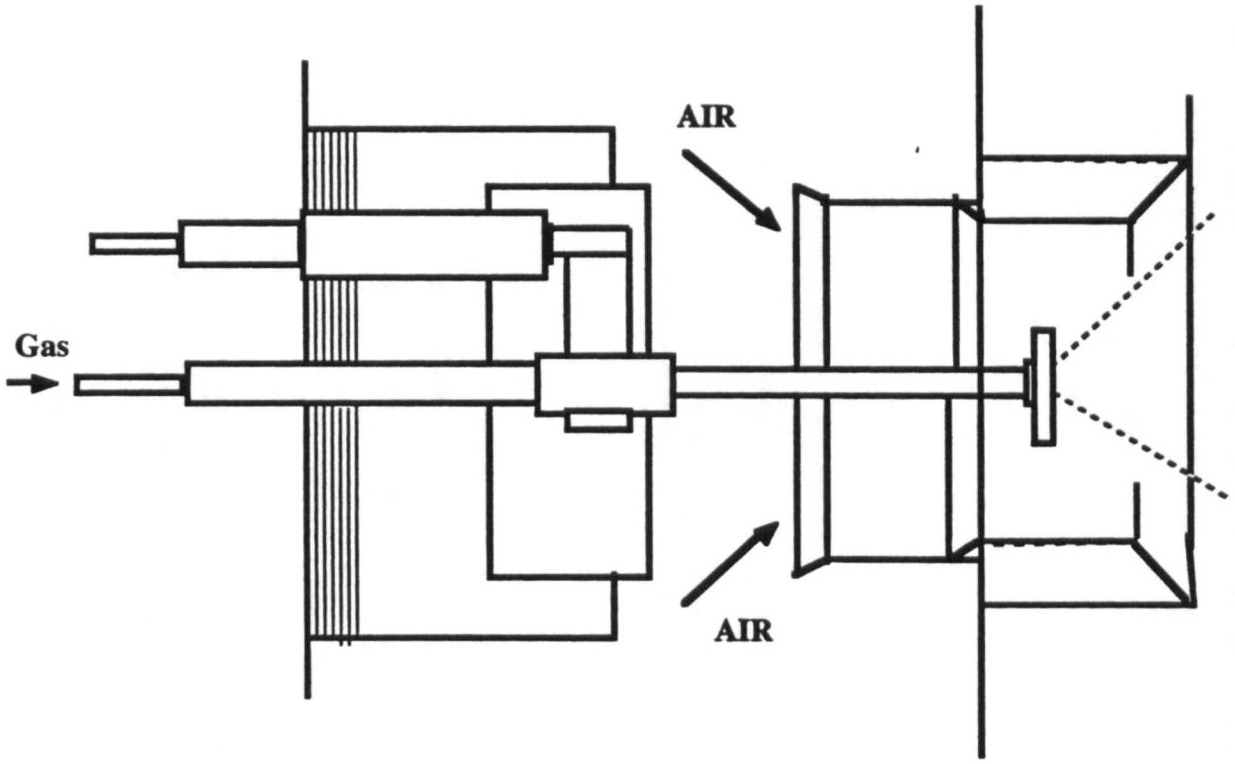


Fig. 4.5 The Burner Geometry

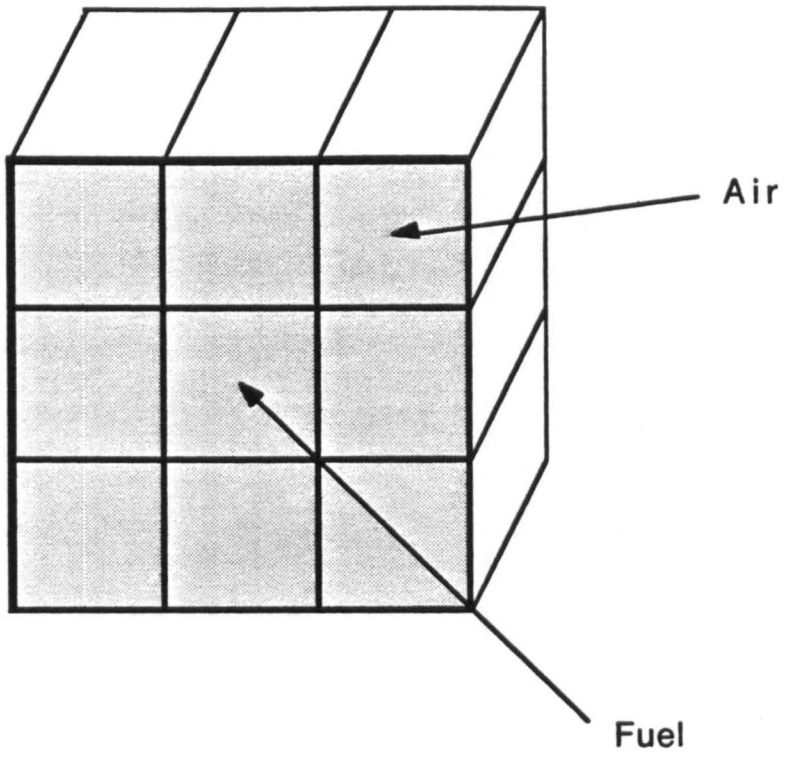


Fig. 4.6 The Burner Representation in Cartesian Co-ordinates

4.3 Operating Conditions

The velocities at the inlet ports has been calculated to ensure that the mass inflow rate is maintained at the real combustor value. The fuel utilised for this simulation is methane. The fuel mass inflow rate has been assessed in such a way as to keep the total thermal input the same as in the case of heavy fuel oil-fired operation presented in chapter 5. The velocities assigned for the inlets are included in Table (4.1).

$V_{A,in}$ (m/s)	56.54
$V_{F,in}$ (m/s)	50.88

Table 4.1 Inlet Velocities

4.4 Results and Discussion.

The results presented refer to the vertical X - Z and Y - Z which are parallel and perpendicular to the burners axes respectively and to the horizontal X - Y planes. The particular planes shown are presented in Tables (4.2 -4)

Y = 1	Section close to the right wall
Y = 5	Plane through the centre of the first column of burners
Y = 8	Plane between the first and second column of burners
Y = 10	Planes through the second column of burners (Plane of Symmetry)
Y = 12	Plane between the second and third column of burners
Y = 15	Plane through the third column of burners
Y = 19	Plane close to the left wall

Table 4.2 The X - Z Planes (Gas Combustion)

X = 1	Section near the front wall
X = 4	Intermediate section
X = 8	Plane at the middle of the hopper
X = 12	Intermediate section
X = 15	Plane near the rear wall (Nose region)

Table 4.3 The Y -Z Planes (Gas Combustion)

Z = 5	Hopper Region
Z = 10	Plane below the first row of burners
Z = 12,17,22	Planes at the centre of the first, second and third row of burners respectively
Z = 32	Plane between the third row of burners and the nose
Z = 38	Plane near the exit of the furnace (Nose Region)

Table 4.4 The X - Y Planes (Gas Combustion)

4.4.1 The Flow Field

The velocity field is three dimensional and very complex and its interpretation through 2-d graphs is extremely difficult . In any case, although the calculation grid used in the near burner region is not very fine (due to computer limitations), the results obtained are encouraging .

In Fig. (4.7 -13) (Y = constant) the projection of the velocity vector field on the X - Z planes is shown. The flow within the hopper in the inter - burner planes appears to be asymmetric, this asymmetry attributed to the horizontal recirculating motion and the effect of the nose, whereas for the planes along the burners axes it is fairly symmetric. The flow in planes parallel to the burner axes appears more symmetric because the set of burners form a 'curtain' of very high momentum that does not allow the downstream region flow to affect that of the hopper region. That is more apparent in the central plane (Y= 10) rather than in the planes passing through the axes of the other columns of burners (Y = 5 and 15).

The velocity vector plots, Figs (4.14 - 20), depict the flow along the horizontal X - Y planes. Strong recirculation zones are formed at the four corners of the furnace as well as in between the burners recirculating hot combustion gases back into the near burner region (NBR). This can be observed especially for the planes passing through the axes of the burners (Z = 12, 17 and 22). Due to the large dimensions of the furnace and the relatively coarse grid the recirculation zones in the immediate vicinity of the burners is poorly depicted. The flow in the hopper region (Z=5) is directed towards the front and rear walls due to the twin recirculation zones induced by the lower row of burners. In the upper part of the furnace, the flow is directed towards the front wall due to the inclined plane of the 'nose', (Z=32 and 38).

In Fig. (4.21 - 25) the flow field in the Y - Z planes (X = constant) is depicted. In planes 1 and 15 the burner arrangement can be clearly seen. Plane 8 is located near the middle plane of the furnace showing the divergence of the opposing jets. The three

dimensionality of the flow field is evident as well in the two recirculation zones in the bottom corners of the hopper.

4.4.2 The Temperature and Oxygen Concentration Fields

In Figs (4.26 - 32) the temperature profiles along the planes parallel to the axes of the burners are shown. A first observation is that as one moves towards the central part of the furnace a hotter region of temperatures higher than 1500 °C is encountered. This is due to the complete mixing of combustion gases at that region together with the strong heat transfer due to radiation. The temperature field observed is consistent with the characteristics of the flow field repeated here following the same trend. This can be observed, for example, in planes Y= 8 and 12, which are equally distanced from the central column of burners. The counter recirculating flow in the hopper region is shifted towards the rear wall, in plane Y = 8 enabling thus the better mixing of the fuel with the incoming air in that region. Consequently, enhanced reaction occurs in this region and resulting in higher gas temperatures. The opposite trend is observed in plane Y= 12 as expected. The temperature contours along the plane passing through the centre of the middle column of burners appears to be quite symmetric being consistent with the predicted symmetric flow field. The temperature profiles at the planes close to the water-cooled lateral walls of the furnace seem to be a mirror image of one to the other.

Figs (4.44 - 52) present the oxygen concentrations for the same X-Z planes as those of the temperature profiles. A first observation is that the oxygen concentration level are low in the locations where high temperatures are encountered. This indicates that complete combustion has occurred in that region. For example, the oxygen concentration in the central region of the furnace where the predicted temperatures are higher than 1500 °C is lower than 2.3% which denotes that enhanced combustion has taken place in that region. The oxygen distribution in the symmetry plane Y = 10 seems to be fairly symmetric as the velocity and temperature fields.

The temperature field in the X - Y plane (Z = constant), see Fig (4.33 -37), shows that in planes passing through the burners axes the temperatures appear to be lower than in the adjacent planes tending to be higher in the planes above the burners rather than below them. This can be attributed to :

a. On planes passing through the burners axes and close to the burners there exists a fuel rich region (core of the flame). This may be seen in Fig. (4.55) where the oxygen concentration near the burners is high (above 15%).

b. Due to the draught towards the exit of the furnace the convective heat transfer is stronger in the downstream direction rather than upstream.

The temperature profiles in the hopper region expectedly appear to be relatively uniform with the hotter region near the centre of the planes. This is because of the recirculating hot combustion gases moving upstream through the central part of the furnace. The asymmetry of the flow in this region analysed in section (4.3.1) can be observed here as the stretched-eight shape of the contour of 1300 C for plane Z= 5. The shift of the recirculation towards the rear wall in the right side-wall region of the furnace (plane Y = 8) is accompanied by the stretching of the temperature contour towards the same wall. The opposite happens in the region near the left side wall of the furnace. The temperature profile for the furnace outlet seems to be quite uniform at about 1200 ^{o}C.

In Fig. (4.38 - 43) the temperature profiles along the Y-Z (X = constant) planes are presented. The temperatures become progressively lower close to the front and rear walls of the furnace, whereas a hotter region is encountered near the middle planes. The temperatures are lower in the central region of these planes due to the existence of the burners and the insufficient mixing in this fuel rich region as indicated by the oxygen profiles, Figs. (4.56 - 58)

4.4.3 The Absorption Coefficient

Since the combustion processes simulated in this test case is one of methane combustion, the values of the absorption coefficient within the flame are expected to be moderate. In Figs. (4.44 -46) the absorption coefficients are shown for planes near the burners. Their values in that region are between 0.2 - 0.3 m^{-1} values that are typical for gaseous flames. In chapter 5 where oil combustion simulation of the same furnace is discussed comparisons will be made for the absorption coefficients because of the expected different optical properties of the flame due to the presence of the soot.

4.4.4 The Heat Fluxes

Fig. (4.59) presents the distribution of the heat fluxes transferred to the right-hand side water-cooled wall of the combustion chamber. The negative sign of the fluxes designates that the net heat flux is outgoing. The fluxes are high (above 250 kw/m^2) near the centre of the wall corresponding to the high temperatures encountered at that level within the chamber. Their magnitude is within range expected from the values of the absorption coefficients, temperature levels and common experience from power generation boilers. A comparison of these fluxes with those predicted from the simulation of the same boiler combustor fired with heavy fuel oil will be presented at the end of chapter 5.

4.5 Conclusions

1. The flow within the hopper in the inter - burner planes appears to be asymmetric, this asymmetry attributed to the horizontal recirculating motion and the effect of the nose, whereas for the planes along the burners axes it is fairly symmetric. The fields along the planes perpendicular to the axes of burners are fairly symmetric as expected.

2. Enhanced reaction is predicted to be taking place in the central region of the furnace with the result that high temperatures (above 1500 oC) and low oxygen concentrations (below 2.3%) are encountered there.

3. The heat fluxes to the side walls are consistent with the predicted temperature profiles, being higher at the level where higher temperatures are encountered. Their magnitude is within the range of values typically expected according to the experience of boiler operators.

5. A higher grid resolution in the near burners region is needed in order to simulate more accurately the mixing and combustion processes in that region. With the current capacity and capabilities of modern computers, this necessitates the development and use of local grid refinement techniques. In addition to this, the cylindrical geometry of the burners should be modelled. This could involve body fitted co-ordinate (BFC) treatment but they are not very convenient for this type of combustor and have proved unstable for two-phase flows. Alternatively, a combination of a LGR technique and unstructured tetrahedral meshes is more likely to provide a solution to this problem.

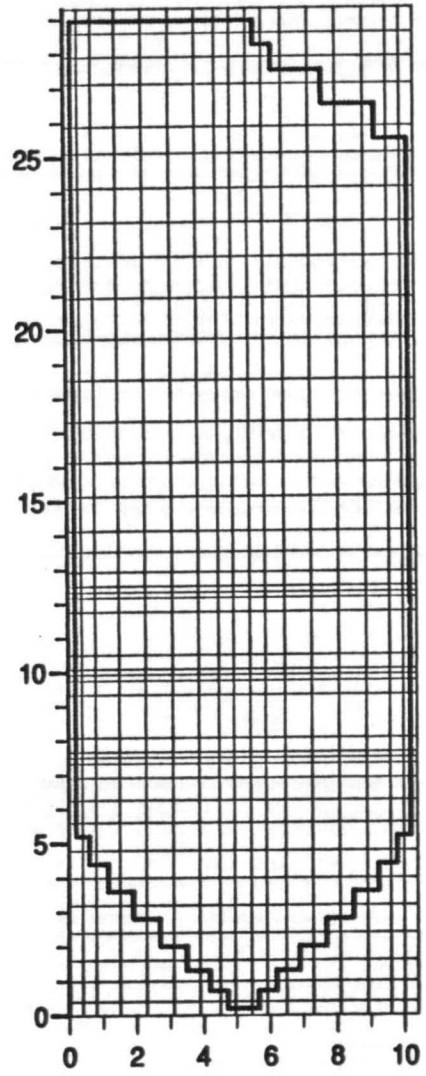


Fig. 4.2 The X-Z Numerical Grid (Gas And Oil Combustion)

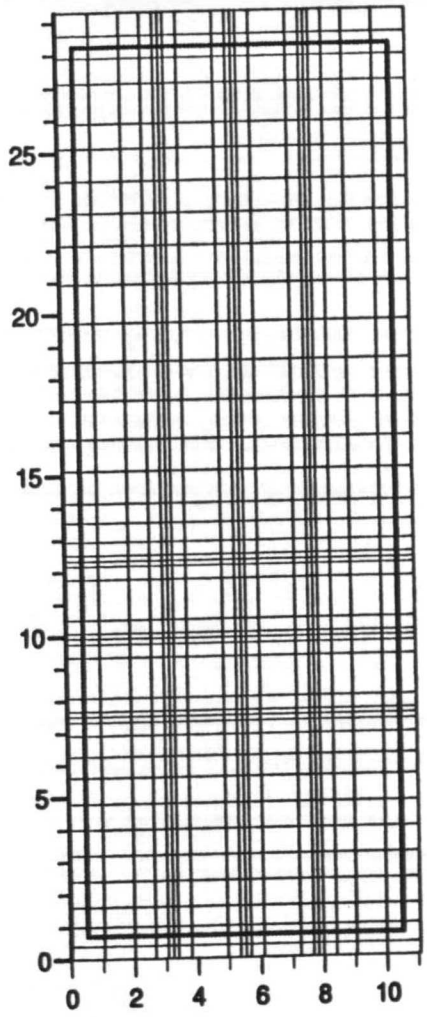


Fig. 4.3 The Y-Z Numerical Grid (Gas And Oil Combustion)

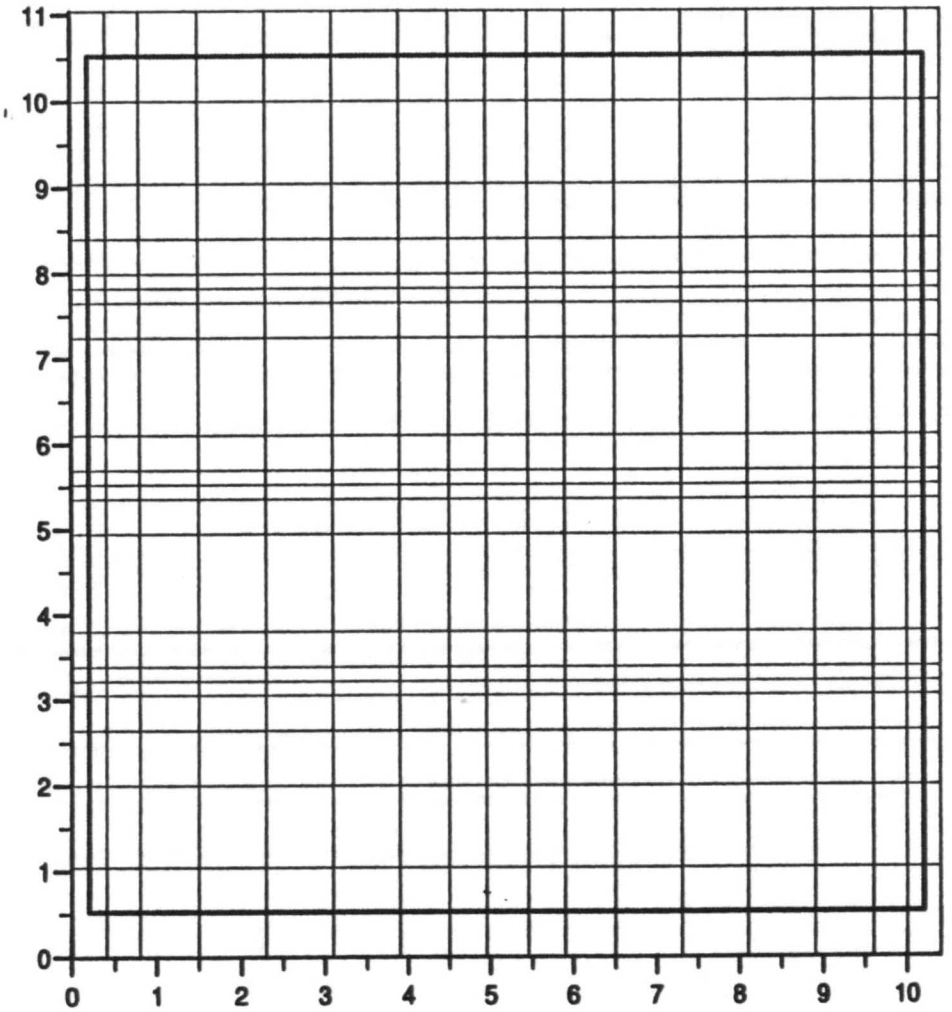


Fig. 4.4 The X-Y Numerical Grid (Gas And Oil Combustion)

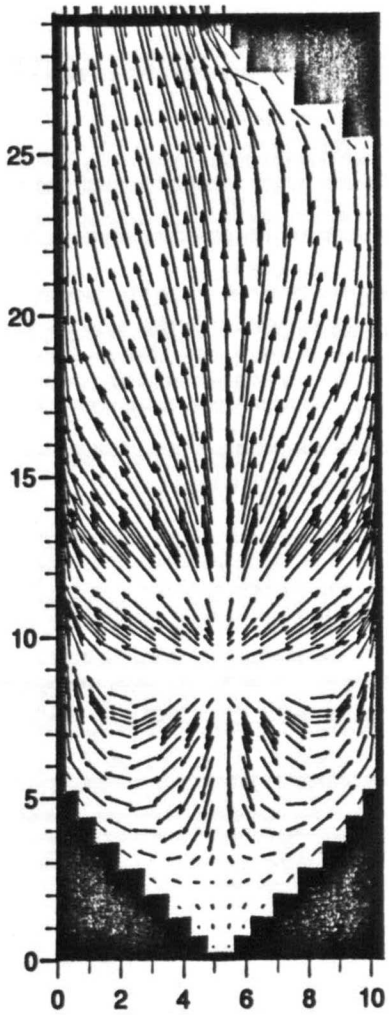


Fig. 4.7 Velocity Vectors For Y = 1 (Gas Combustion)

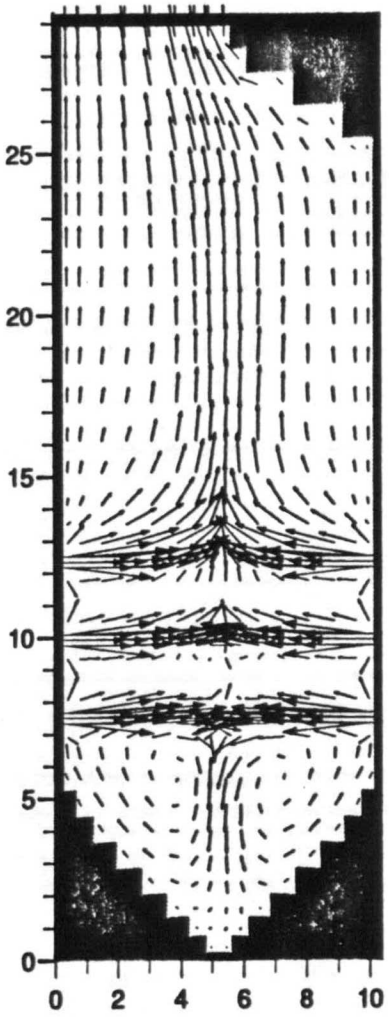


Fig. 4.8 Velocity Vectors For Y = 5 (Gas Combustion)

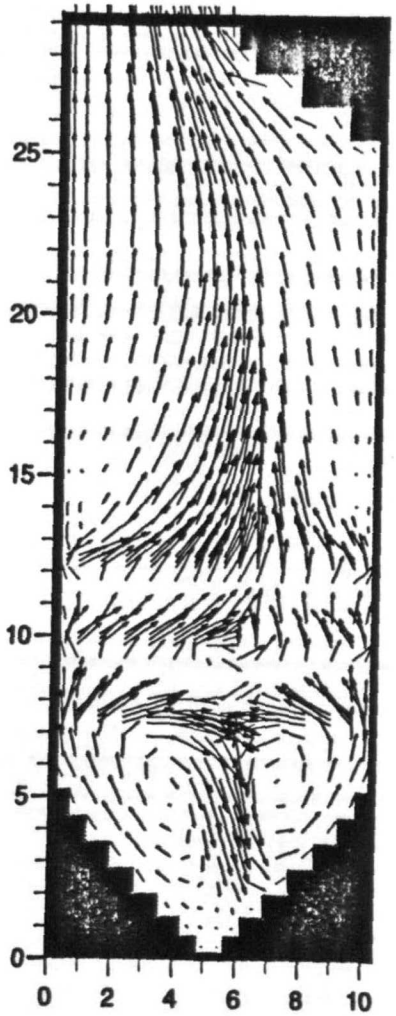


Fig. 4.9 Velocity Vectors For Y = 8 (Gas Combustion)

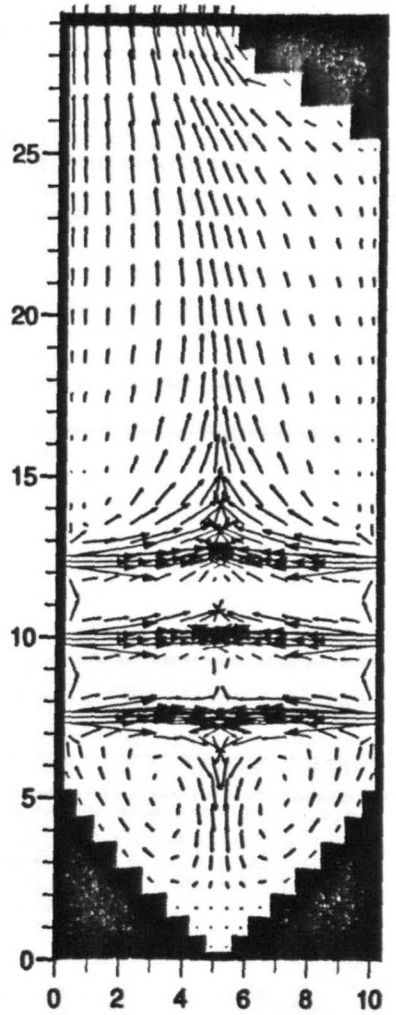


Fig. 4.10 Velocity Vectors For Y = 10 (Gas Combustion)

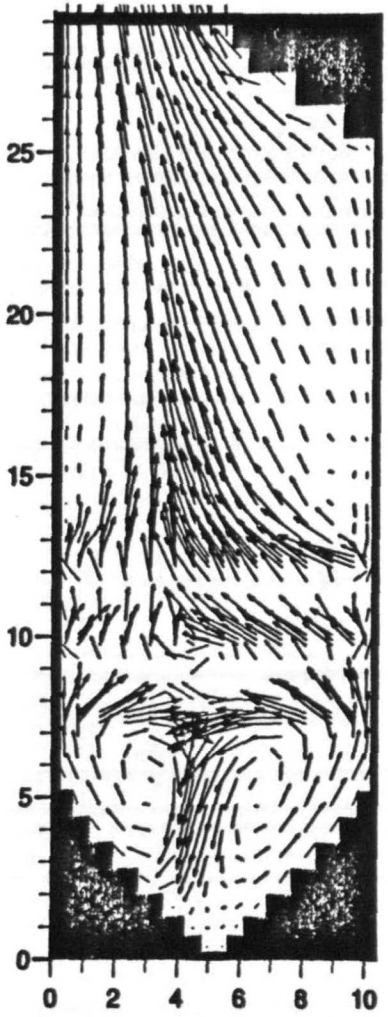


Fig. 4.11 Velocity Vectors For Y = 12 (Gas Combustion)

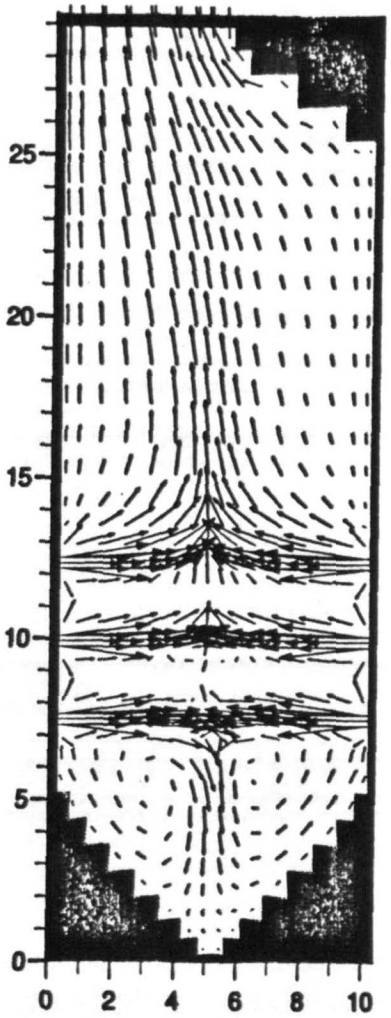


Fig. 4.12 Velocity Vectors For Y = 15 (Gas Combustion)

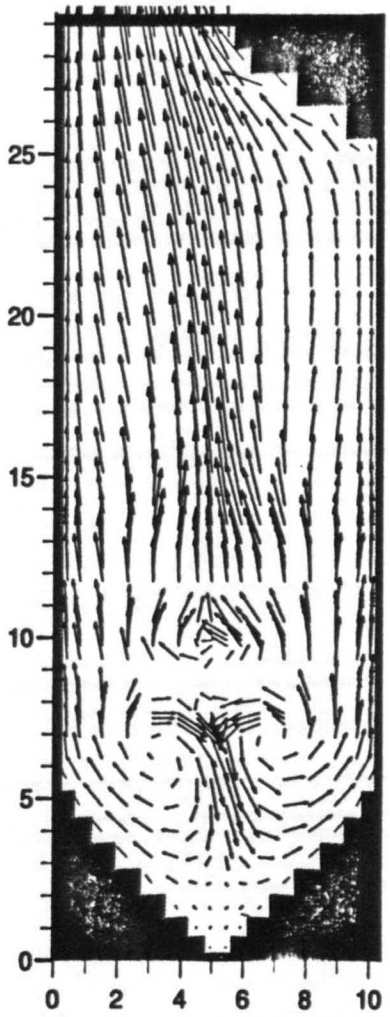


Fig. 4.13 Velocity Vectors For Y = 19 (Gas Combustion)

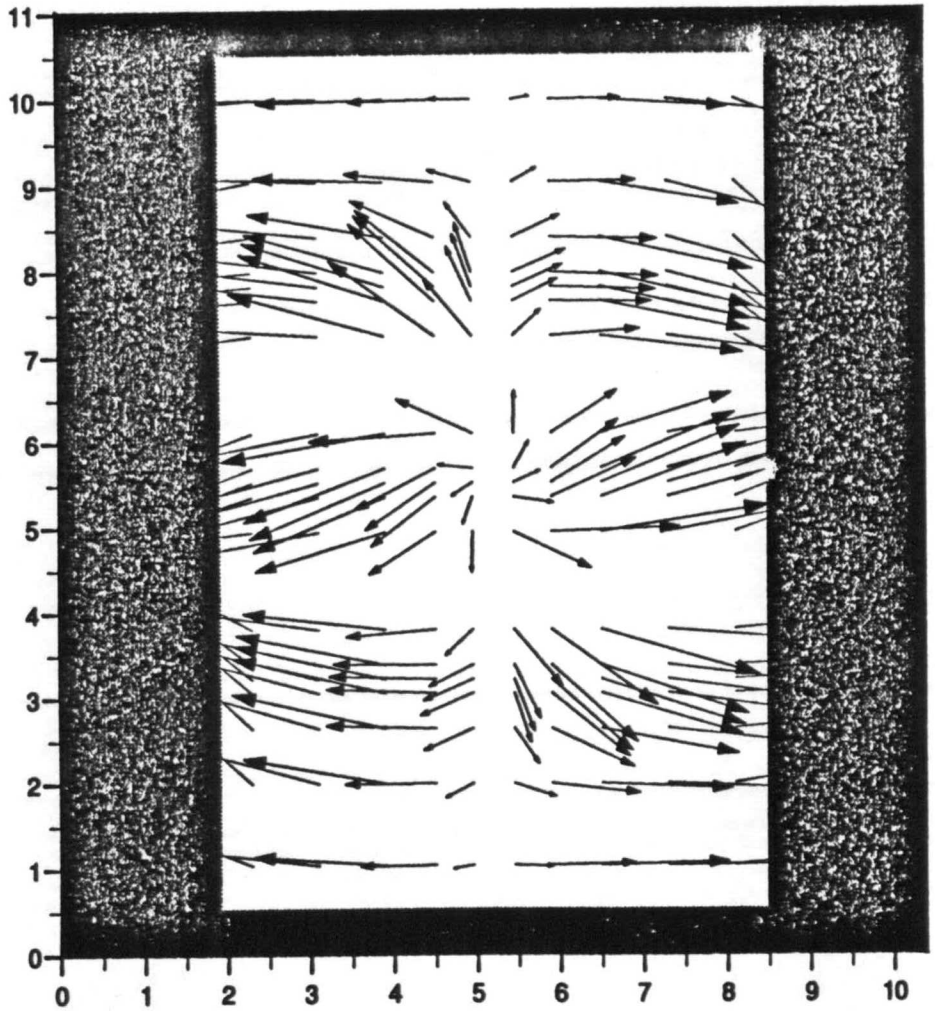


Fig. 4.14 Velocity Vectors For Z = 5 (Gas Combustion)

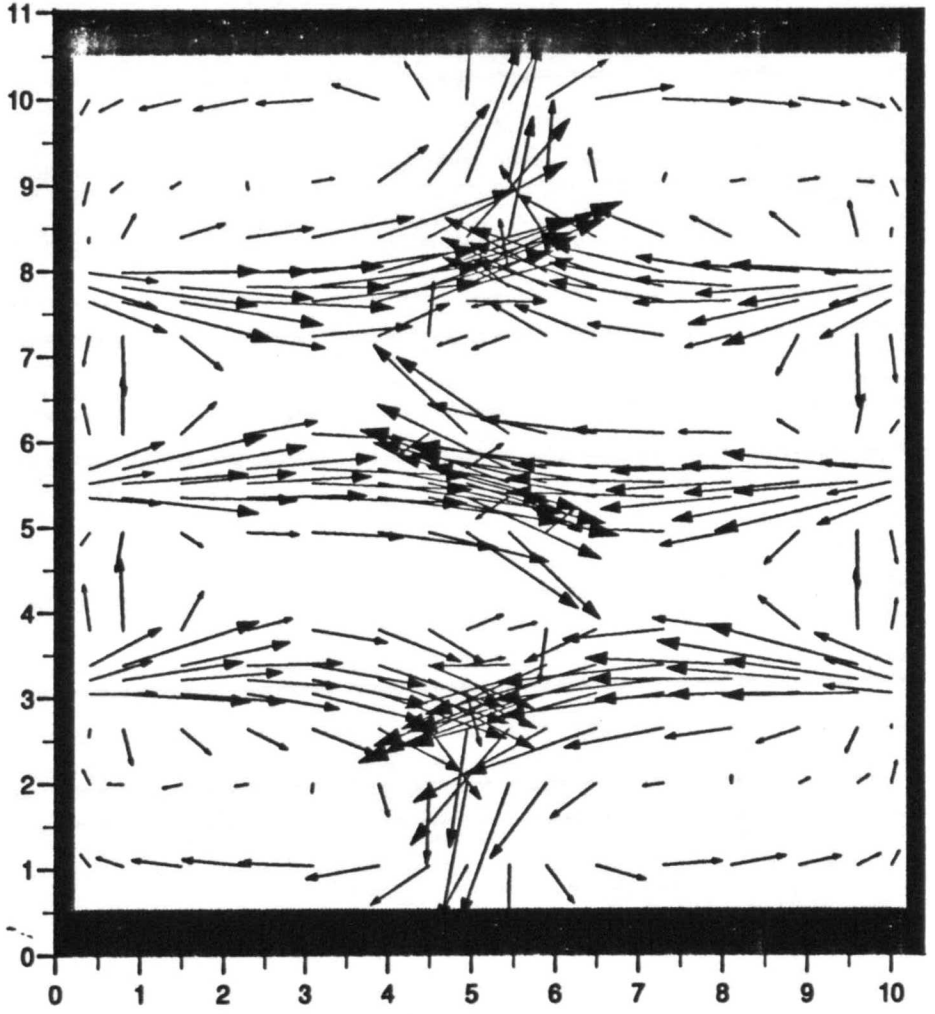


Fig. 4.15 Velocity Vectors For Z = 10 (Gas Combustion)

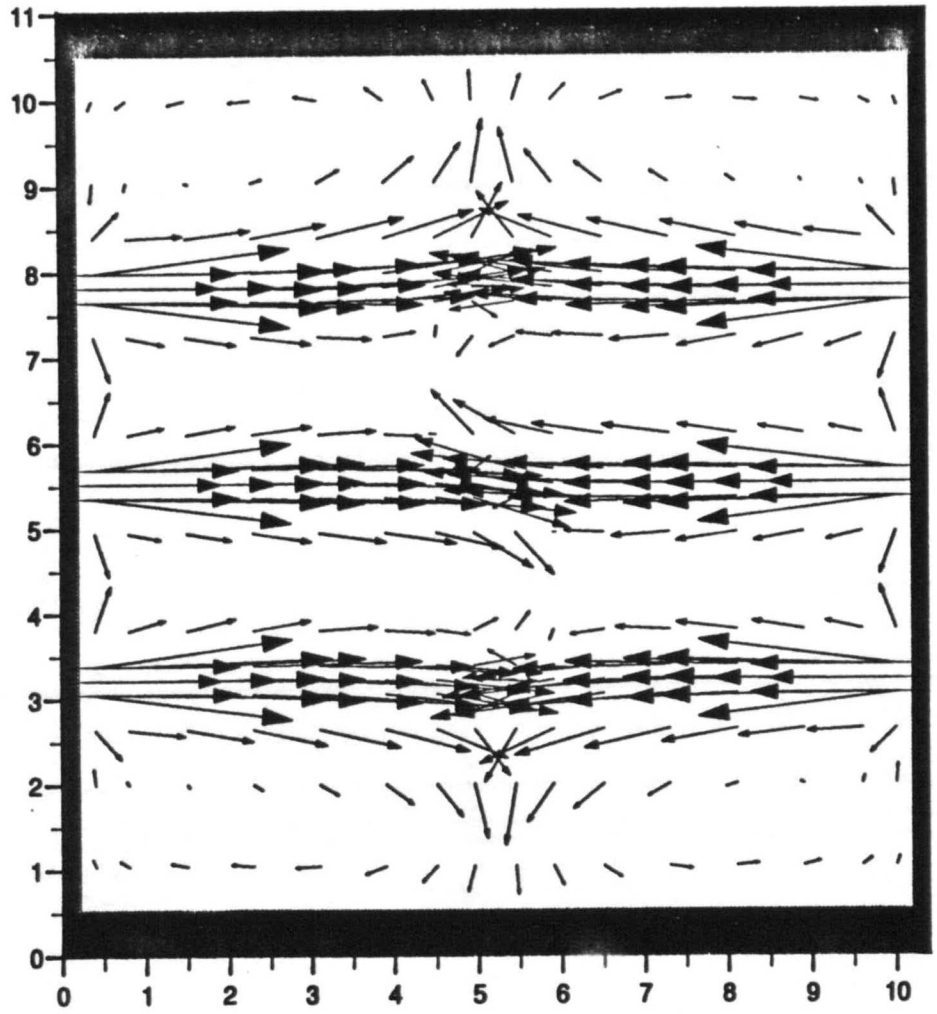


Fig. 4.16 Velocity Vectors For Z = 12 (Gas Combustion)

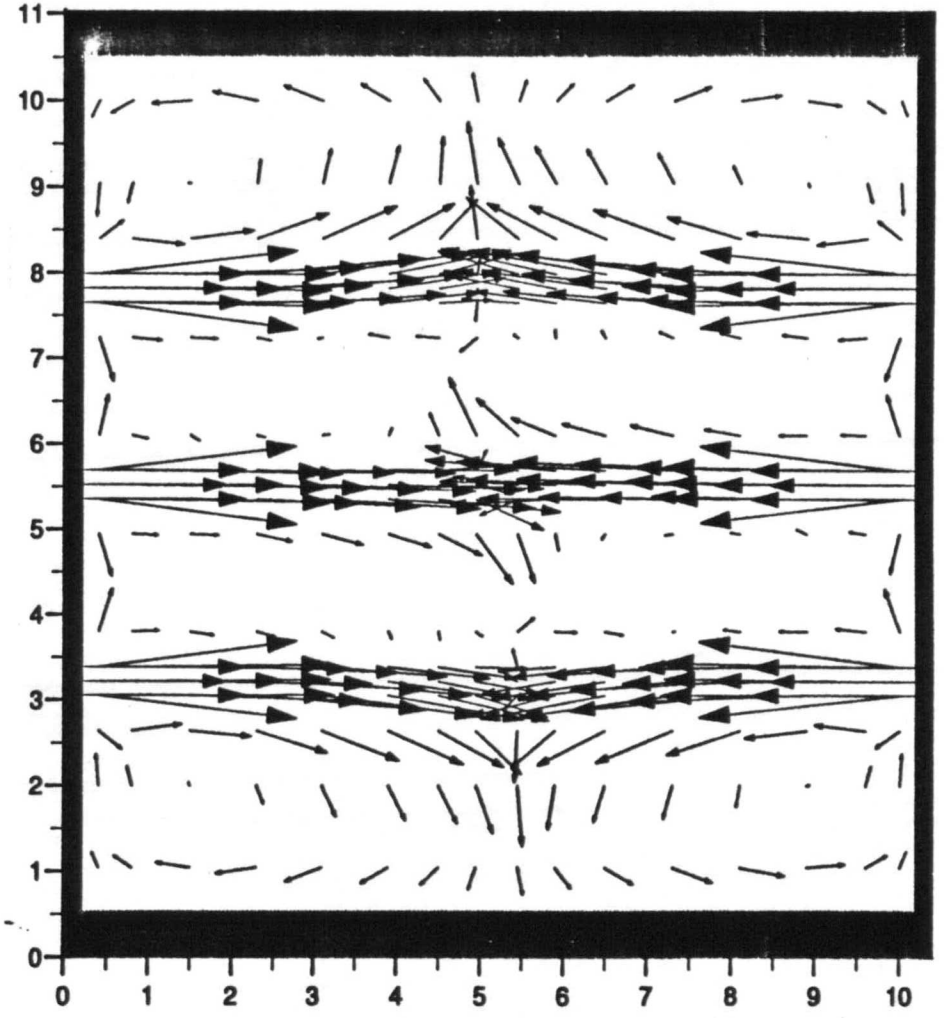


Fig. 4.17 Velocity Vectors For Z = 17 (Gas Combustion)

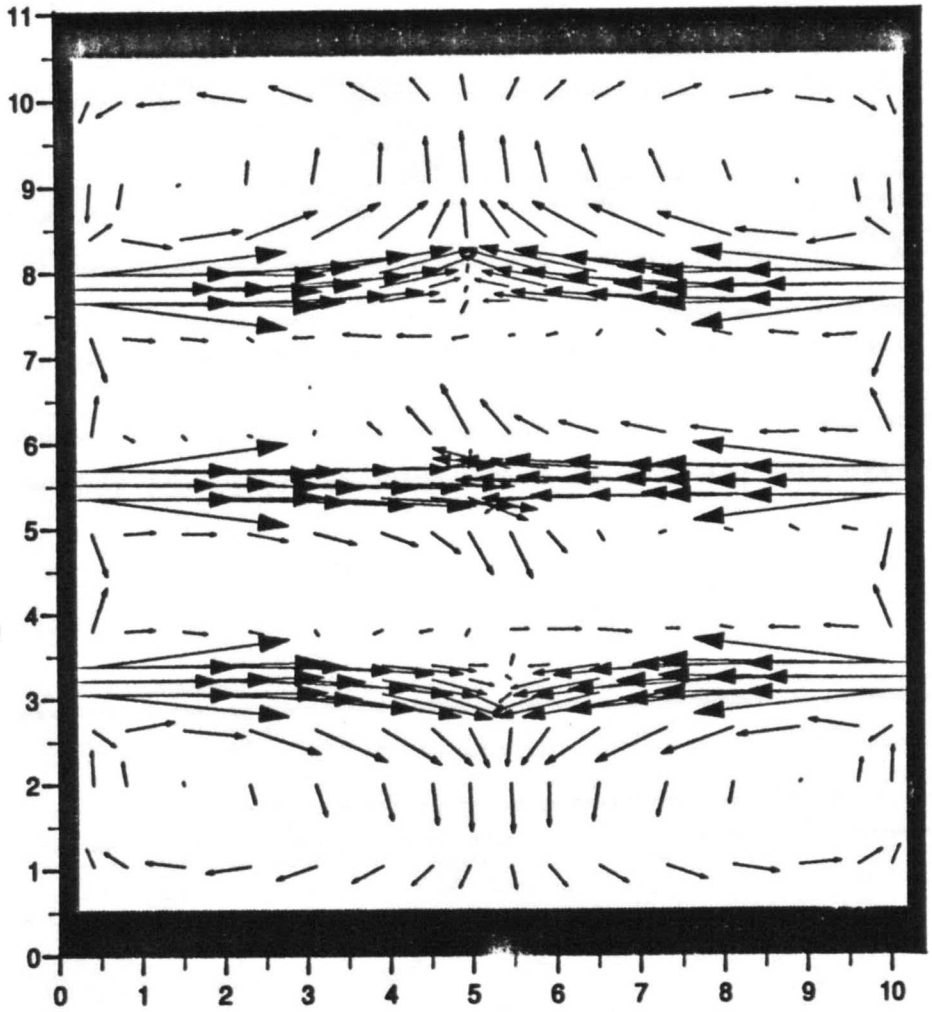


Fig. 4.18 Velocity Vectors For Z = 22 (Gas Combustion)

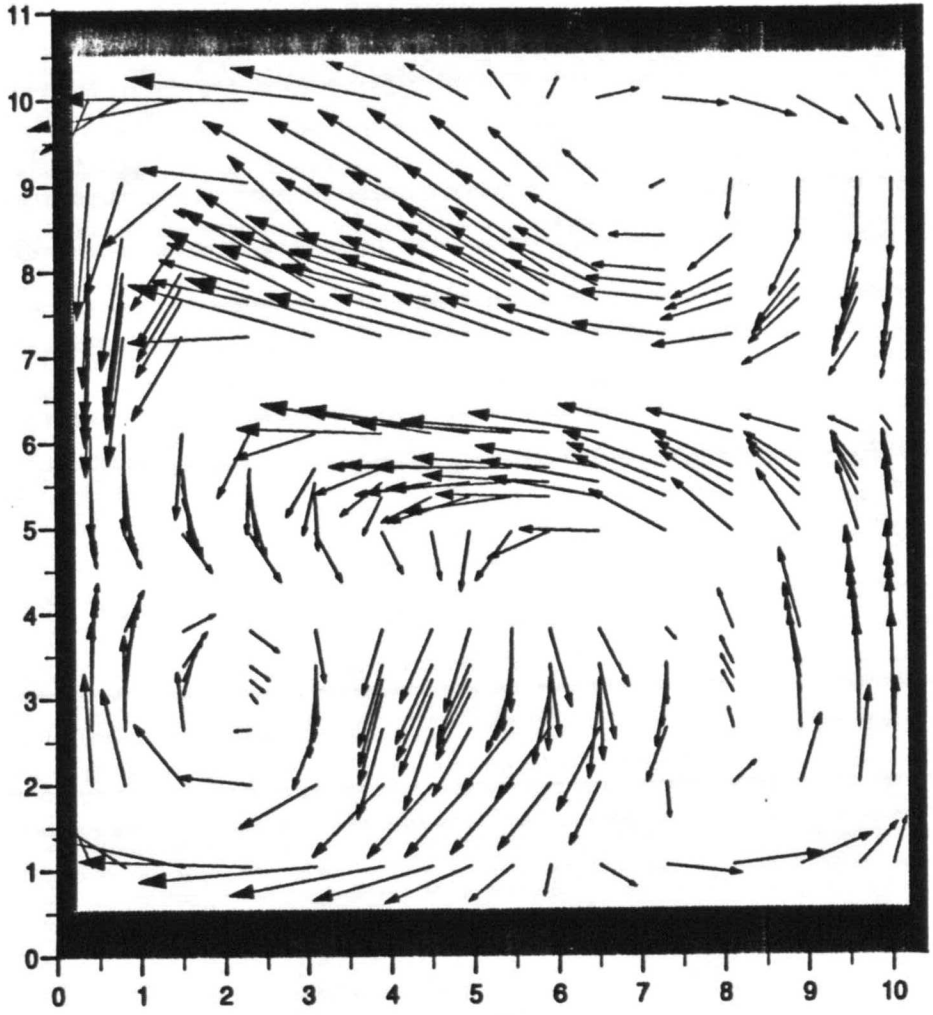


Fig. 4.19 Velocity Vectors For Z = 32 (Gas Combustion)

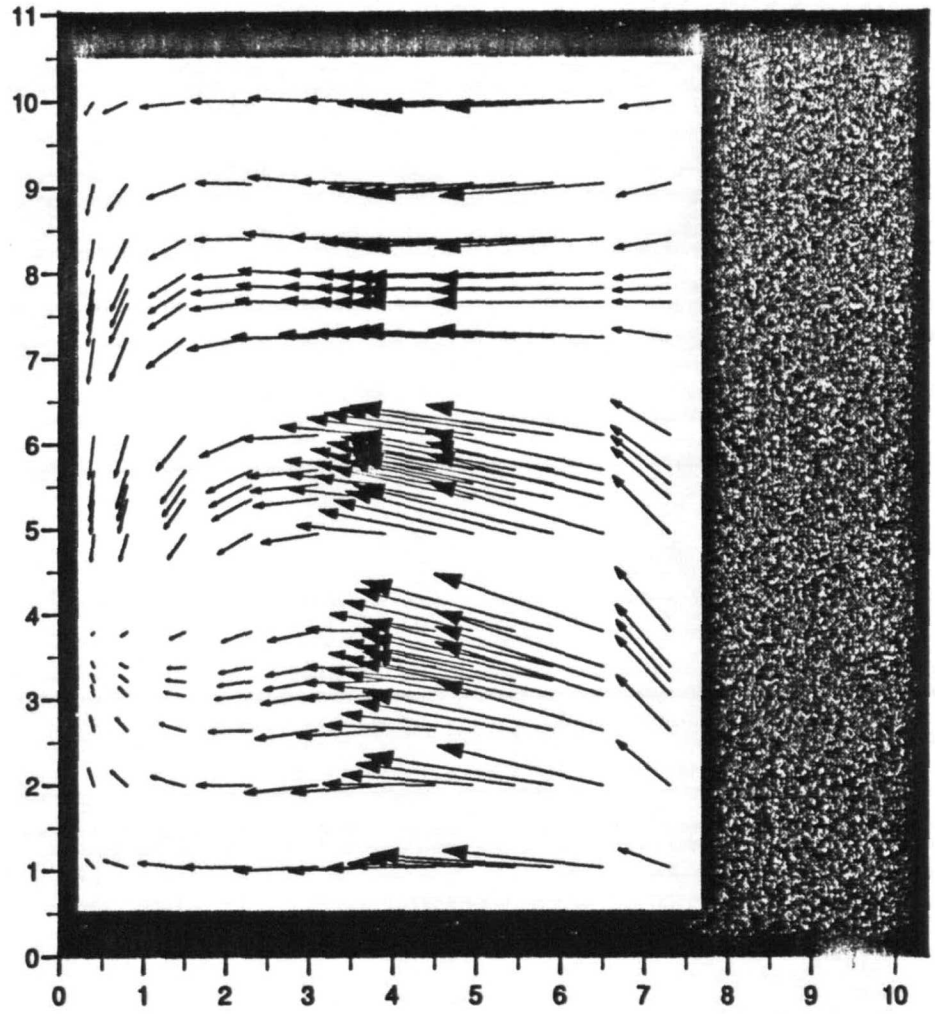


Fig. 4.20 Velocity Vectors For Z = 38 (Gas Combustion)

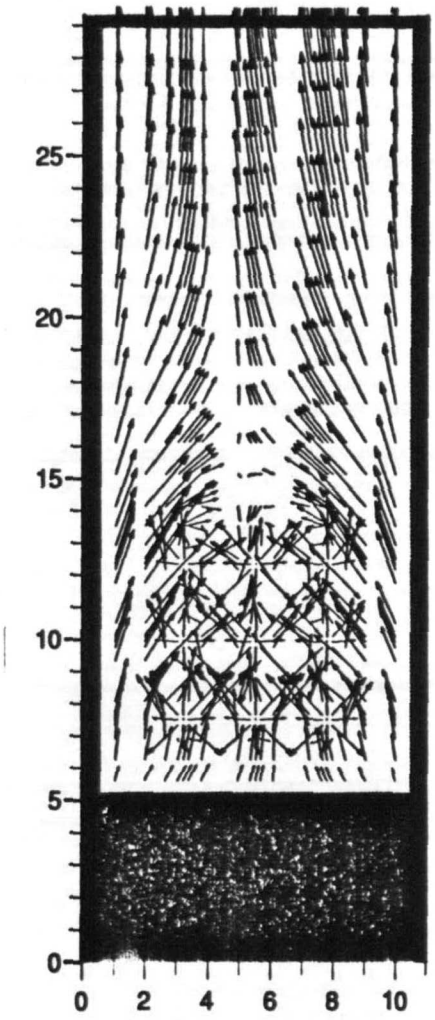


Fig. 4.21 Velocity Vectors For X = 1 (Gas Combustion)

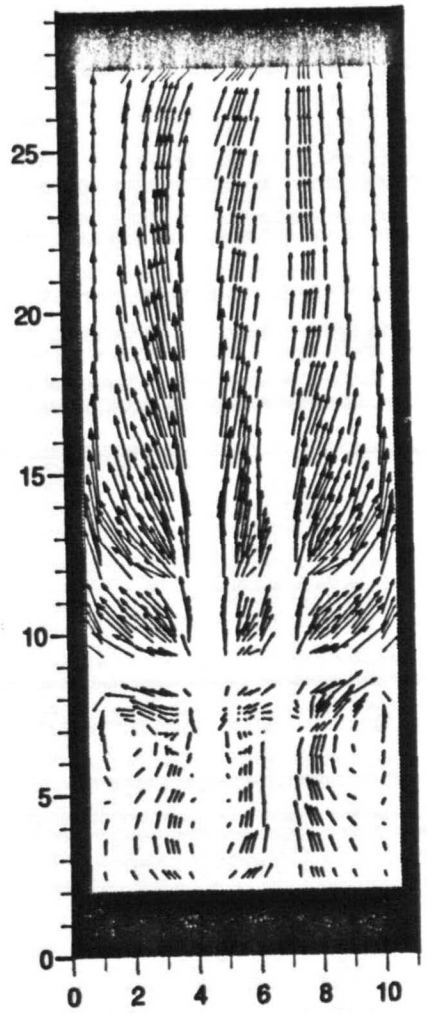


Fig. 4.22 Velocity Vectors For X = 4 (Gas Combustion)

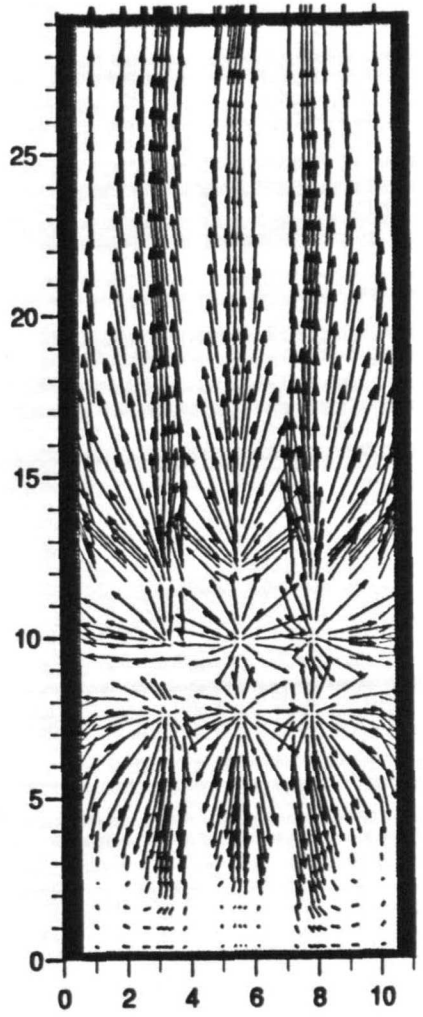


Fig. 4.23 Velocity Vectors For X = 8 (Gas Combustion)

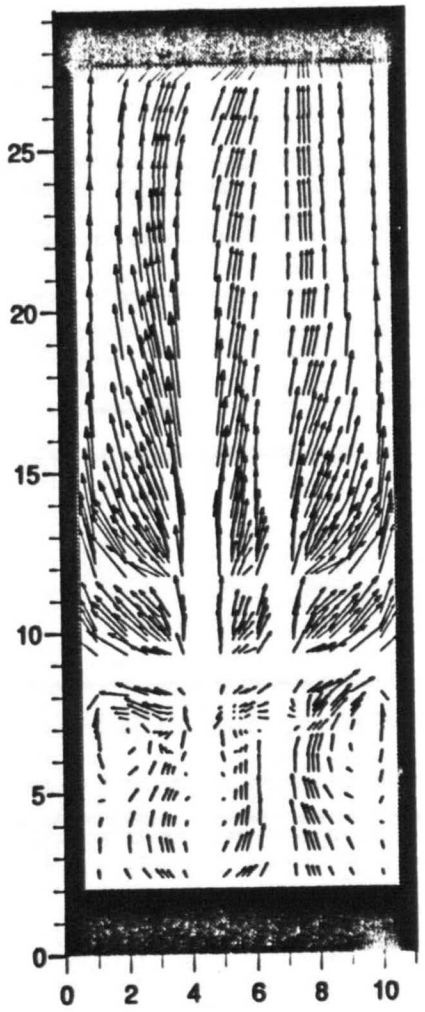


Fig. 4.24 Velocity Vectors For X = 12 (Gas Combustion)

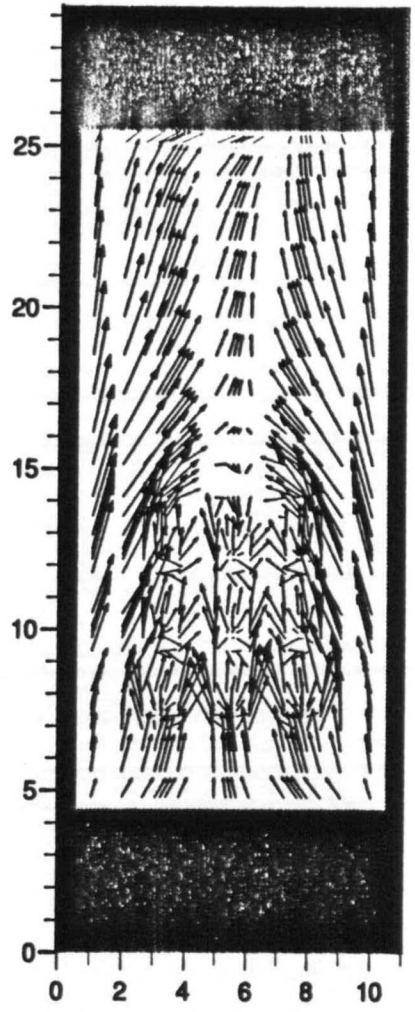


Fig. 4.25 Velocity Vectors For X = 15 (Gas Combustion)

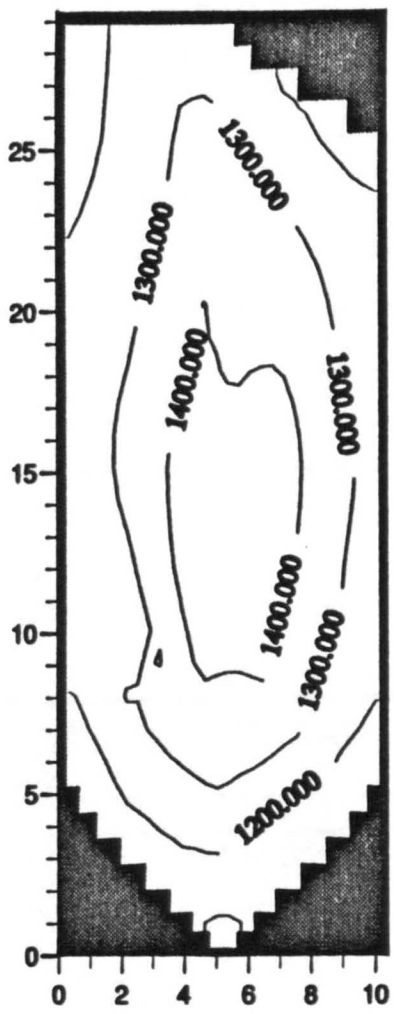


Fig. 4.26 Temperature Contours (^{O}c) For Y = 1 (Gas Combustion)

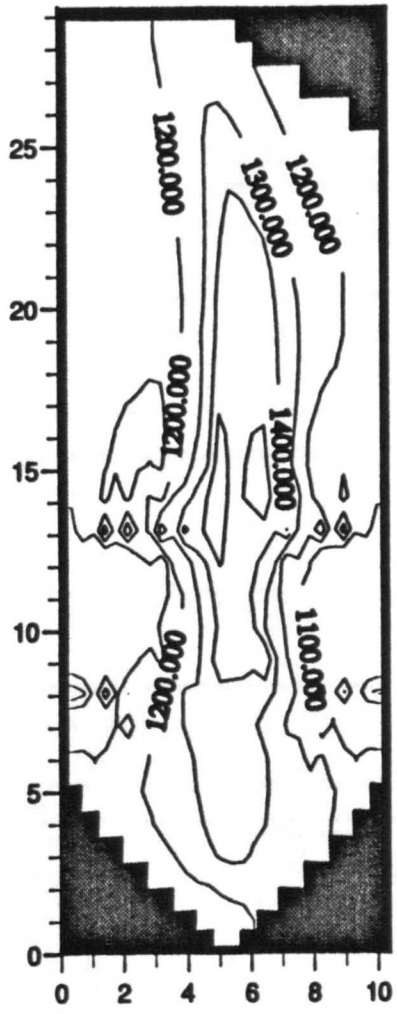


Fig. 4.27 Temperature Contours (^{O}c) For Y = 5 (Gas Combustion)

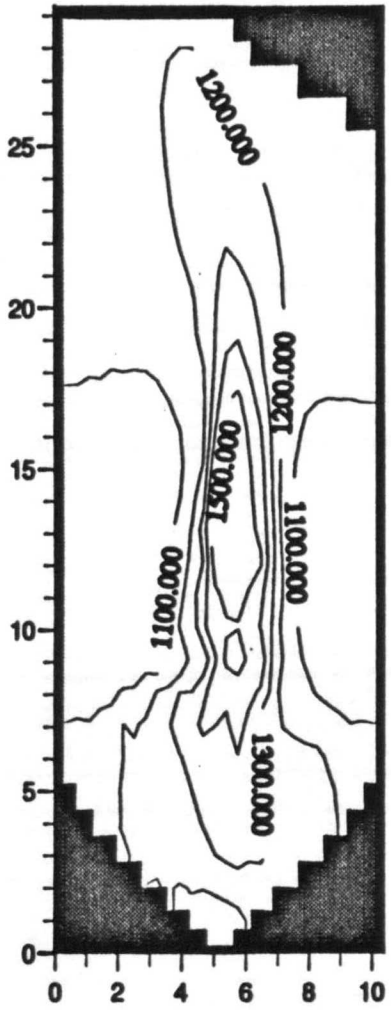


Fig. 4.28 Temperature Contours (^{O}c) For Y = 8 (Gas Combustion)

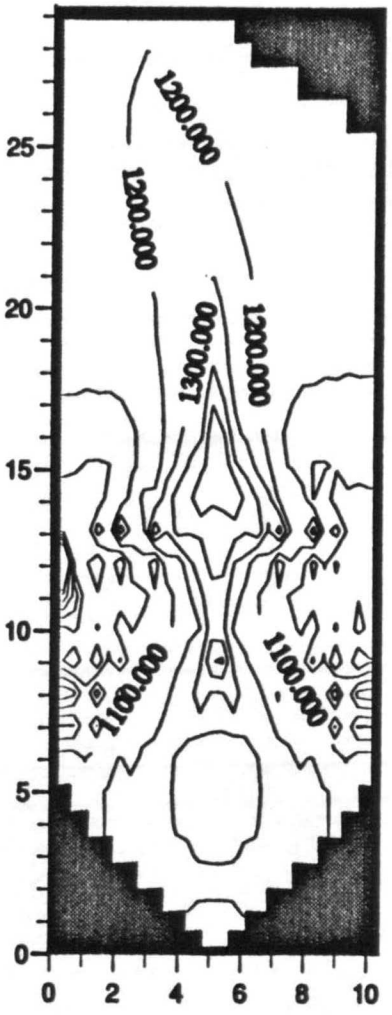


Fig. 4.29 Temperature Contours (^{O}c) For Y = 10 (Gas Combustion)

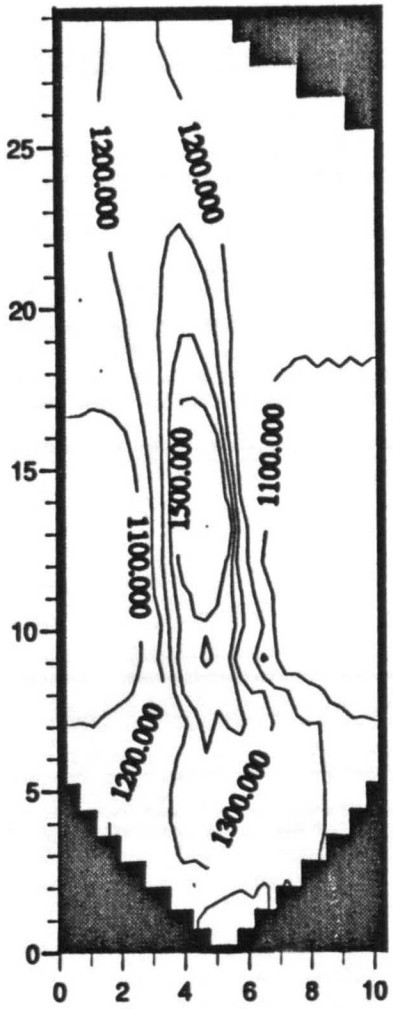


Fig. 4.30

Temperature Contours (^{o}c)

For Y = 12 (Gas Combustion)

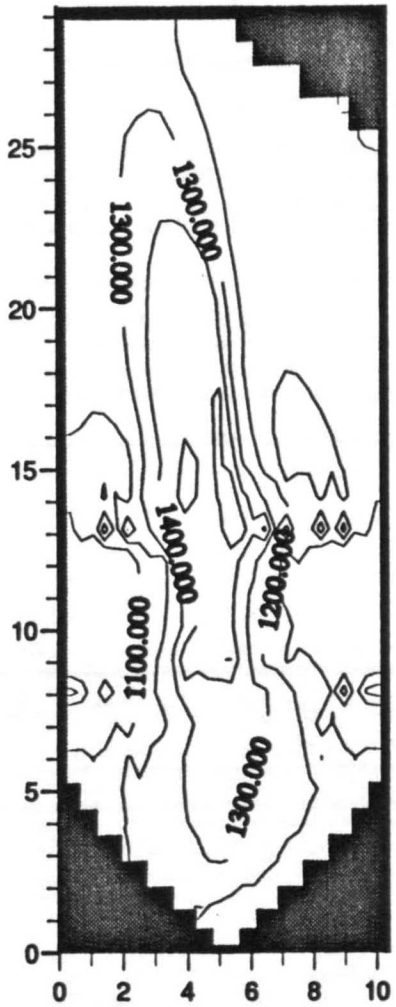


Fig. 4.31

Temperature Contours (^{o}c)

For Y = 15 (Gas Combustion)

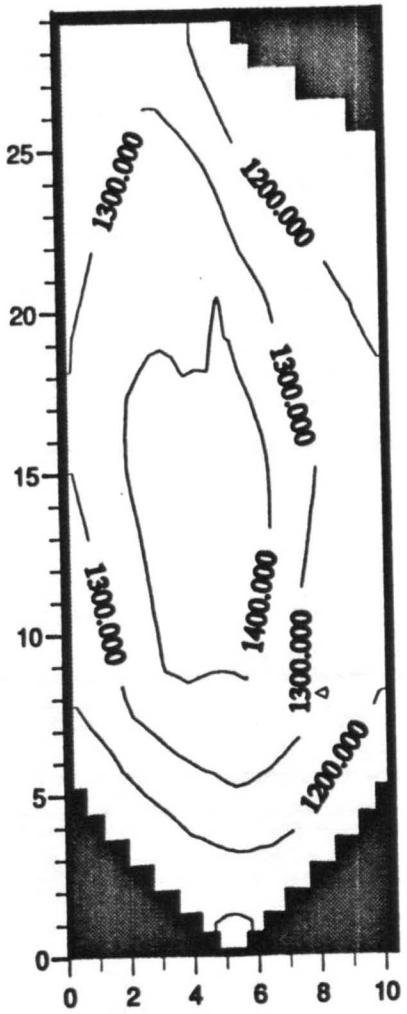


Fig. 4.32

Temperature Contours (^{o}c)

For Y = 19 (Gas Combustion)

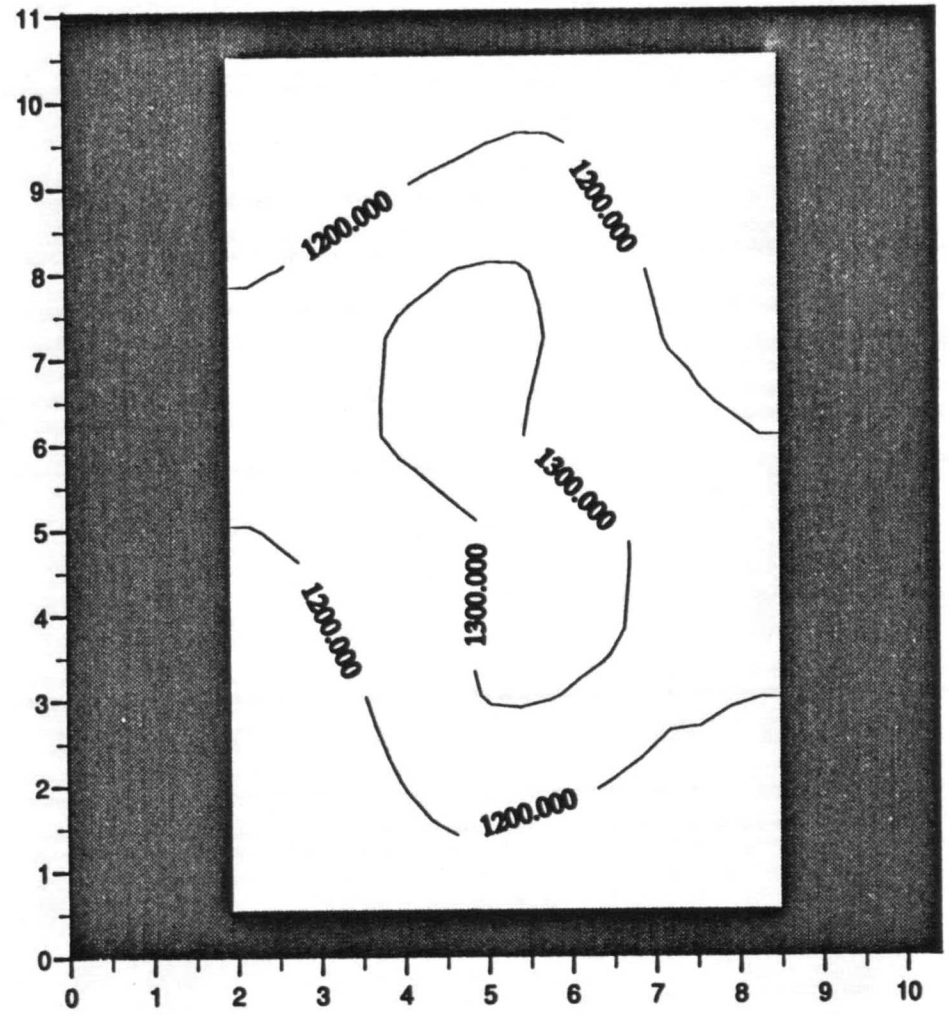


Fig. 4.33 Temperature Contours (^{O}c) For Z = 5 (Gas Combustion)

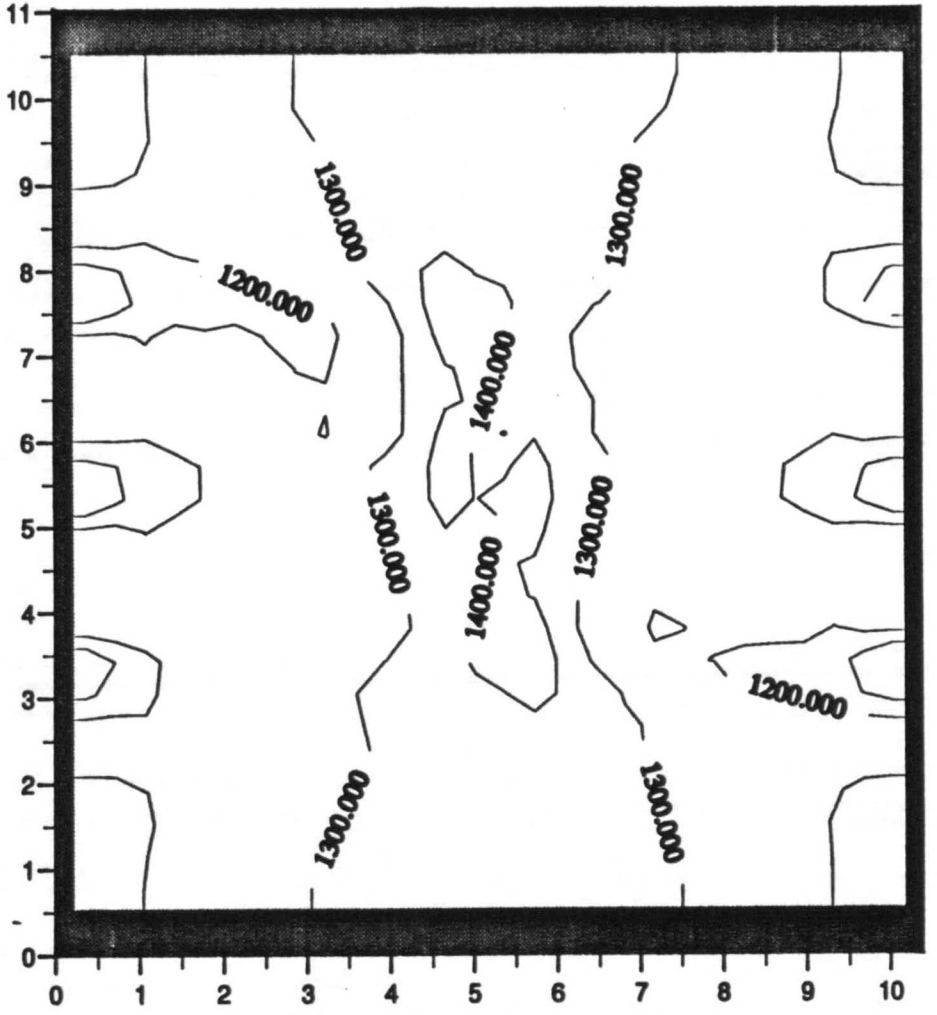


Fig. 4.34 Temperature Contours (^{O}c) For Z = 10 (Gas Combustion)

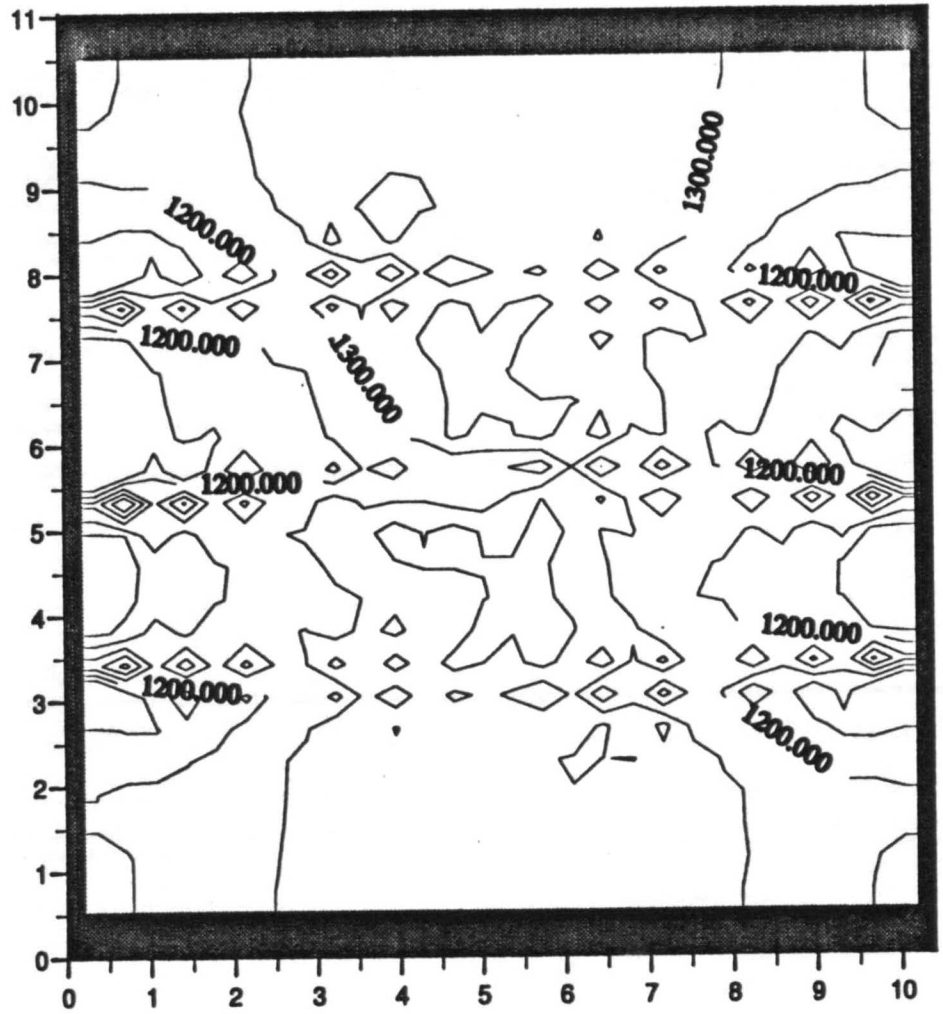


Fig. 4.35 Temperature Contours (^{o}c) For Z = 12 (Gas Combustion)

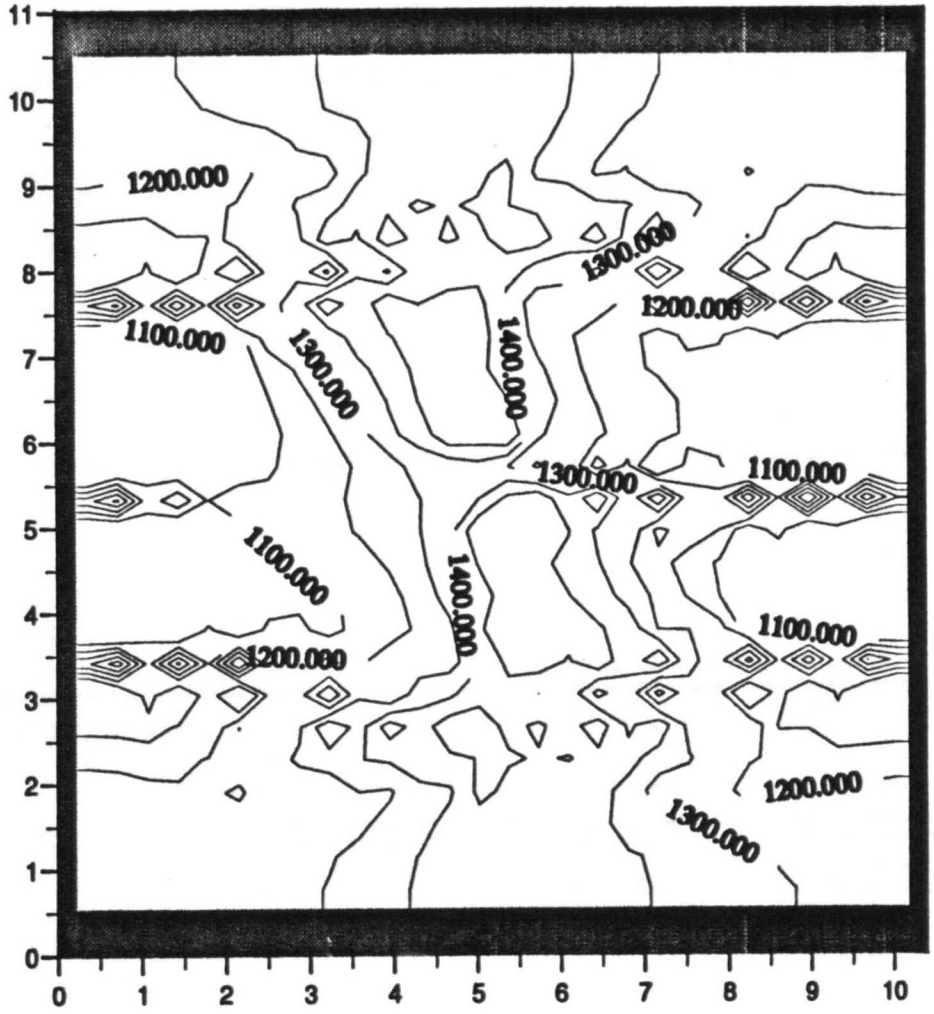


Fig. 4.36 Temperature Contours (^{o}c) For Z = 17 (Gas Combustion)

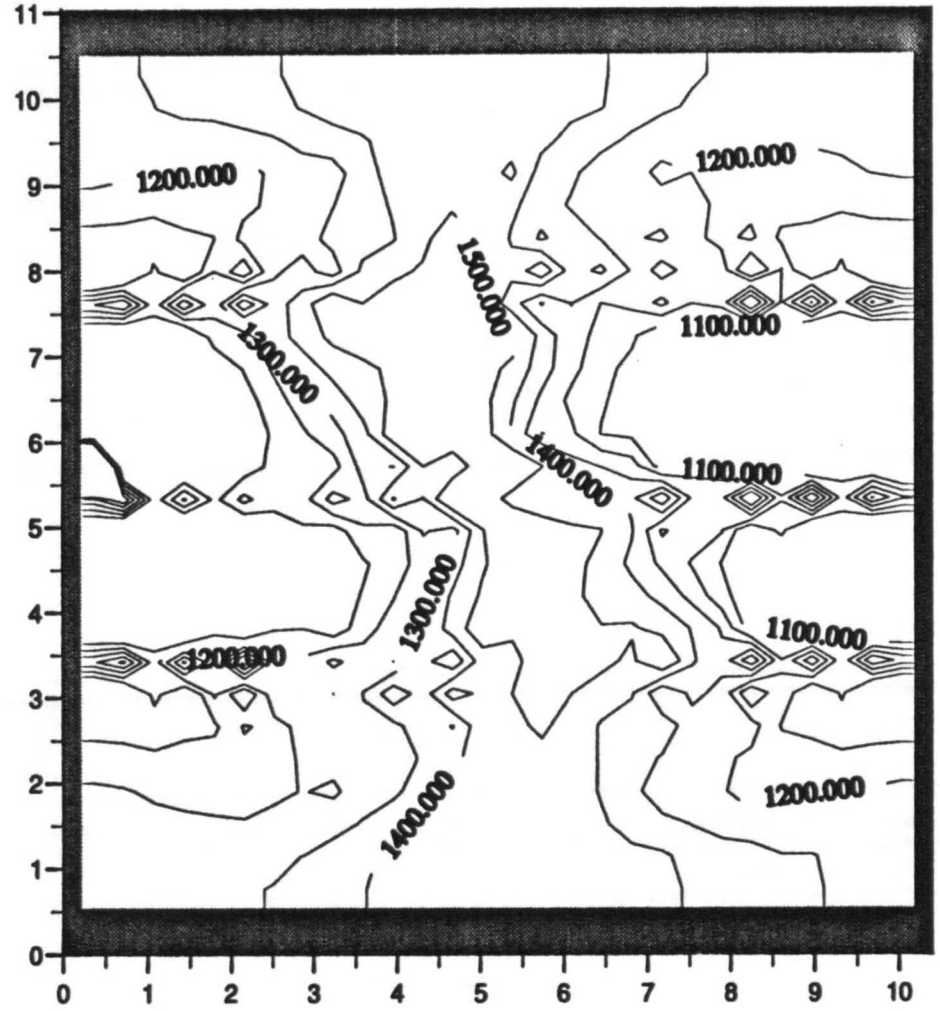


Fig. 4.37 Temperature Contours (^{o}c) For Z = 22 (Gas Combustion)

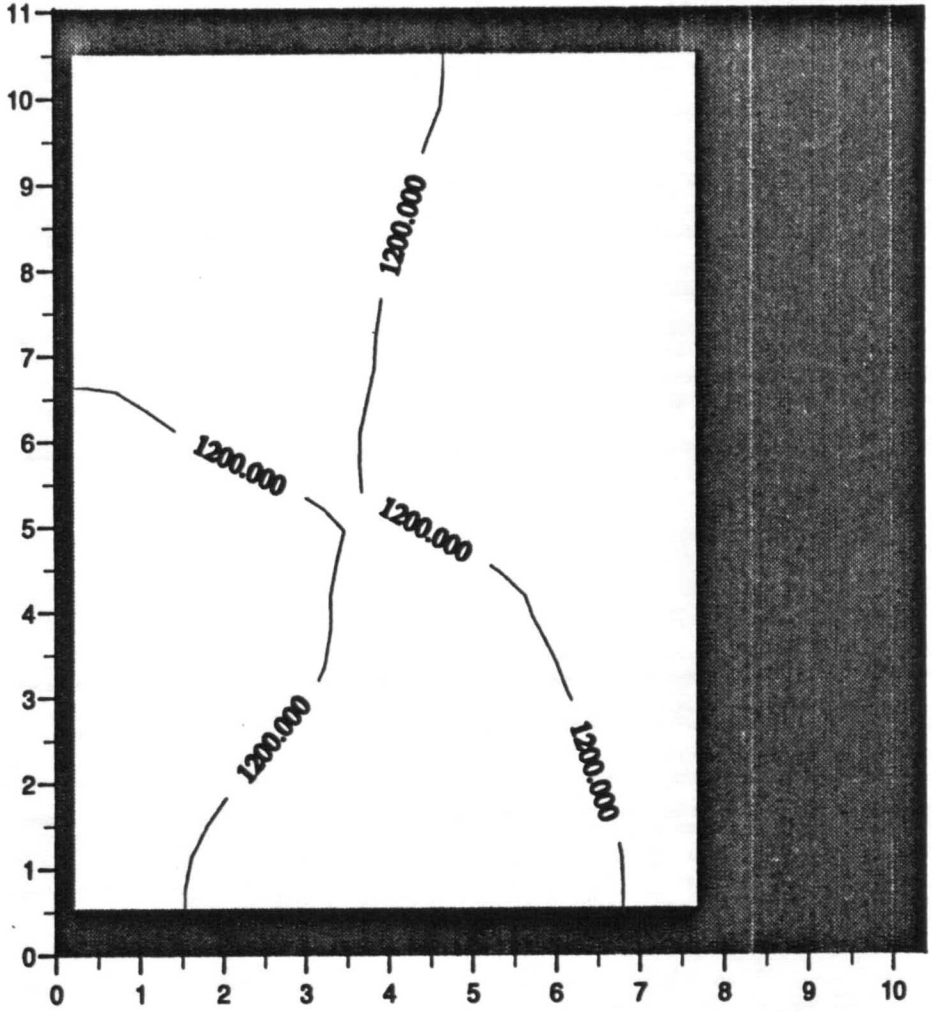


Fig. 4.38 Temperature Contours (^{o}c) For Z = 38 (Gas Combustion)

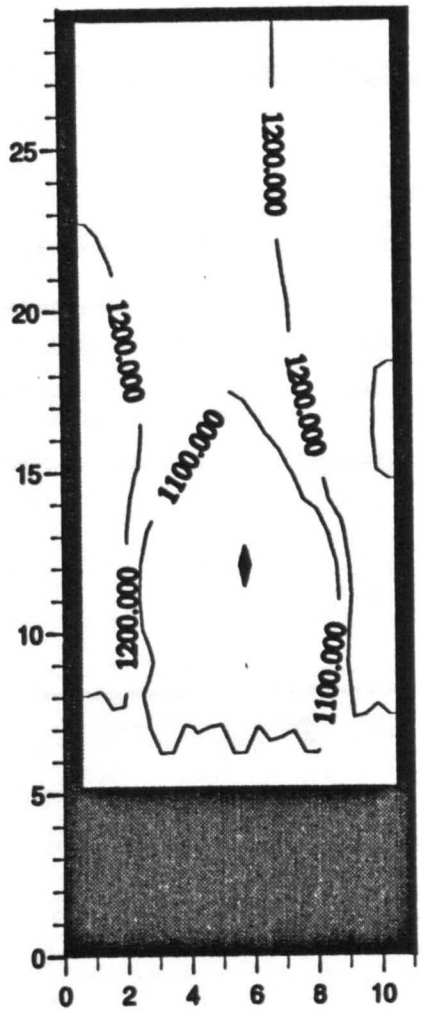


Fig. 4.39 Temperature Contours (^{O}c) For X = 1 (Gas Combustion)

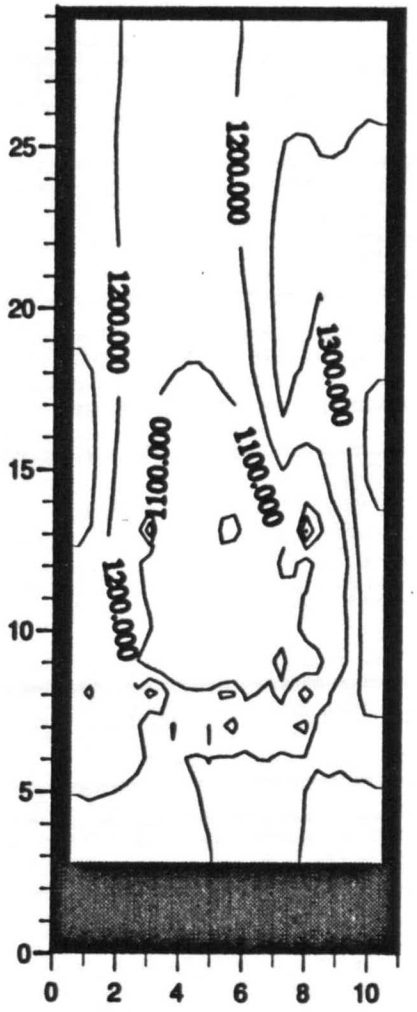


Fig. 4.40 Temperature Contours (^{O}c) For X = 4 (Gas Combustion)

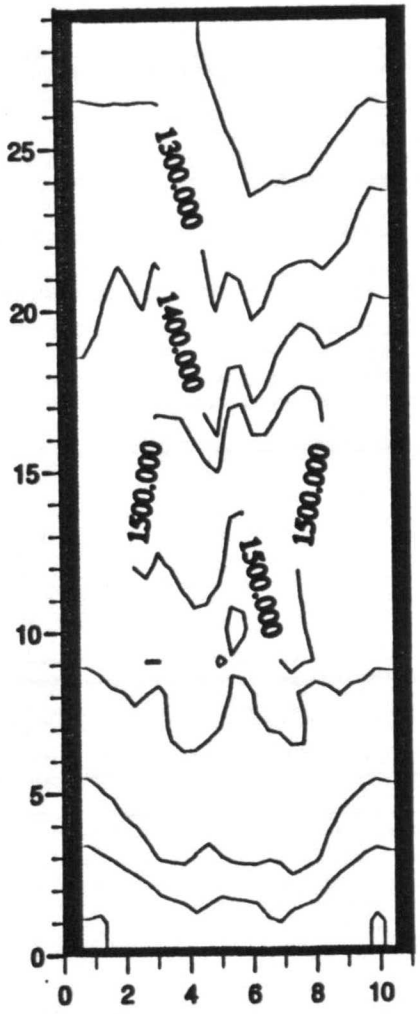


Fig. 4.41 Temperature Contours (^{O}c) For X = 8 (Gas Combustion)

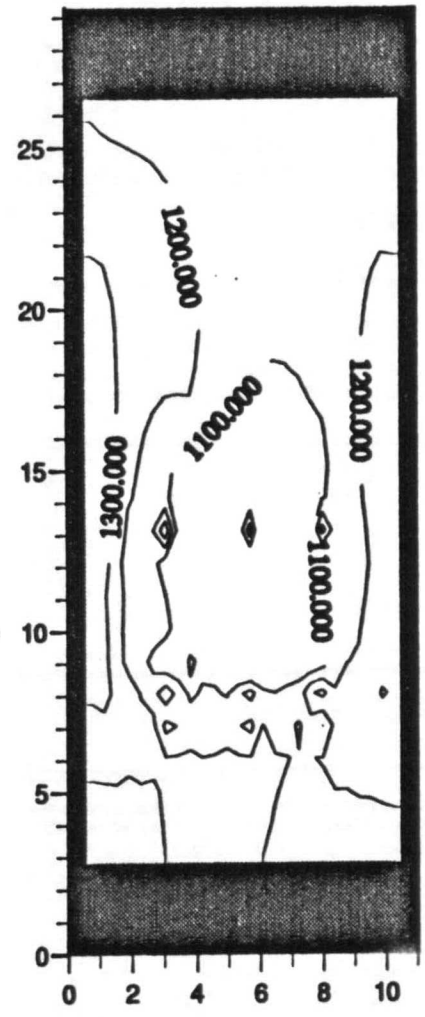


Fig. 4.42 Temperature Contours (^{O}c) For X = 12 (Gas Combustion)

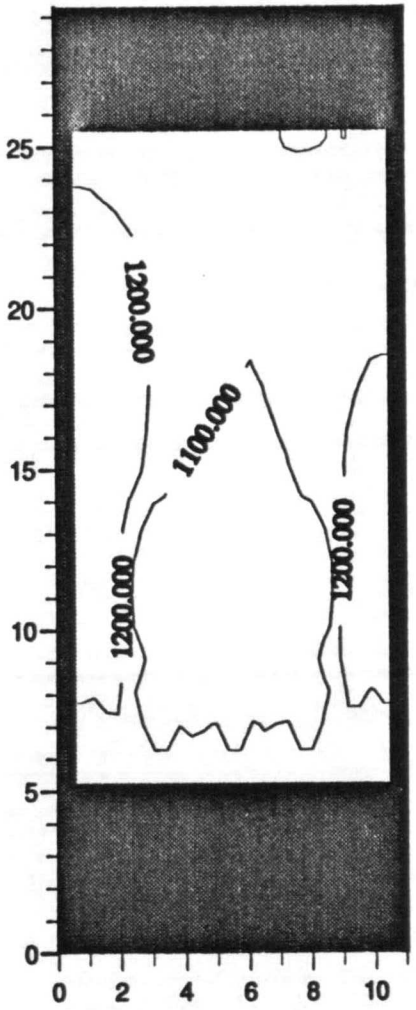


Fig. 4.43 Temperature Contours (^{O}c) For X = 15 (Gas Combustion)

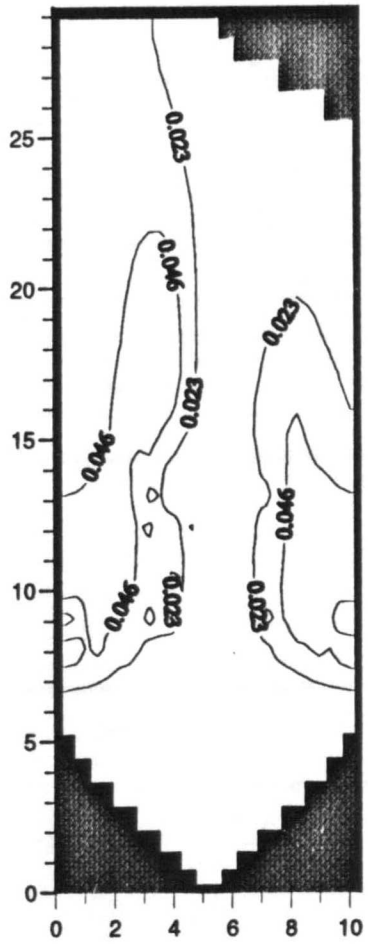


Fig. 4.44

Oxygen Concentration Contours (%) For Y = 3

(Gas Combustion)

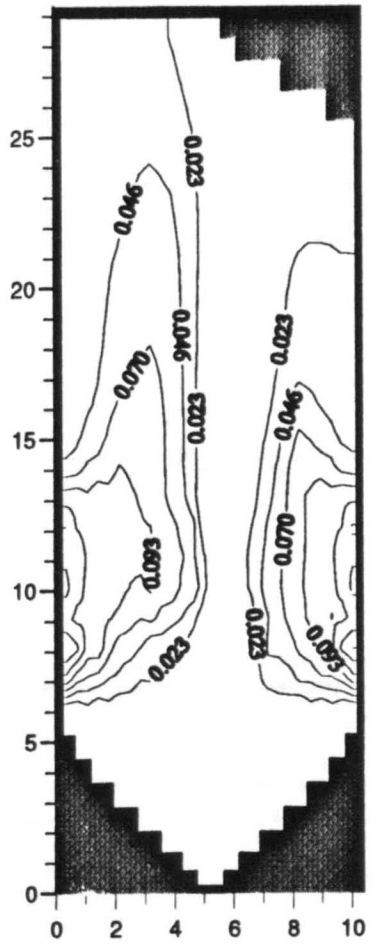


Fig. 4.45

Oxygen Concentration Contours (%) For Y = 6

(Gas Combustion)

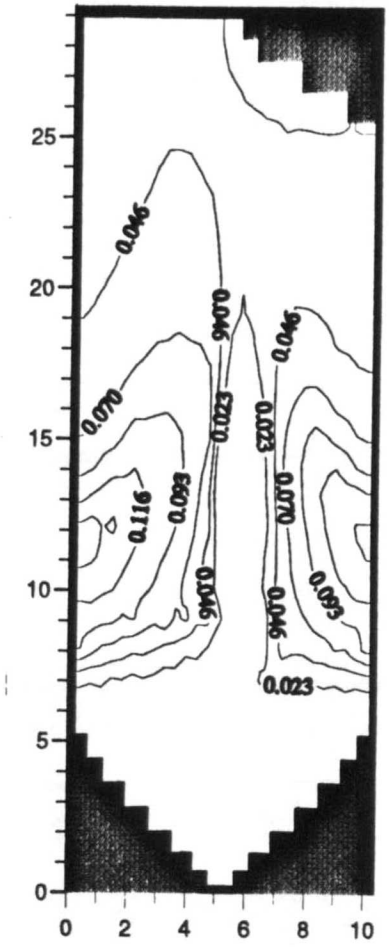


Fig. 4.46

Oxygen Concentration Contours (%) For Y = 8

(Gas Combustion)

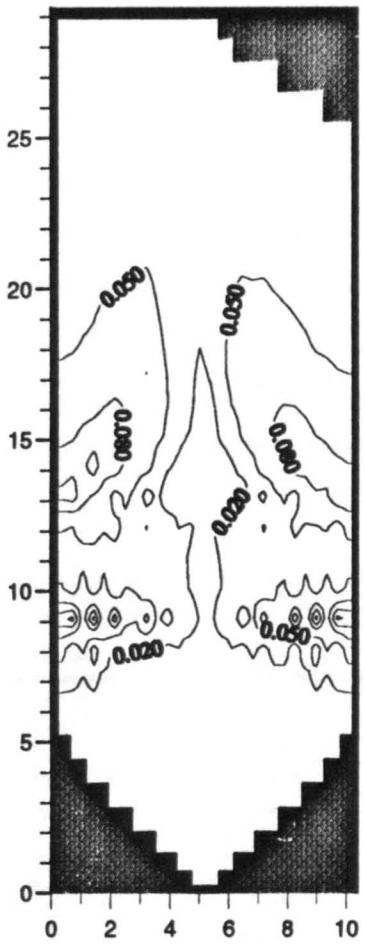


Fig. 4.47

Oxygen Concentration Contours (%) For Y = 10

(Gas Combustion)

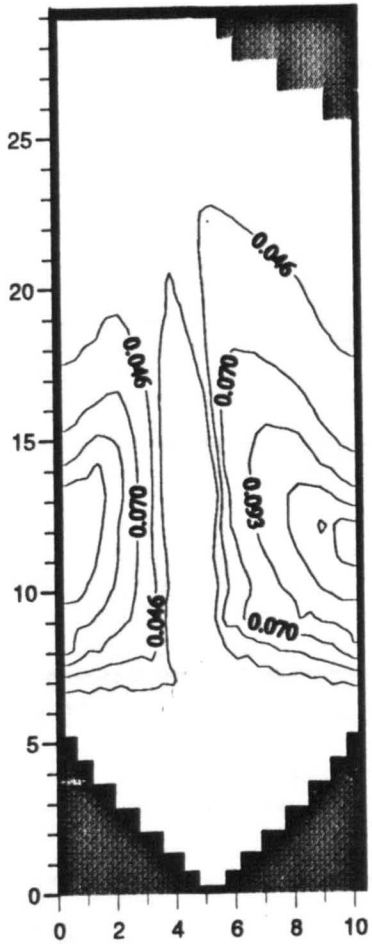


Fig. 4.48

Oxygen Concentration Contours (%) For Y = 12

(Gas Combustion)

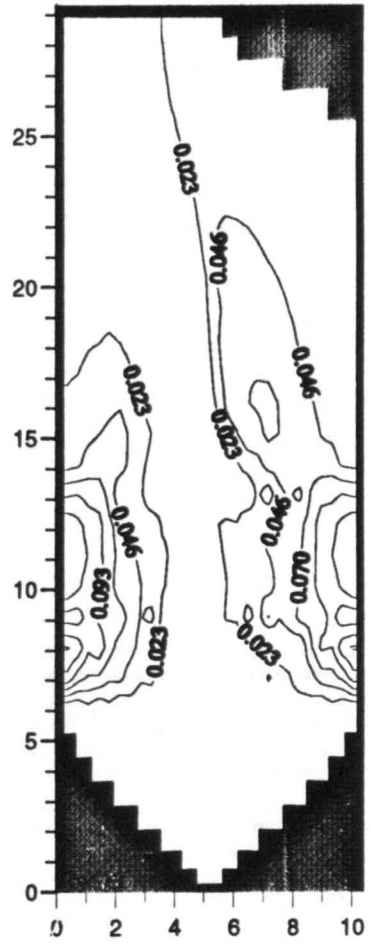


Fig. 4.49

Oxygen Concentration Contours (%) For Y = 16

(Gas Combustion)

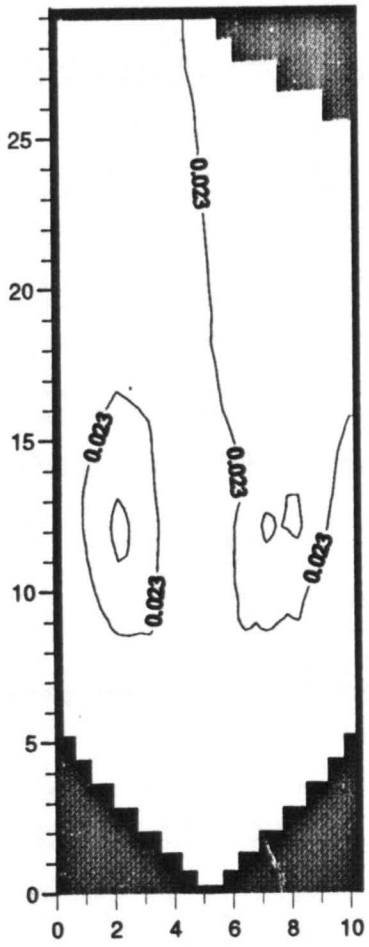


Fig. 4.50

Oxygen Concentration Contours (%) For Y = 18

(Gas Combustion)

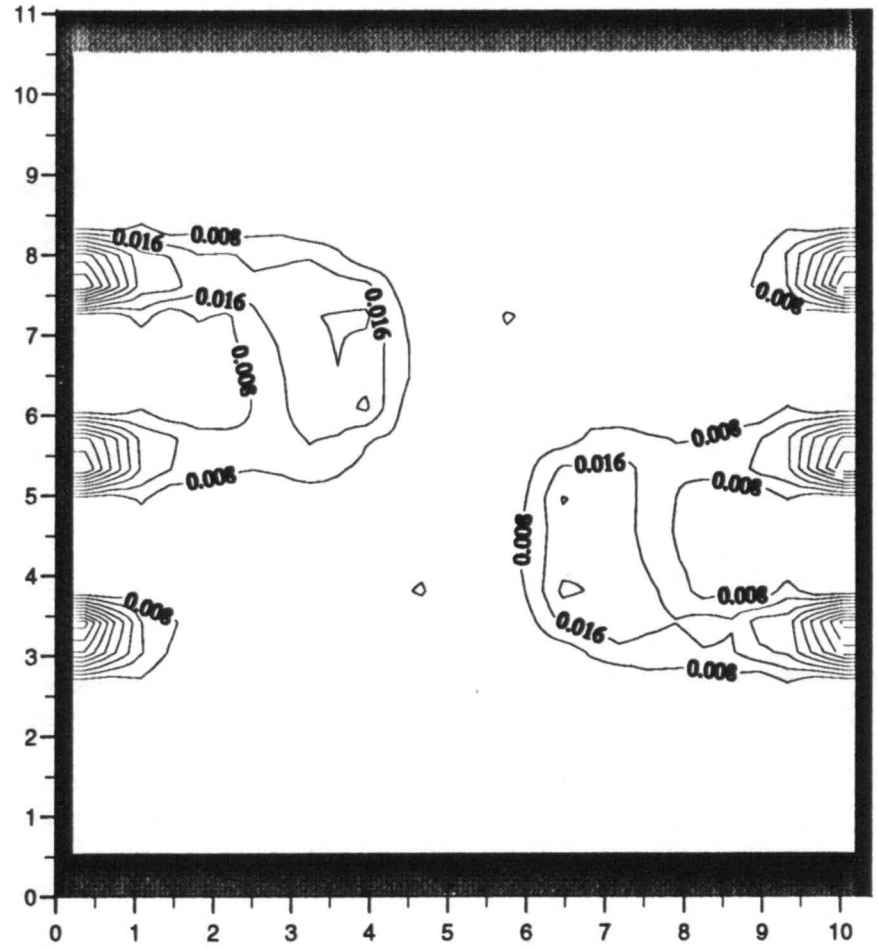


Fig. 4.51 Oxygen Concentration Contours (%) For Z = 10 (Gas Combustion)

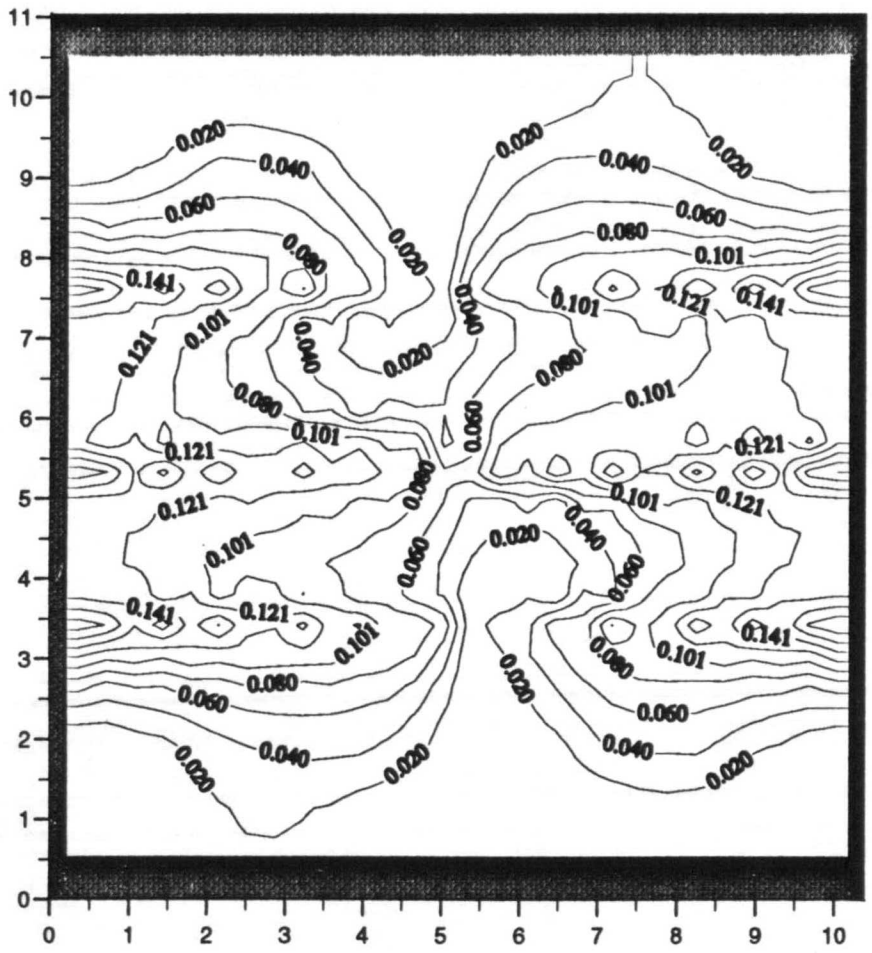


Fig. 4.52 Oxygen Concentration Contours (%) For Z = 16 (Gas Combustion)

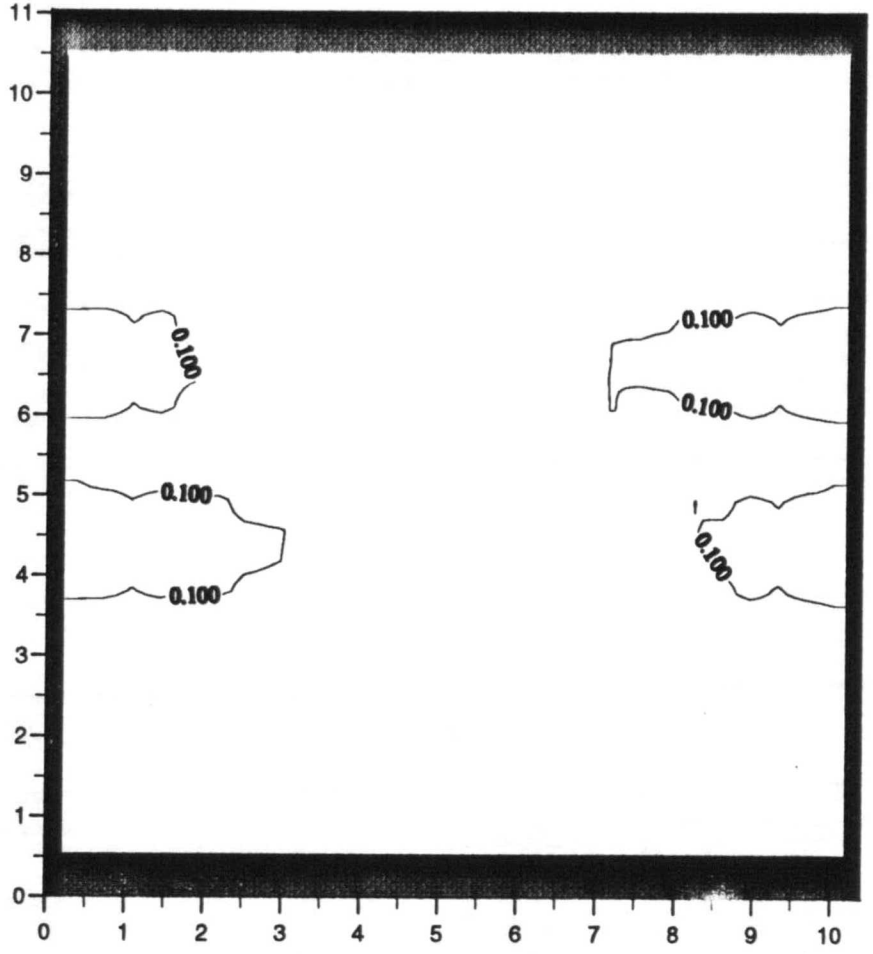


Fig. 4.53 Oxygen Concentration Contours (%) For Z = 22 (Gas Combustion)

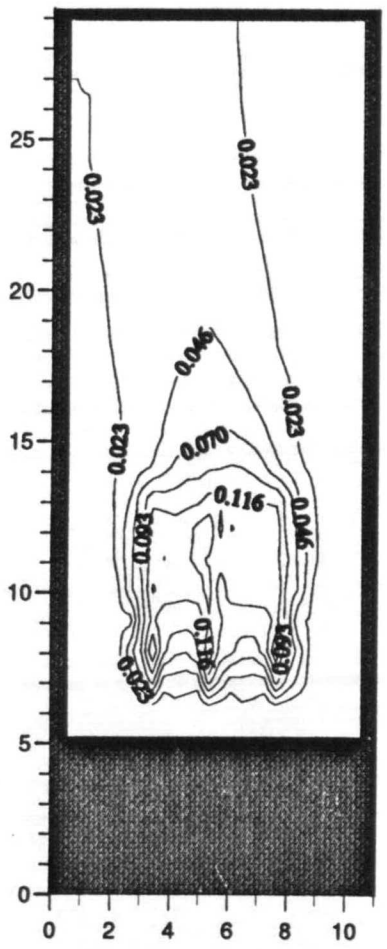


Fig. 4.54

Oxygen Concentration Contours (%) For X = 1

(Gas Combustion)

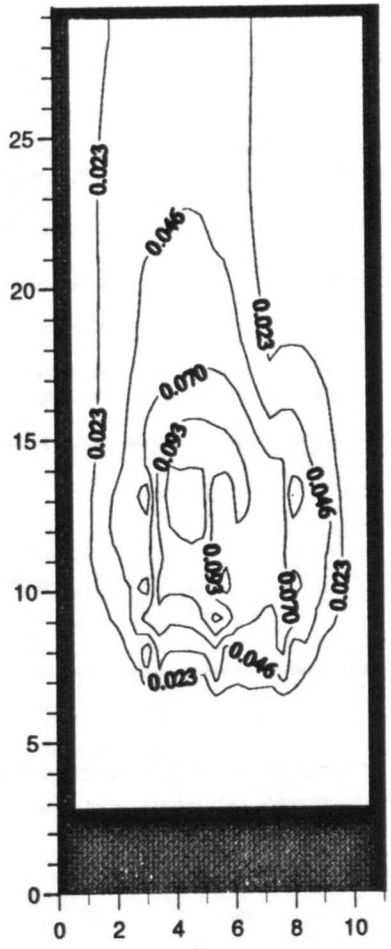


Fig. 4.55

Oxygen Concentration Contours (%) For X = 4

(Gas Combustion)

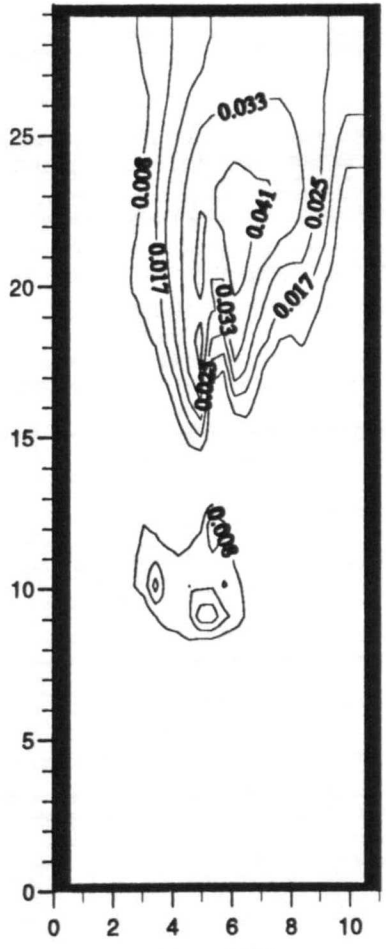


Fig. 4.56

Oxygen Concentration Contours (%) For X = 8

(Gas Combustion)

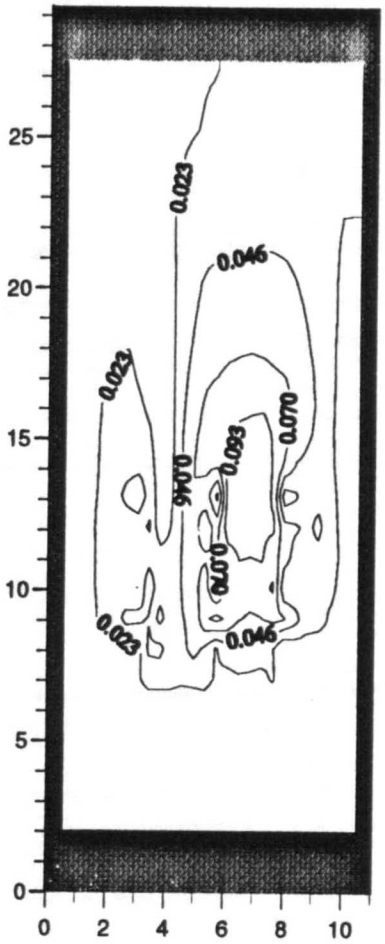


Fig. 4.57

Oxygen Concentration Contours (%) For X = 12

(Gas Combustion)

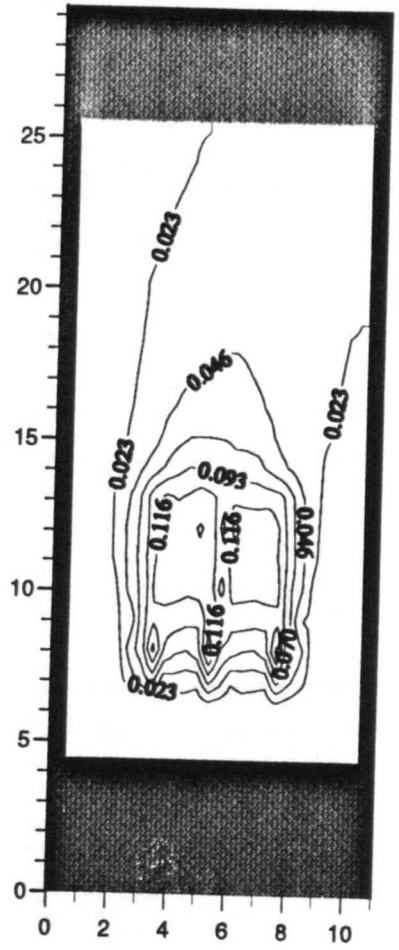


Fig. 4.58

Oxygen Concentration Contours (%) For X = 15

(Gas Combustion)

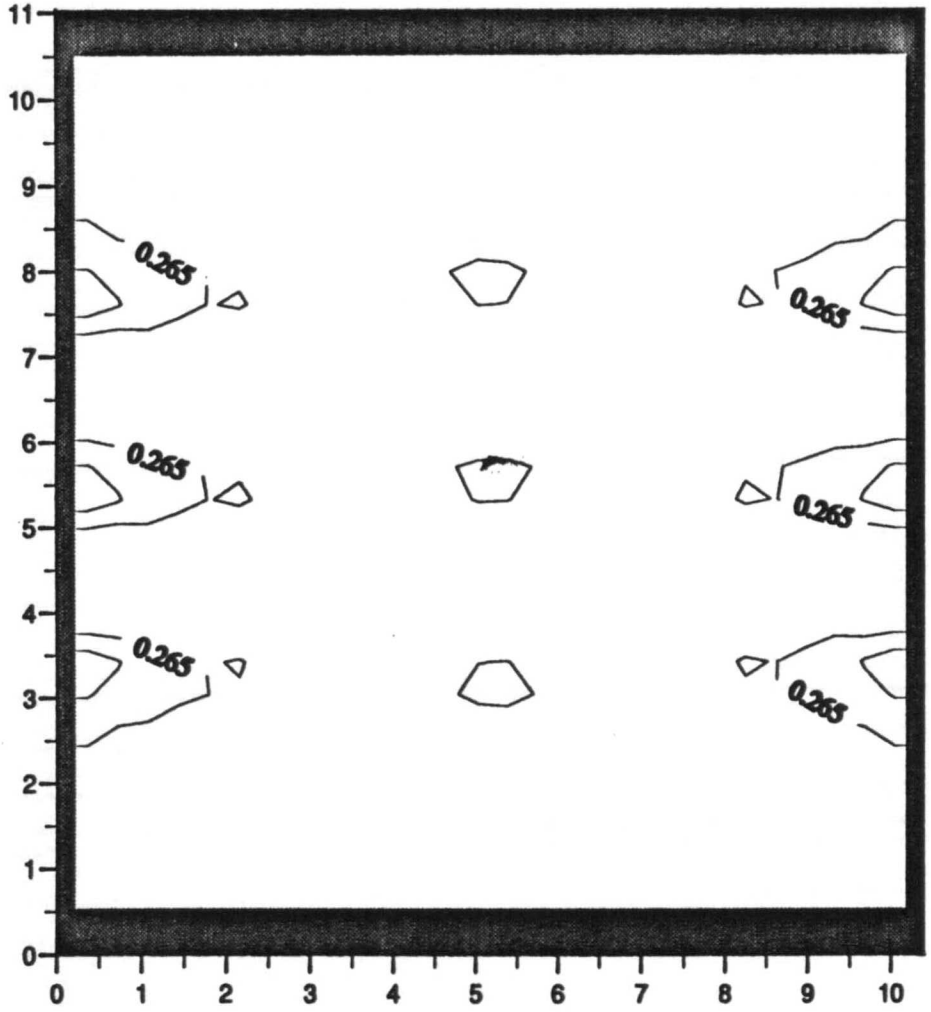


Fig. 4.59 Absorption Coefficient Contours (M^{-1}) For Z = 11

(Gas Combustion)

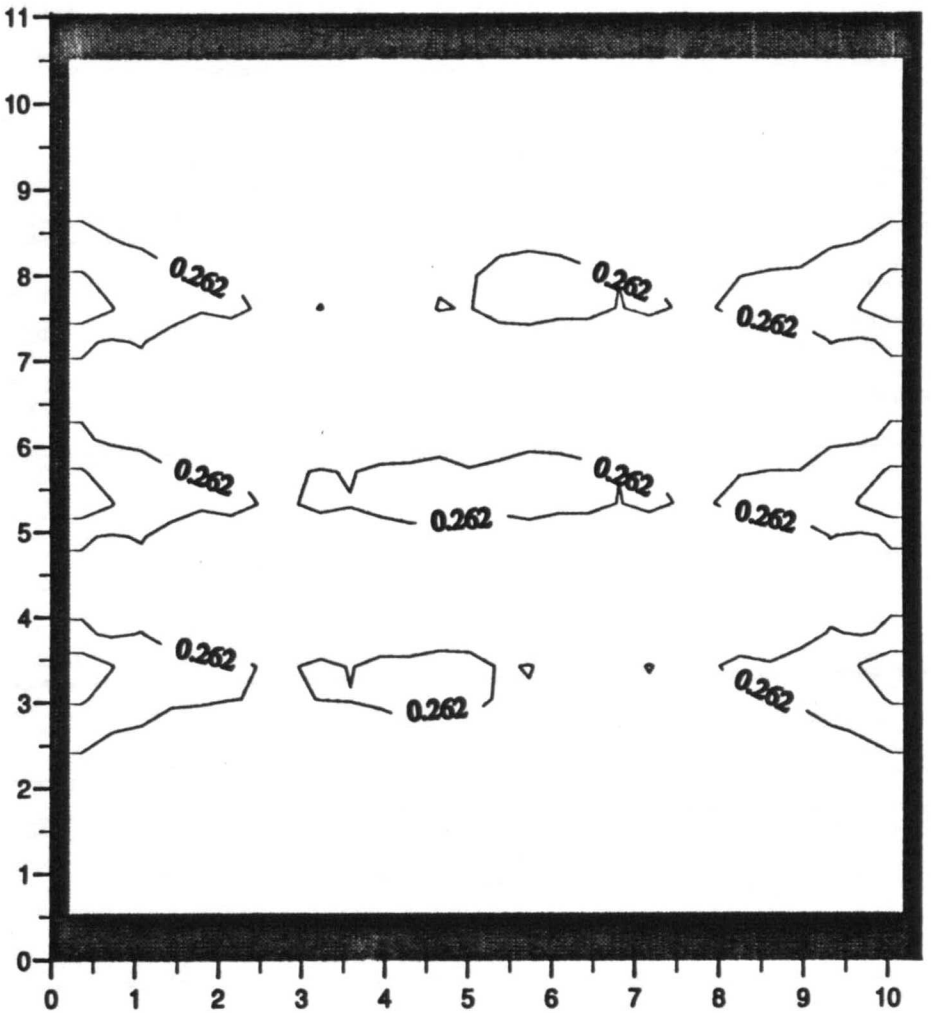


Fig. 4.60 Absorption Coefficient Contours (M^{-1}) For Z = 16

(Gas Combustion)

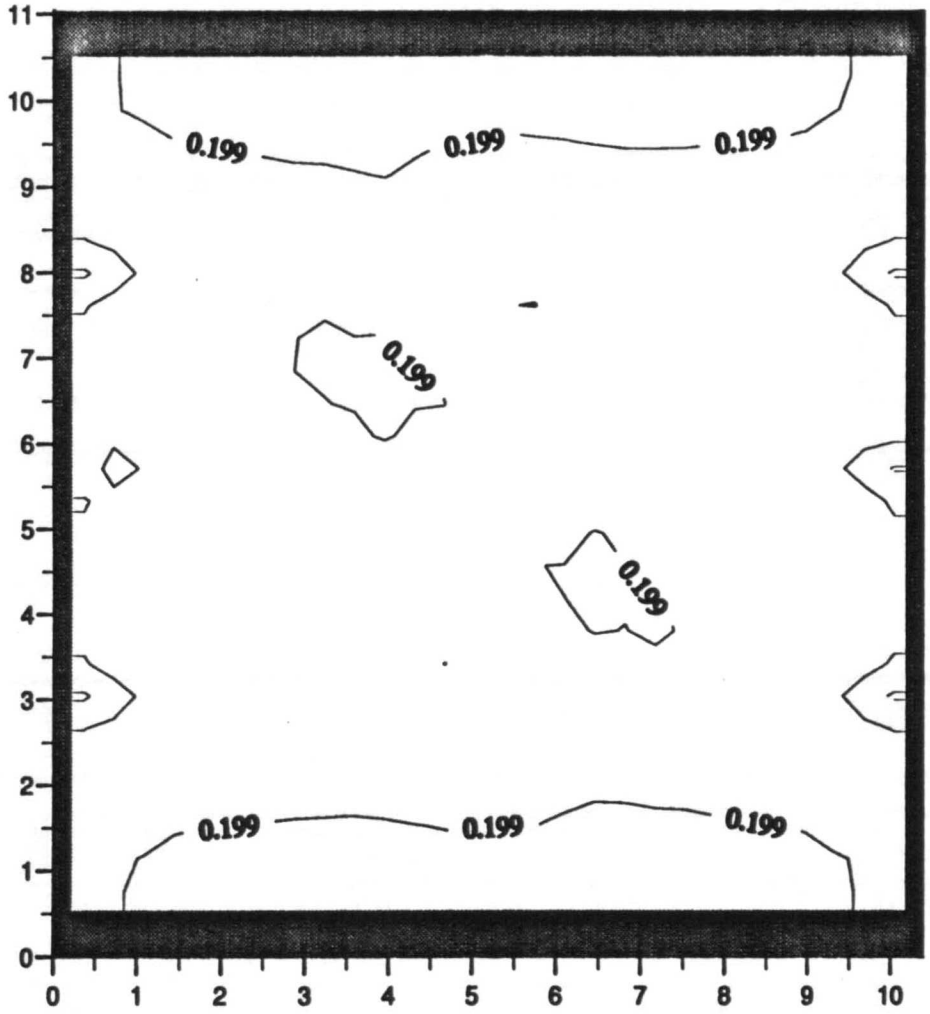


Fig. 4.61 Absorption Coefficient Contours (M^{-1}) For Z = 22 (Gas Combustion)

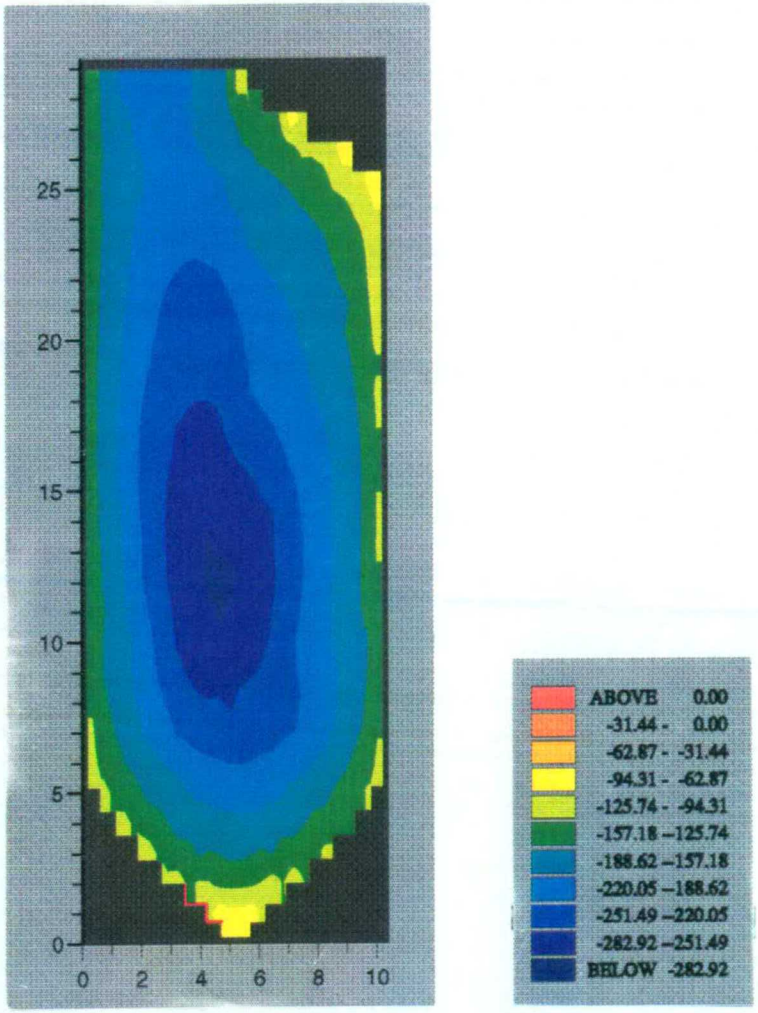


Fig. 4.62 Heat Fluxes To The Lateral Wall (Kw/M^2) (Gas Combustion)

CHAPTER 5

OIL COMBUSTION CALCULATIONS

5.1 Introduction

The modelling of an oil-fired power plant furnace is the subject of this section. The furnace chosen is the same as the one in section 4 and therefore the description of the geometrical details will be omitted herein. An additional operational variation has been introduced in this simulation to assess the effect of Flue Gases Recirculation (FGR), through the furnace hopper. This technique is generally adopted in the industry in order to reduce the NO emissions. In this method the combustion air is diluted with the outlet gases either at the burner or through the hopper which reduces locally the concentration of oxygen and increases the level of inert gases with overall lower temperatures and subsequent lower thermal NO formation.

5.2 The Numerical Grid

The numerical grid utilised for these calculations has the same size as in the case of presented in section 4.

5.3 The Operating Conditions

The operating conditions provided are summarised in Tables (5.1 and 2). In Table (5.1) the prevailing conditions for the air ports are introduced. In Table (5.2) the operating conditions for the fuel are presented.

Total air inflow rate	291.214 Kg/s
Air inflow Rate Per Burner	16.18 Kg/s
Excess air	8.5 %
Air Temperature	290 C
Air Density	0.6271 Kg/m^3

Table 5.1 The Furnace Operating Conditions (Air)

Oil Temperature	120 °C
Total Oil Inflow Rate	19.44 Kg/s
Oil Inflow Rate per Burner	1.08 Kg/s

Table 5.2 The Furnace Operating Conditions (Oil)

5.4 The Oil Characteristics

The characteristics of the heavy fuel oil fired in the furnace are presented in Table (5.3). The saturation temperature was determined as the temperature of the major peak of the burning profile of an oil with similar Carbon to Hydrogen ratio, see for example Weidman and Utterback (1976). The burning profile may be defined as the rate of

weight change of a fuel when it is heated at a fixed rate in an air atmosphere. Initially, this analysis was developed by the Babcock and Wilcox Company, (B&W), and has been extensively practised to evaluate fuels in order to select the optimum boiler and burner design. B&W has found that liquid fuels having similar burning profiles behave in a similar manner when fired in a boiler. The burning profile is a characteristic fingerpoint of the fuel oxidised under standard conditions, and it is not intended to provide absolute kinetic and thermodynamic data. The burning profile is of value for relative evaluations of combustion characteristics of fuels.

Calorific Value of oil	40.82 MJ/Kg
Oil Droplet Saturation Temperature	450 °C
Oil droplet density	930 Kg/m^3
Oil Composition	Carbon : 87 % Hydrogen 13 %

Table 5.3 The Oil Characteristics

5.5 The Calculation Set-up

(i) *The Primary Air*

The primary air (atomising air) partition and velocities are presented in Table (5.4).

Cross Sectional Area	.1478 m^2
Air Partition	8%
Axial Velocity	13.96 m/s

Table 5.4 The Primary Air

(ii) *The Secondary Air*

Table (5.5) summarises the secondary air port conditions.

The swirling component of the air velocity is calculated through the formula:

$$W = 3/2\ N_S\ U\frac{R_o(R_o^2 - R_o^2)}{R_o^3 - R_i^3} \qquad (5.1)$$

where U is the axial component of the air velocity, N_s is the swirl number, R_o and R_i are the outer and inner radii of the secondary annulus of the burner.

The adjacent burners in the burner arrangement are counter swirling as shown in Fig. (5.1). The positive sign by convention designates a clockwise swirling motion whereas the negative anti-clockwise one as seen from outside the combustion chamber.

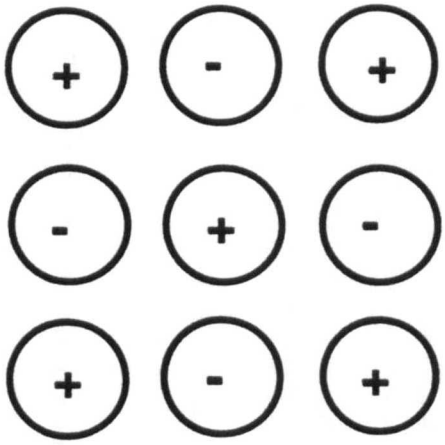


Fig. 5.1 Sense of Swirl of Adjacent Burners

Cross Sectional Area	0.7654 m^2
Air Partition	92 %
Axial Velocity	31 m/s
Swirl Number	1.2
Swirling Component	49.95 m/s

Table 5.5 The Secondary Air

(iii) *The Flue Gas Recirculation*

The mass inflow rate of the flue gas recirculation is given as the 3 % of the total air flow rate through the burners and is introduced through the hopper, see Fig 5.2.

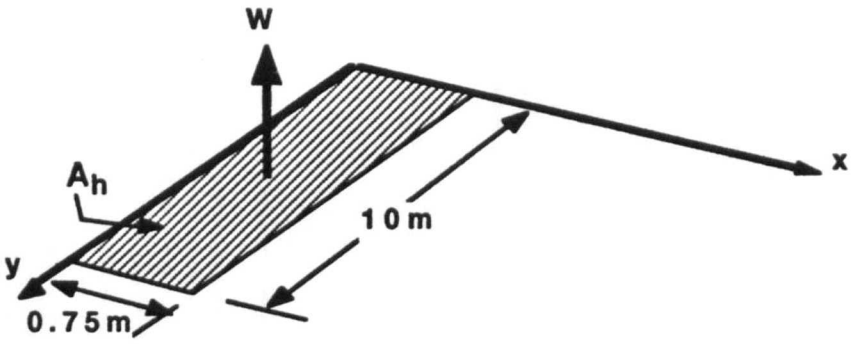


Fig. 5.2 The Flue Gas Recirculation through the Bottom of the Hopper

Flue Gas Mass Inflow Rate	13.11 Kg/s
Temperature	350 C
Density	0.5564 Kg/m^3
Total Hopper base area	9.59 m^2
Vertical Velocity	2.457 m/s

Table 5.6 The Flue Gas Recirculation Conditions

The introduction of the flue gases is modelled by assigning a boundary (inlet) value to the mixture fraction equation of 0.0624 (the stoichiometric mixture fraction is calculated 0.0674). taking into account the excess oxygen present in the flue gases (1.65 %).

(iv) ***Oil Droplet Inlet Conditions***

Data on this particular oil droplet size distribution was unavailable during the course of these calculations. The modelled spray is, for computational economy reasons,

assumed to consist of monosize droplets with a diameter calculated as the mass weighted average of typical size distribution, see for example Costa (1992).

Droplet diameter	97.3μm

Table 5.7 Oil Inlet Conditions

5.6 Results and Discussion.

The results presented are in the X - Z (parallel to the burners axes) and Y - Z (perpendicular to the burners axes) and in the X - Y planes. In particular the shown planes correspond to :

Y = 1	Section close to the right wall
Y = 5	Plane through the centre of the first column of burners
Y = 8	Plane between the first and second column of burners
Y = 10	Planes through the second column of burners (Plane of Symmetry)
Y = 12	Plane between the second and third column of burners
Y = 15	Plane through the third column of burners
Y = 19	Plane close to the left wall

Table 5.8 The X - Z Visualisation Planes (Oil Combustion)

X = 1	Section near the front wall
X = 4	Intermediate section
X = 8	Plane at the middle of the hopper
X = 12	Intermediate section
X = 16	Plane near the rear wall (Nose region)

Table 5.9 The Y -Z Visualisation Planes (Oil Combustion)

Z = 5	Hopper Region
Z = 9	Plane below the first row of burners
Z = 12	Plane through the axis of the first, row of burners
Z = 19	Plane between the second and third row of burners
Z = 33	Plane between the third row of burners and the nose
Z = 38	Plane near the exit of the furnace (Nose Region)

Table 5.10 The X - Y Visualisation Planes (Oil Combustion)

5.6.1 The Flow Field

A general comment about the flow field is that it is dominated by two characteristics of the operating conditions. These characteristics are:

a. The swirling secondary air flow through the burners

b. The draught caused by the introduction of the flue gases through the hopper.

The velocity field in the X - Z (Y = constant) direction is depicted in Fig (5.3 -9). There is a strong horizontal recirculation in the hopper region which is more apparent in the X - Y velocity vector plots which are discussed later in this section. This has an effect of destroying the draught caused by the flue gases (planes 2 and 19) whereas it can be clearly seen in the near the symmetry plane region where this draught is quite strong and penetrates through the burners region. This is assisted by the burner swirl that shortens the penetration of the burner jets into the central region of the furnace in contrast with the flow field discussed in section 4. The other effect of the inflow through the hopper is the reverse sense of the recirculation zones below the first row of burners in comparison with the modelling presented in section 4. An additional attribute of the flow is that it is not symmetric in the region close to the lateral walls. This is due to the fact that the incoming secondary air jets through adjacent and opposite burners is counter-swirling.

In Figs (5.10 -14) the flow field in the Y - Z (X = constant.) direction is presented. The swirling flow can be easily seen in the planes near the front and rear walls of the furnace. But as the flow develops close to the plane passing through the hopper this pattern disintegrates and the downstream draught is dominant. In this plane, two fairly symmetric recirculation zones are formed in the hopper near the side walls. This flow pattern shows again the destruction of the flue gas flow though the hopper. Moving nearer the rear wall and below the 'nose' (plane X = 12) one can observe a recirculation zone that corresponds with the sense of the swirling jets. The centre of this

recirculation zone can be seen in Fig. (5.8 -9) as well indicating the three-dimensional pattern of the flow.

The flow field in the X-Y direction is plotted in Figs (5.15-21). The strong recirculation in the hopper region can be seen in plane Z = 5. But as one traverses downstream close to the burner 'curtain' it seems to be strongly affected by the swirling jets of the burners (plane Z= 9). At the level of the first row of burners only in the central region of the furnace this cyclonic flow pattern is maintained. In plane Z = 33 the three-dimensional recirculation can again be observed. Finally in plane Z = 38 (exit region) the effect of the 'nose' in accelerating the flow towards the exit is clearly visible.

5.6.2 The Temperature and Oxygen Concentration Fields

A first characteristic of the temperature field is the low values which exist in the hopper region. This is expected due to the presence of the incoming flue gas which in addition to its low temperature (350 °C) contributes very little to the combustion processes (1.65 $\%O_2$). This has an effect especially in the first row of burners where the air /fuel ratio after the mixing with the flue gases is well below stoichiometry resulting in a region of low temperatures. This is desirable in order to reduce the NO production levels.

In Figs. (5.22 - 30) the temperature field in seen in the X-Z (Y = constant) direction. It can be seen that the temperatures near the first row of burners is around 200 °C lower than that in the region near the second and third rows of burners. The shape of the temperature contours in the hopper region close to the side walls can be considered as being a mirror image of one another (planes for example 4 and 14). This is because of the horizontal recirculation that exists in this region. Additionally the temperature values near the side walls are lower by around 200 -300 °C and this is due to the radiative and convective heat fluxes to the walls. A hotter region (about 1600 °C) is encountered in the centre and upper part of the furnace where the mixing of fuel and gases is complete and the radiation contribution by the sooting flame in strong. Again in agreement with

the flow field in the region close to the far lateral wall (plane Y=16) a cooler region exists due to the recirculation zone which results in a poorer mixing.

Figs. (5.45 - 50) show the oxygen profiles for the same planes as those for the velocities temperature. In general. they appear to be consistent with the combustion pattern depicted in the temperature plots. The values of oxygen are in the hopper region due to the recirculated flue gases as well as in the regions where high temperatures are encountered. In the latter case, the low oxygen levels provide an additional indication that enhanced combustion occurs in those regions.

In Figs (5.31 - 36) the temperature profiles in the Y - Z (X = constant) planes are given. It can be seen that the temperatures near the wall planes (1 and 16) are lower due to the evaporation processes of the droplets and the incomplete mixing and combustion. The oil droplets evaporate within the first two to three cells of the computational grid (about 1m downstream of the burner exit with a residence time of about 17 - 20 ms). Moving further into the central region of the furnace (plane through the hopper X= 8) the temperatures are higher whereas again the cooler region in the aforementioned recirculation below the nose is again apparent (plane 14).

Figs. (5.53 - 57) present the oxygen concentration in the Y - Z (X = constant) planes. The burners are represented in Figs () as regions of high oxygen levels (above 12%) in the front and rear walls of the furnace. The concentration of oxygen becomes lower as combustion progresses near the central planes of the combustion chamber.

Finally, in Figs (5.37 - 44) the temperature field can be seen in the X -Y direction. The temperature values in the hopper are clearly low, as expected, following the vortex motion induced by the swirling burners which have a core of 700 -900 °C. As one moves downstream this vortex disintegrates. In levels Z = 8 and 10 the effect of the counter swirling burners can be observed. These planes are located below the first row of the burners and show a diagonal symmetry in the temperature pattern which is apparent in the oxygen profiles as well (Figs. 5.58 - 60). This is because of the burner

interaction giving better mixing where the sense of rotation of the flow of two adjacent burners reinforces the mixing rather than reducing it. Moving further up and on the first row of burners (Z=12, which is the plane through the burners axes) one can see that in the near the burners regions the flow is dominated as expected by the incoming jets rather than by the upcoming draught. Higher in the furnace the temperature field becomes simpler characterised by a hot central region as well as a cooler region mentioned earlier (plane Z=28).

5.6.3 The Absorption Coefficient

Due to the presence of soot the optical properties of an oil flame are quite different than those of a gas flame. In Figs (6.61 -66) contour plots of the absorption coefficients of the gas mixture are given. A first observation is that the values are considerably higher than those encountered for the gas flames of chapter 4 and that is expected. The values in the hopper region are quite low close to the ones found in a gas flame but moving higher in the furnace it can be seen that the values increase up to more than three times of their values in the hopper (0.3 - 0.92) in the near burner regions. In between the burner levels (plane 14) there is a reduction of the value of the absorption coefficient and this is due to the reduction of the soot concentration through oxidation.

5.6.4 The Heat Fluxes

The predicted heat fluxes one of the lateral walls is consistent with the temperature field, Fig. (5.67). The same convention with the one presented in Chapter 4 is followed herein, where the negative sign for the heat fluxes designates the net outgoing flux. Higher fluxes (above 350kW/m^2) are encountered near the central regions of the wall at which level the temperatures are higher. The magnitude of these fluxes in the hopper region are significantly lower due to the much lower temperatures prevailing in this region. The heat fluxes in this case as compared with the case presented in Chapter 4 (Fig 4.58) appear to be somewhat 20% higher. This may be attributed to the higher

radiative properties of the combustion mixture due to the presence of soot discussed in section (2.5.2).

5.7 Conclusions

1. The result of the FGR through the hopper is that the flow field exhibits an overall draught motion towards the furnace exit and significantly reduces the hopper temperatures from 1200 to about 700 °C. Additionally, because of the swirl of the burners adjacent to the 'hopper' a horizontal rotational motion occurs about the vertical central line of the furnace– a flow field resembling tangentially-fired configurations.

2. Comparing the two cases, presented in chapters 4 and 5 for the same furnace, the flames appear to be shorter in the oil-fired case which is attributed to the swirling flows of the burners. Most importantly, it is found that the reduced emissivity of the gas flame, as compared with that of an oil flame, is compensated for by its higher temperature so that the total heat transfer due to the fuel conversion is affected be about 20%.

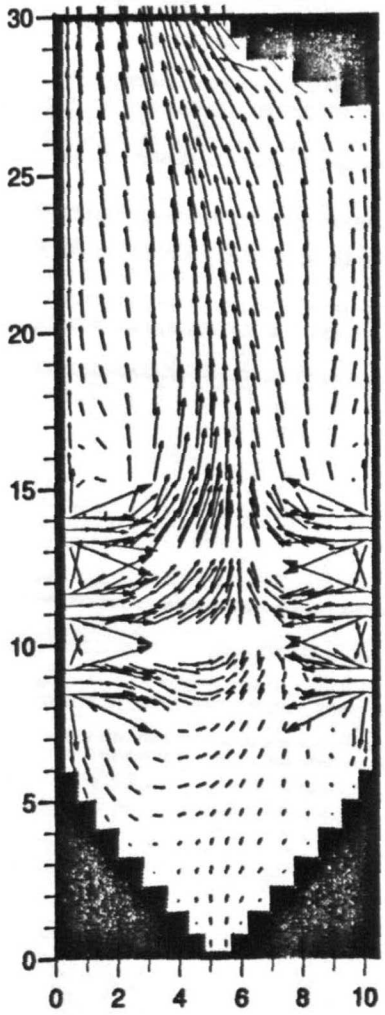


Fig. 5.3 Velocity Vectors For Y = 1 (Oil Combustion)

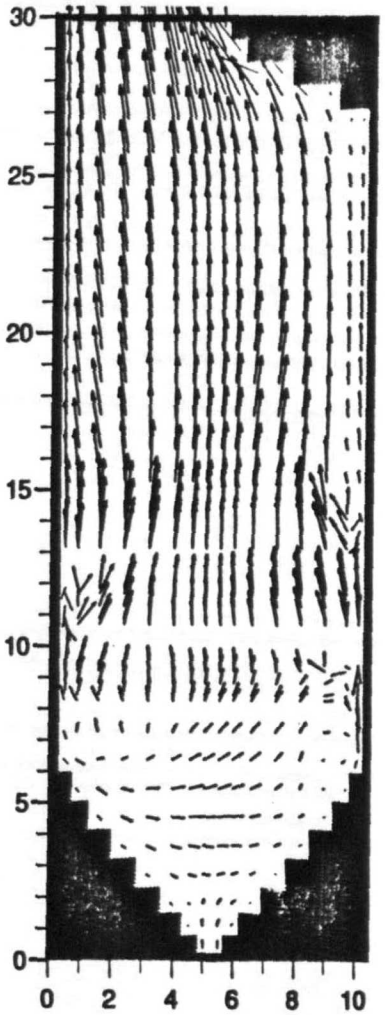


Fig. 5.4 Velocity Vectors For Y = 5 (Oil Combustion)

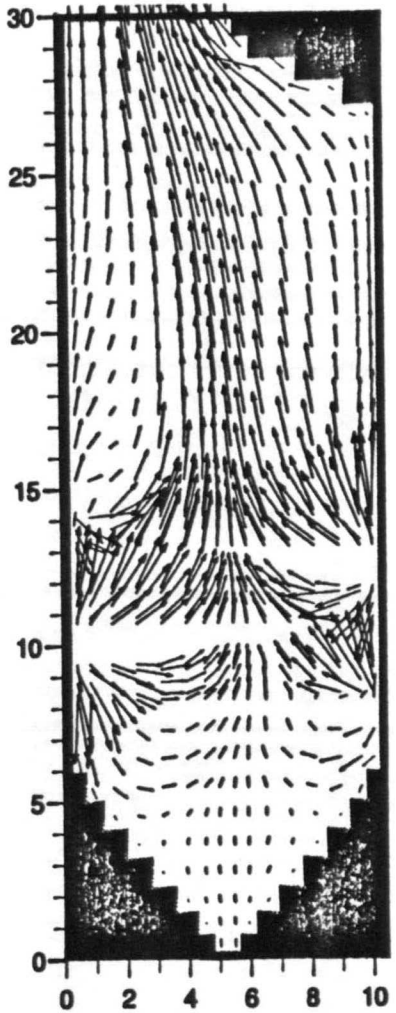


Fig. 5.5 Velocity Vectors For Y = 8 (Oil Combustion)

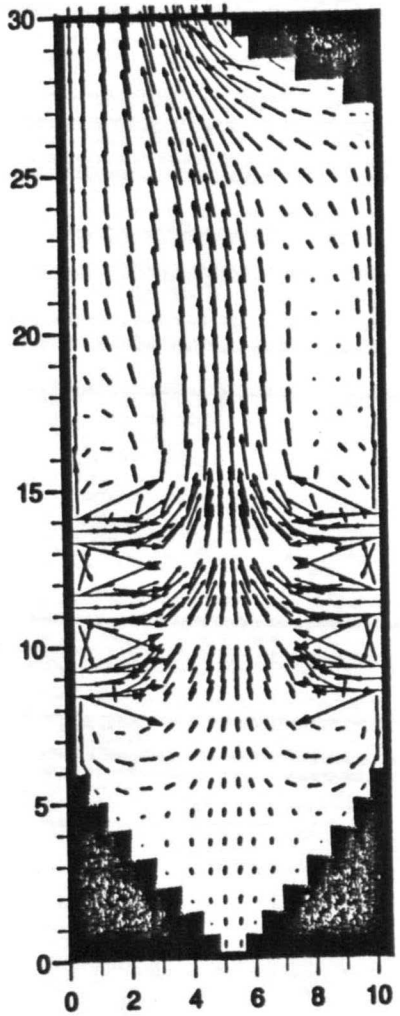


Fig. 5.6 Velocity Vectors For Y = 10 (Oil Combustion)

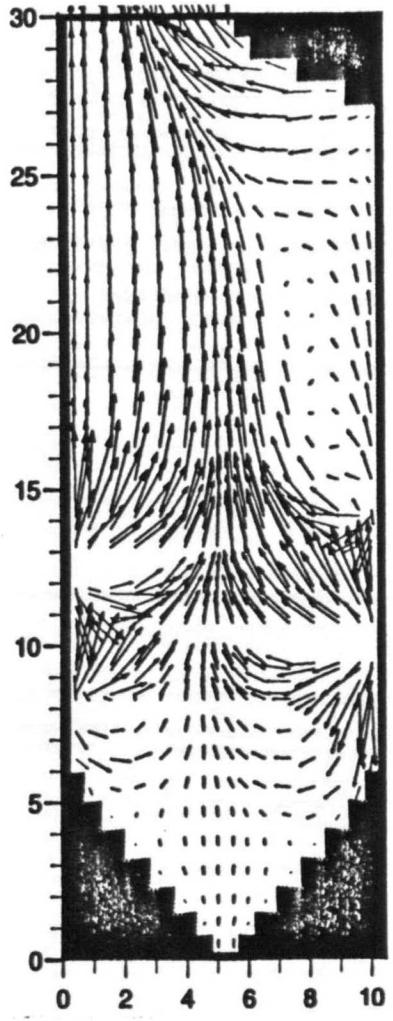


Fig. 5.7 Velocity Vectors For Y = 12 (Oil Combustion)

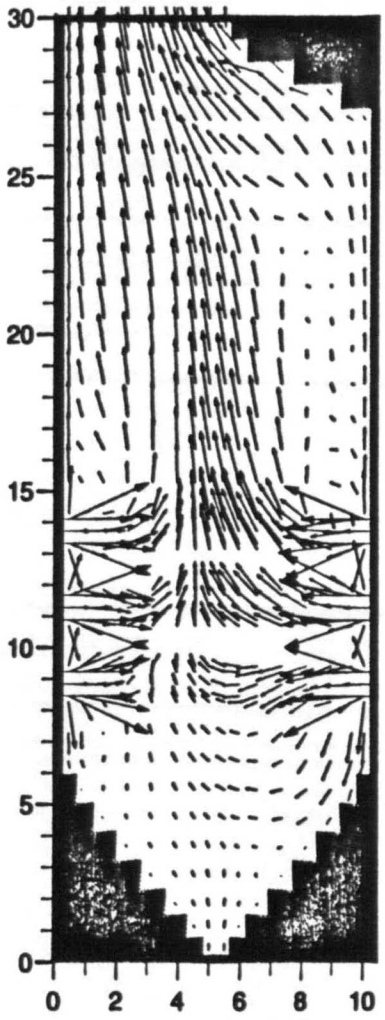


Fig. 5.8 Velocity Vectors For Y = 15 (Oil Combustion)

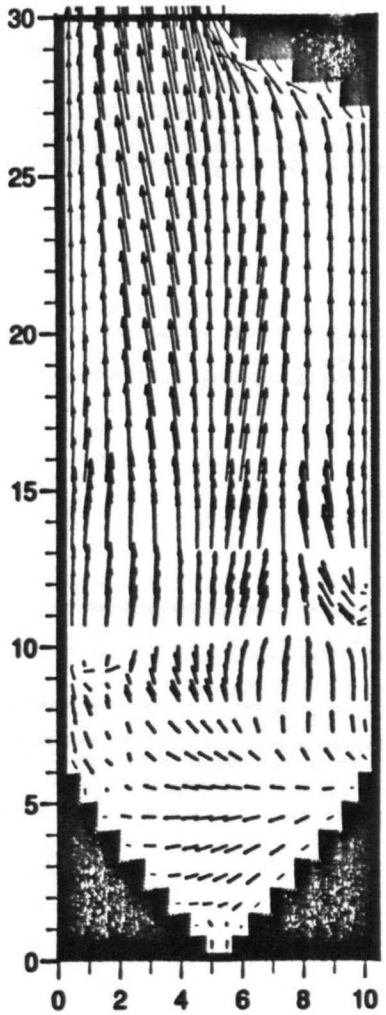


Fig. 5.9 Velocity Vectors For Y = 19 (Oil Combustion)

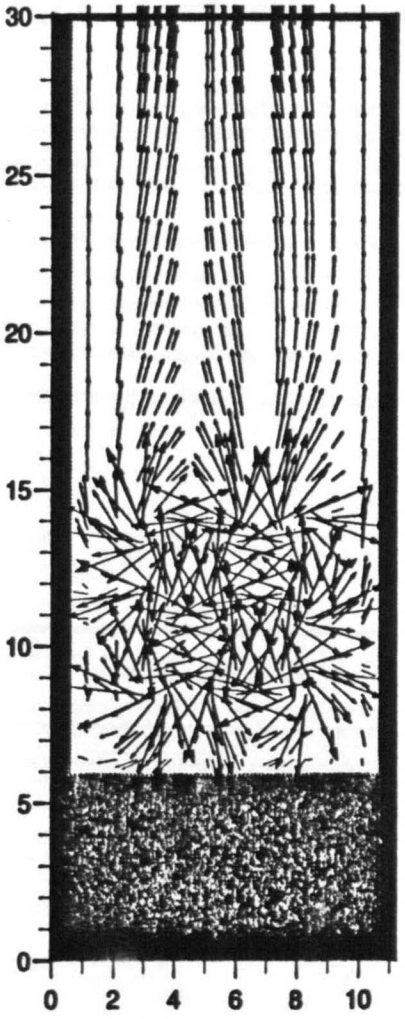


Fig. 5.10 Velocity Vectors For X = 1 (Oil Combustion)

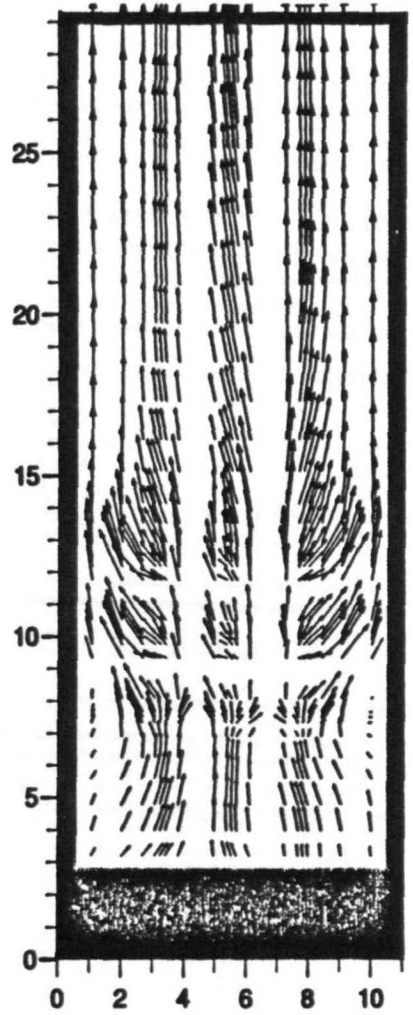


Fig. 5.11 Velocity Vectors For X = 4 (Oil Combustion)

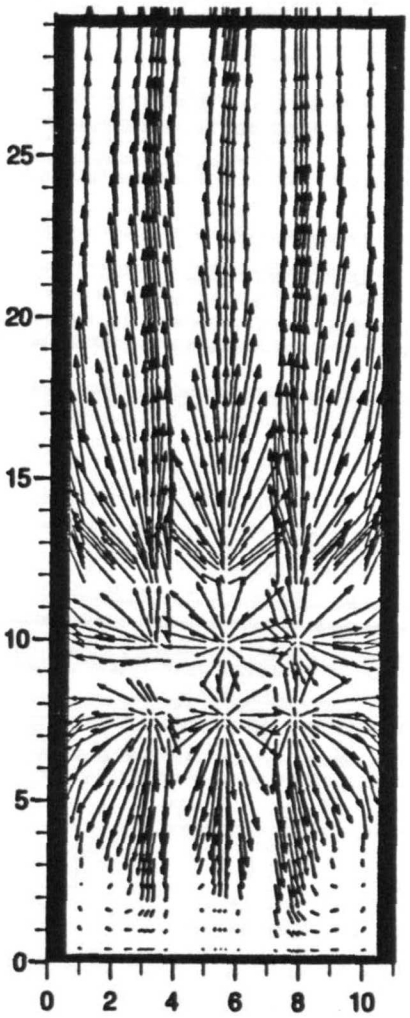


Fig. 5.12 Velocity Vectors For X = 8 (Oil Combustion)

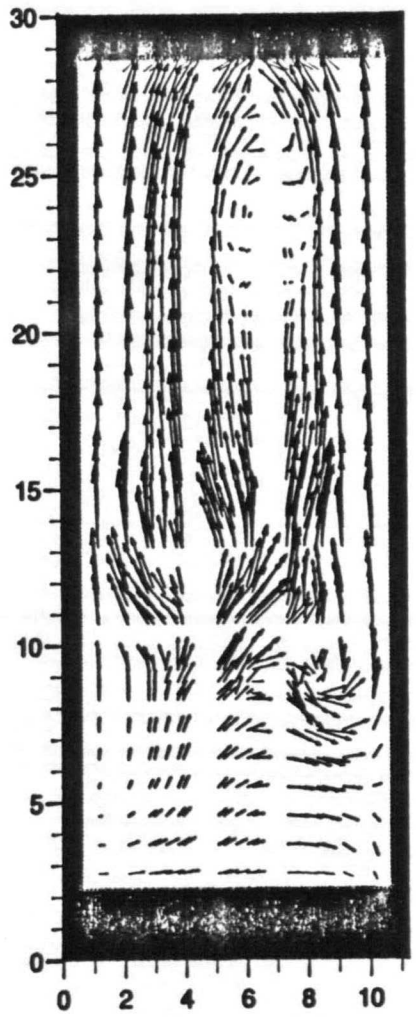


Fig. 5.13 Velocity Vectors For X = 12 (Oil Combustion)

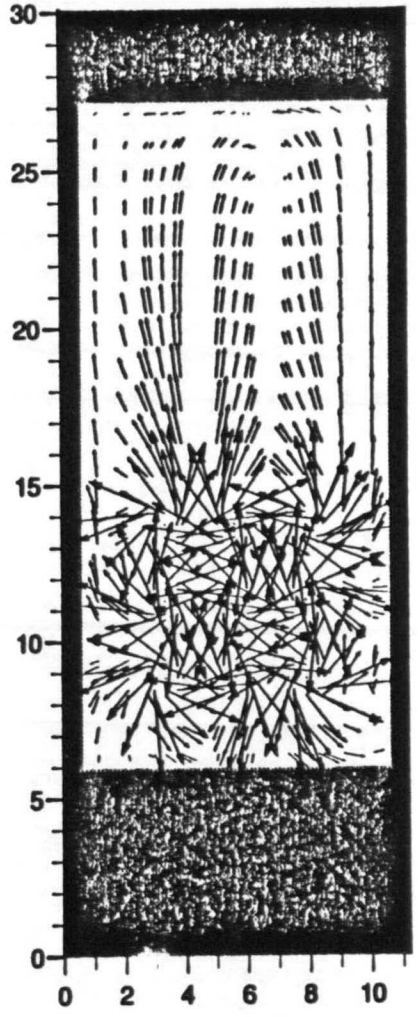


Fig. 5.14 Velocity Vectors For X = 16 (Oil Combustion)

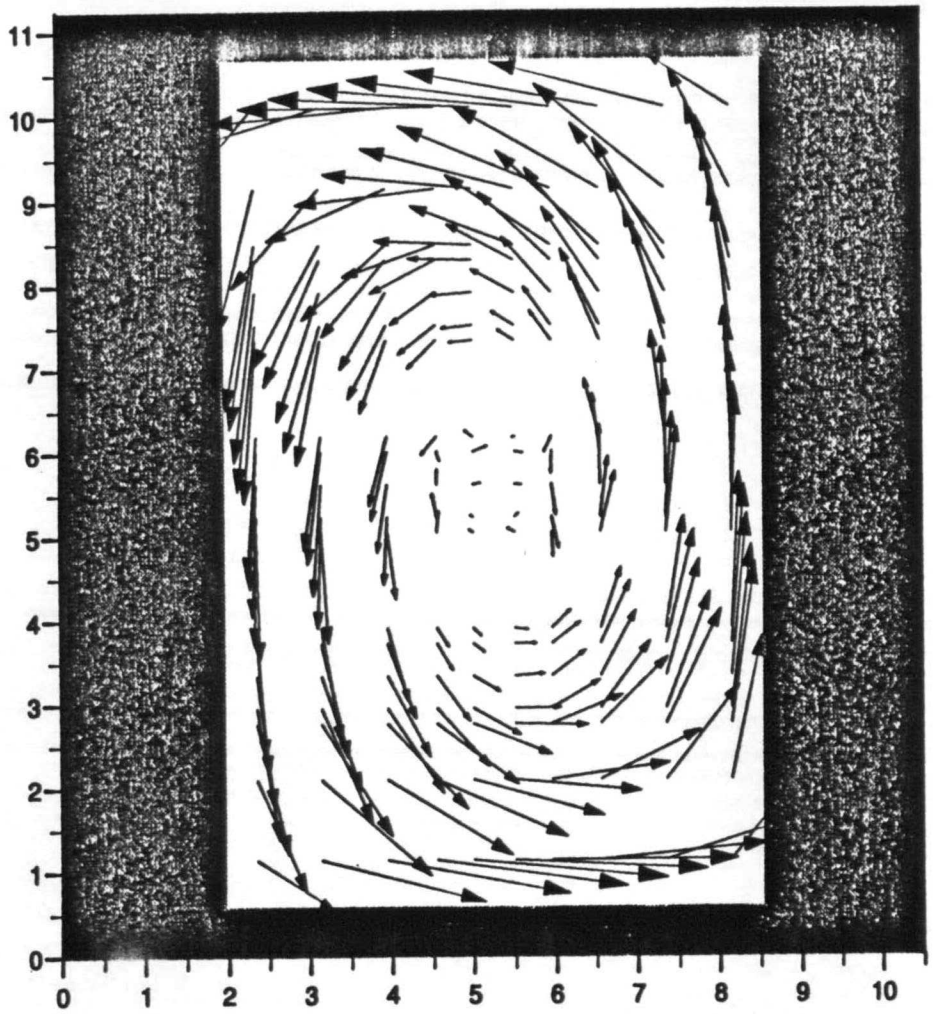


Fig. 5.15 Velocity Vectors For Z = 5 (Oil Combustion)

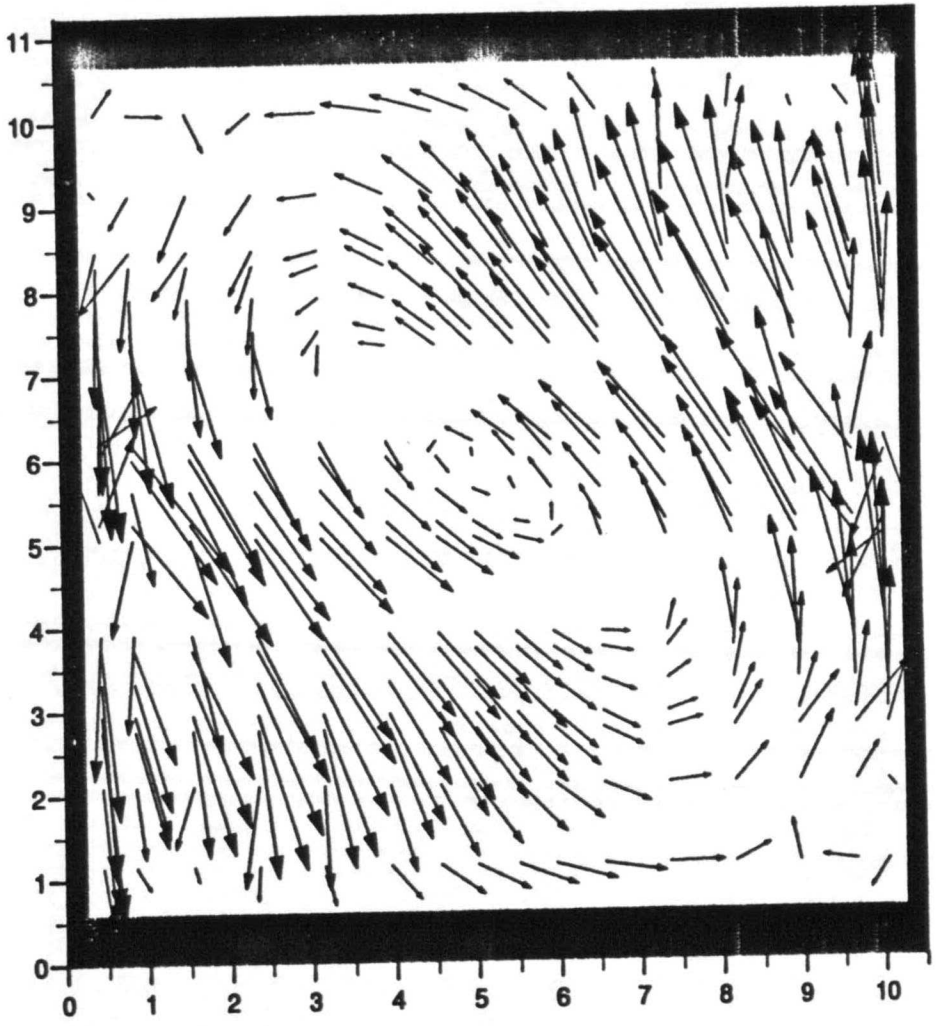


Fig. 5.16 Velocity Vectors For Z = 9 (Oil Combustion)

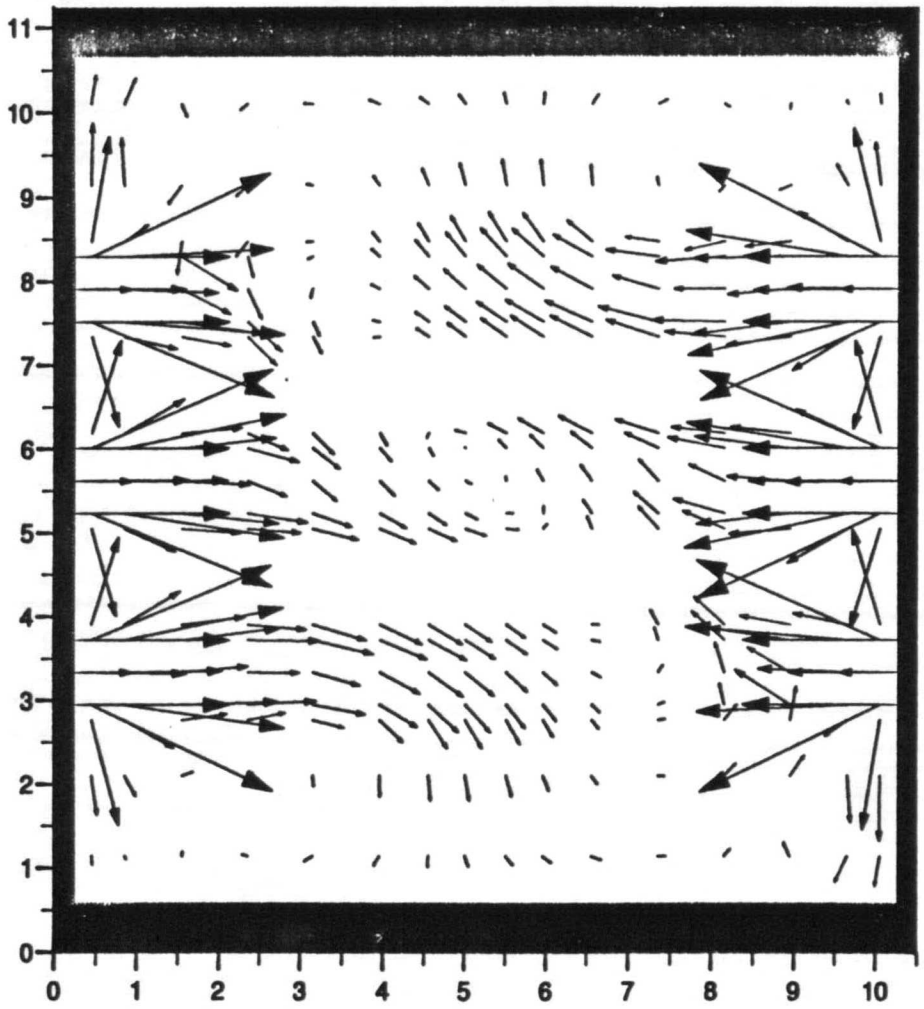


Fig. 5.17 Velocity Vectors For Z = 12 (Oil Combustion)

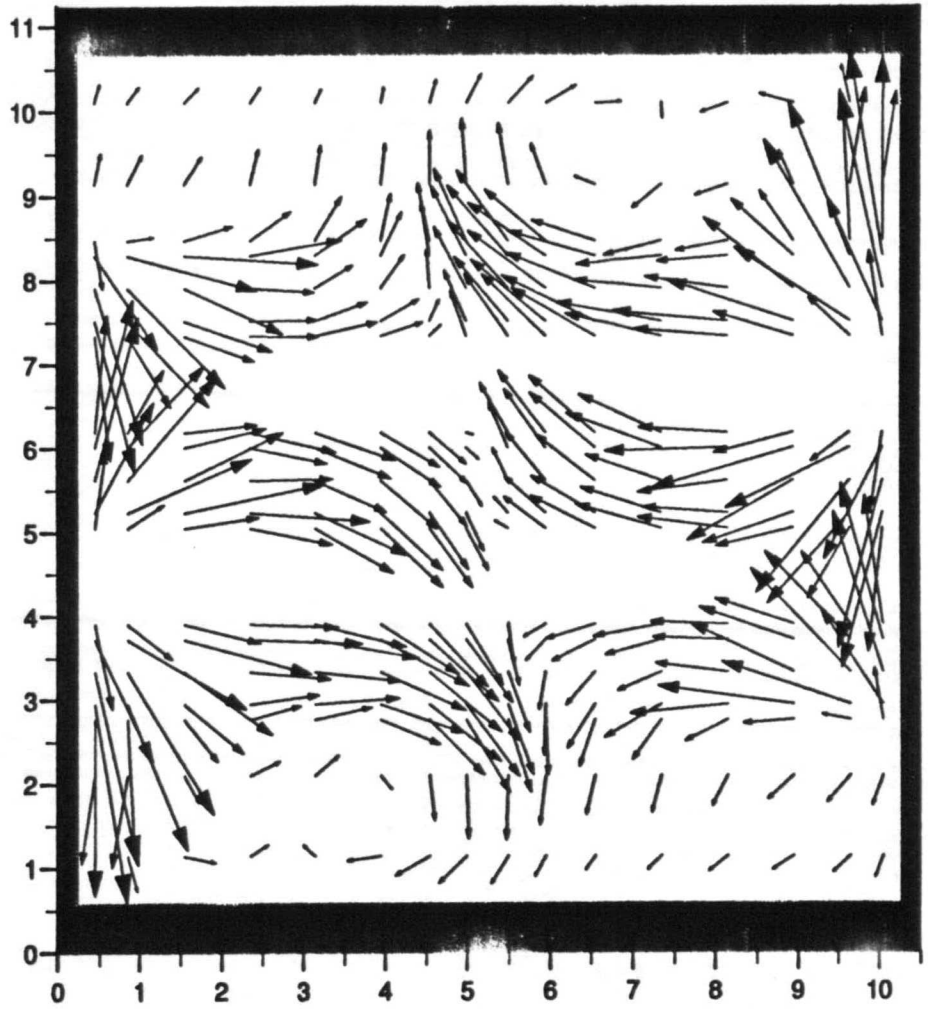


Fig. 5.18 Velocity Vectors For Z = 19 (Oil Combustion)

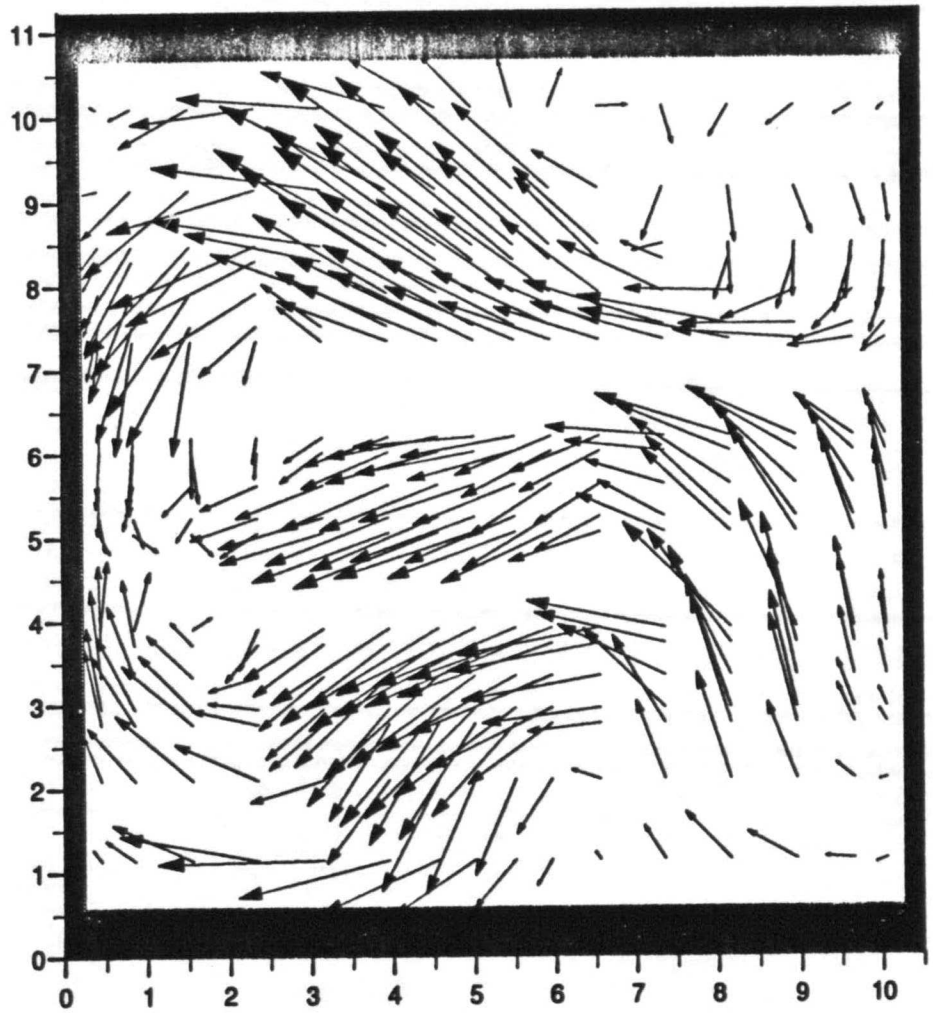


Fig. 5.19 Velocity Vectors For Z = 33 (Oil Combustion)

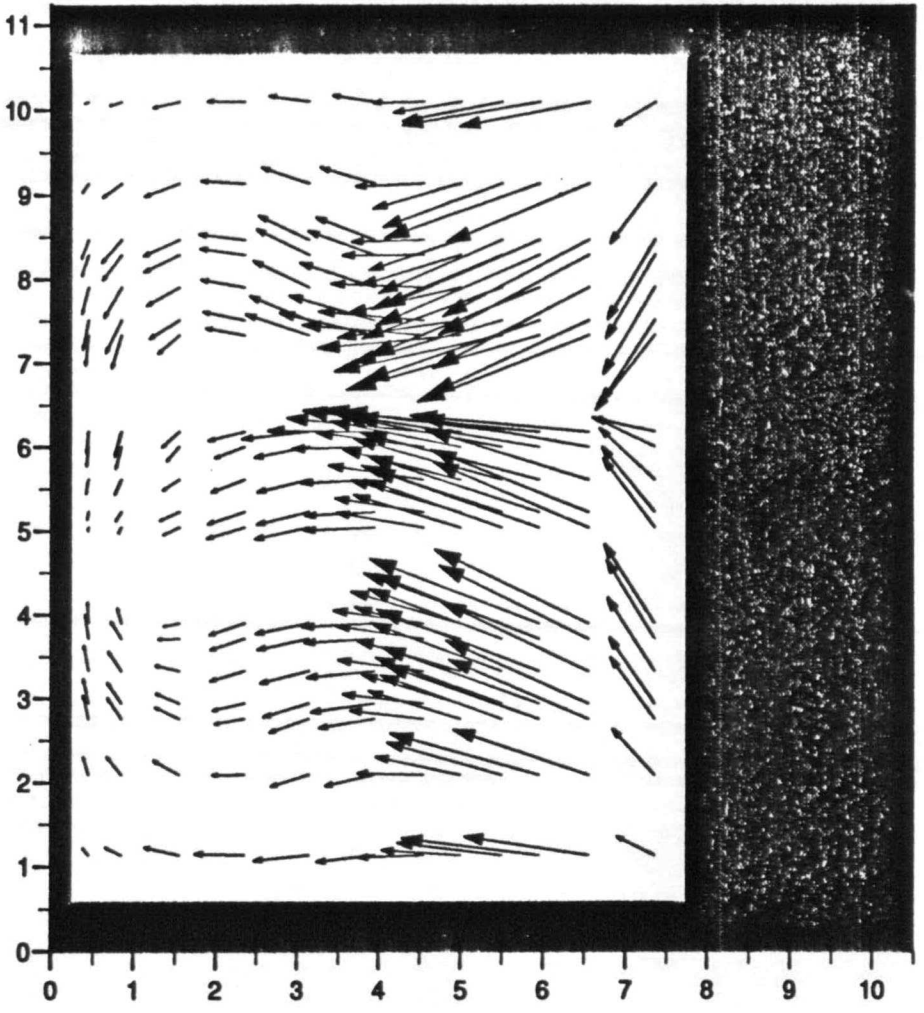


Fig. 5.20 Velocity Vectors For Z = 38 (Oil Combustion)

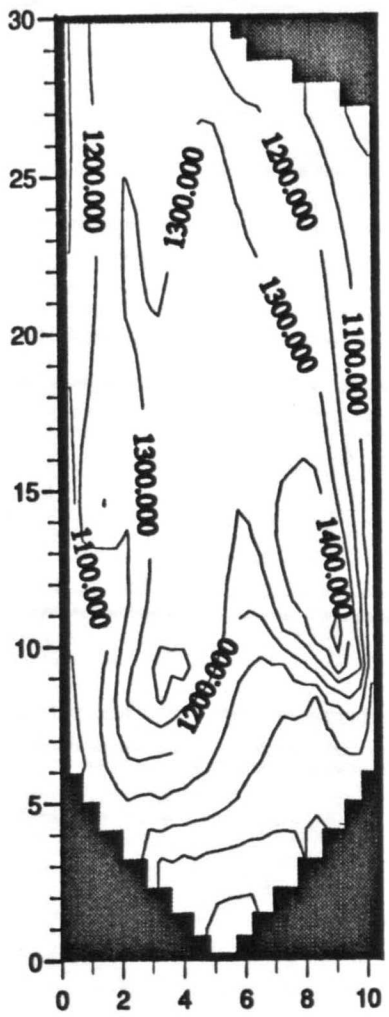


Fig. 5.21

Temperature Contours (^{O}c) For Y = 1 (Oil Combustion)

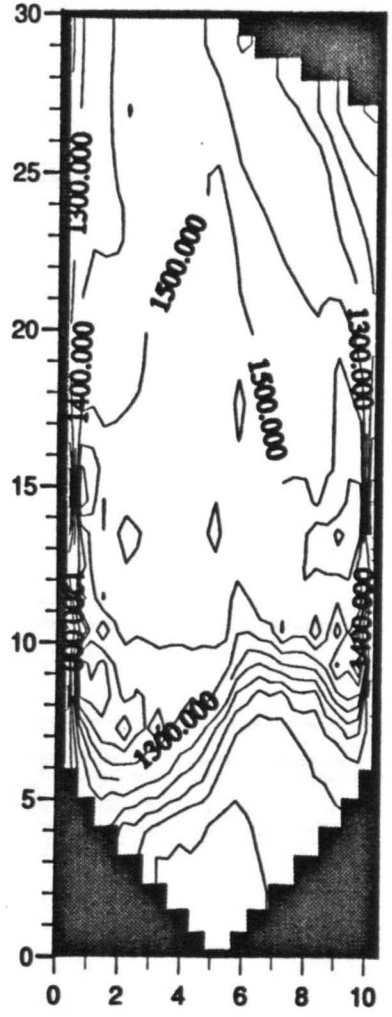


Fig. 5.22

Temperature Contours (^{O}c) For Y = 4 (Oil Combustion)

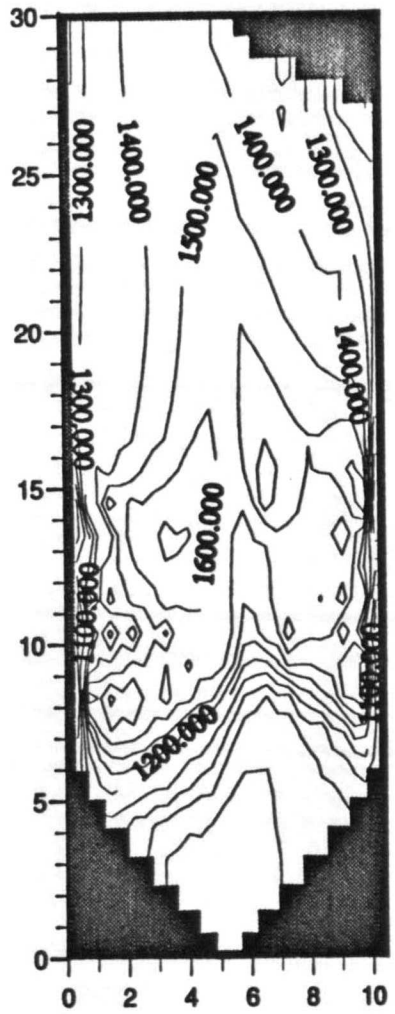


Fig. 5.23

Temperature Contours (^{O}c) For Y = 6 (Oil Combustion)

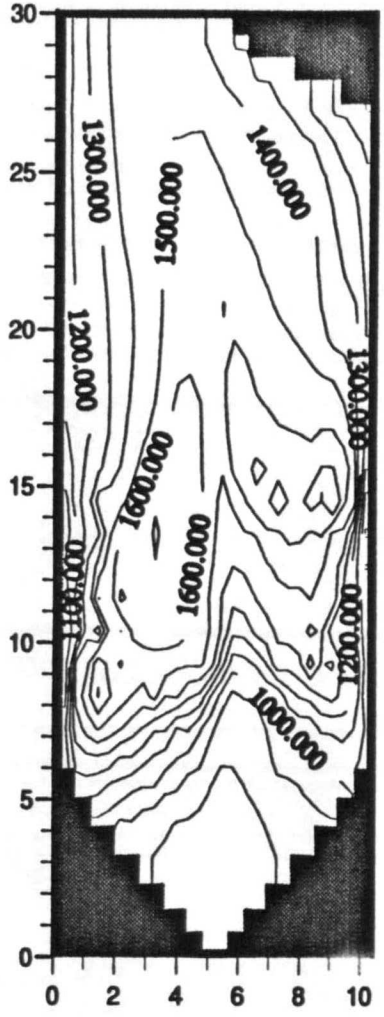


Fig. 5.24

Temperature Contours (^{O}c) For Y = 8 (Oil Combustion)

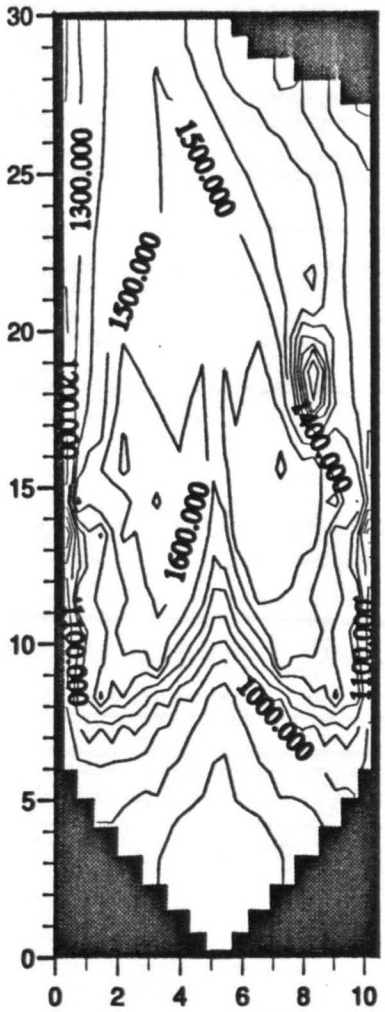


Fig. 5.25

Temperature Contours (^{o}c) For Y = 10 (Oil Combustion)

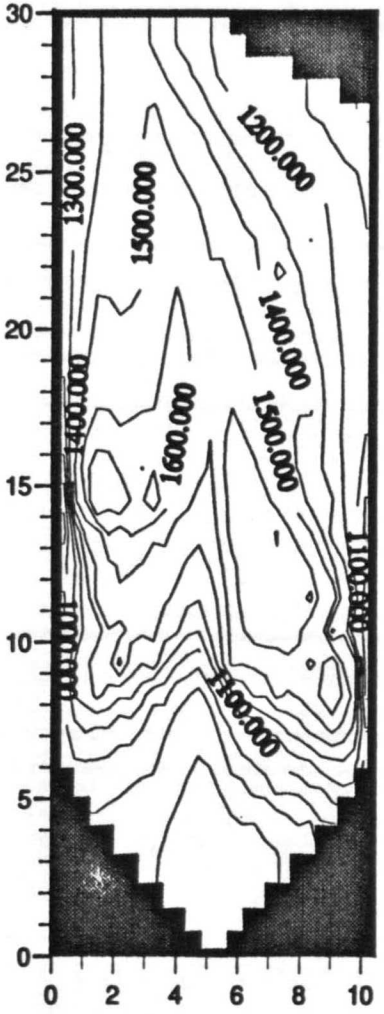


Fig. 5.26

Temperature Contours (^{o}c) For Y = 12 (Oil Combustion)

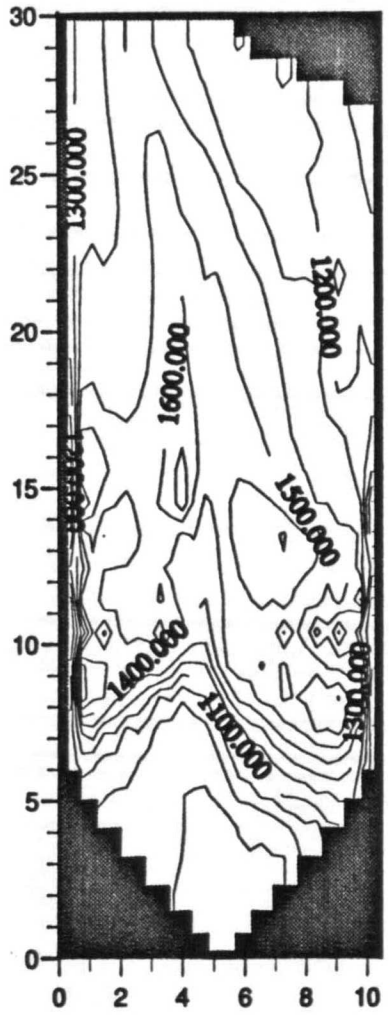


Fig. 5.27

Temperature Contours (^{O}c) For Y = 14 (Oil Combustion)

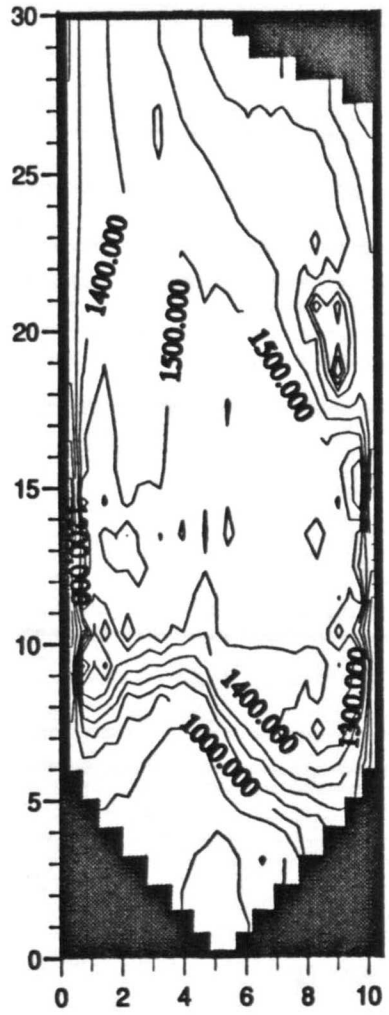


Fig. 5.28

Temperature Contours (^{O}c) For Y = 16 (Oil Combustion)

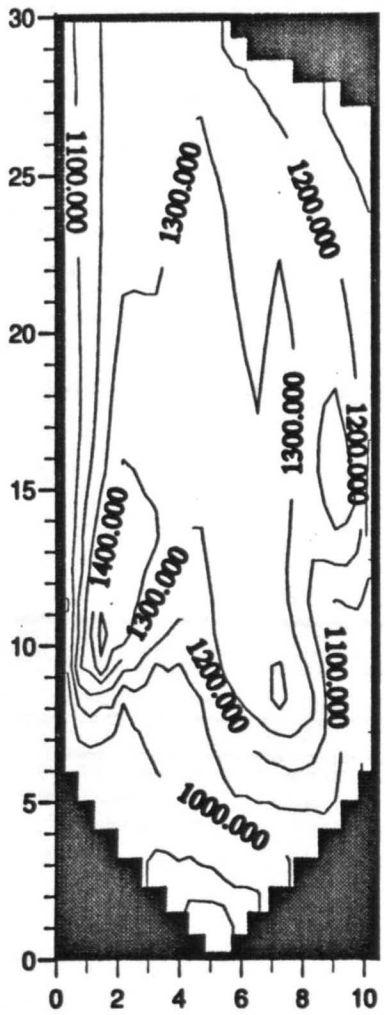


Fig. 5.29

Temperature Contours (^{O}c) For Y = 19 (Oil Combustion)

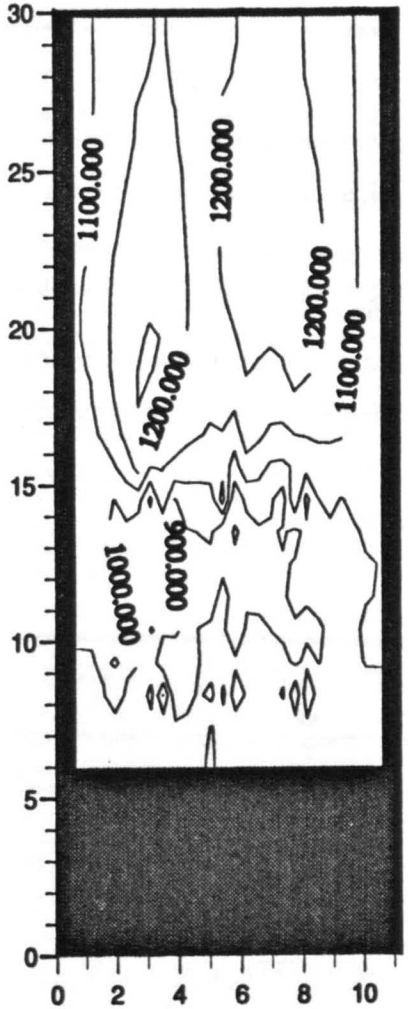


Fig. 5.30

Temperature Contours (^{O}c) For X = 1 (Oil Combustion)

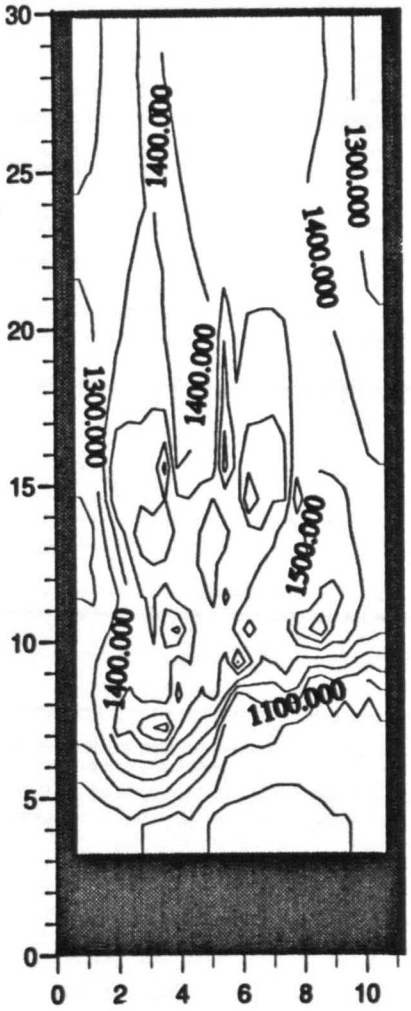


Fig. 5.31

Temperature Contours (^{O}c) For X = 4 (Oil Combustion)

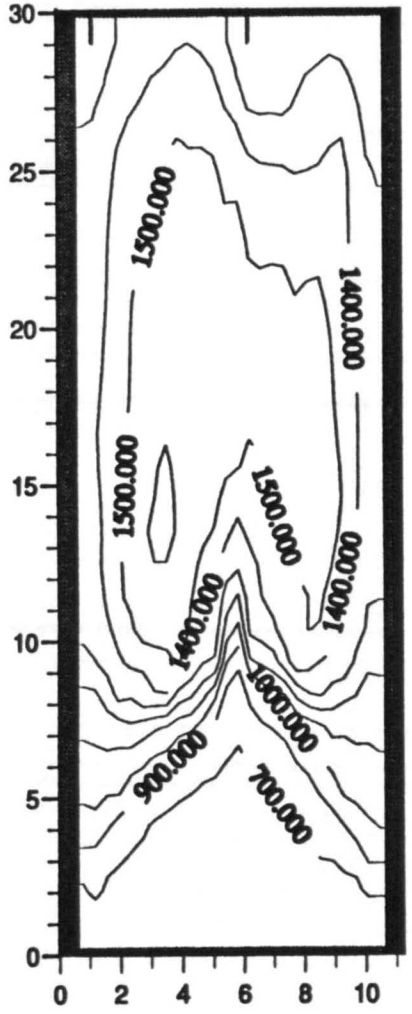


Fig. 5.32

Temperature Contours (^{O}c) For X = 8 (Oil Combustion)

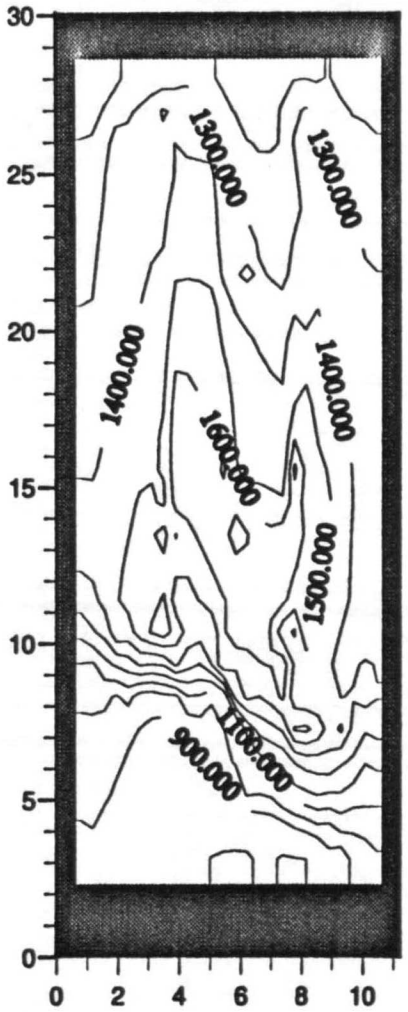


Fig. 5.33

Temperature Contours (^{O}c) For X = 12

(Oil Combustion)

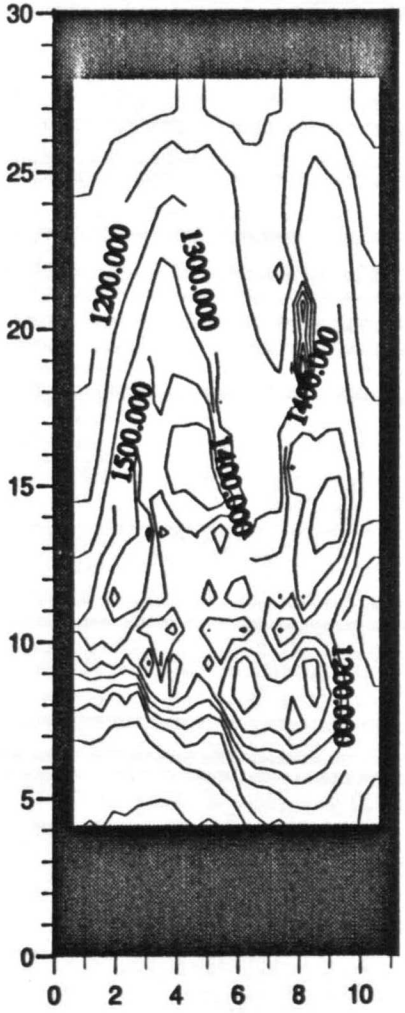


Fig. 5.34

Temperature Contours (^{O}c) For X = 14

(Oil Combustion)

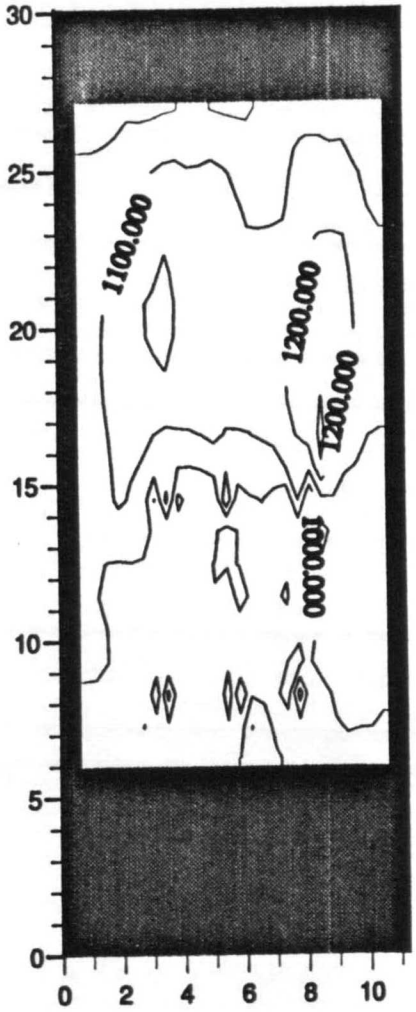


Fig. 5.35

Temperature Contours (^{O}c) For X = 16

(Oil Combustion)

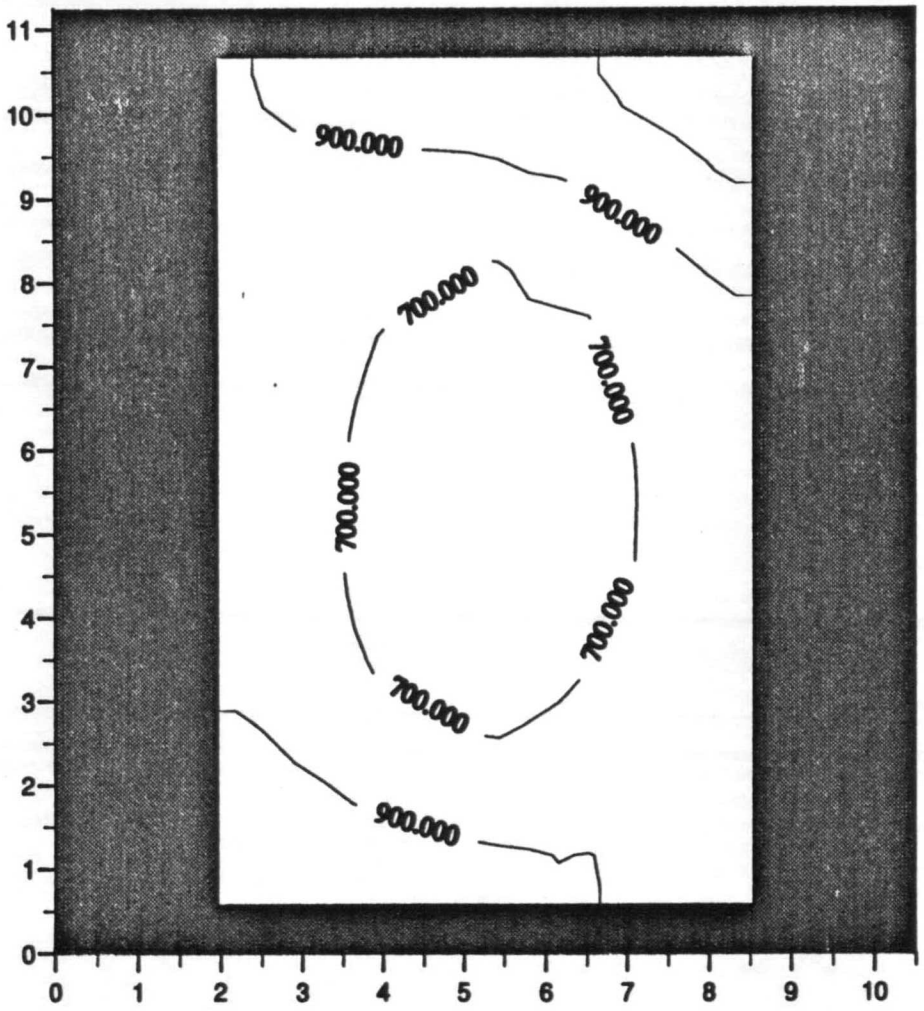


Fig. 5.36 Temperature Contours (^{O}c) For Z = 5 (Oil Combustion)

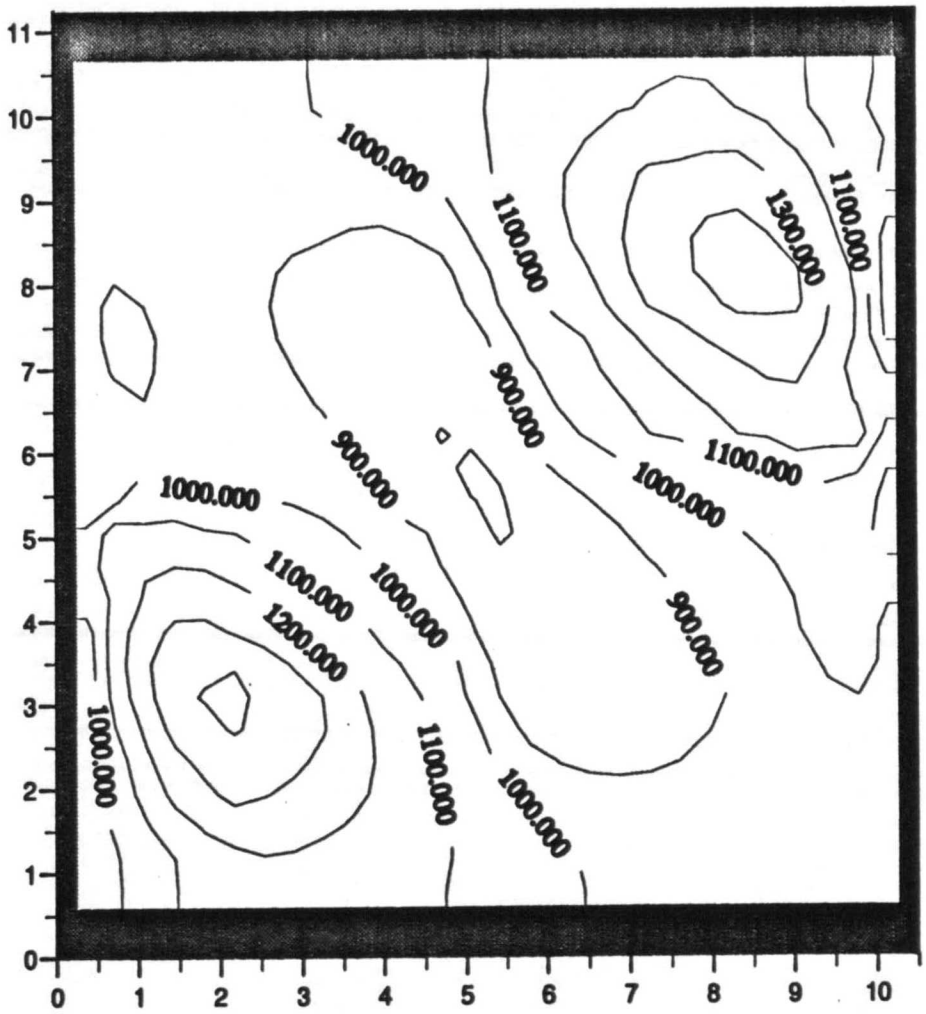


Fig. 5.37 Temperature Contours (^{O}c) For Z = 8 (Oil Combustion)

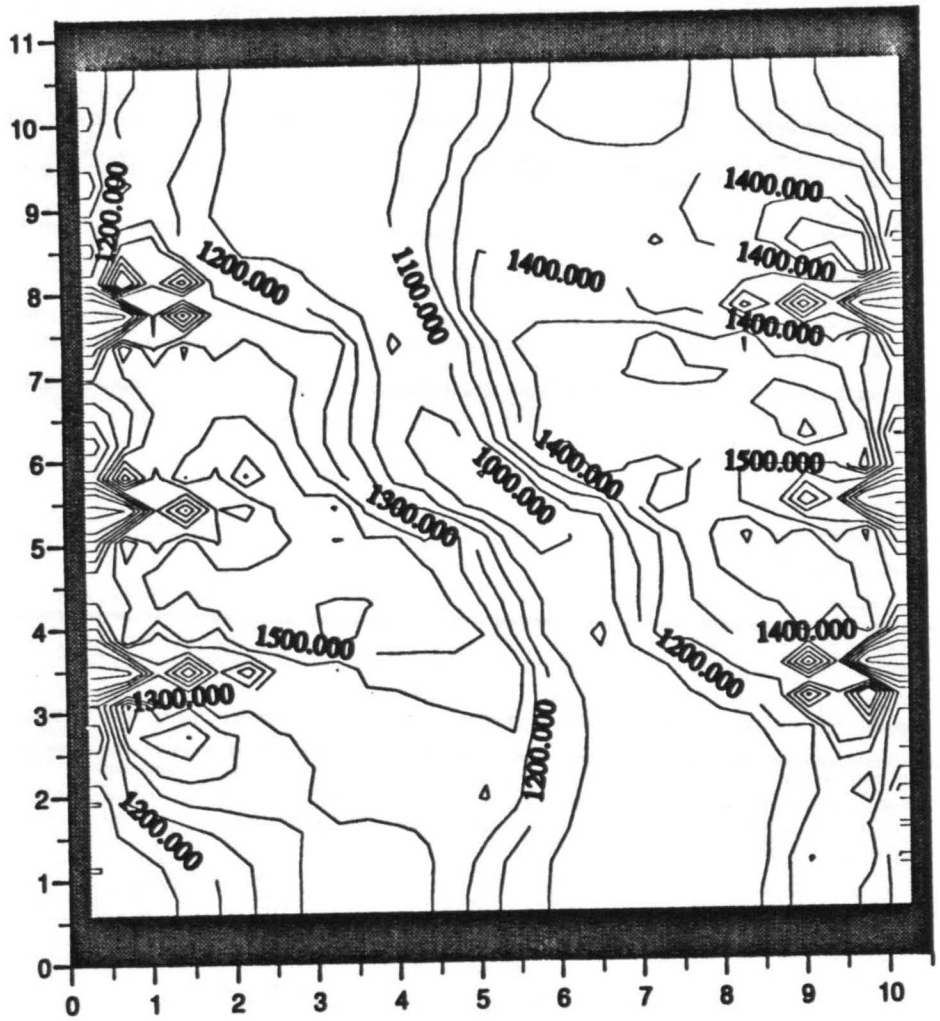


Fig. 5.38 Temperature Contours (^{o}c) For Z = 10 (Oil Combustion)

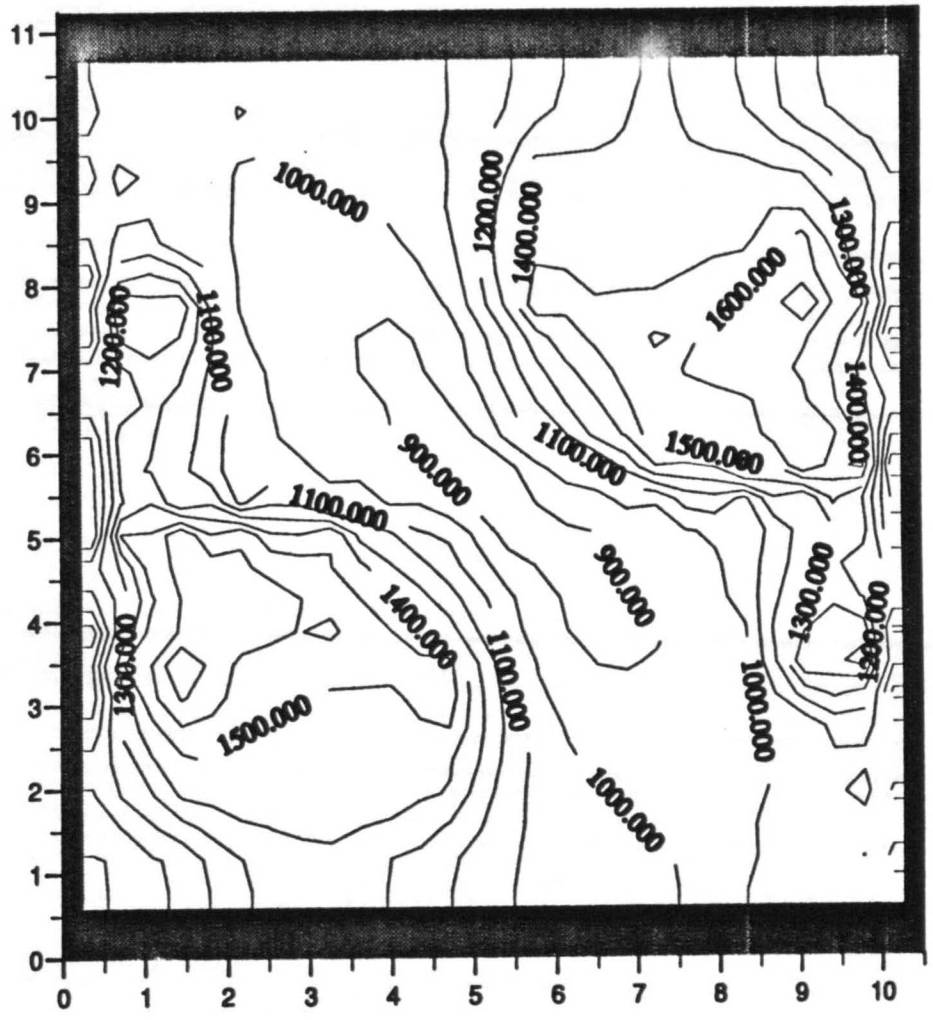


Fig. 5.39 Temperature Contours (^{o}c) For Z = 12 (Oil Combustion)

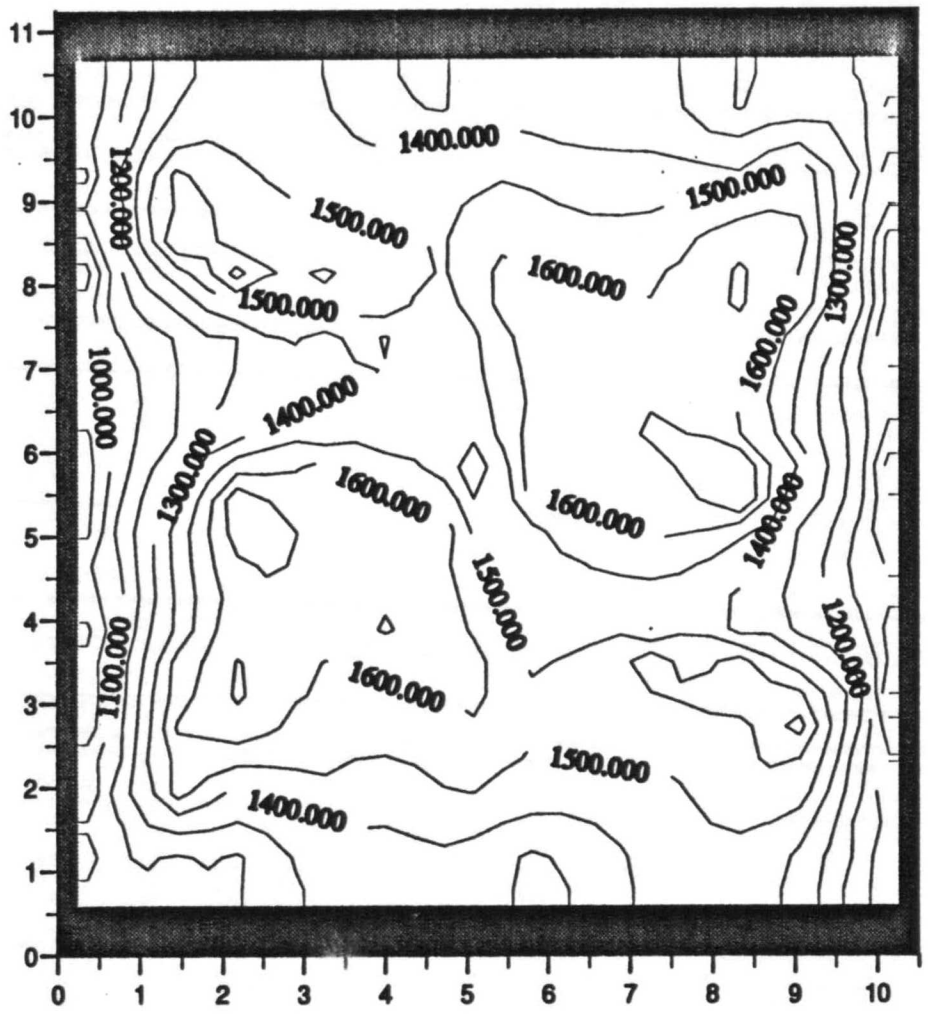


Fig. 5.40 Temperature Contours (^{O}c) For Z = 20 (Oil Combustion)

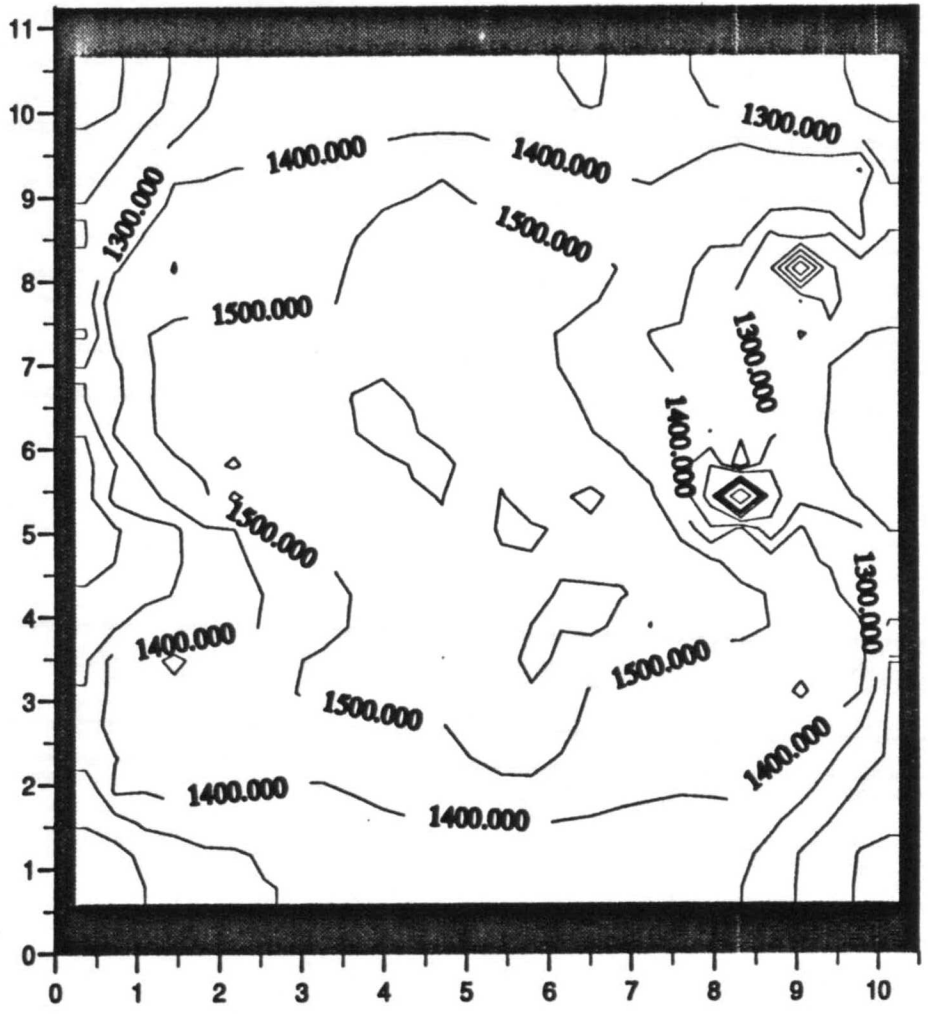


Fig. 5.41 Temperature Contours (^{O}c) For Z = 28 (Oil Combustion)

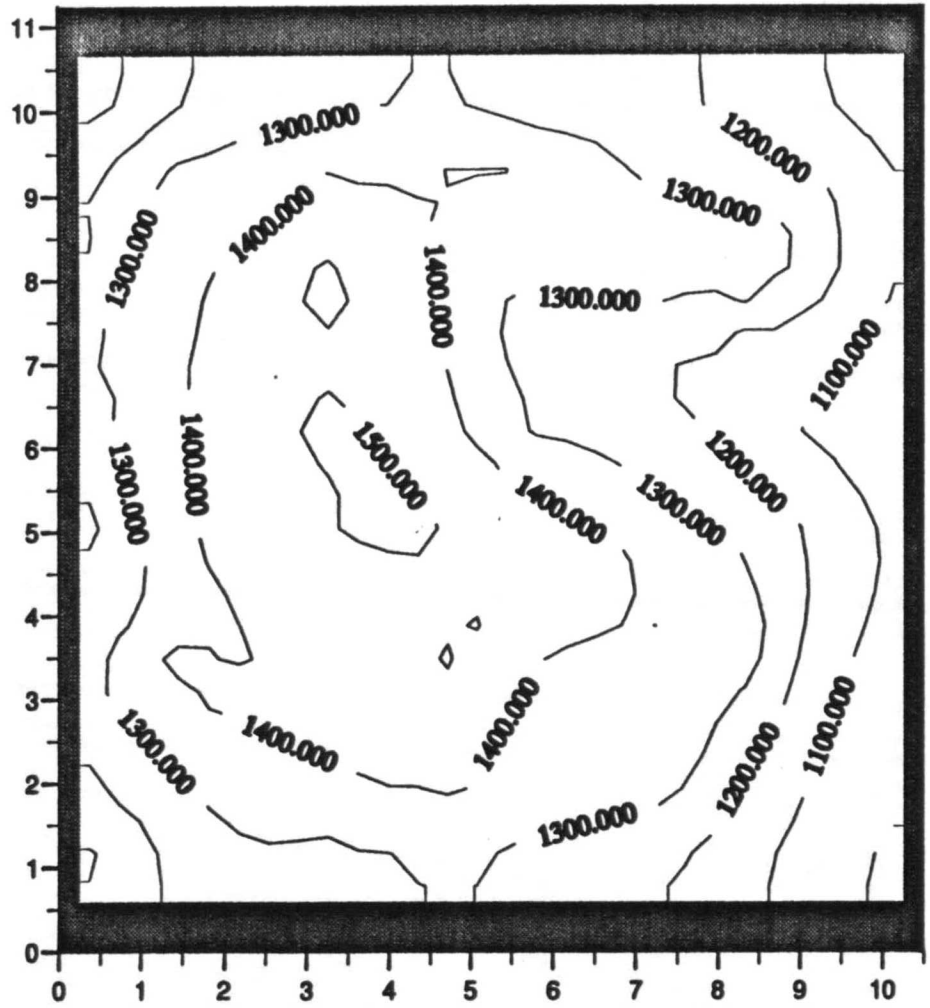


Fig. 5.42 Temperature Contours (^{O}c) For Z = 35 (Oil Combustion)

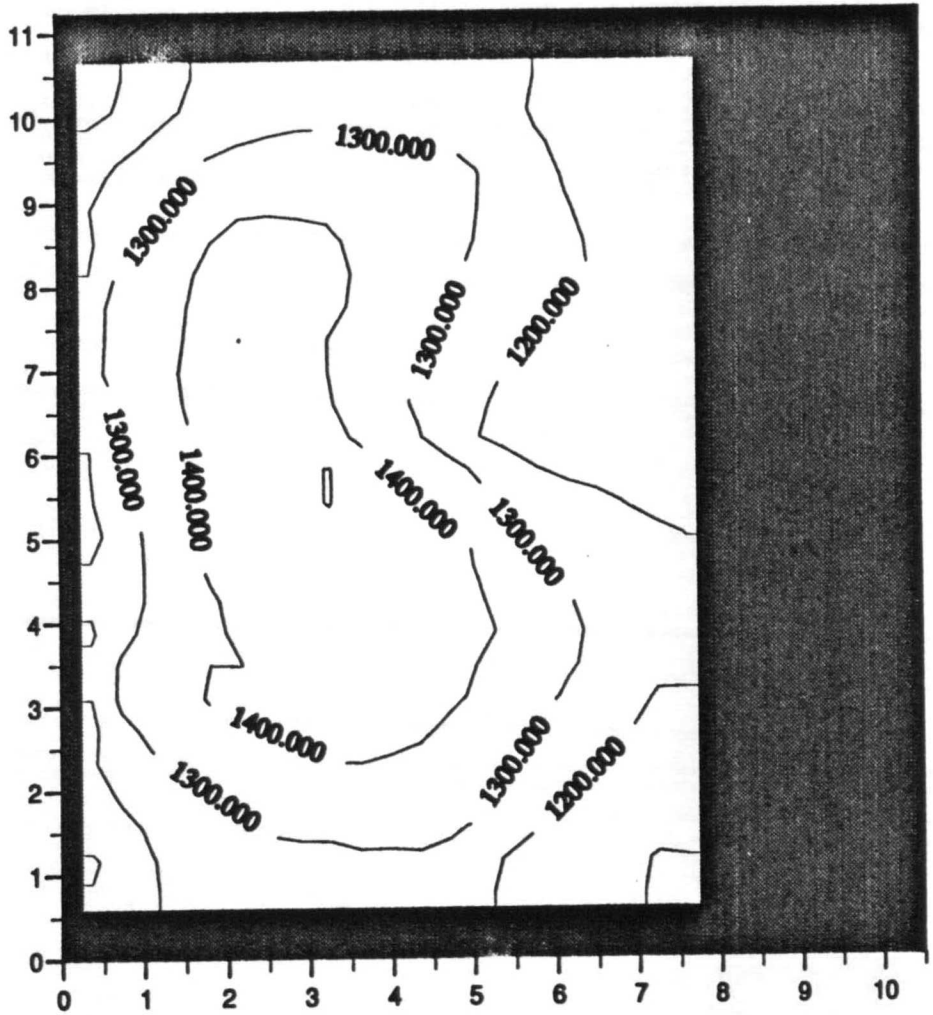


Fig. 5.43 Temperature Contours (^{O}c) For Z = 38 (Oil Combustion)

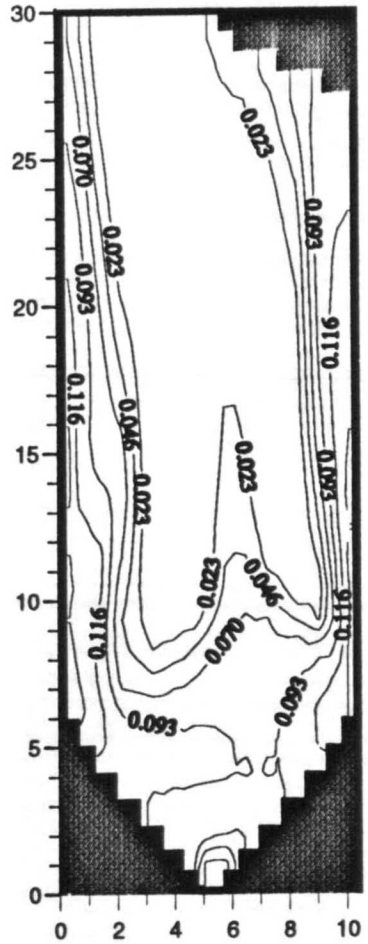


Fig. 5.44

Oxygen Concentration Contours (%) For Y = 1

(Oil Combustion)

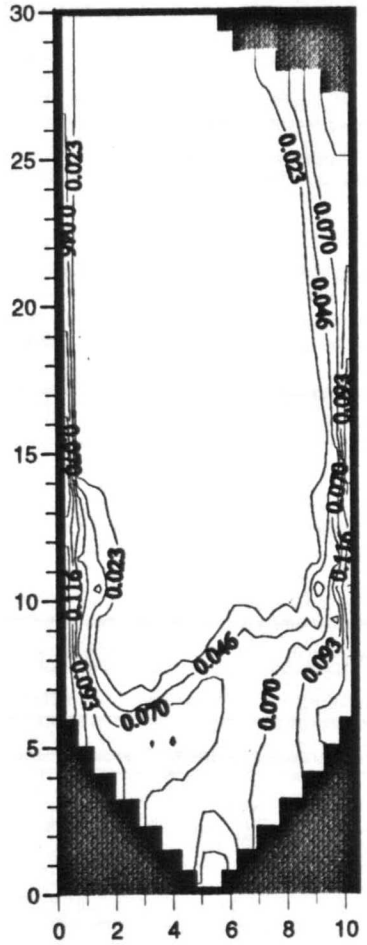


Fig. 5.45

Oxygen Concentration Contours (%) For Y = 3

(Oil Combustion)

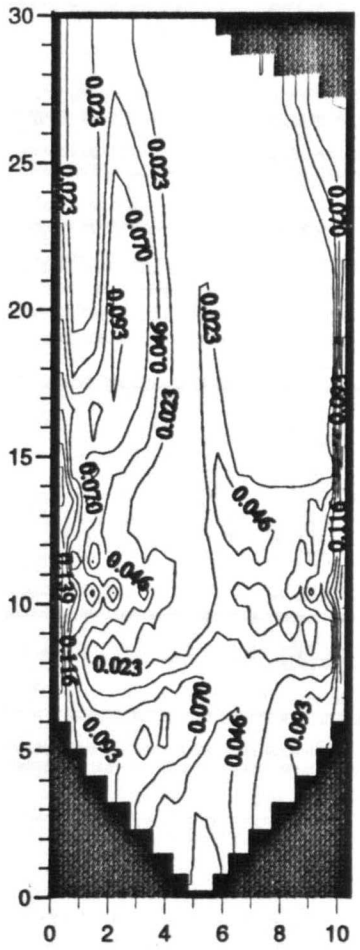


Fig. 5.46

Oxygen Concentration Contours (%) For Y = 6

(Oil Combustion)

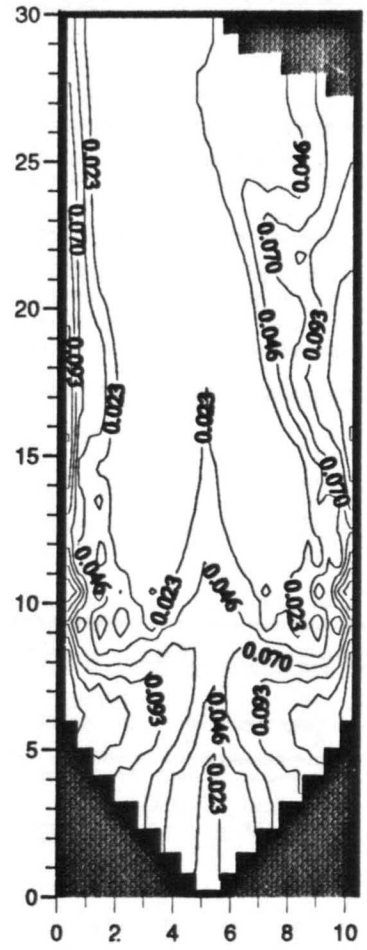


Fig. 5.47

Oxygen Concentration Contours (%) For Y = 8

(Oil Combustion)

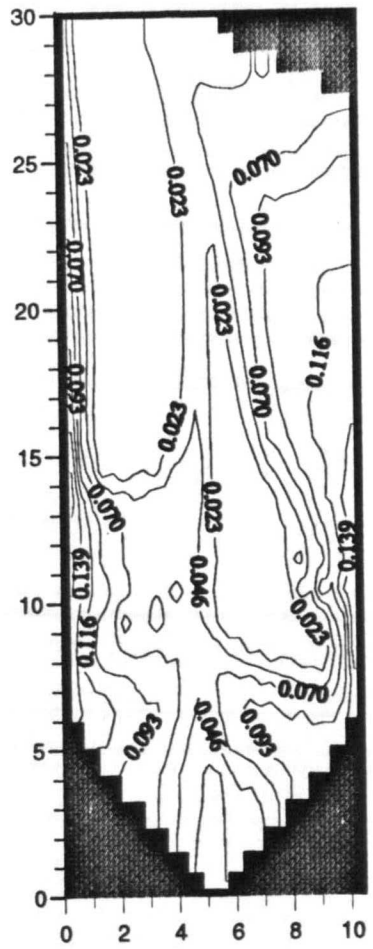


Fig. 5.48

Oxygen Concentration Contours (%) For Y = 10

(Oil Combustion)

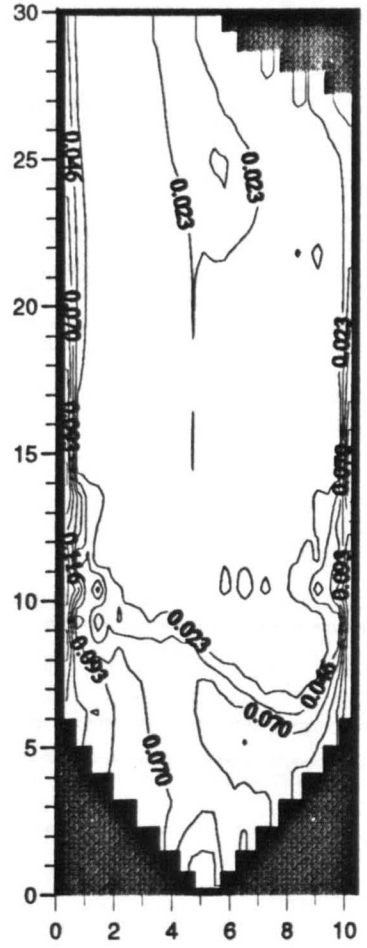


Fig. 5.49

Oxygen Concentration Contours (%) For Y = 12

(Oil Combustion)

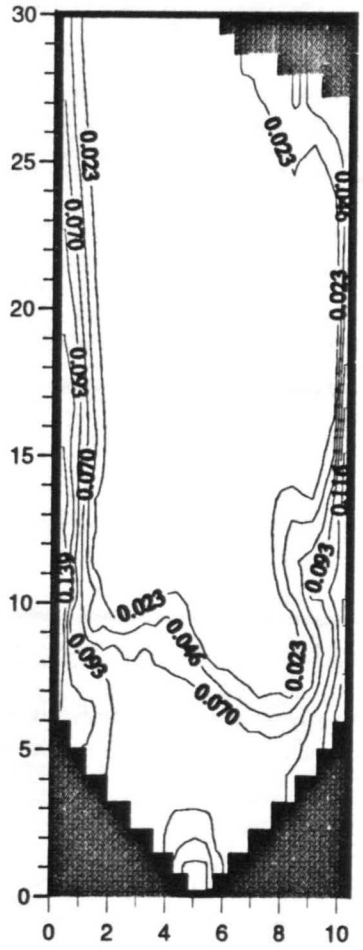


Fig. 5.50

Oxygen Concentration Contours (%) For Y = 16

(Oil Combustion)

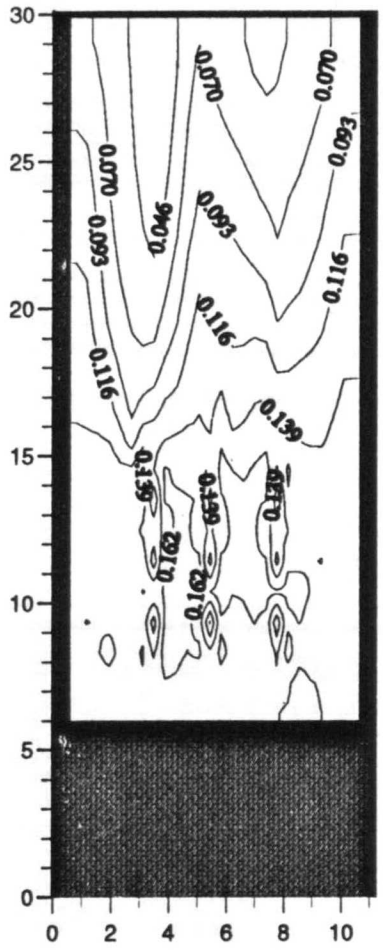


Fig. 5.51

Oxygen Concentration Contours (%) For X = 1

(Oil Combustion)

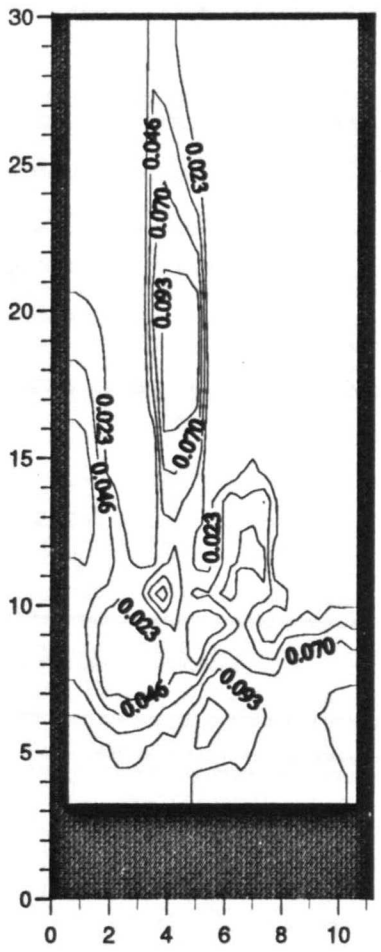


Fig. 5.52

Oxygen Concentration Contours (%) For X = 4

(Oil Combustion)

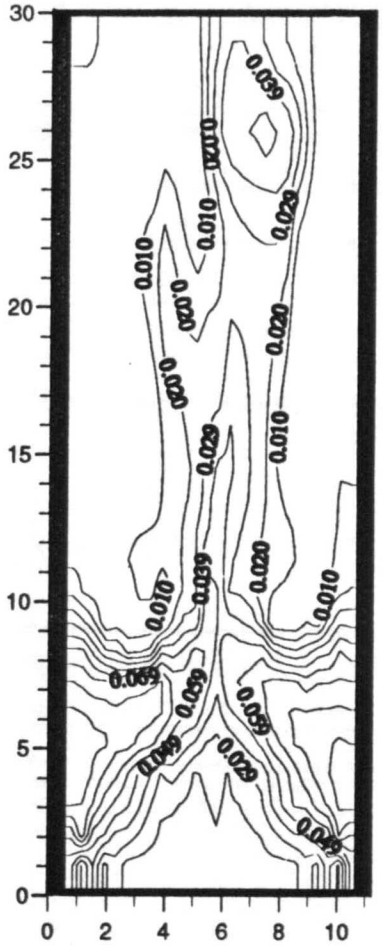


Fig. 5.53

Oxygen Concentration Contours (%) For X = 8

(Oil Combustion)

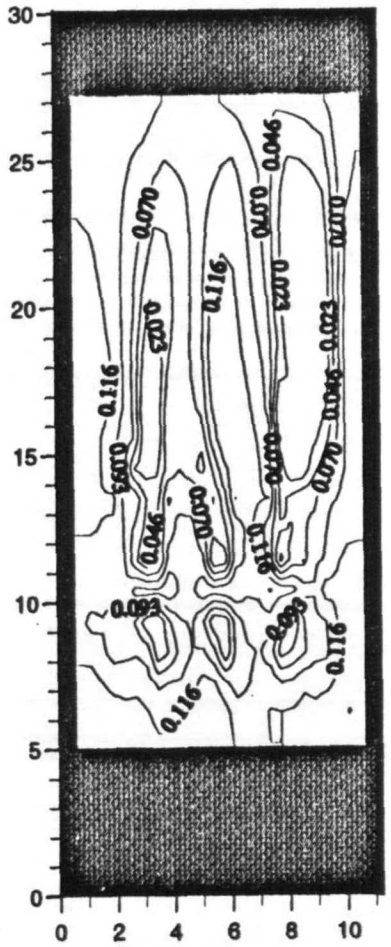


Fig. 5.54
Oxygen Concentration Contours (%) For X = 15
(Oil Combustion)

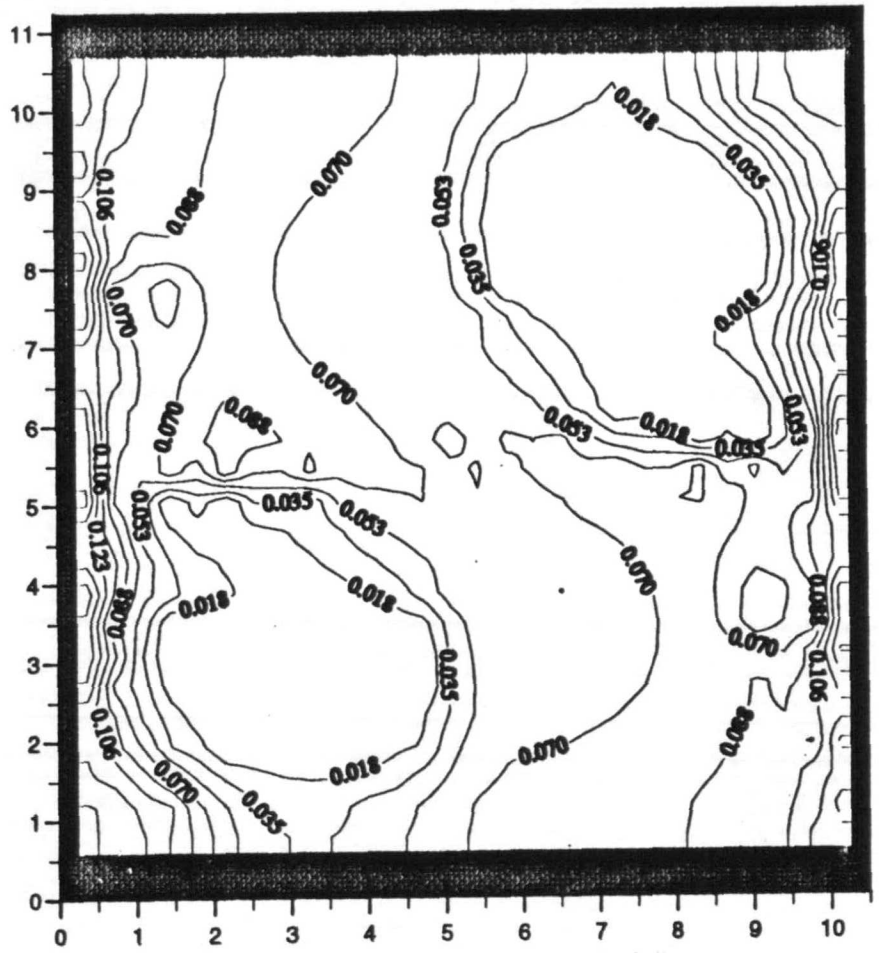
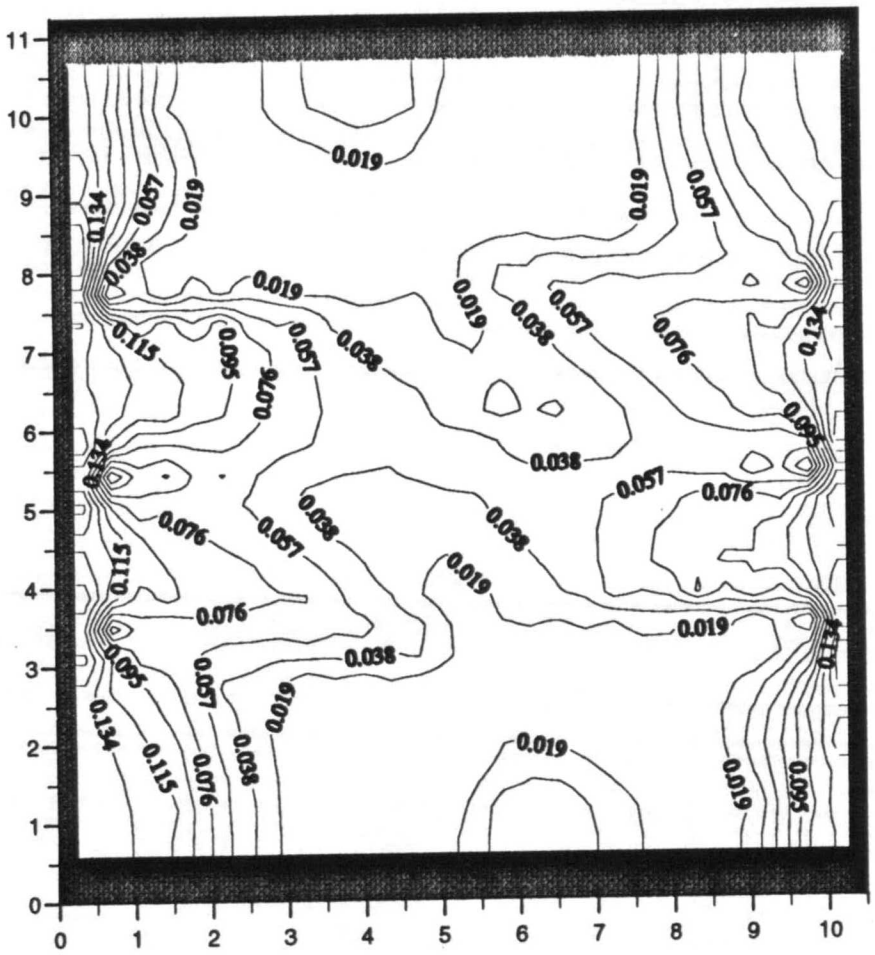


Fig. 5.55 Oxygen Concentration Contours (%) For Z = 10 (Oil Combustion)



5.56 Oxygen Concentration Contours (%) For Z = 16 (Oil Combustion)

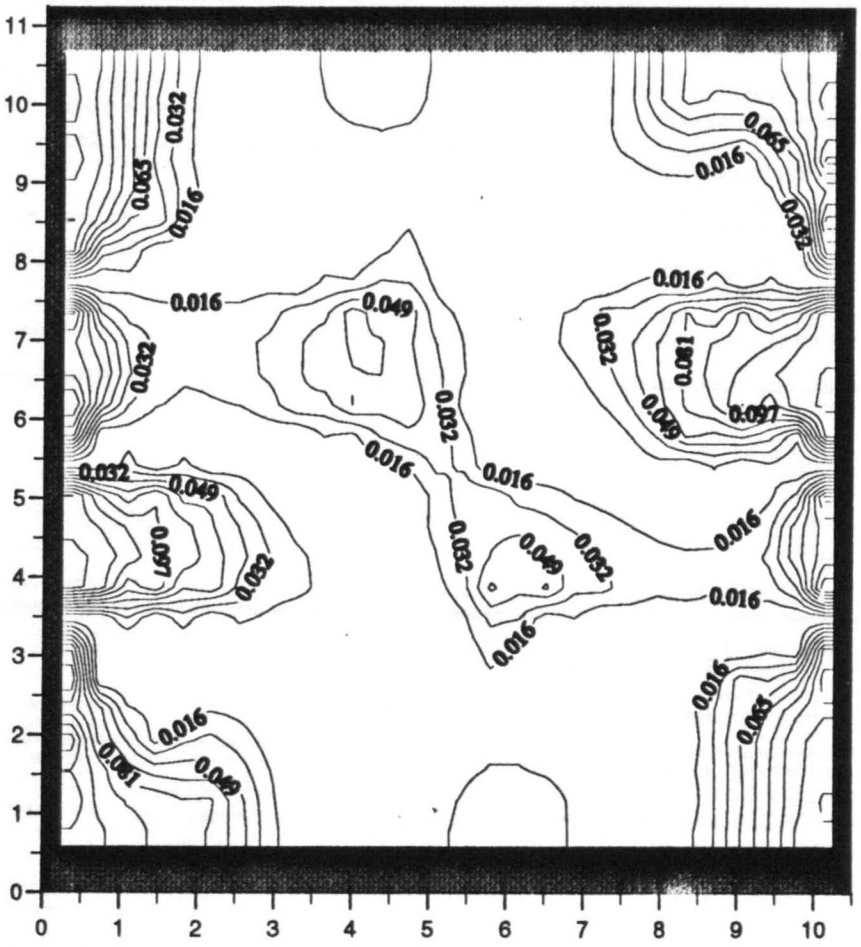


Fig. 5.57 Oxygen Concentration Contours (%) For Z = 22 (Oil Combustion)

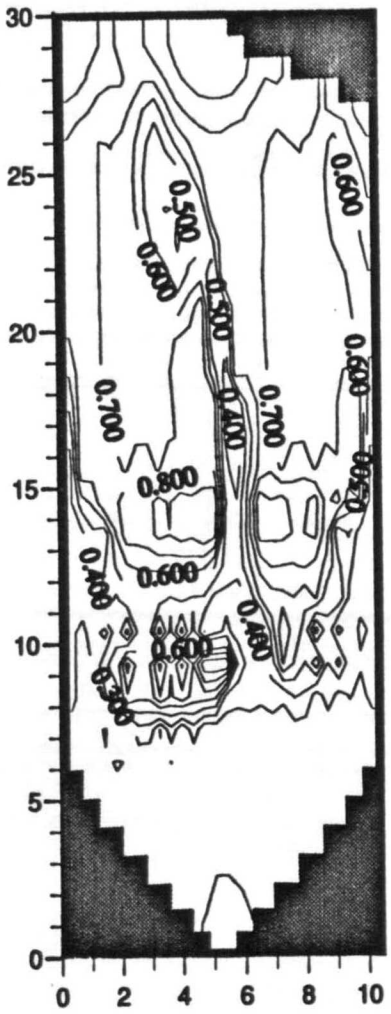


Fig. 5.58

Absorption Coefficient Contours (M^{-1}) For X = 4

(Oil Combustion)

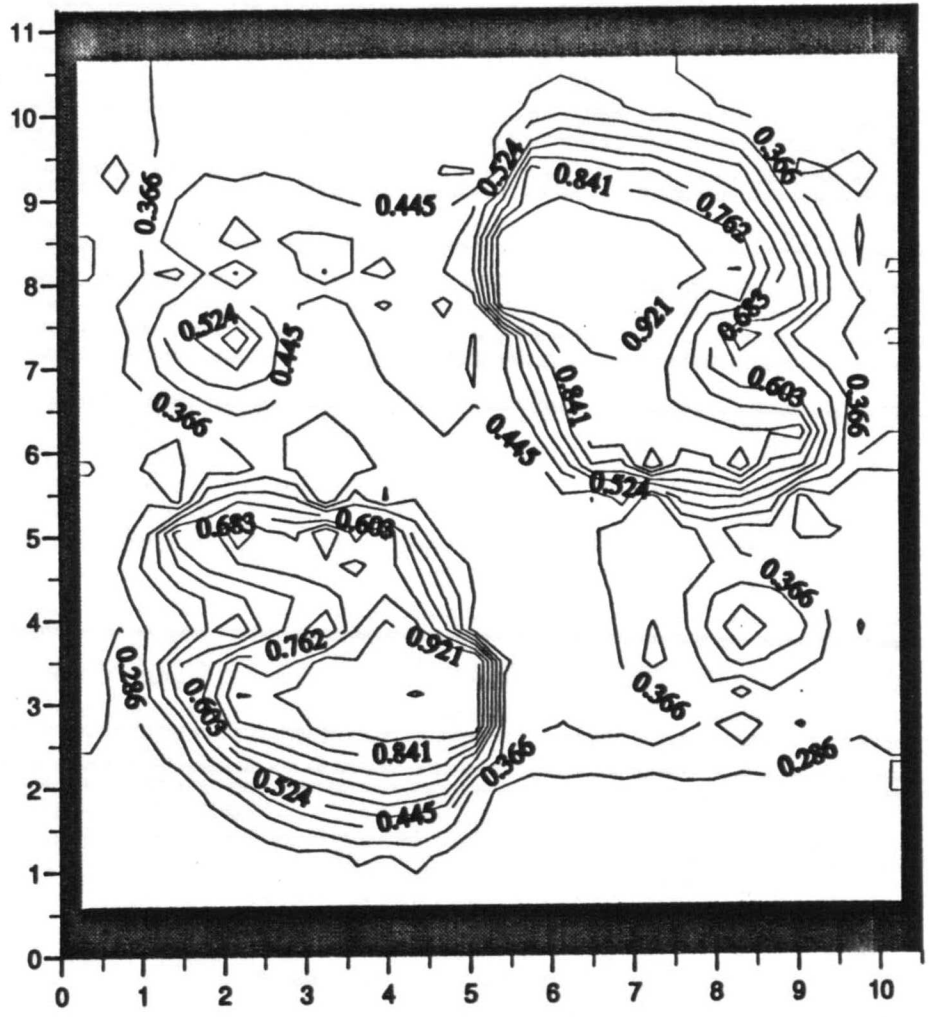


Fig. 5.59 Absorption Coefficient Contours (M^{-1}) For Z = 11 (Oil Combustion)

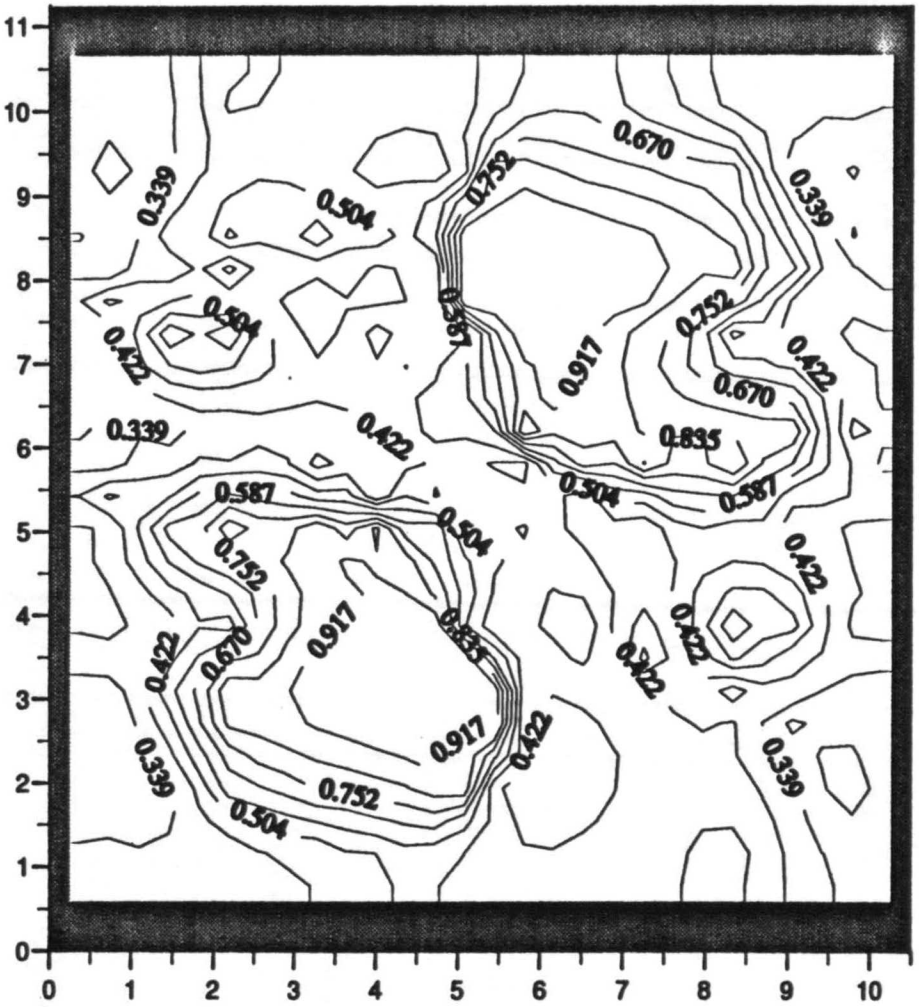


Fig. 5.60 Absorption Coefficient Contours (M^{-1}) For Z = 12 (Oil Combustion)

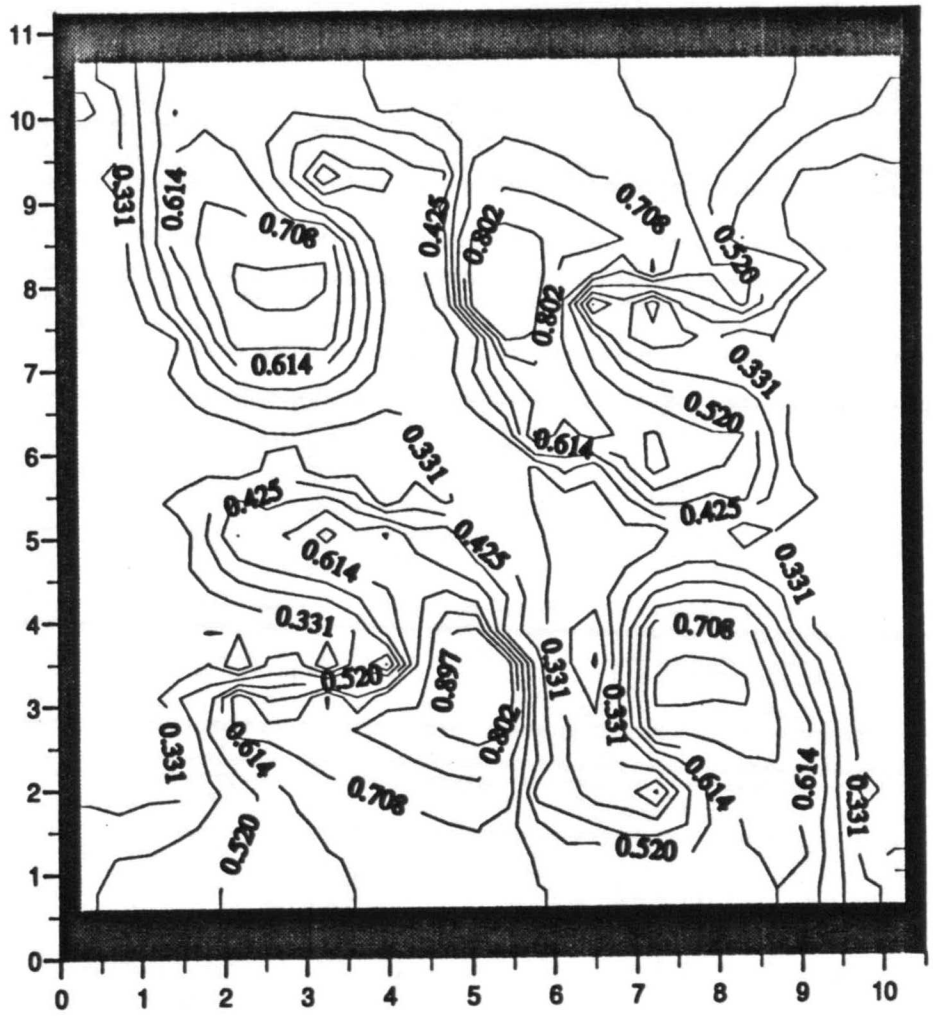


Fig. 5.61 Absorption Coefficient Contours (M^{-1}) For Z = 14 (Oil Combustion)

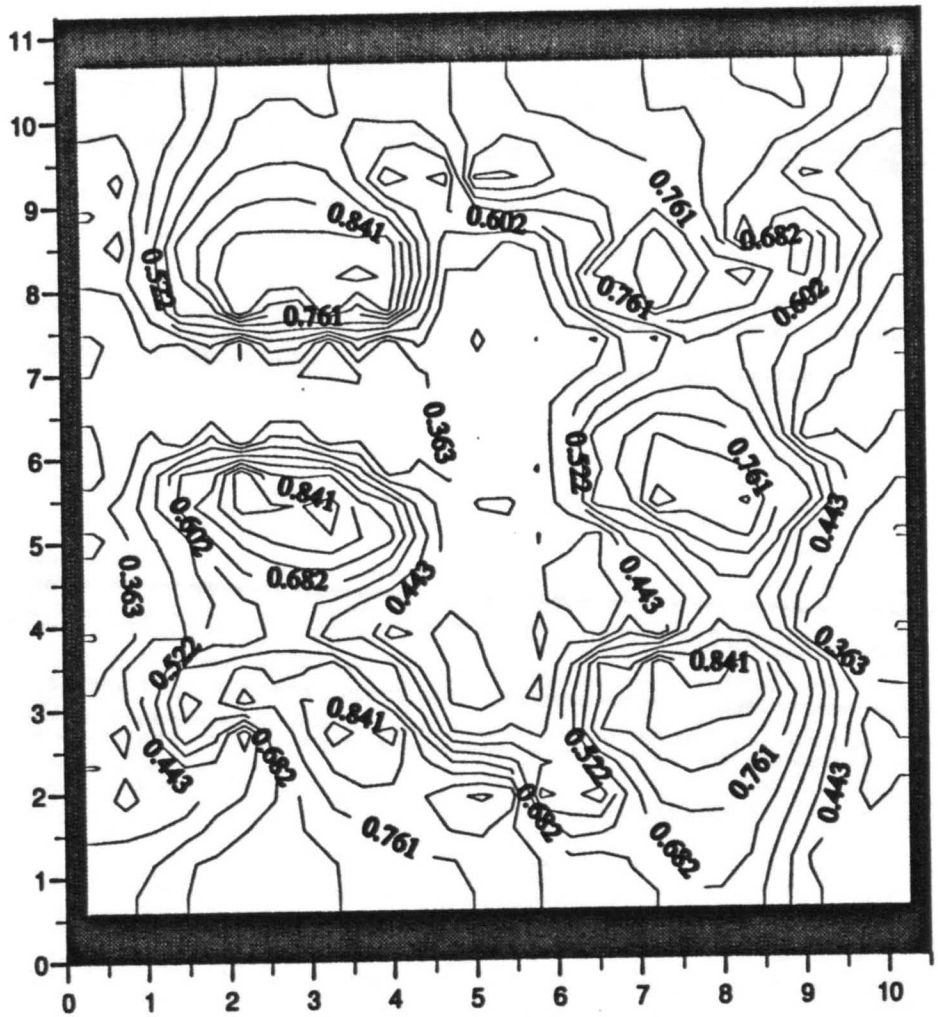


Fig. 5.62 Absorption Coefficient Contours (M^{-1}) For Z = 18 (Oil Combustion)

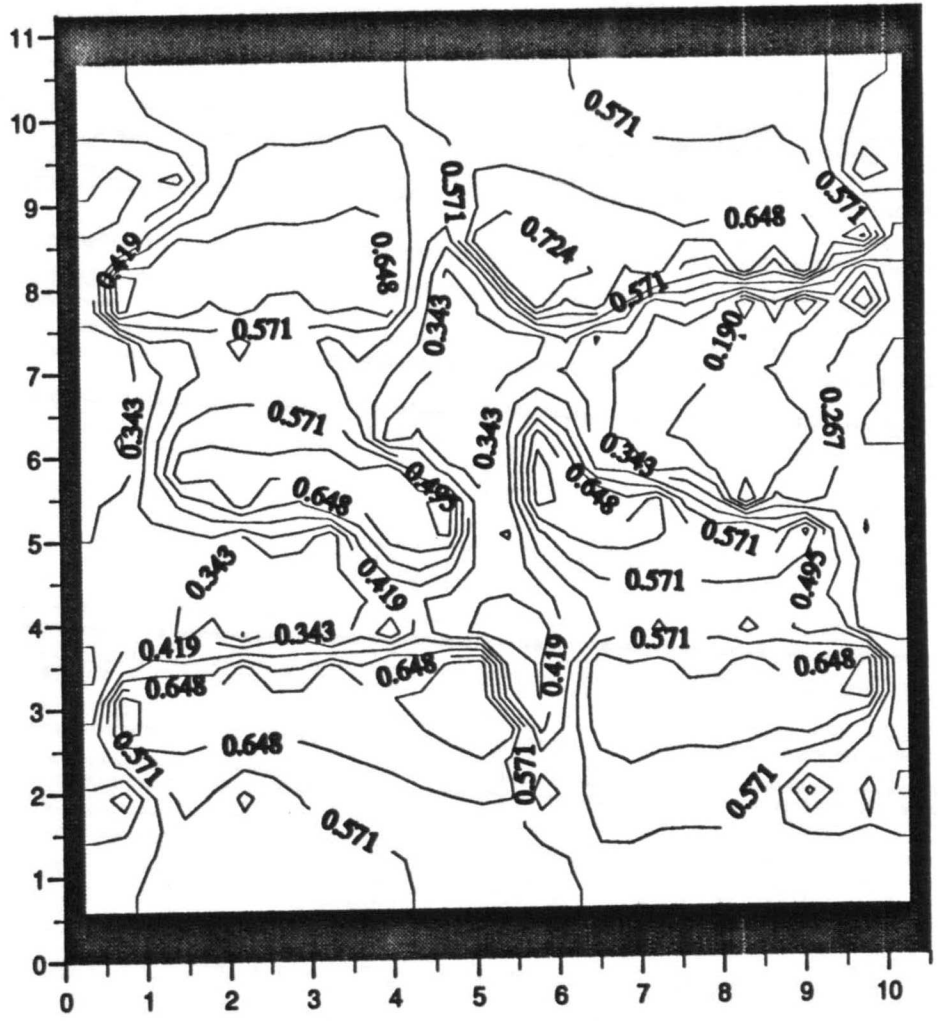


Fig. 5.63 Absorption Coefficient Contours (M^{-1}) For Z = 25 (Oil Combustion)

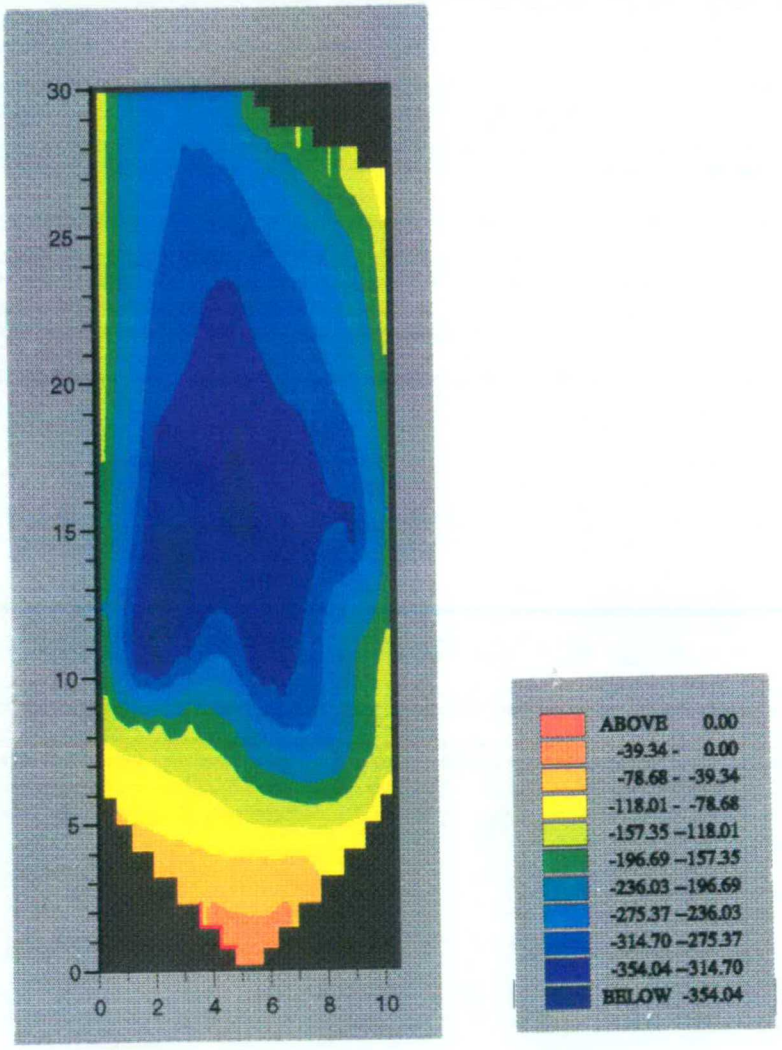


Fig. 5.64 Heat Fluxes To The Lateral Wall (Kw/M^2) (Oil Combustion)

CHAPTER 6

COAL COMBUSTION CALCULATIONS

6.1 Introduction

The simulated furnace serves a 500 MWe (1700 t/h of steam) power production boiler and is designed to operate with coal, whose characteristics are presented in Tables (6.2), (6.3) and (6.4). The dimensions of the combustion chamber are 16.5 x 16.5 x 39.0 m approximately. The furnace is of the opposed-fired type and is equipped with 48 burners arranged in four rows of six burners each at the front and rear walls, see Figs. (6.1) and (6.2). The present calculations pertain to a configuration of the plant producing 500 MWe (89.86% of maximum continuous load) obtained with 36 burners operating. The upper rows of the burners on both the front and rear walls are out of service (BOOS). The description of the furnace geometry used for the numerical simulation is restricted at the combustion chamber up to the height corresponding to the nose. (~39 m height from the bottom of the hopper).

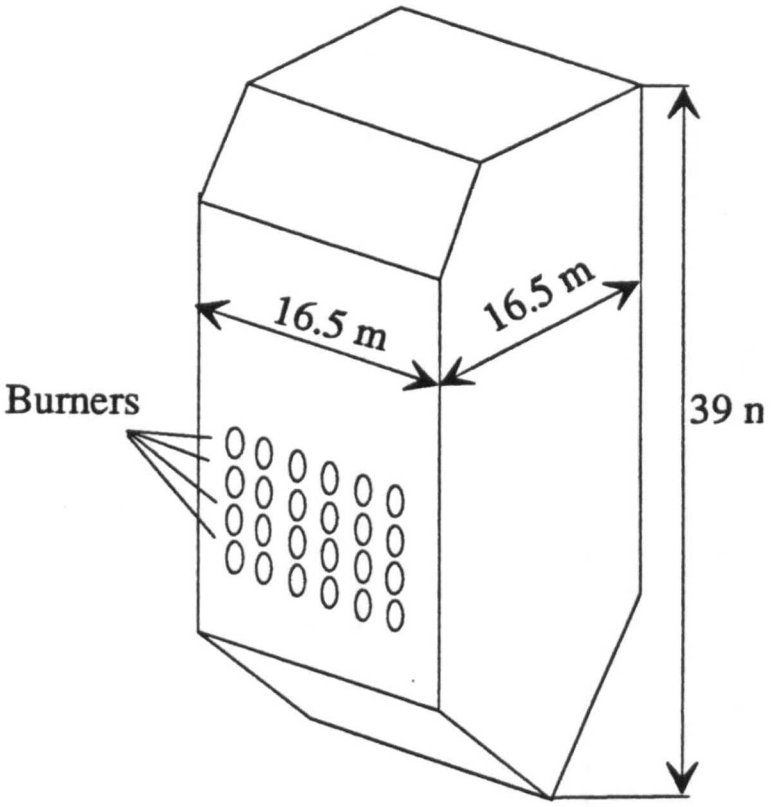


Fig. 6.1 The Coal-Fired Combustion Chamber Geom

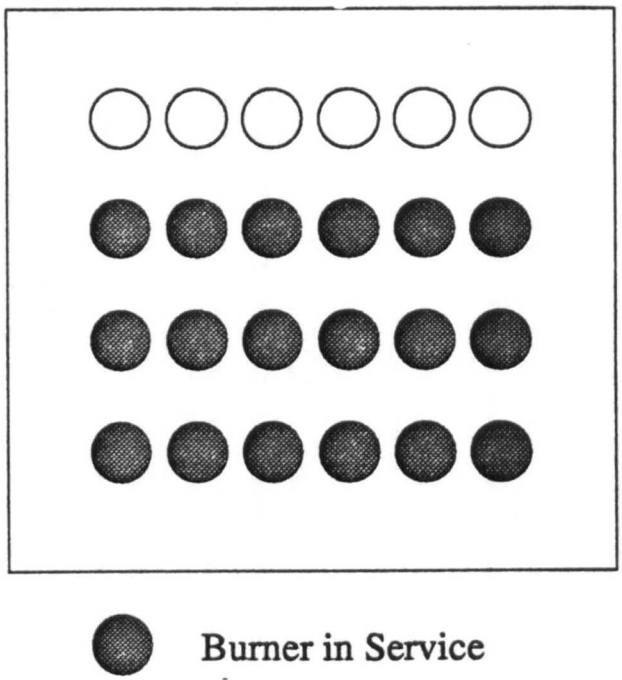


Fig. 6.2 The Arrangement of the Burners

6.2 The Furnace Operating Conditions

The air inflow rate for stipulated excess air at 20% as well as the coal flow rate necessary to guarantee the required thermal load are summarised in Table 6.1.

Power Production	500 MWe (1700t/h Steam)
Coal Mass Inflow Rate	100.72 kg/s total or 2.79 kg/s per burner
Stoichiometric Requirements	4.301 kg air/kg PF
Excess Air	20%
Total Air Inflow Rate	519.85kg/s total or 14.44kg/s per burner

Table 6.1. The Operating Conditions

6.3 The Coal Characteristics

For the following simulation the Indian Design Coal has been used, the composition of which, in terms if proximate and ultimate analysis, is given in Tables (6.2) and (6.3) as mass fractions of the original coal mass. The calorific values of the coal (gross and net) are presented in Table (6.4).

Volatiles %	Fixed Carbon %	Ash %	Moisture %
16.9	27.5	42.5	13.0

Table 6.2 The Coal Composition. (Proximate Analysis)

Hydrogen H (%)	Carbon C (%)	Oxygen O(%)	Nitrogen N(%)	Sulphur S(%)	Ash (%)	H_2O (%)
1.88	34.82	6.57	0.72	0.41	42.6	13.0

Table 6.3 The Coal Composition (Ultimate Analysis)

Gross Calorific Value	12.615 MJ/kg
Net Calorific Value	13.397 MJ/kg
Coal Particle Density	980 kg/m^3

Table 6.4 The Coal Characteristics

6.4 The Calculation Set-Up

The simulation carried out utilised a calculation grid composed of 25 x 28 x 39 = 27300 volume elements in the three X, Y and Z directions respectively. In Figs. (6.3), (6.4) and (6.5), the X - Z (parallel to the axis of the burners), Y - Z (perpendicular to the

axis of the burners) and X -Y (horizontal) grids are shown. Because a cartesian co-ordinate framework is used the inclined walls constituting the hopper and the nose are represented in a step-wise manner. The burners are represented by one cell each. The dimensions of the cells representing the burners are simulated in order to conserve the mass air inflow rate at each single burner.

For optimising the calculation time and to limit the memory demands a single particle size of 75 μm (obtained as a weight average from the ROSIN - RAMMLER diagram) is considered to represent the particle size distribution. A single particle is injected into the combustion chamber exactly at the centre of each burner.

6.5 Computational Details

The computations for this case have been performed on a DecStation 5000/240 series computer with 64Mbyte RAM memory. It required 9650 iterations to convergence. The radiation calculation procedure, which is more memory and CPU time consuming was called every 10 iterations. The average time per iteration was around 50sec when the radiation was not called and around 5min when radiation calculations were performed.

6.6 Results And Discussion

The results presented refer to the vertical X - Z and Y - Z which are parallel and perpendicular to the burners axes respectively and to the horizontal X - Y planes. The particular planes shown are presented in Tables (6.5 - 7)

Y = 2	Plane close to the right wall
Y = 8	Plane between the first and second column of burners
Y = 12	Plane after the third column of burners
Y = 16 and 20	Plane on the fourth and fifth column of burners
Y = 27	Plane close to the left wall

Table 6.5 The X - Z Visualisation Planes (Coal Combustion)

X = 2	Plane near the front wall
X = 6, 10 and 15	Intermediate planes
X = 24	Plane near the rear wall

Table 6.6 The Y -Z Visualisation Planes (Coal Combustion)

Z = 7	Hopper Region
Z = 18	Plane through the centre of the second row of burners
Z = 30	Plane below the 'nose'
Z = 38	Plane near the exit of the furnace ('nose' region)

Table 6.7 The X - Y Visualisation Planes (Coal Combustion)

6.6.1 The Flow Field

The velocity field is highly three-dimensional and very complex and its interpretation through 2-d graphs is extremely difficult. Although the calculation grid used in the near burner region is not very fine (due to computer limitations), the results obtained are encouraging.

In Fig.(6.6 -11) (Y = constant) it appears that the presence of the nose induces an asymmetry in the flow field in the vertical direction that influences directly the behaviour of the air flux that comes in from the burners as well as the particle trajectories. This imposes a regime of asymmetry even in the hopper zone; this is much more evident as we shift from the side walls to the centre of the boiler. This conclusion is reinforced by the fact that during the initial part of the study of this furnace (modelling with gaseous fuel maintaining the same thermal load with this analysis) utilising a much finer grid with 16 cells per burner the same flow pattern was predicted Fig. (6.12) and (6.13).

Moreover, there exists a broad zone of recirculation between the second and the third horizontal rows of burners.

As we travel along the Y - axis the flow field seems fairly symmetric as expected.

Figs. (6.14 - 18) (X = constant) show that , in the direction parallel to the axes of the burners, the incoming air maintains its momentum initially to be split finally in two motions (one ascending in the direction of the outlet, the other descending in the direction of the hopper) in the proximity of the middle of the combustion chamber.

In Figs. (6.19 -22) the projection of the flow field in the X - Y planes is illustrated. The asymmetry mentioned earlier is apparent even within the hopper region where the down - going flow can be observed to be shifted towards the rear wall of the furnace. Even at the level of the second row of burners the flow pattern is consistently maintained.

6.6.2 The Particle Trajectories

It can be seen in Figs. (6.23 and 24) that the particles emerging from the bottom row of the front wall burners end up in the hopper following the prevailing gas field whereas the particles from the rear wall exit the furnace through the outlet. The particles are here traced even after they have fully burnt out, which means that the final portions of the trajectories shown represent ash particles.

The coal particles release their volatiles in one step within the first cell of the calculation domain after a flight time of 30.5 ms. This happens because the devolatilsation process is a relatively fast process for the prevailing temperatures and heating rates within this industrial combustion chamber and also because the grid is coarse relative to the near burner phenomena.

For the char reaction, which is a much slower one, the time required to complete combustion is much higher. Typical times calculated for particles emerging from the front wall burners is of the order of 250 to 300 ms. The particle burnout against the residence time is depicted in Fig. 6.25.

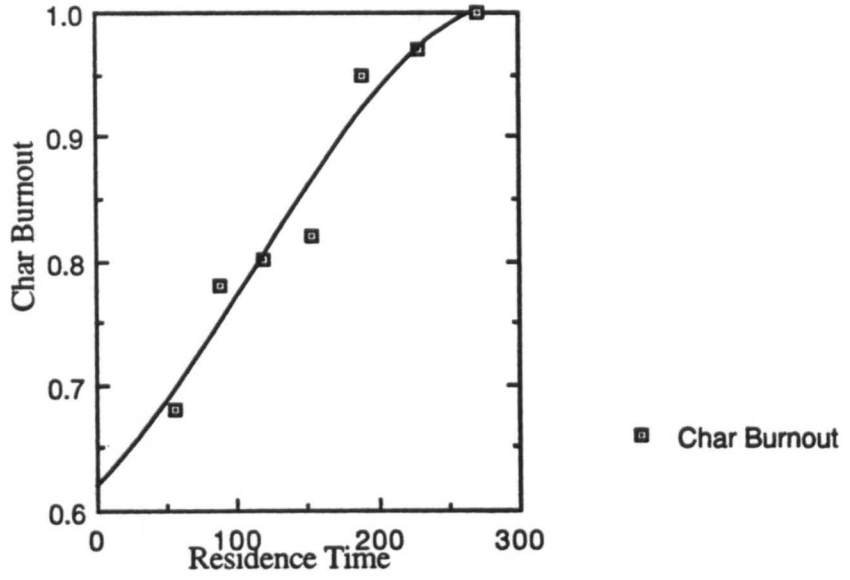


Fig. 6.25 Char Burnout Against Residence Time for a Front Wall Burner in the Bottom Row

A full burnout of 100% has been predicted. The mass balance for the particulate phase was calculated and is presented in Table (6.8):

Incoming Mass	**101 kg/s**	**100%**
Ash Mass Exiting the Chamber	**29.8 kg/s**	**29.58%**
Burnt Mass	**57.8 kg/s**	**57.4%**
Ash Mass Sticking on the Walls	**13.1 kg/s**	**13.02%**

Table 6.8 The Overall Mass Balance for the Particulate Phase

6.6.3 The Temperature and Oxygen Concentration Fields.

Figs. (6.26 - 39) show the temperature field expressed in degrees Celsius. Figs. (6-40 -48) depict the predicted oxygen concentration profiles in terms of mass fraction contours.

In Figs. (6.26 -32) the temperature profiles in the X - Z planes are shown. It can be seen here that there is a hot spot near the centre and upper part of the furnace. This can be attributed to the asymmetry observed in the flow field which results in higher particle concentrations in this region as well as better mixing in the near the front wall regions than that in the rear wall. This has as a result that in the near burner region of the rear wall the combustion is delayed causing lower temperatures than those near the front wall. As can be observed from Figs. (6.26 and 6.32) the profiles near the side walls are fairly symmetric, which is consistent with the predicted flow field symmetry.

The oxygen concentration profiles, Figs. (6.40 - 45), are consistent with the predicted temperature field. The aforementioned region of high temperatures at the centre and upper part of the furnace is represented here as a lean oxygen region of concentrations below 4%, Figs. (6.41 - 44). This region extends to the rear wall of the hopper where the particles from the first row of the front wall burners end up and where temperatures higher than those prevailing near the front wall are encountered. This indicates that more complete combustion is taking place in these regions. The oxygen level close to the rear wall burners is higher than that of the region near the front wall burners. This indicates the delayed combustion in the former region as already indicated by the temperature levels in the same region. The oxygen concentrations near the side walls, Figs. (6.40 and 45) are low (about 4-7%) due to the horizontal recirculation of the hot combustion gases.

In Figs. (6.33 -38) the temperature profiles in the Y - Z planes are depicted. As one travels along the X - axis, again the hot region near the central planes and in the upper part of the furnace is encountered. From Figs. (6.33 and 35) the delay of the combustion near the rear wall can be observed. Figs. (6.46 - 50) reinforce this conclusion showing higher oxygen concentrations near the rear wall burners rather than the front wall ones.

Because the temperature and oxygen concentration profiles in the hopper and 'nose' regions are relatively flat, only one horizontal profile (X - Y plane) of the distribution of each of these parameters have been introduced herein. They are shown in Figs (6.39) and (6.51) respectively for Z = 18 which is the plane passing through the centre of the second row of burners. The asymmetry and the delay of combustion is quite apparent in these profiles.

The fact that in the near burner region of the rear wall the temperature seems rather uniform and relatively low can be attributed to the asymmetry of the flow resulting in lower mixing conditions near the rear wall. The mean exit temperature is about 1300 ^{o}C.

One general comment here is that the temperature and oxygen profiles are not very smooth in the near burner region (NBR). This may be attributed to two reasons:

1. The spatial resolution in the burner zone is not high enough to account for the phenomena taking place in the NBR.

2. Only one size of particles per burner has been tracked with the result that the mean trajectories predicted do not provide a detailed distribution of the fuel in the near burner region. In addition to this, the turbulent dispersion of the particles is not modelled which augments the inaccuracies in the prediction of the near burner aerodynamics and combustion phenomena.

6.6.4 Wall Heat Fluxes

The distribution of the heat flux to the right side wall is shown in Fig. (6.52). The negative sign in the values designates that the net heat fluxes are outgoing It can be seen that the largest values of the heat flux (above 350 KW/m^2) occur again in the upper region of the furnace, shifted towards the front wall, which is consistent with the predicted flow patterns and temperature fields. The heat transfer in the hopper region is relatively small but not insignificant. They are up to 100% higher in the rear part following the flow and temperature patterns. There are no experimental data with which the predictions can be compared. All that can be said with certitude is that the magnitudes of the predicted values are consistent with power station experience, see for example Dolezal (1967).

6.7 Conclusions

1. The asymmetry along planes parallel to the axes of the burners is attributed to the presence of the nose. This results in delayed mixing and combustion for the rear wall burner flows. The particles injected from the bottom row of front wall burners end up to the rear part of the hopper resulting in higher temperatures and reducing oxygen conditions in that region. This could have an effect on the ash deposition as well as raising corrosion problems.

2. The fields along the planes perpendicular to the axes of burners are fairly symmetric as expected.

3. The heat fluxes to the side walls are consistent with the predicted temperature profiles, being higher at the level where higher temperatures are encountered. Their magnitude is within the range of values typically expected according to the experience of boiler operators.

4. The high oxygen concentrations encountered close to the rear wall burners might result in high fuel NO formation in that region. A more detailed, however, simulation of the burner geometry and operating conditions would be needed to assess the impact of this asymmetry on the emission levels.

5. A higher grid resolution in the near burners region is needed in order to simulate more accurately the mixing and combustion processes in that region. With the current capacity and capabilities of modern computers, this necessitates the development and use of local grid refinement techniques. In addition to this, the cylindrical geometry of the burners should be modelled. This could involve body fitted co-ordinate (BFC) treatment but they are not very convenient for this type of combustor and have proved unstable for two-phase flows. Alternatively, a combination of a LGR technique and unstructured tetrahedral meshes is more likely to provide a solution to this problem.

6. More than one size of particles per burner need to be tracked, permitting the computer limitations. Furthermore, the turbulent dispersion of the coal particles should be modelled. At present only the mean trajectories of the particles are predicted. A combination of these elaborations will result in more dispersed particle trajectories with a twofold effect: a) a better distribution of the sources introduced into the gas phase equations so increasing the numerical stability, and b) smoother temperature profiles and more realistic representation of the flames. Additionally, this can assist future work in ash deposition modelling.

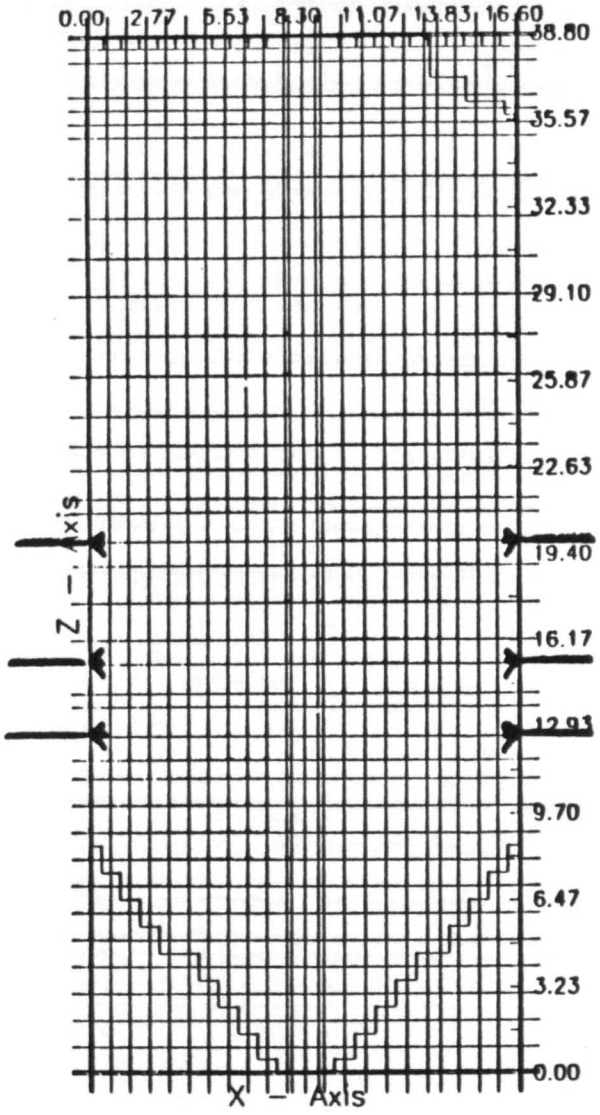


Fig. 6.3 The X-Z numerical grid (Coal Combustion)

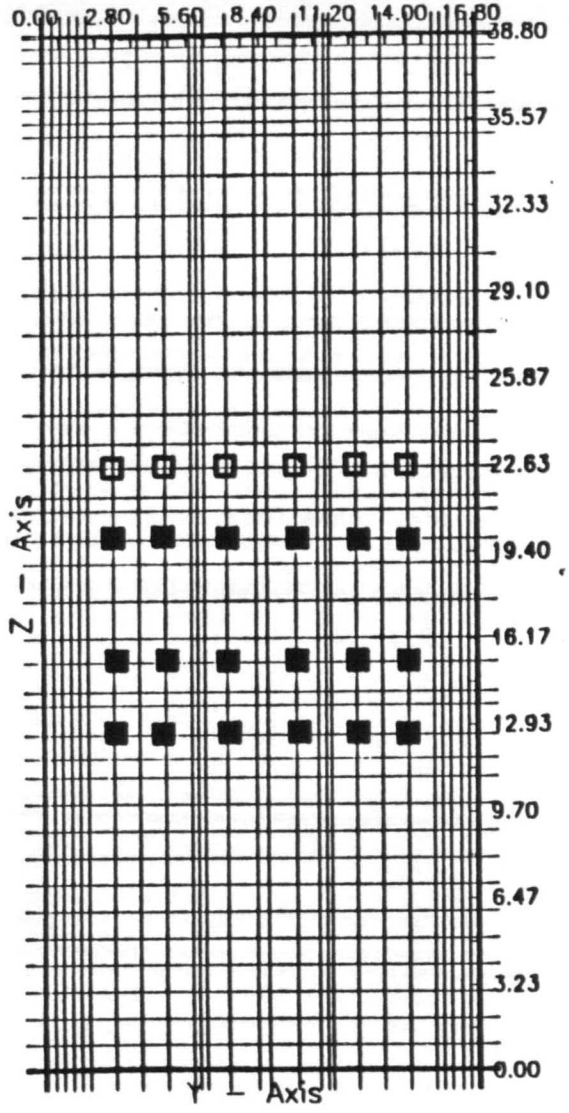


Fig. 6.4 The Y-Z numerical grid (Coal Combustion)

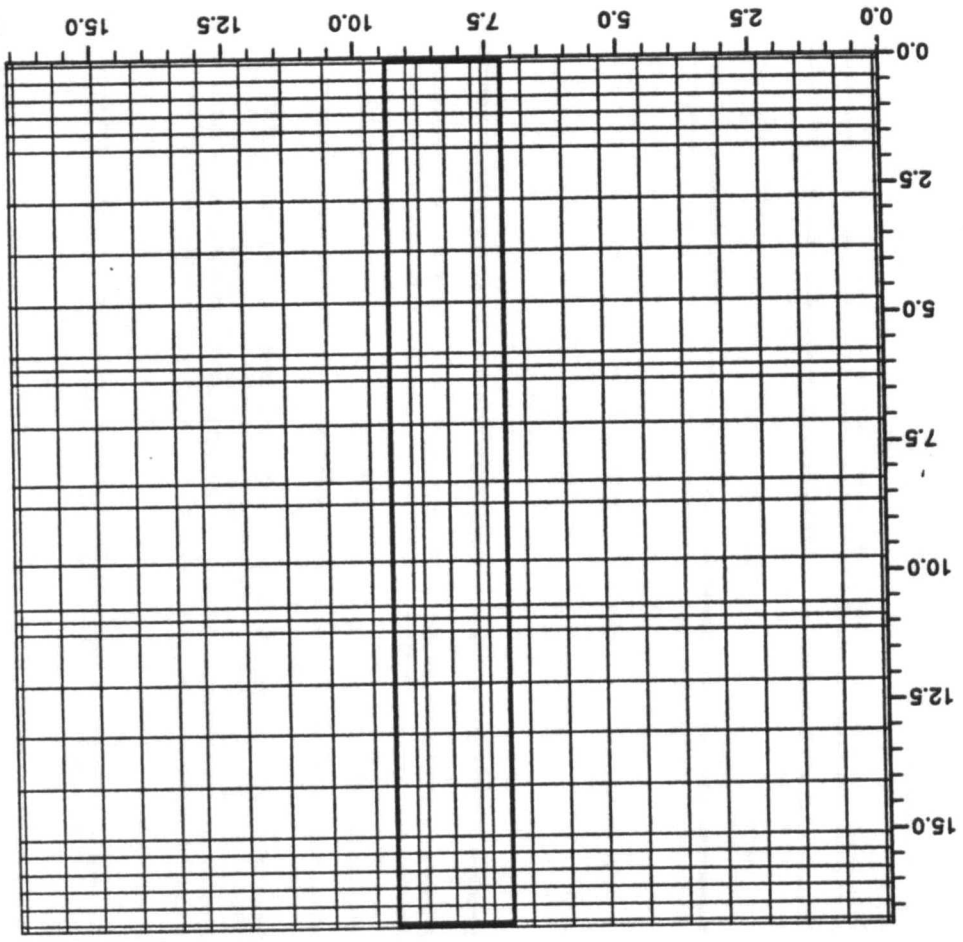


Fig. 6.5 The X-Y numerical grid (Coal Combustion)

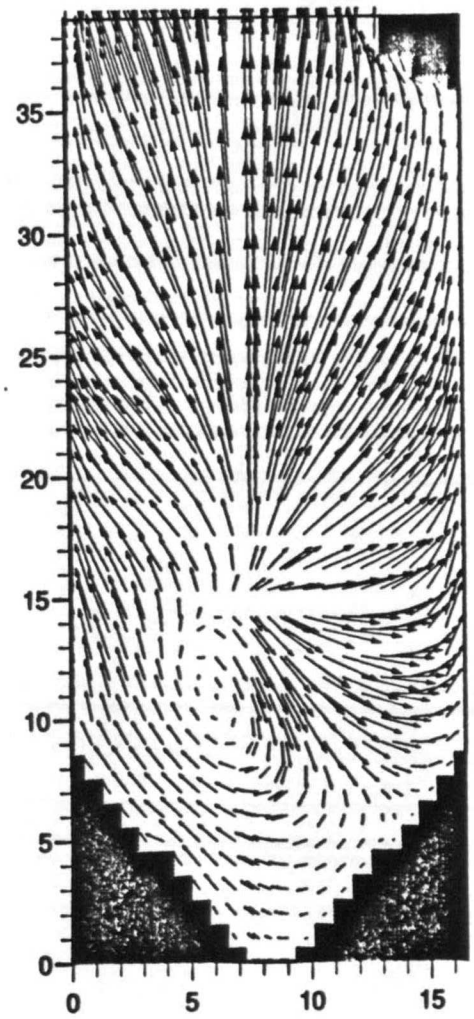


Fig. 6.6 Velocity Vectors for Y = 2 (Coal Combustion)

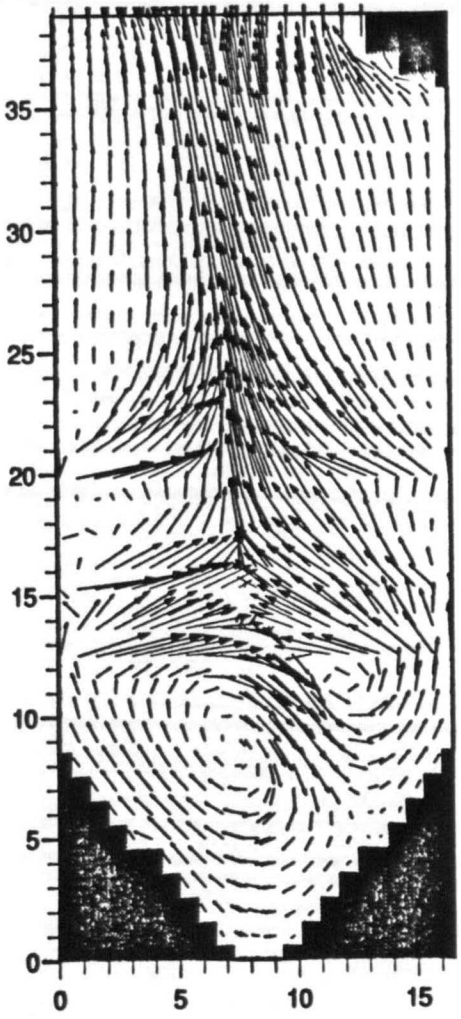


Fig. 6.7 Velocity Vectors for Y = 8 (Coal Combustion)

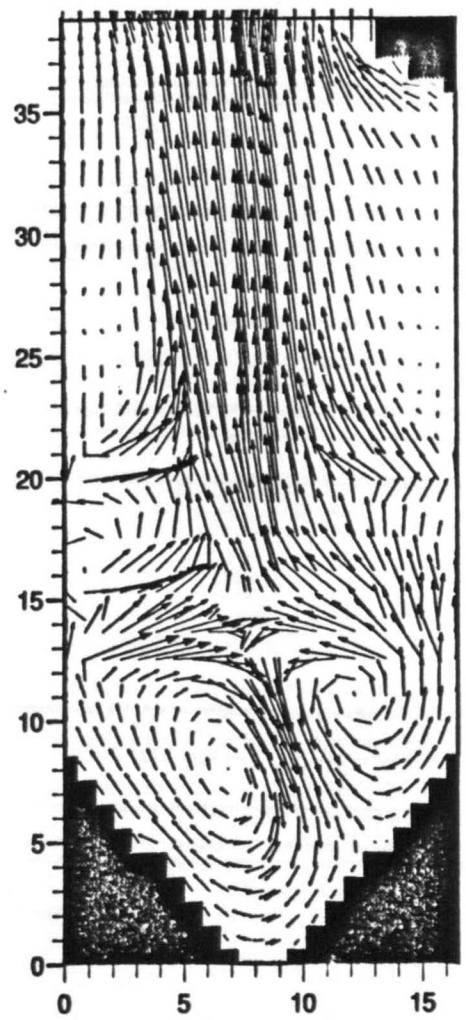


Fig. 6.8 Velocity Vectors for Y = 12 (Coal Combustion)

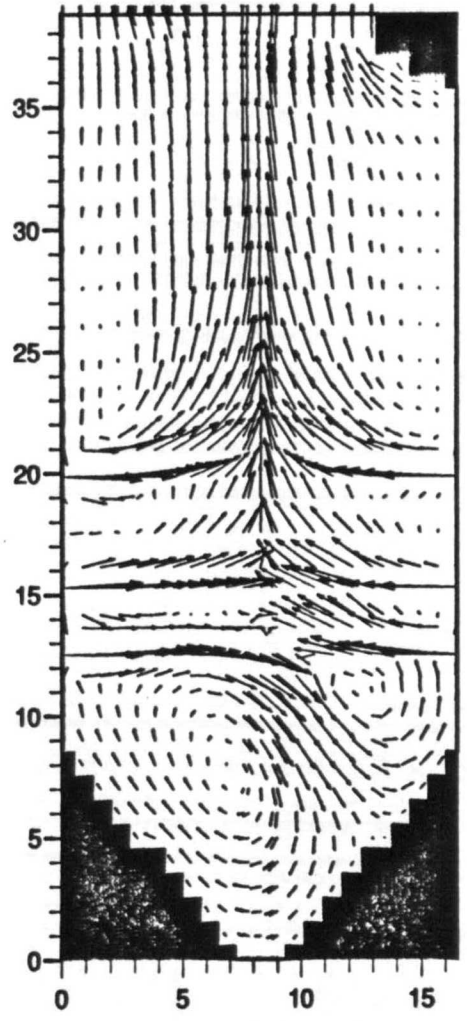


Fig. 6.9 Velocity Vectors for Y = 16 (Coal Combustion)

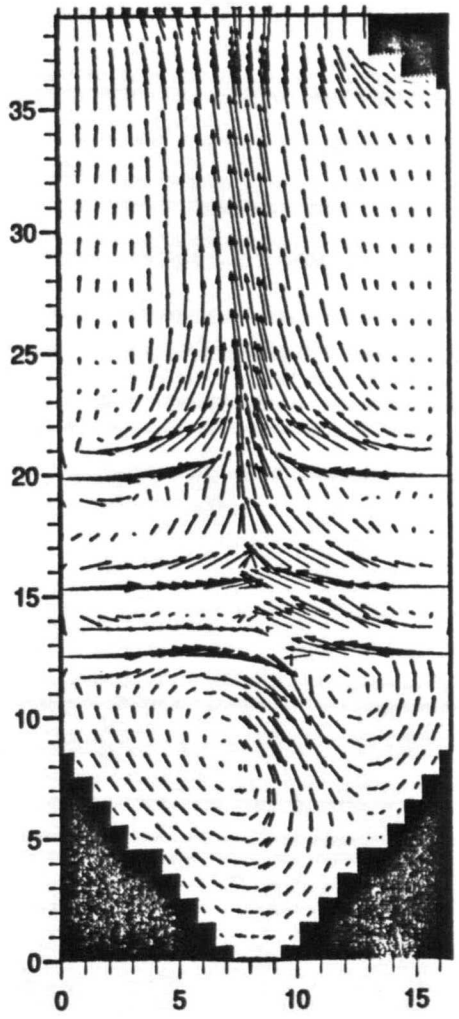


Fig. 6.10 Velocity Vectors for Y = 20 (Coal Combustion)

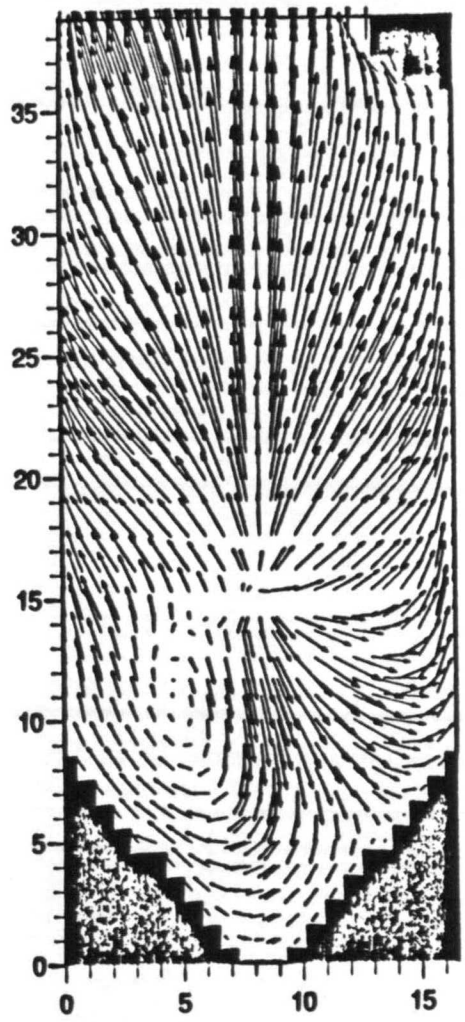


Fig. 6.11 Velocity Vectors for Y = 27 (Coal Combustion)

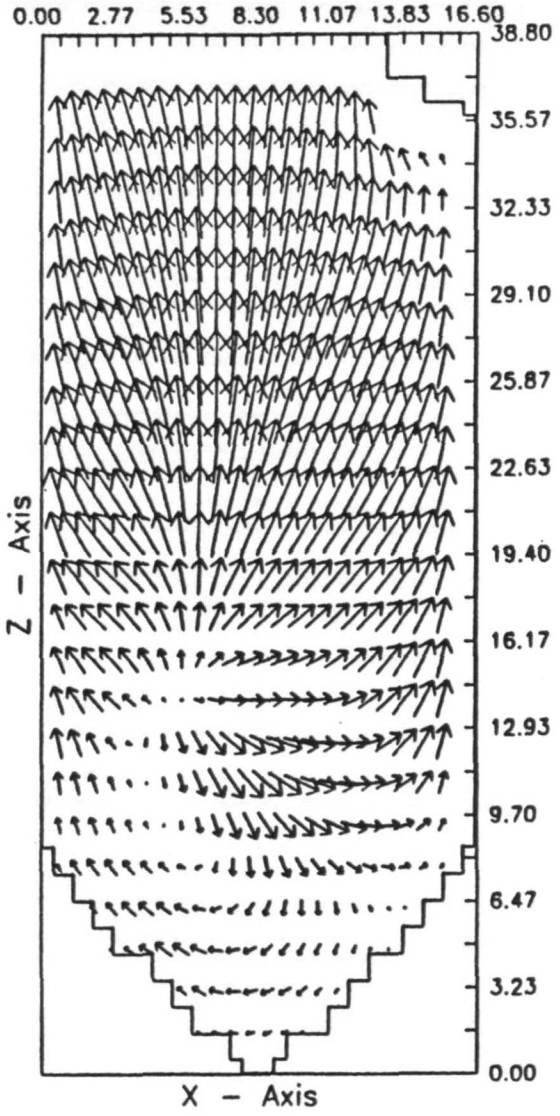


Fig. 6.12 Velocity Vectors for Y = 1 (Gas Combustion)

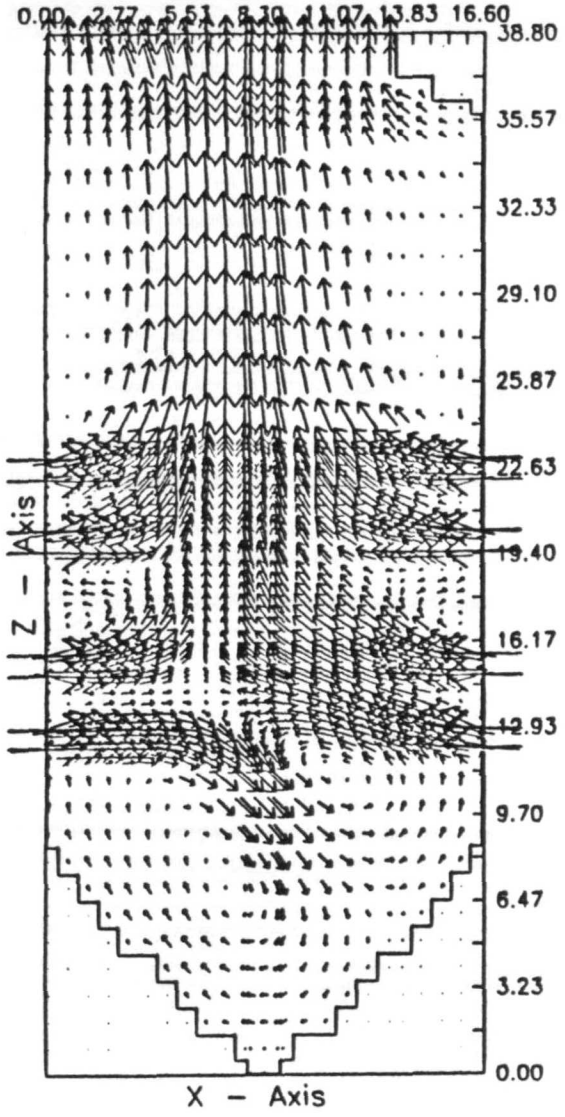


Fig. 6.13 Velocity Vectors for Y = 21 (Gas Combustion)

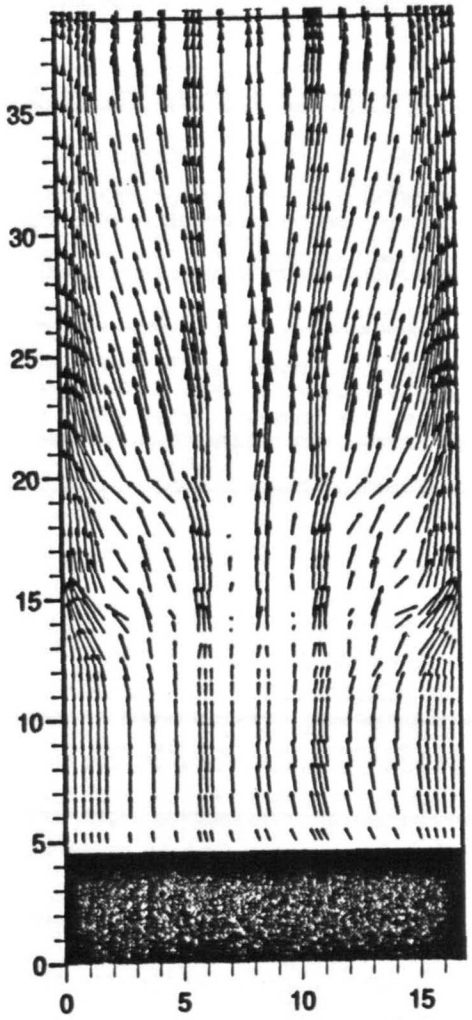


Fig. 6.14 Velocity Vectors for X = 2 (Coal Combustion)

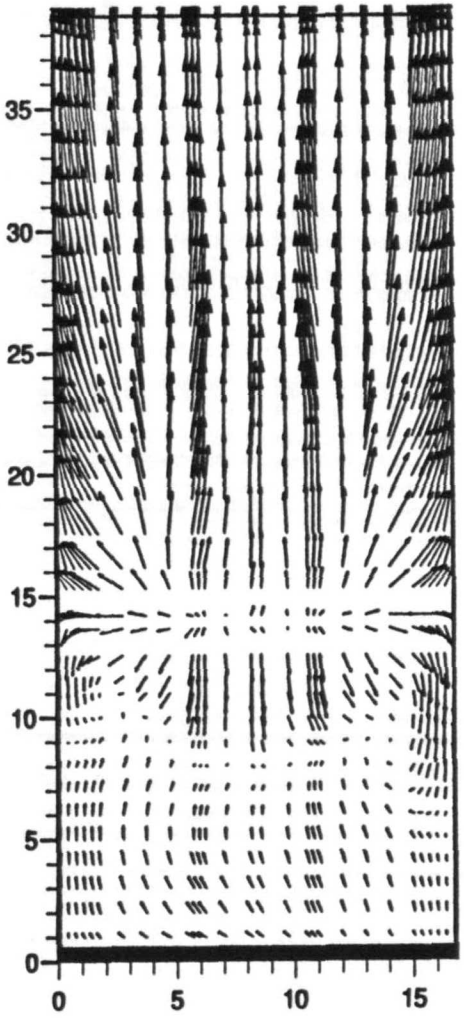


Fig. 6.15 Velocity Vectors for X = 6 (Coal Combustion)

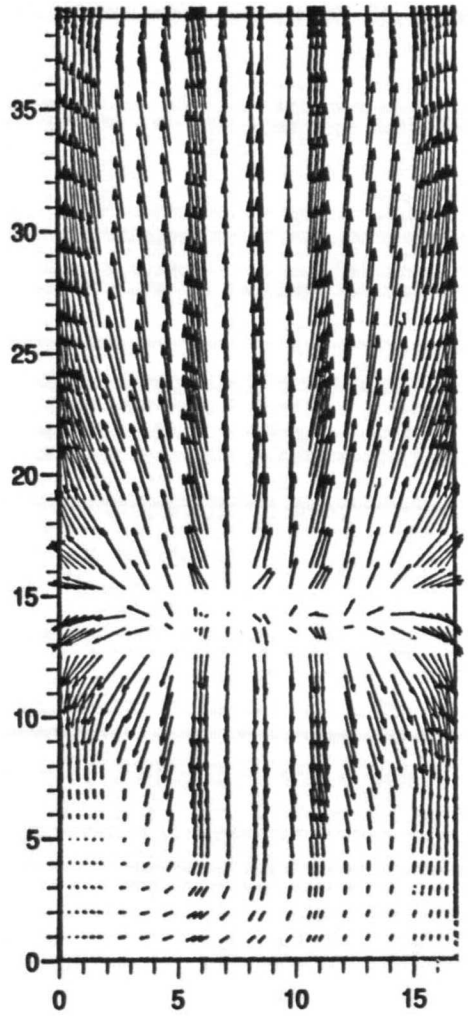


Fig. 6.16 Velocity Vectors for X = 10 (Coal Combustion)

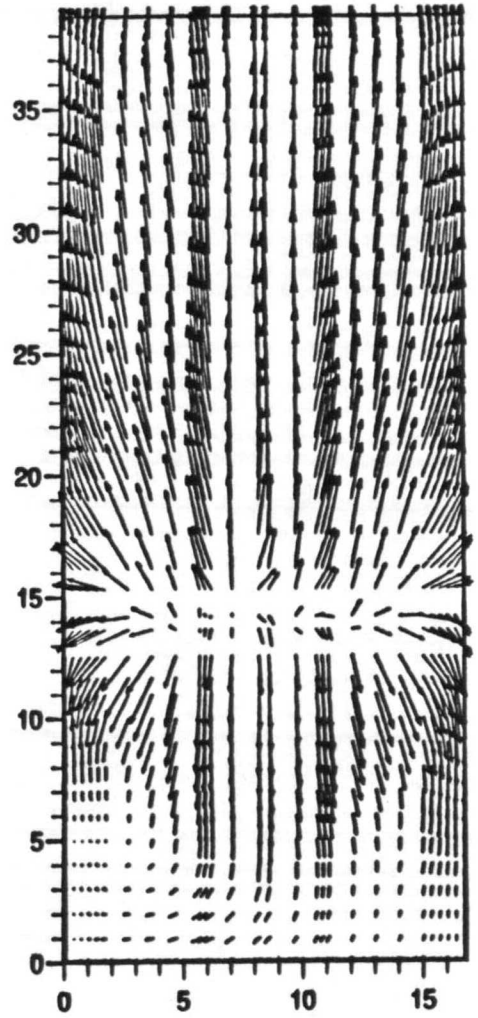


Fig. 6.17 Velocity Vectors for X = 15 (Coal Combustion)

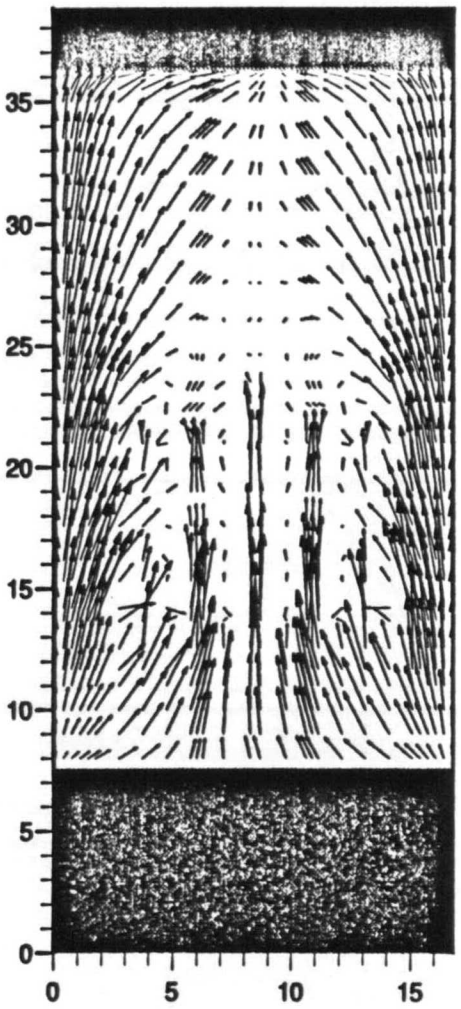


Fig. 6.18 Velocity Vectors for X = 24 (Coal Combustion)

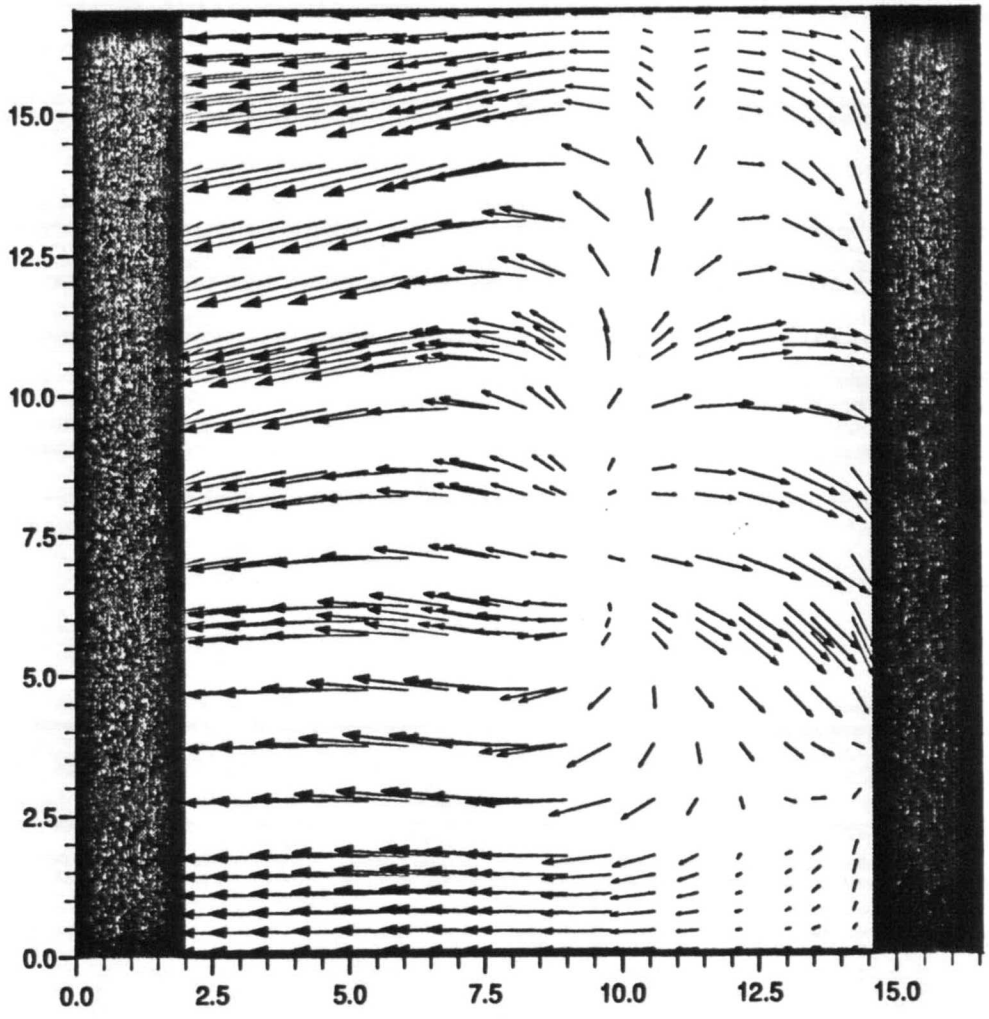


Fig. 6.19 Velocity Vectors for Z = 7 (Coal Combustion)

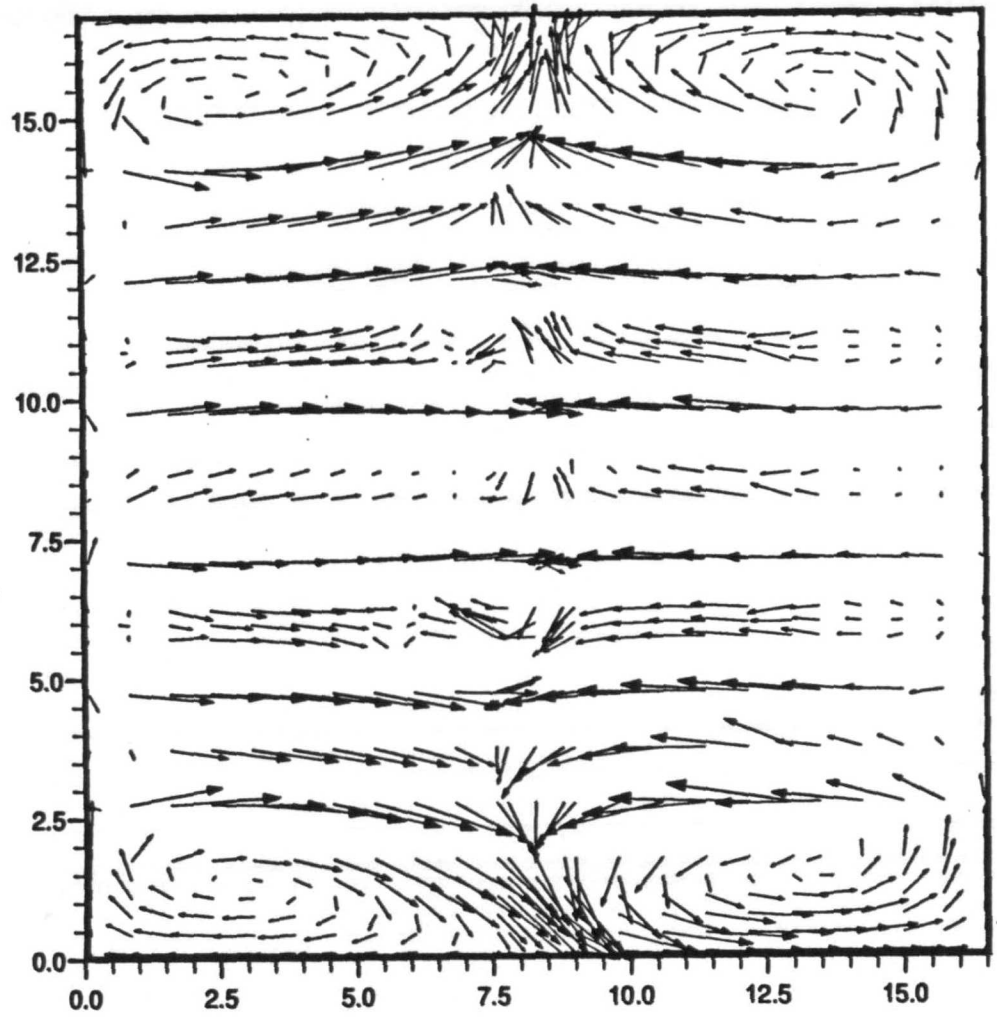


Fig. 6.20 Velocity Vectors for Z = 18 (Coal Combustion)

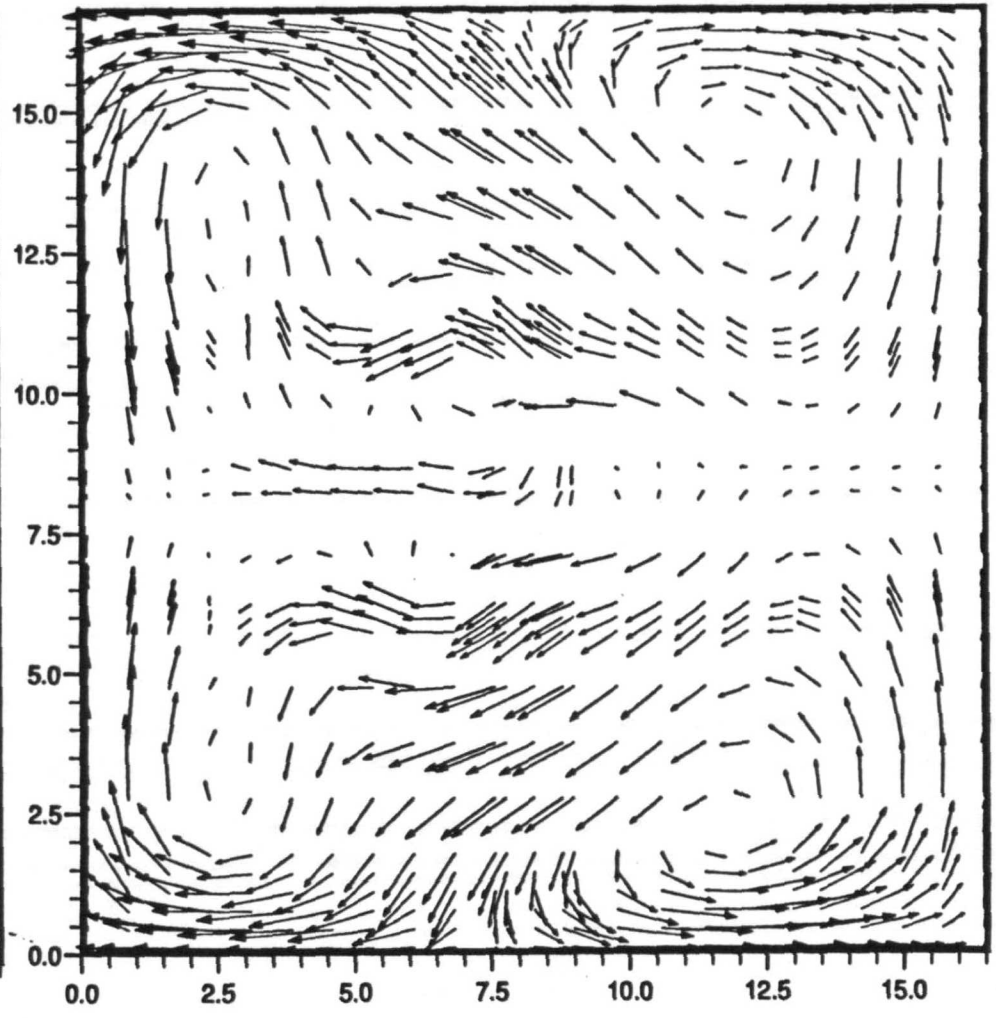


Fig. 6.21 Velocity Vectors for Z = 30 (Coal Combustion)

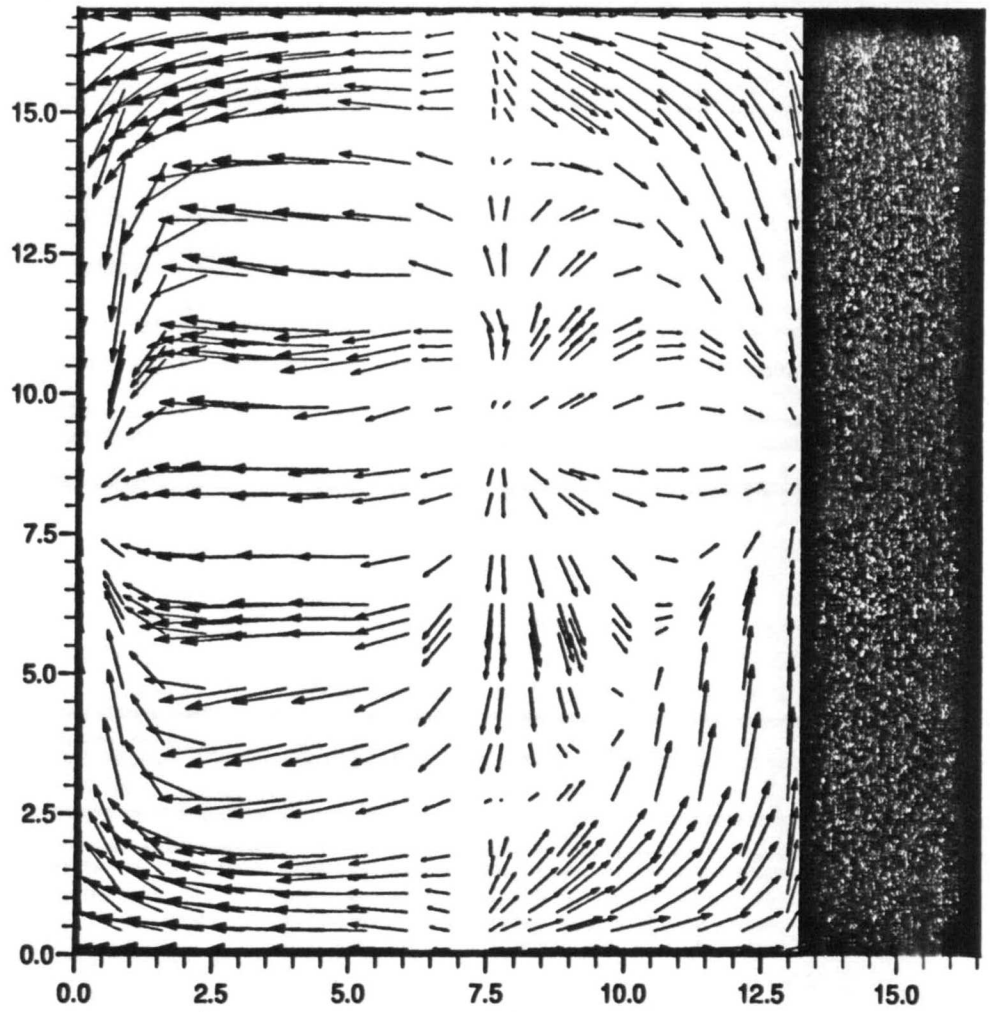


Fig. 6.22 Velocity Vectors for Z = 38 (Coal Combustion)

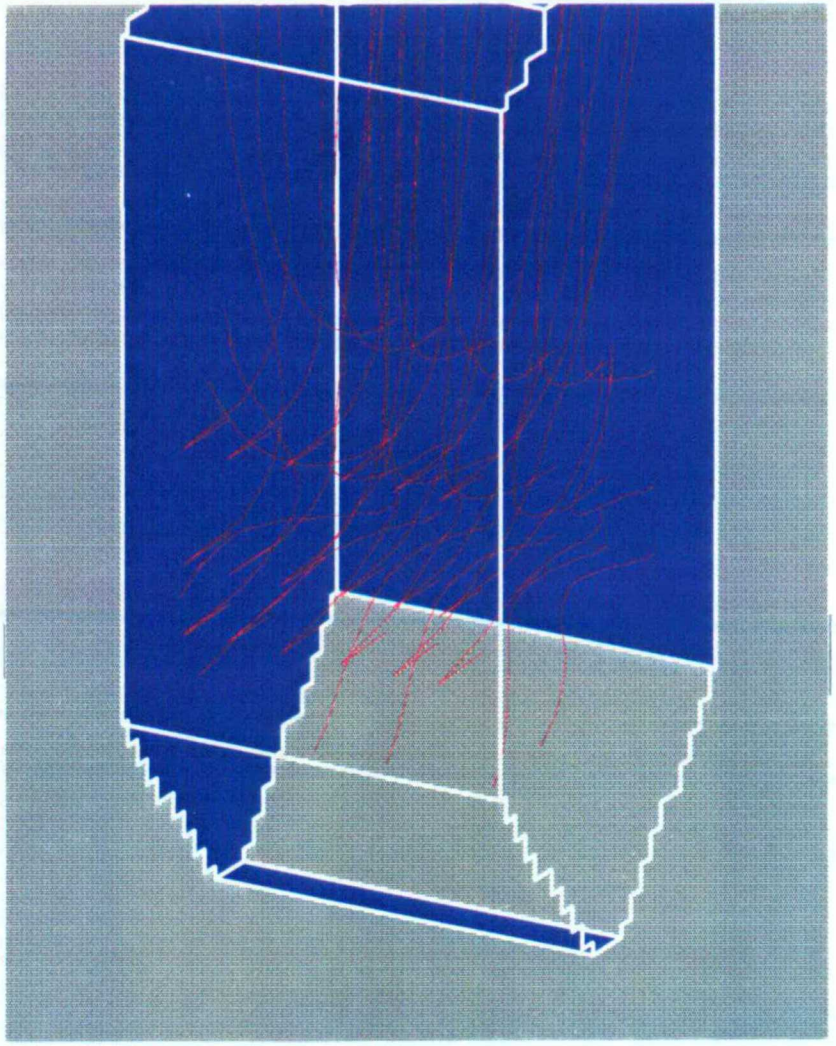


Fig. 6.23 3-D Particle Trajectories

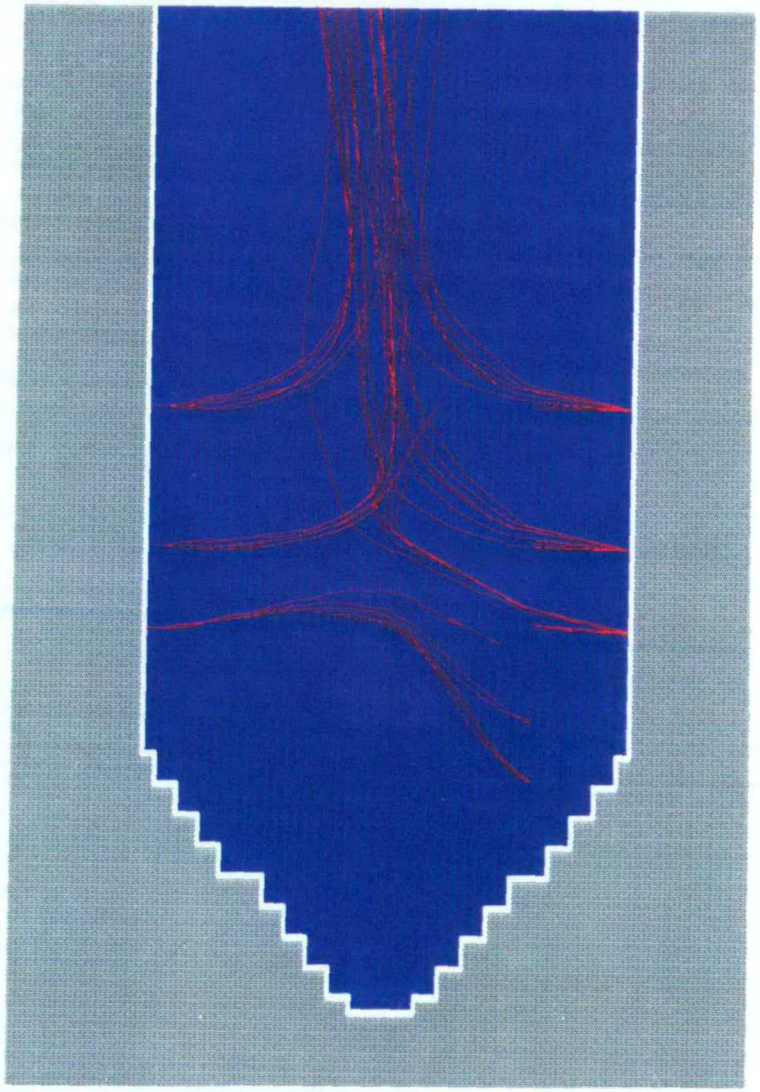


Fig. 6.24 Projection of the Particle Trajectories in the X-Z Plane

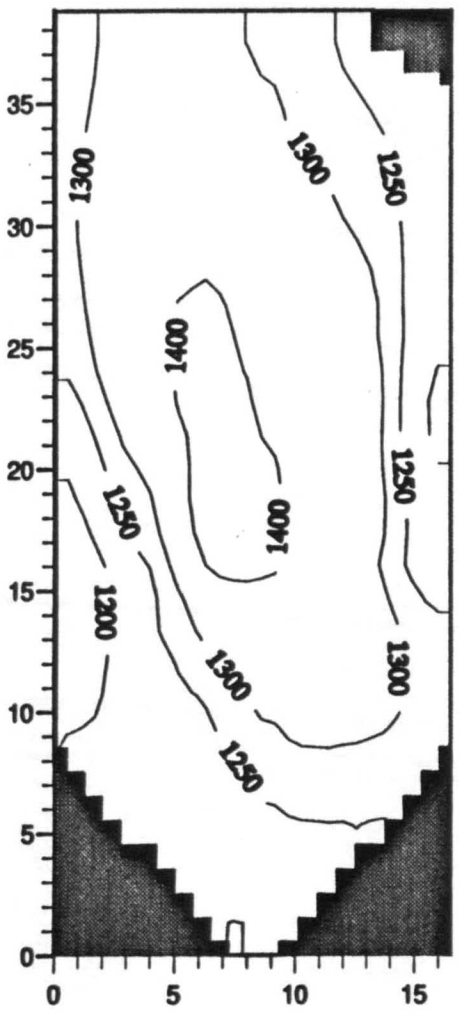


Fig. 6.26 Temperature Contours (°C) for Y = 2 (Coal Combustion)

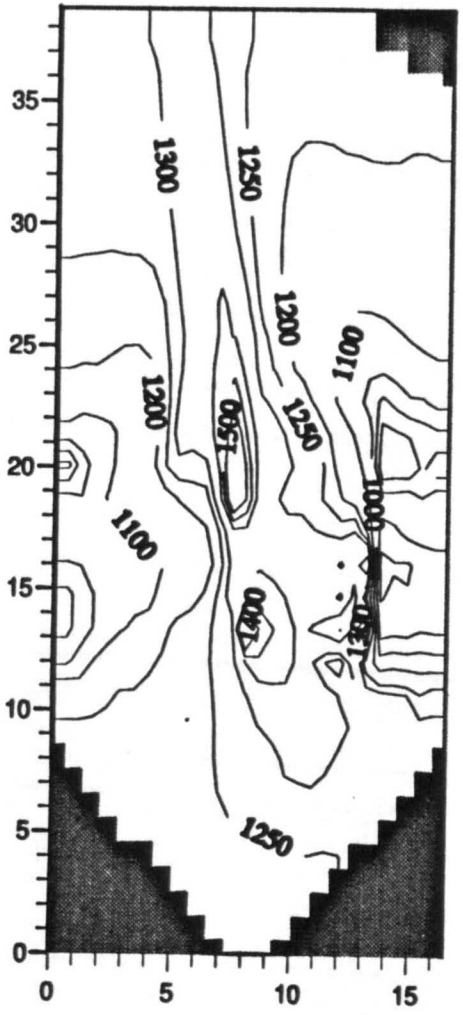


Fig. 6.27 Temperature Contours (°C) for Y = 8 (Coal Combustion)

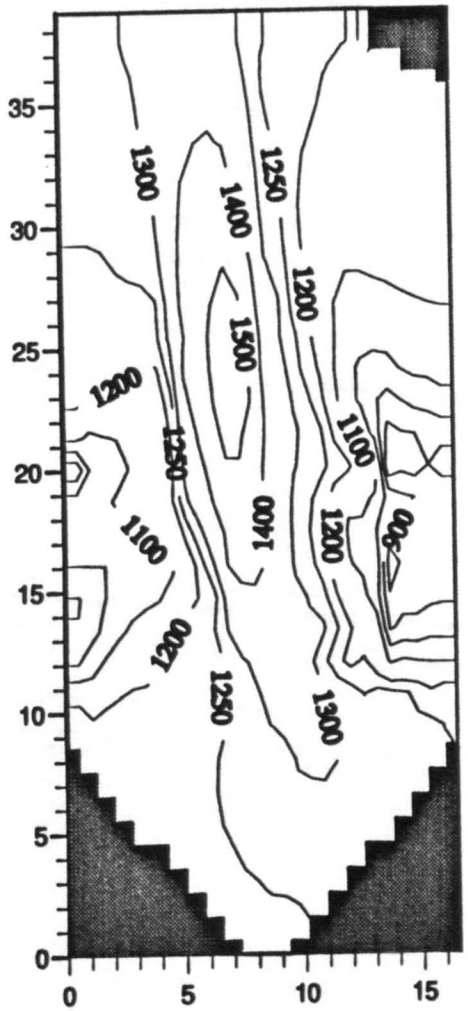


Fig. 6.28 Temperature Contours (°C) for Y = 12 (Coal Combustion)

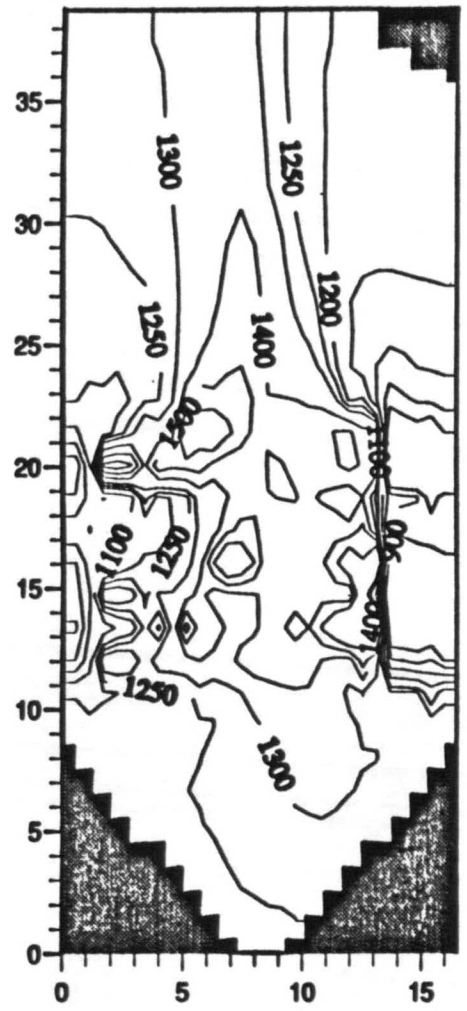


Fig. 6.29 Temperature Contours (°C) for Y = 16 (Coal Combustion)

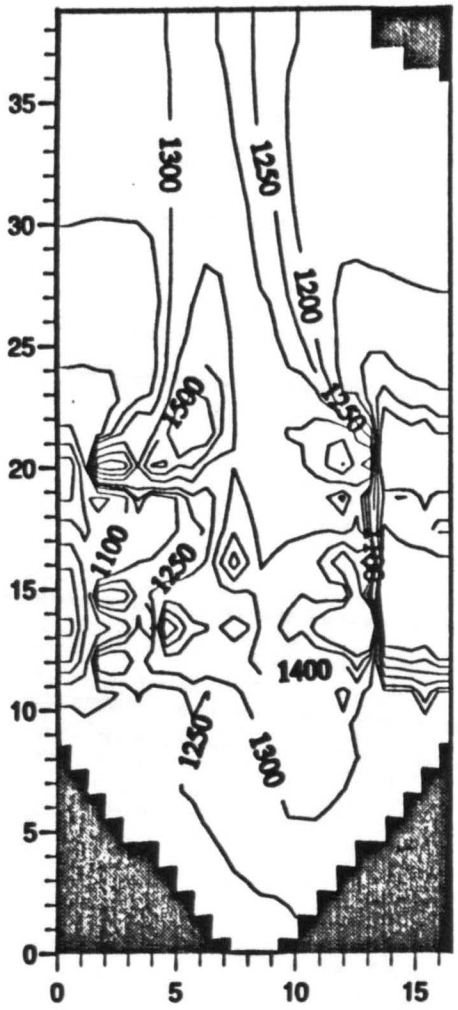


Fig. 6.30 Temperature Contours (°C) for Y = 20 (Coal Combustion)

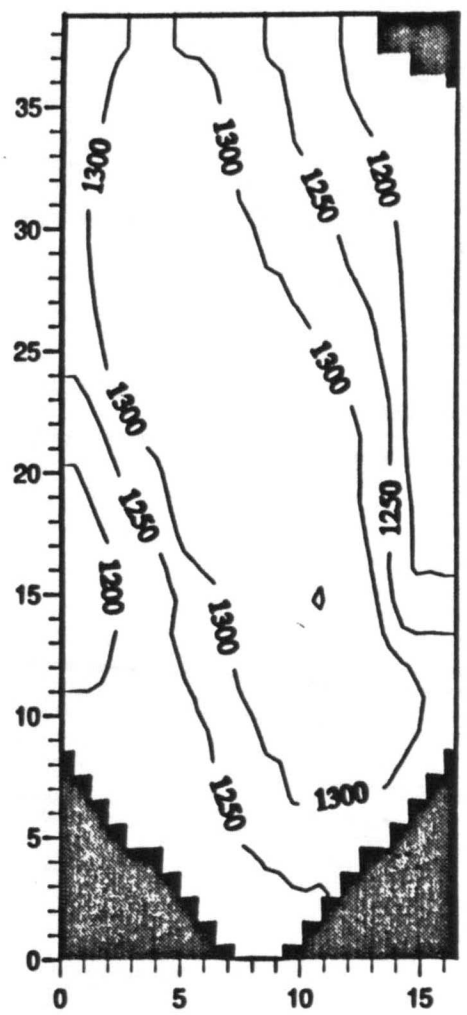


Fig. 6.31 Temperature Contours (°C) for Y = 27 (Coal Combustion)

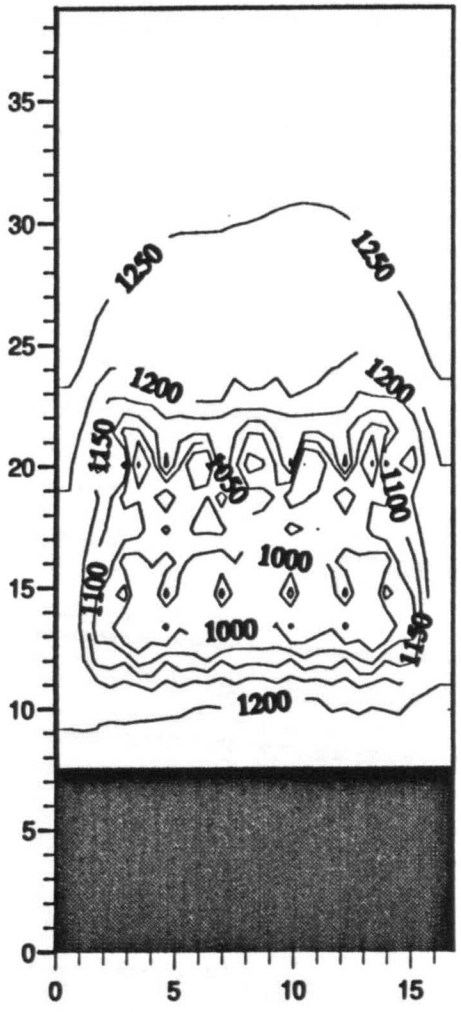


Fig. 6.32 Temperature Contours (°C)

for X = 2 (Coal Combustion)

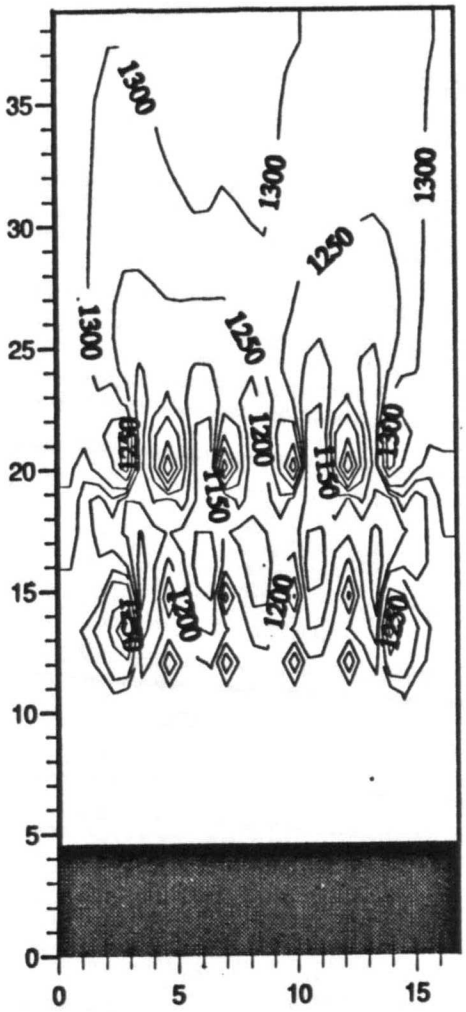


Fig. 6.33 Temperature Contours (°C)

for X = 6 (Coal Combustion)

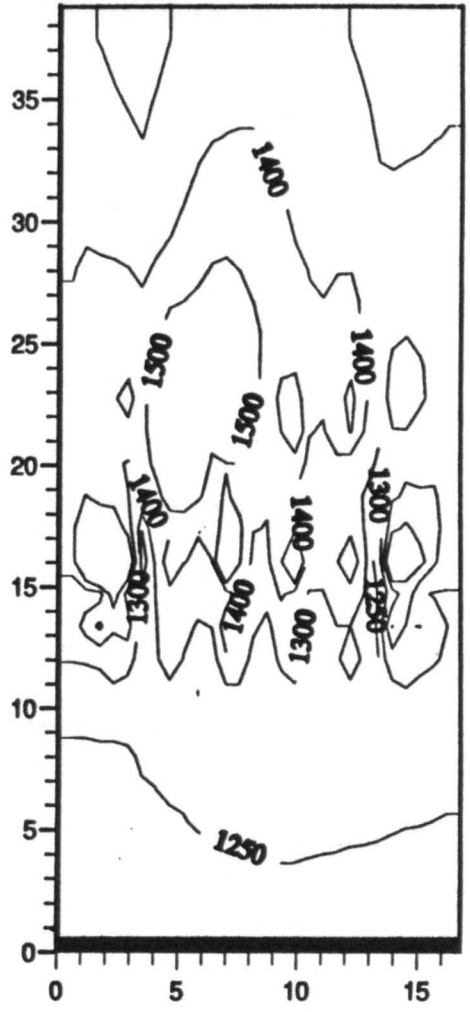


Fig. 6.34 Temperature Contours (°C)

for X = 10 (Coal Combustion)

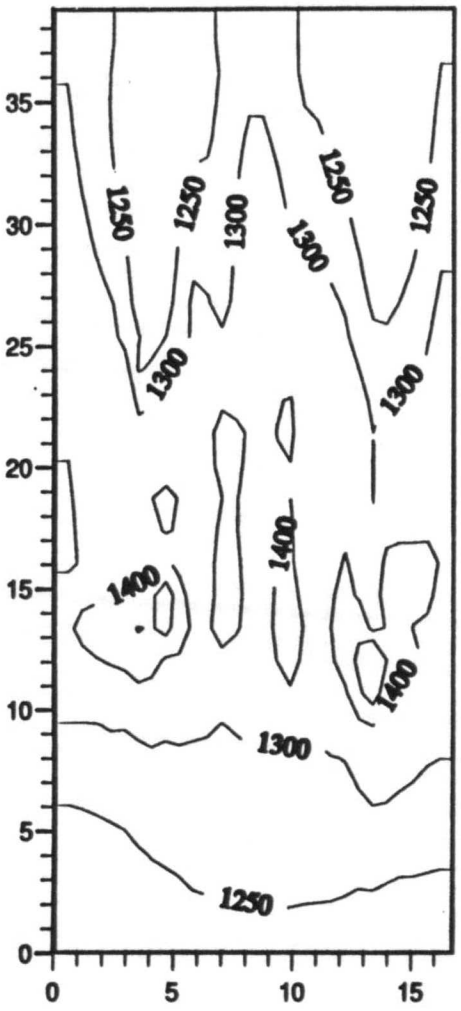


Fig. 6.35 Temperature Contours (°C) for X = 15 (Coal Combustion)

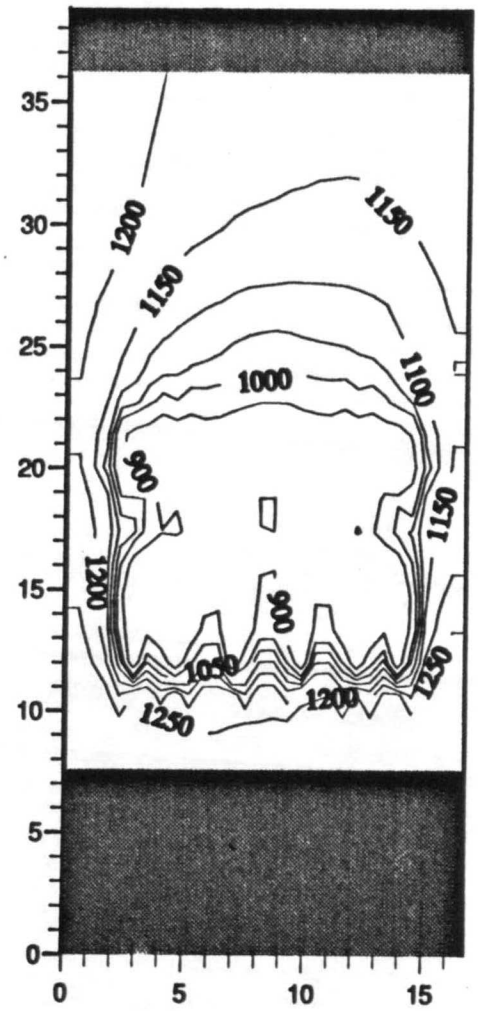


Fig. 6.36 Temperature Contours (°C) for X = 24 (Coal Combustion)

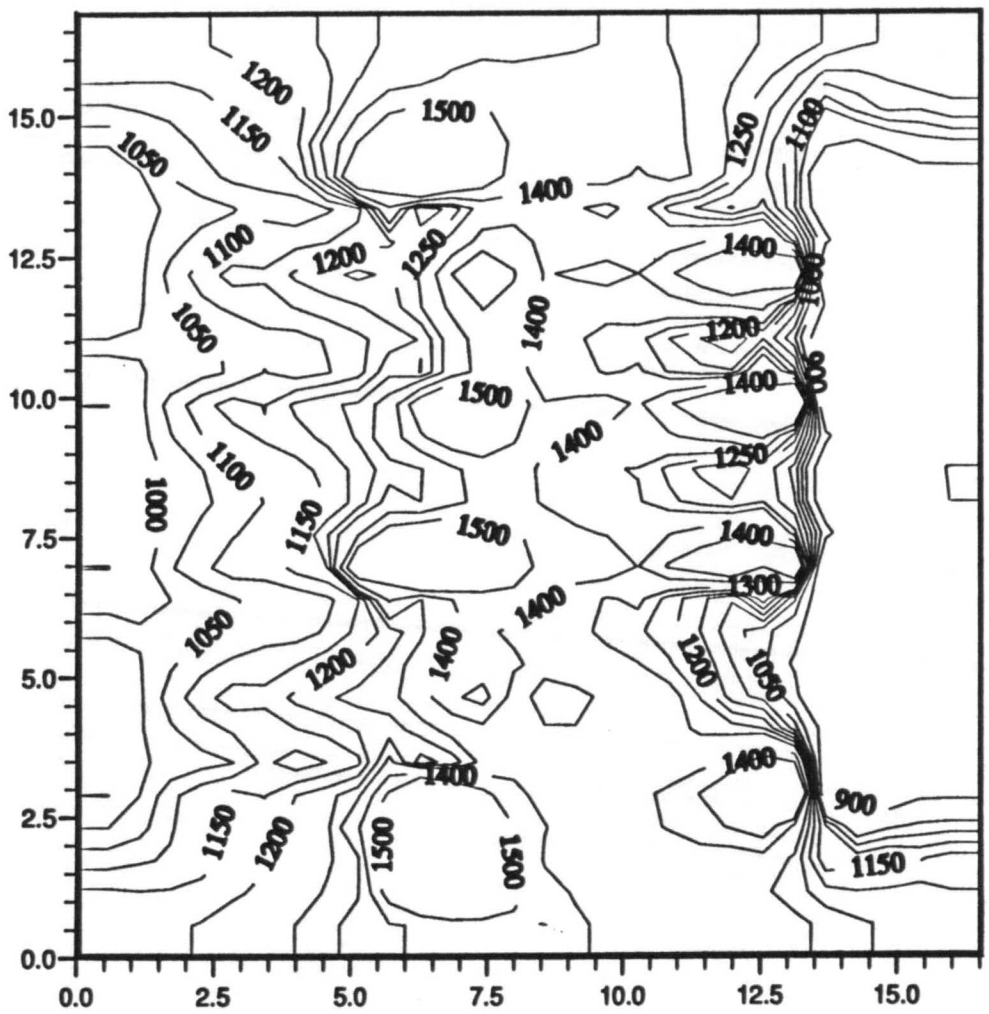


Fig. 6.37 Temperature Contours (°C) for Z =1 8 (Coal Combustion)

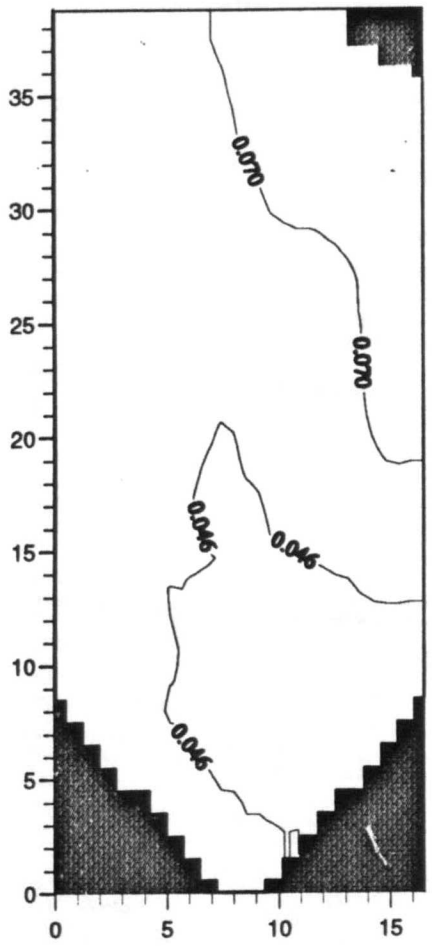


Fig. 6.38 Temperature Contours (°C) for Y = 2 (Coal Combustion)

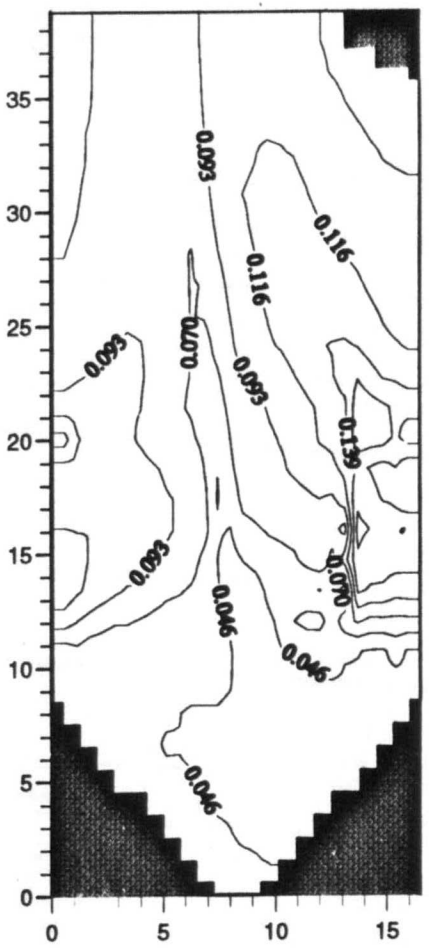


Fig. 6.39 Temperature Contours (°C) for Y = 8 (Coal Combustion)

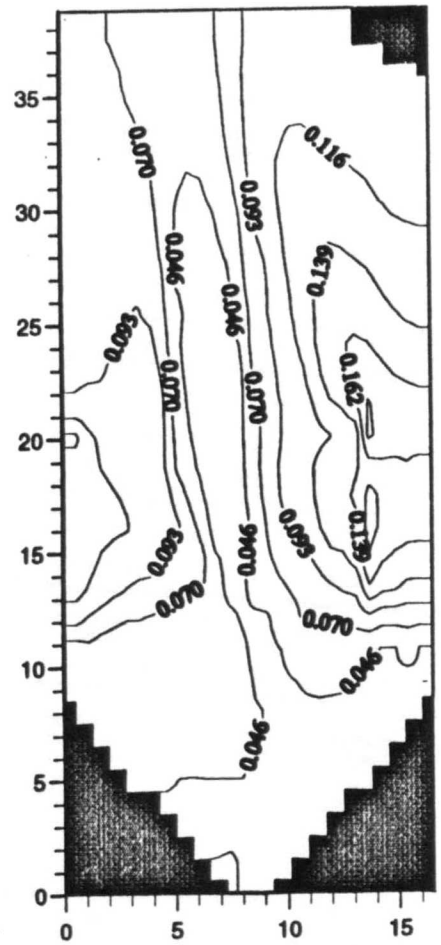


Fig. 6.40 Oxygen Concentration Contours (%) for Y = 12 (Coal Combustion)

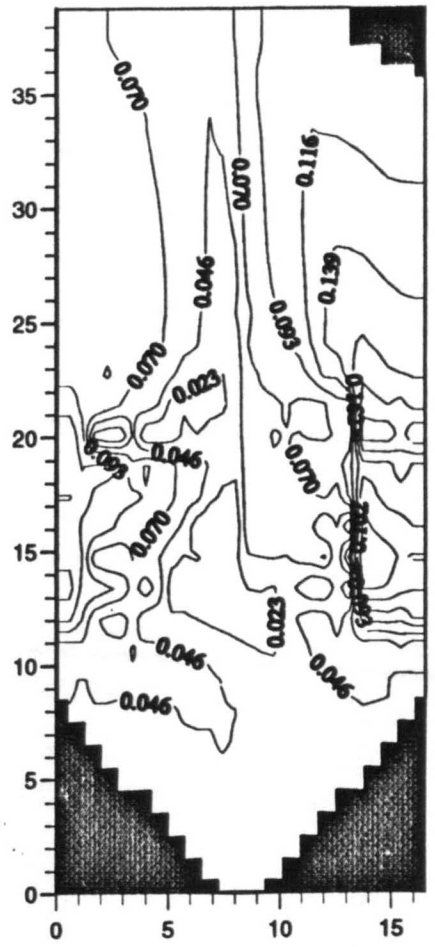


Fig. 6.41 Oxygen Concentration Contours (%) for Y = 16 (Coal Combustion)

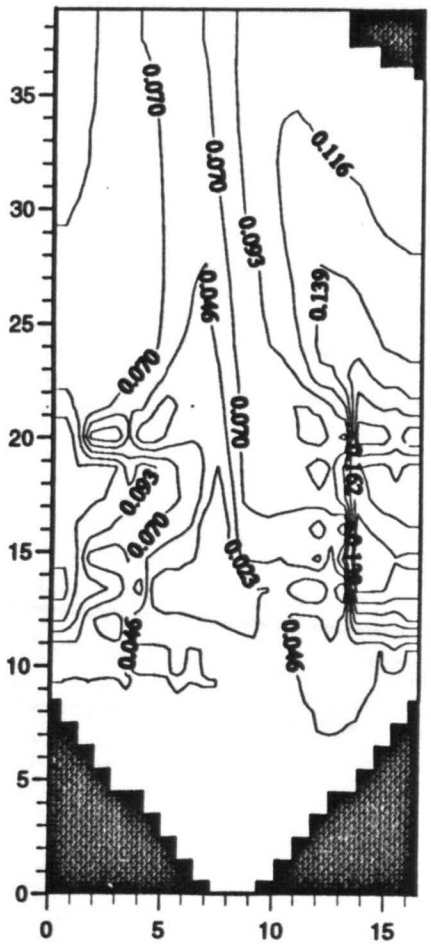


Fig. 6.42 Oxygen Concentration Contours (%) for Y = 20
(Coal Combustion)

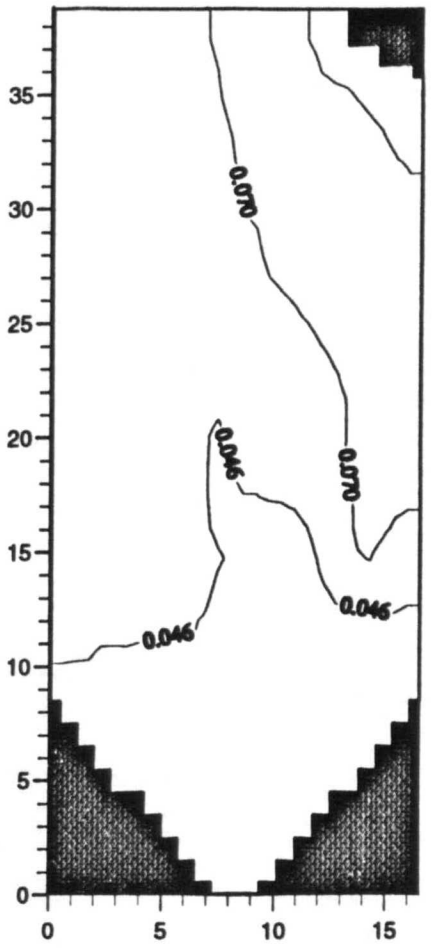


Fig. 6.43Oxygen Concentration Contours (%) for Y = 27
(Coal Combustion)

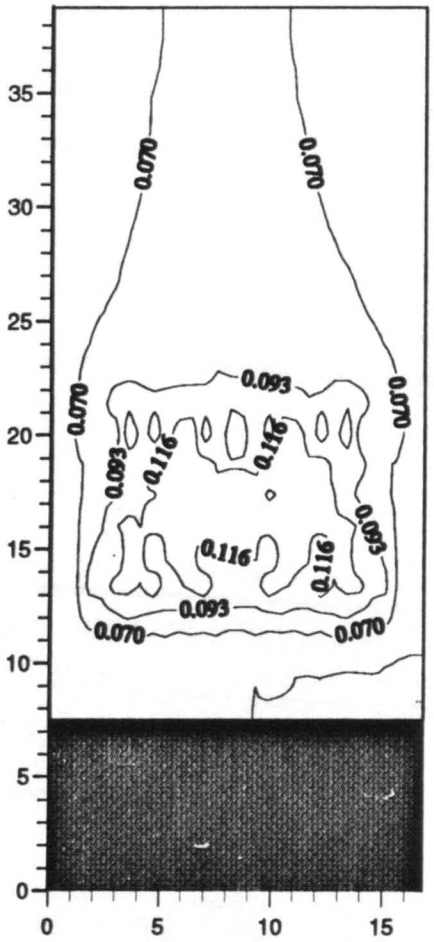


Fig. 6.44 Oxygen Concentration Contours (%) for X = 2 (Coal Combustion)

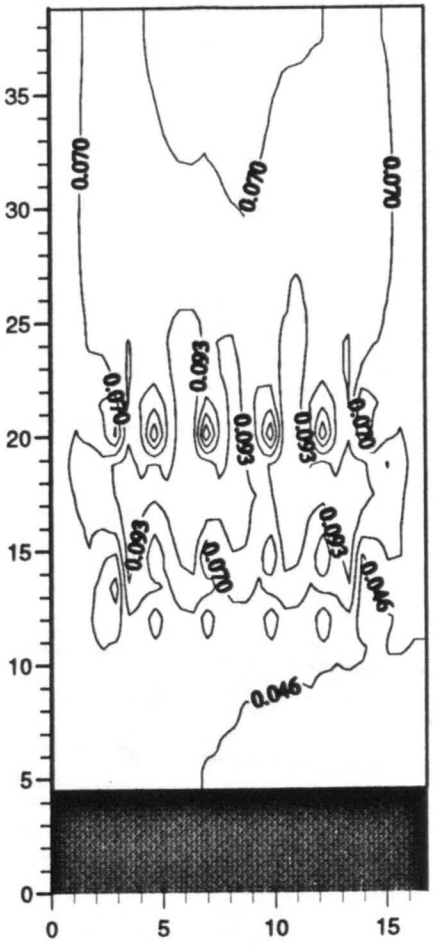


Fig. 6.45 Oxygen Concentration Contours (%) for X = 6 (Coal Combustion)

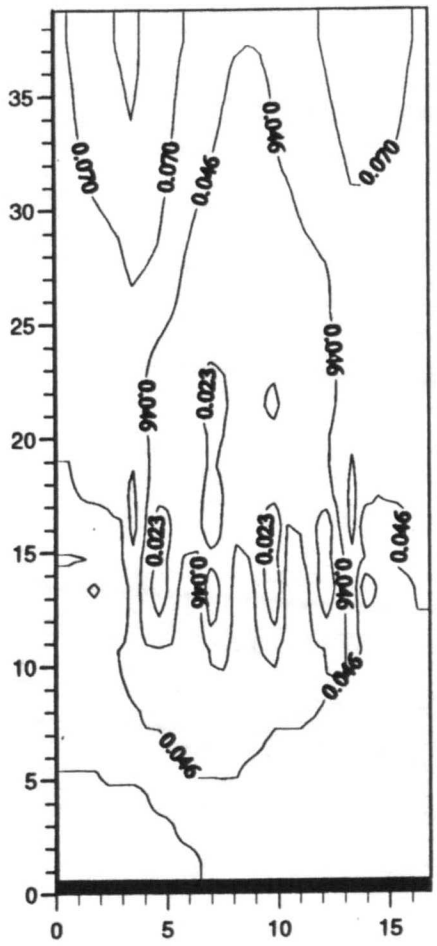


Fig. 6.46 Oxygen Concentration Contours (%) for X = 10 (Coal Combustion)

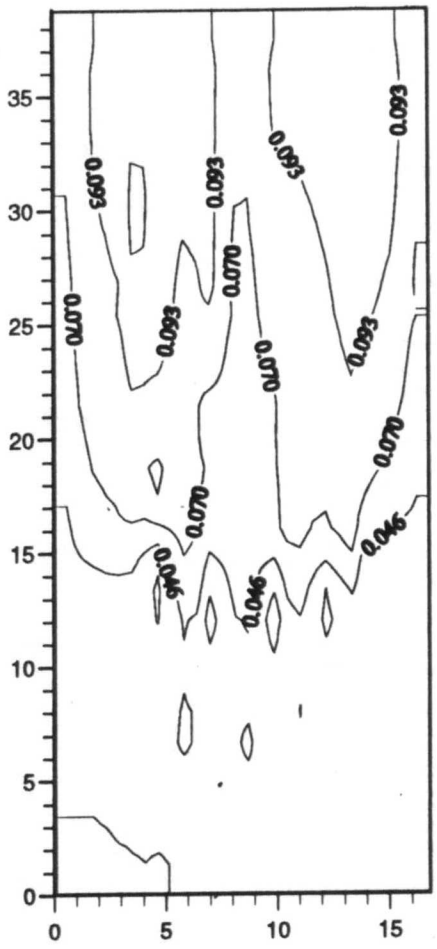


Fig. 6.47 Oxygen Concentration Contours (%) for X = 15 (Coal Combustion)

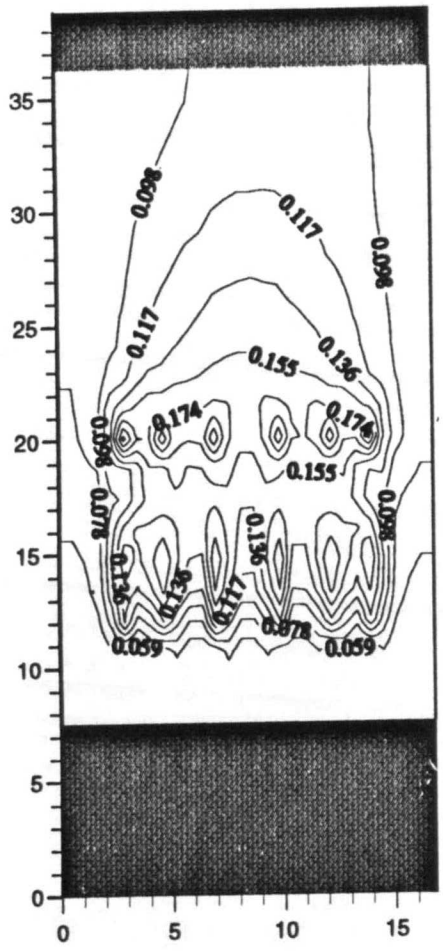


Fig. 6.48 Oxygen Concentration Contours (%) for X = 24 (Coal Combustion)

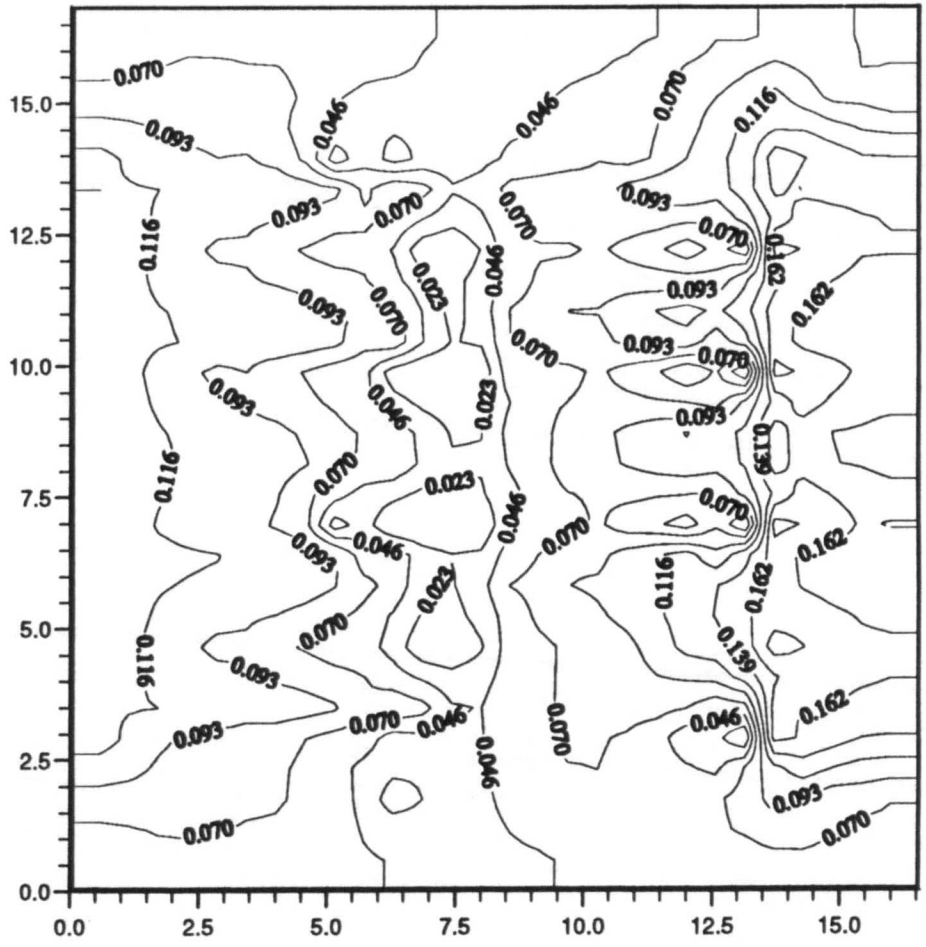


Fig. 6.49 Oxygen Concentration Contours (%) for Z = 18 (Coal Combustion)

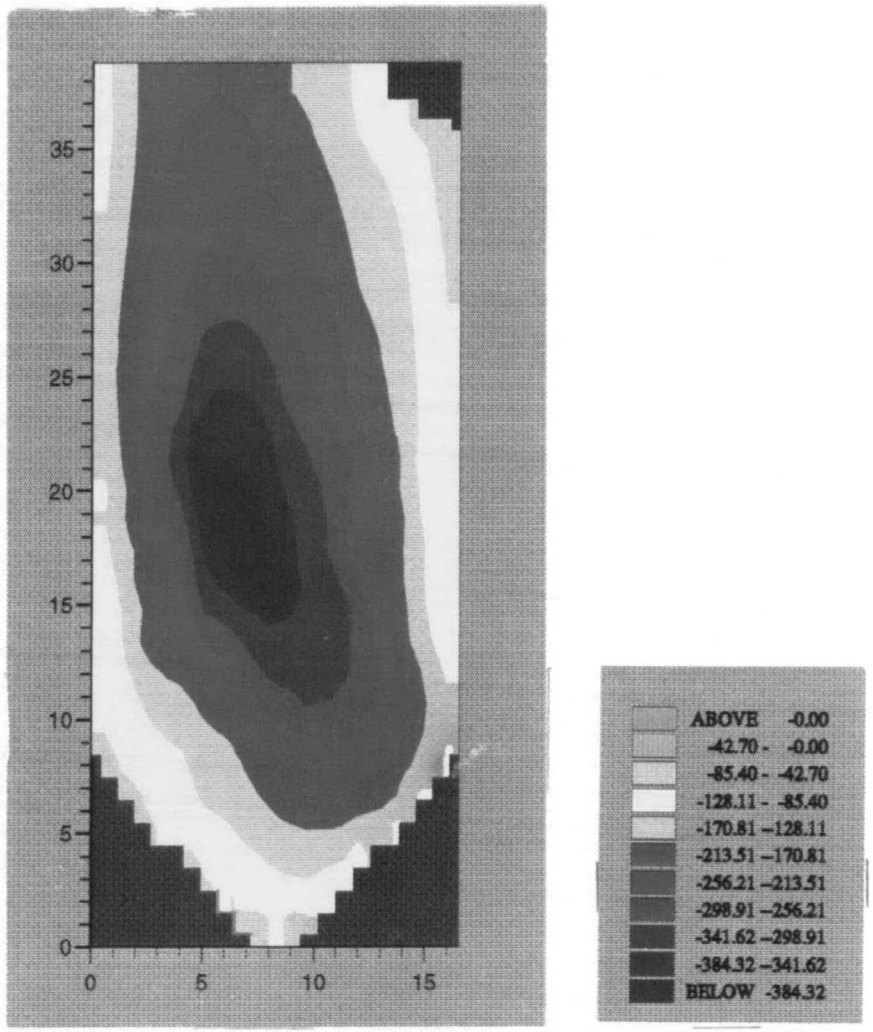


Fig. 6.50 Heat Fluxes to the Lateral Wall (kW/m^2) (Coal Combustion)

CHAPTER 7

CLOSURE

7.1 Introduction

This chapter concludes the thesis, summarises the work performed during this study and outlines the main findings and contributions in relation to the problem considered. In previous chapters short summaries have already been included regarding each separate portion of the project; section 7.2 gathers these together and lists the main conclusions and implications which have emerged. Finally, section 7.3 outlines some recommendations for future work.

7.2 Summary

As stated at the beginning this present thesis the main objective was the development of a general mathematical model that can be used as a design tool for design engineers of industrial combustion chambers, particularly those of power stations. To obtain this objective, modules to account for, oil and pulverised coal combustion have been developed and incorporated into the existing general three-dimensional CINAR code. The versatility of the code which has resulted from the work of this thesis allows the researcher to concentrate on the actual problem of predicting the flow and heat transfer, investigate the effect of the numerical algorithms incorporated in the code on the predictions and evaluate the stability, convergence rate and the accuracy of the numerical solution. The versatility of the code allows the user to model different geometries,

imposing the boundary conditions at will. It can and should be used as the vehicle for testing different algorithms and physical models.

The Eulerian formulation is adopted to describe the gaseous phase, whereas the Lagrangian one is used for the discrete (coal particles or oil droplets) phase. Effort has been made, where possible, to adopt a universal modelling approach. To achieve this, the same non-linear second order differential equations describing the flow field and heat transfer have been discretised and integrated, adequately modified for each type of fuel. This task has been described in detail in chapters 2 and 3 and is summarised as follows:

7.2.1 Gas Combustion and Thermal Radiation

For modelling the gas combustion processes the 'Simple Chemically Reacting System has been used. This results in a solving of the enthalpy and mixture fraction transport equations in addition to those of the main flow. The thermal radiation heat transfer is modelled through the 'Discrete Transfer' method of Lockwood and Shah (1982). For the absorption coefficient values of the combustion mixture, the relations of Truelove (1976) for a grey gas mixture have been utilised which prescribe the absorption coefficient as a function of the gas composition and gas temperature.

7.2.2 Oil Combustion

(i) Eulerian Phase

The presence of soot in oil flames results in considerable change of the absorption coefficient of the combustion mixture, especially in the NBR region. For this purpose, models for soot production and oxidation have been incorporated into the code, namely those of Khan and Greeves (1974) and Magnussen et al (1976). In addition to that a transport equation for the soot concentration has been discretised and solved, using as sink and source terms the quantities calculated from the respective just mentioned models.

(ii) Lagrangian Phase

The atomised oil droplets have been traced within the combustion chamber using a Lagrangian particle tracking technique. The droplet energy balance equation has been solved to provide the droplet temperature. A droplet evaporation model has been introduced based on the calculation of the droplet diameter diminution, assuming that no evaporation takes place until the droplet temperature reaches a certain value, the saturation temperature. Through these Lagrangian calculations, interaction source terms are determined for the momenta, mass, enthalpy and mixture fraction which are introduced explicitly into the relevant equations of the Eulerian framework.

(iii) Thermal Radiation

The 'Discrete Transfer' radiation method is again used for the calculations for oil firing. Appropriate modifications, due to the presence of soot in an oil flame, have been introduced in the calculation of the absorption coefficient of the combustion mixture. This has been achieved by utilising the expressions given by Truelove (1976) for a grey gas/soot mixture which give the absorption coefficient of the mixture as a function of the temperature, gas composition and soot concentration.

7.2.3 Coal Combustion

(i) Eulerian Phase

A new combustion model has been developed and incorporated into the code to account for the coal combustion. The problem to be addressed is that of the presence of two different fuel combustion mechanisms, namely volatile and char combustion having different stoichiometries, competing for the available oxygen. The basic assumption of the model is that in the presence of both volatiles and char, gas phase combustion first occurs and followed by a subsequent heterogeneous reaction, provided that there is an excess of oxygen. This is justified because the volatiles reaction is several orders of magnitude faster than the char reaction. The model is computationally economical

because it solves the same number of equations as in the gas combustion case, an extremely important consideration for three-dimensional calculations.

(ii) Lagrangian Phase

The PF particles are tracked using the same technique as for the oil droplets. The particle energy balance equation has been analytically integrated to provide its temperature as a function of the time of flight in the combustion chamber. A single reaction devolatilisation model has been introduced. The modelling of the heterogeneous combustion mechanism has been achieved assuming that the reaction rate is controlled by two parallel mechanisms, that of the oxygen diffusion from the gas mixture through the particle boundary layer to the particle and that of the chemical kinetic rate. The two phases are coupled through the 'Particle Source In Cell' (PSIC) method of Migdal and Agosta (1967), by the appropriate calculation of the explicit source terms to be introduced in the Eulerian gas phase equations. These comprise source terms for momenta, mass, enthalpy and mixture fraction.

(iii) Thermal Radiation

The 'Discrete Transfer' radiation method has been used again. The absorption coefficient for a PF flame is calculated by using empirical expressions for the gas, soot char and ash particle contributions due to Gibb and Joyner (1973).

7.2.4 Applications

The code has been applied to the prediction of the flow field and heat transfer in three cases of opposed-fired power station combustors, for each type of fuel. Some general comments follow :

The computation of the power station boiler is hindered by the cylindrical geometry of the burners set in the essentially Cartesian geometry of the combustion chamber and by the large discrepancy of physical scale between the burners and the chamber. In spite of the current numerical limitations, quite reasonable predictions of the power station

combustor are obtained. These are summarised in the following paragraphs for each case run.

For the gas and oil predictions, a 320 MWe opposed-fired furnace, equipped with 18 burners arranged in two opposing 3x3 arrays, has been modelled. The thermal loading has been kept the same for the two separate test cases. In the case of oil firing, a part of flue gases where recirculated through the hopper, and the code has proved versatile enough to cope with this additional operational variation. The flue gas recirculation (FGR) is one of the industrial practices, which is employed in order to reduce NO emissions by combustion modifications, the other being the staged combustion (air or fuel). The FGR consists in diluting the combustion air with the low temperature outlet gases from the boiler, either at the burner or through the hopper. This contributes in decreasing the flame temperature because of the reduced oxygen concentration and the increased inert gas proportion . The result is that the flow field exhibits an overall draught motion towards the furnace exit and significantly reduces the hopper temperatures from 1200 to about 700 ^{o}C. Additionally, because of the swirl of the burners adjacent to the 'hopper' a horizontal rotational motion occurs about the vertical central line of the furnace– a flow field resembling tangentially-fired configurations.

Comparing the two cases, presented in chapters 4 and 5 for the same furnace, the flames appear to be shorter in the oil-fired case which is attributed to the swirling flows of the burners. Most importantly, it is found that the reduced emissivity of the gas flame, as compared with that of an oil flame, is compensated for by its higher temperature so that the total heat transfer due to the fuel conversion is not strongly affected.

For the pulverised fuel predictions, a 500 MWe opposed-fired furnace has been simulated. The furnace is equipped with 48 burners arranged as arrays of 4 rows of 6 burners each located in two opposite walls. The results obtained with the model proposed by this thesis are encouraging in terms of computer economy. Given the lack of experimental data for industrial furnaces, the results of the simulations performed do not conflict with the existing engineering knowledge and appear reasonable. For the

design considered the predictions give warning of the likely existence of wall hot spots. They reveal an unexpected level of flow activity in the hopper region, the engineering consequences of which are however probably small. And they reveal that the 'nose' which precedes the convective section perturbs the flow to an unexpected extent throughout the entirety of the combustion chamber.

7.3 Recommendations for Future Work

The recommendations for future work can be divided into two categories. The first is the extension of its application into other types of industrial combustor. The second relates to modelling work and can be classified as follows:

(i) Incorporation of turbulent dispersion of particles

In the present study only the main particle trajectories have been predicted. The incorporation of an appropriate turbulent particle dispersion model will yield, smoother and therefore more realistic temperature fields.

(ii) The Near Burner Region

The overall dimensions of an industrial combustor are extremely disproportionate with the scales of the Near Burner Region (NBR) phenomena which influence strongly the overall behaviour of the combustor, in terms of combustion characteristics and pollutant emissions. On the other hand the capabilities of modern computers, however advanced, prohibit the use of very fine numerical grids that could account for the very complicated phenomena occurring in the NBR region. In addition to this difficulty the burners usually exhibit cyclic symmetry, whereas the combustion chambers are better described in an orthogonal Cartesian framework. Therefore, Local Grid Refinement (LGR) numerical techniques are adopted so that the phenomena occurring in the NBR are more adequately described, see for example Lockwood et al (1992). This should be done in such a way that the cyclic symmetry of the burners is simulated, a far from easy task. This could involve body fitted co-ordinate (BFC) treatment but they are not very convenient for this type of combustor and have proved unstable for two-phase flows. Alternatively, combination of a LGR and unstructured tetrahedral meshes is more likely to provide a solution to this problem (Lockwood and Pikoulas, 1994).

(iii) Reburn

As mentioned in section (7.2.4) the combustion modification techniques employed in order to abate NO emissions from a boiler are flue gas recirculation (FGR) and staged combustion. The code, at present, can simulate combustion processes in furnaces fired with one fuel at a time. This means that it can simulate air-staged combustion conditions. It cannot though simulate fuel staging (reburn) in which there has been much recent interest when the reburn fuel is a different kind of fuel than that of the main fuel. For this purpose, the combustion models must be extended so that they can handle such operating conditions as coal/gas, coal/oil and coal/coal (when the reburn PF is different from the main fuel) reburn. Additionally, NO production and reduction models under reburn conditions (such as those involving NH_i and CH_i radicals reactions that result in NO reduction) require to be developed and introduced, preferably in the form of a post-processor.

(iv) Ash deposition and Wall Temperatures

In the present study the wall temperatures were kept constant. In reality though, the wall temperatures are affected by fouling because of ash deposition in coal-fired furnaces. Thus models should be developed to incorporate these processes since they significantly affect the net heat transfer (predominantly radiative) to the water-cooled walls in industrial coal-fired boilers. The models should in the first instance simulate the ash formation and its deposition in order to assess the degree of fouling, see for example Lee et al (1993). Subsequently, wall temperature and wall emissivity calculation models require o be introduced to account for the effect of fouling on the heat transfer characteristics of the combustor.

REFERENCES

Abbas, A.S. (1982). Predicting the Performance of Heavy Oil - Fired Combustors. PhD Thesis, University of London.

Abbas, A.S., Koussa, S.S. and Lockwood, F.C. (1981a). 'The Prediction of the Particle Laden Flows', Eighteenth Symposium (International) on Combustion, The Combustion Institute, pp 1427 - 1437.

Abbas, A.S., Lockwood, F.C. and Koussa, S.S. (1981b). 'The Prediction of a Variety of Heavy Oil Flames', American Society of Mechanical Engineers, 81 - WA/HT - 48.

Abbas, A.S., Lockwood, F.C. and Salooja, A.P. (1984). 'The Prediction of Combustion and Heat Transfer of a Refinery Heater', Combustion and Flame, Vol. 58, p. 91.

Abbas, A.S. and Lockwood, F.C. (1985a). 'The prediction of Several Residual Oil Flames', Journal of Engineering for Gas Turbines and Power, 107, pp. 726 - 733.

Abbas, A.S. and Lockwood, F.C. (1985b). 'Note of the Prediction of Soot Concentrations in Turbulent Diffision Flames' Journal of the Institute of Energy, Vol. 58, pp. 112 - 115.

Abbas, A.S. and Lockwood, F.C. (1986). 'Prediction of Power Station Combustors', Twenty - First Symposium (International) on Combustion, The Combustion Institute, pp. 285 - 292.

Amsden, A.A. and Ruppel, H.M. (1981). 'SALE - 3D : A Simplified ALE Computer Program for Calculating Three - Dimensional Fluid Flow', Los Alamos National Laboratory, Report No NUREG/CR - 2185 LA - 8905.

Anderson, D . A ., Tannehill, J . C . and Pletcher, R . H . (1984). 'Computational fluid mechanics and heat transfer', Series in Computational Methods in Mechanics and Thermal Sciences, Hemisphere Publishing Company.

Anthony, D.B., Howard, J.B., Hottel, H.C., and Meissner, H.P. (1975). 'Rapid Devolatilisation of Pulverised Coal', 15th Symposium (International) on Combustion, The Combustion Instiitute, pp. 1303-1316.

Bagnaro, M.A. (1982). The Prediction of Some Room Fires with a Field Model, PhD Thesis, University of London.

Barreiros, A., Carvalho, M.G., Costa, M. and Lockwood, F.C. (1993) ' Prediction of the Near Burner Region and Measurements of NO_x and Particulate Emissions in heavy Fuel Oil Spray Flames', Combustion and Flame, Vol. 92, pp. 231 - 240.

Baum, M.M., and Street, P.J.(1971). 'Predicting the Combustion Behaviour of Coal Particles,' Combustion Science and Technology, Vol. 3, pp. 231-243.

Beacher, B ., Tabakoff, W. and Hamed, A . (1982). ' Improved particle trajectory calculations through turbomachinery affected by coal ash particles', Transactions of ASME, Journal of Engineering for Power, Vol. 104, p. 64.

Blazowski, W.S. (1978). 'Future Jet Fuel Combustion Problems and Requirements', Progress in Energy and Combustion Science, Vol. 4, pp. 177 - 199.

Blazowski, W.S. (1980). 'Dependence of Soot Production on Fuel Structure in back Mixed Combustor', Combustion Science and Technology, Vol 21, pp. 87 - 96.

Bonvini, M., Piana, C. and Vigevano, L. (1991). 'Predictions of Thermal NO_x Emissions from Utility Boiler Furnaces', First International Conference on Combustion Technologies for a Clean Environment, Vilamura, Portugal.

Boothroyd, R.G. (1971). Flowing Gas - Solids Suspensions, Chapman and Hall Ltd.

Boussinesq, J. (1877). 'Essai Sur la Theorie des Eaux Courantes', Memoires presentes par diverts savants a l' academie des sciences, Vol. 23, p.46.

Boyd, R.K. and Kent, J.H. (1986). 'Three - Dimensional Furnace Computer Modelling' Twenty - First Symposium (International) on Combustion, The Combustion Institute, pp. 265 - 274.

Bradshaw, P. (1978). Turbulence, Topics in Applied Physics, Vol 12, Springer - Verlag.

Bradshaw. P. Ferris,D.H. and Atwell, N.P. (1967). 'Calculation of Boundary Layer Development Using the Turbulent Energy Equation, Journal of Fluid Mechanics, 28,p 593.

Bray, K.N.C. (1975). 'Modelling of Pollutant Formation in Combustors', Paper No ARC 35891 Comb. 167, presented at the Aeronautical Research Council, London.

Caretto, L.S., Gosman, A.D., Patankar, S.V. and Spalding, D.B. (1972). 'Two Calulation Procedures for Steady, Three - Dimensional Flows with Recirculation', Proceedings of Third International Conference on Numerical Methods in Fluid Mechanics, pp. 60 - 68.

Carvalho, M.G. (1983). Computer Simulationof a Glass Furnace, PhD Thesis, University of London.

Carvalho, M.G. and Coelho, P. (1990). 'Numerical Prediction of an Oil - Fired Water Tube Boiler', Engineering Computations, 7, pp. 227 - 234.

Chakravarty, A. (1984). The Prediction of Turbulent Flame Extinction, PhD Thesis, University of London.

Chigier, N.A. and Yule, A.J. (1977). 'Vaporisation of Droplets in High Temperature Gas Streams, Physical Chemistry and Hydrodynamics', LEVICH Birthday Conference, Oxford.

Costa, M., Costen, P., Lockwood, F.C. and Mahmud, T. ' Detailed Measurements in and Modelling of an Industry - Type Pulverised - Coal Flame', Twenty - Third Symposium (International) on Combustion, The Combustion Institute, pp 973 - 980.

Cozzi, C. and Carodin, D. (1972). 'Nucleation, Growth and Coagulation of Solid Particles in Flames', Combustion Science and Technology, Vol. 5, pp. 213 - 218.

Crowe, C.T. (1976). 'Conservation Equations for Vapor-Droplet Flows Including Boundary-Droplet Effects', Lawrence Livermore Laboratory, University of California, Report No. UCRL-52184.

De Michele, G., Ghiribelli, L., Pasini, S.and Tozzi, A. (1989). 'A 3 - D Code for Predicting Radiative and Convective Heat Transfer in Boilers', ASME 26th National Heat Transfer Conference, Philadelphia, Pennsylvania.

Dolezal, R. (1967). Large Boiler Furnaces. Theory, Construction and Control, Elsevier Publishing Company, Amsterdam.

Drew, D.A. and Segel, L.A. (1971). 'Averaged Equations for Two - Phase Flows', Studies in Applied Mathematics, Vol. L, No 3, p. 205.

Edelman, R.B., Turan, A., Harsha, P.T., Wong, E. and Blazowski, W.S. (1979). 'Fundamental Characterisation of Alternative Fuel Effects in Continuous Combustion Systems', AGARD 54th, DFVLR, Koln, W.Germany.

Emmons, H.W. (1954). 'Shear Flow Turbulence', Proceedings of the 2nd U.S. National Congress in Applied Mechanics, ASME.

Faeth, G.M. (1983). 'Evaporation and Combustion of Sprays', Progress in Energy and Combustion Science, Vol. 9, p.1.

Field,M.A., Gill, D.W., Morgan, B.B., and Hawksley, P.G.W. (1967). Combustion of Pulverised Coal, The British Coal Utilisation Research, Leatherhead.

Fiveland, W.A. and Wessel, R.A. (1988). 'Numerical Model for Predicting Performance of Three - Dimensional Pulverised - Fuel Fired Furnaces', Journal of Engineering for Gas Turbine and Power, Transaction of ASME, pp. 117 - 126.

Fox, R. W. and McDonald, A.T. (1978). Introduction to Fluid Mechanics, 2nd Edition, John Wiley, New York.

Gaffen, D.J., Benocci, C. and Olivari, D. (1985). 'Application of a Lagrangian Dispersion Model to Environmental Problems', von Karman Institute, TM38.

Gibb, J. and Joyner,P.L.(1979). 'Liddel Boiler Reheater Metal Temperature : Gas Side Heat Transfer Analysis', Report no. R/M/NI029, Central Elactricity Generating Board, Marchwood Eng. Laboratoty, England.

Gibson,M.M., Jones,W.P., McGuirk,J.J., Whitelaw,J.H.(1987). Lectures on Turbulence Models for Computational Fluid Dynamics, Fluids Section, Mechanical Engineering Dept., Imperial College, London, England

Glassman, I. (1979). 'Phenomenological Models of Soot Processes in Combustion Systems', Dept. of Mech. and Aerospace Eng., Report No 1450, Princeton University,

Goener, R. and Zinser, W. (1986). 'Predictions of Three - Dimensional Flows in Utility Boiler Furnaces and Comparison with Experiments', ASME 107th Annual Meeting, Anheim, California.

Gosman, A.D., Lockwood, F.C and Salooja, A.P. (1978). 'The prediction of Cylindrical Furnaces Fueled with Premixed and Diffusion Burners, Seventeenth Symposium (International) on Combustion, The Combustion Institute, pp 747 - 760.

Gosman, A.D.and Ideriah, F.J.K. (1983.). ' TEACH 2E : A General Computer Program for Two Dimensional Turbulent Recirculating Flows', Imperial College Report, FM/83/2

Hanjalic, K. (1970). Two - Dimensional Asymmetrical Turbulent Flow in Ducts. PhD Thesis, University of London.

Harlow, F.H. and Nakayama, P.I. (1968). 'Transport of Turbulence Energy Decay Rate' Los Alamos Scientific Laboratory, University of California, Report No LA - 3854.

Hinze, J.O. (1959). Turbulence, an Introduction to its Mechanism and Theory, McGraw Hill Book Company.

Hottel, H.C. and Cohen, E.S. (1958). 'Radiative Heat Exchange for Non Uniformity of Gas Temperature', American Institute of Chemical Engineers Journal, Vol. 4, p. 3.

Hottel, H.C. and Sarofim, A.F. (1967). Radiative Transfer, McGraw Hill, New York.

Howell, J.R. (1968). 'Application of Monte Carlo to Heat Transfer Problems', Advance in Heat Transfer, Academic Press, New York.

Ingebo, R.D. (1962). ''Heat Transfer and Drag Coefficients for Ethanol Drops in a Rocket Chamber Burning Ethanol and Liquid Oxygen', Eighth Symposium (International) on Combustion, the Combustion Institute, pp.1104 - 1113.

Issa, R.I. (1982). Solution of Implicitly Discretised Fluid Flow Equations by Operatot Splitting. Departement of Mineral Resources, Imperial College, London.

Jones, W.P. and Launder, B.E. (1972). 'The prediction of Laminarisation with a two - equation Model of Turbulence', International Journal of Heat and Mass Transfer, Vol. 15, p. 1119.

Jones, W.P. and Launder, B.E. (1973). 'Predictions of Low Reynolds Number Phenomena with a Two - Equation Model of Turbulence', International Journal of Heat and Mass Transfer, Vol. 16, p. 119.

Jones, W.P and Whitelaw, J.H. (1978). Coupling of Turbulence and Chemical Reaction', Fluid Section Report FS/78/13, Departement of Mechanical Engineering, Imperial College, London.

Jones, W.P and Whitelaw, J.H. (1984). 'Modelling and Measurements in Turbulent Combustion', Twenteeth Symposium (International) on Combustion, The Combustion Institute, pp. 233 - 249.

Kays, W.M. (1975). Convective Heat and Mass Transfer, McGraw Hill.

Khalil, E.E., Spalding,D.B. and Whitelaw, J.H. (1975). 'The Calculation of Local Properties in Two - Dimensional Furnace', International Journal of Heat and Mass Transfer, Vol. 18, pp. 775 - 791.

Khan, I.M. and Greeves,G. (1974). 'A Method for Calculating the Formation and Combustion of Soot in Diesel Engines', Heat Transfer in Flames, (Afgan and Beer, Eds.), Hemisphere, New York, p. 391.

Kobayashi, H., Howard, J.B., Sarofim, A.F. (1977). 'Coal Delolatilisation at High Temperatures', Sixteenth Symposium (International) on Combustion, The Combustion Institute, pp. 411-425.

Kolmogorov, A.N. (1942). 'Equations of Turbulent Motion of an Incompressible Fluid', IZV. Akad. Nauk. SSSR, Ser. Phys. VI, No 1 -2, 56 - 58.

Kuo,K.K. (1986). Principles of Combustion, J. Wiley.

Launder, B.E. and Spalding, D.B. (1972). Mathematical Models of Turbulence, Academic Press.

Launder, B.E. and Spalding, D.B.(1974). 'The Numerical Computation of Turbulent Flows', Progress in Combustion Science, Vol. 4, pp. 221 - 270, Pergamon Press, Oxford, England.

Lee, C.C.F., Ghobadian, A. and Riley, G.S. (1993). 'Predictions of Ash Deposition in a 2D Axisymmetric Furnace', Eng. Foundation Conference, Solihul, Birmingham.

Leonard, B.P. (1979). 'A Stable and Accurate Convective Modelling ProcedureBased on Quadratic Upstream Interpolation', Computer Methods in Applied Mechanics and Engineering, (19), p. 59.

Leschziner, M.A. (1980). 'Practical Evaluation of Three Finite Difference Schemes for the Computation of Steady - State Recirculating Flows', Computre Methods in Applied Mechanics nad Engineering, Vol. 23, p. 293.

Leung, K.M., Lindstedt, R.P and Jones, W.P. (1991). 'A Simplified Reaction Mechanism for Soot Formation in Nonpremixed Flames', Combustion and Flame, Vol. 87, pp. 289 - 305.

Lockwood, F.C. and Naguib, A.S. (1975). 'The Prediction of the Fluctuationsin the properties of Free, Round - Jet, Turbulent Diffusion Flames, Combustion and Flame, Vol. 24, pp. 109 -124.

Lockwood, F.C. and De Marco. (1975). ' A New Flux Model for the Calculation of Radiation in Furnaces' Italian Flame Day, La Rivista dei Combustibili, No 5 - 6, Vol. 59, p 184.

Lockwood, F.C. and Shah, N.G. (1976). 'An Improved Model for the Calculation of Radiation Heat Transfer in Combustion Chambers', Proceedings of the ASME - AIChE National Heat Transfer Conference, St. Louis.

Lockwood, F.C. and Syed, S.A. (1977). 'Prediction of Coal Fired Furnaces', Report to CEGB, Imperial College, Mech. Eng. Dept., Technical Note, FS/78/1.

Lockwood, F.C. and Shah, N.G. (1981). 'A New Radiation Method for Incorporation in General Combustion Prediction Procedures', Eighteenth Symposium (International) on Combustion, The Combustion Institute, pp. 1405-1413.

Lockwood, F.C. McGuirk, J.J. and Shah, N.G. (1982) ' Radiation Transfer in gas Turbine Combustors', AIAA 18th Thermophysics Conference, AIAA - 83 - 1506

Lockwood, F.C., Risvi, S.M.A., Lee, G.K., and Whaley, H. (1984). 'Coal Combustion Model Validation Using Cylindrical Furnace Data', Twentieth Symposium (International) on Combustion, The Combustion Institute, pp. 513-522.

Lockwood, F.C. (1987). 'Transfer of Fundamental Results to the Modelling of Burners and Boilers. Fundamentals of the Physical - chemistry of Pulverised Coal Combustion.',Editors: J. Lahaye and G. Prado, NATO ASI Series E, Applied Sciences, No 137, pp. 395 - 423, Martinus Nijhoff Publishers.

Lockwood, F.C., Papadopoulos, C. and Abbas, A.S. (1987). ' Computation of Power Station Combustors', Calculation of Turbulent Reactive Flows, Edited by So, R.M.C., Whitelaw, J.H.and Mongia, H.C., ASME AMD Vol. 81, p. 127.

Lockwood, F.C., Papadopoulos, C., and Abbas, A.S. (1988). 'Prediction of a Corner Fired Power Station Combustor', Combustion Science and Technology, Vol.58, pp. 5-23.

Lockwood, F.C. and Mahmud, T. (1988). ' The Prediction of Swirl Burner Pulverised Coal Flames', Twenty - Second Symposium (International) on Combustion, The Combustion Institute, pp 165 - 173.

Lockwood, F.C, Malalasekera, W.M.G. and Papadopoulos, C. (1988). 'Experiences with the CINAR Code for Three Dimensional Furnace Predictions', British Flame Days.

Lockwood, F.C., Papadopoulos, C. and Abbas, A.S. (1988). 'Prediction of a Corner - Fired Power Station Combustor', Combustion Science and Technology, 58, pp. 5 - 23.

Lockwood, F.C., Pikoulas, C. and Shah, N.G. (1992). 'A New Multi-Level Local Grid Refinement Technique for the Solution of the 3D Navier-Stokes Equations', British Flame Days Meeting, 21-22 Sept.

Lockwood, F.C., Pikoulas, C. (1994). 'Application of Unstructured Meshes for the Solution of the 3D Navier-Stokes Equations in Complex Geometries'. In Preparation.

Looney, M.K., Issa, R.I., Gosman, A.D. and Politis, S. (1985). 'Modelling of the Turbulent Flow of Solid - Liquid Suspensions in Stirred Vessels', Proceedings the 5th International Conference on Mathematical Modelling, Berkeley, USA.

Malalasekera, W.M.G. (1988). Mathematical Modelling of Fires and Related Processes, PhD Thesis, University of London.

Magnussen, B.F. and Hjertager, B.H. (1976). 'On Mathematical Modelling of Turbulent Combustion with Special Emphasis on Soot Formation and Combustion', Sixteenth Symposium (International) on Combustion, The Combustion Institute, p 719.

Magnussen, B.F. and Hjertager, B.H., Olsen, J.G. and Bhaduri, D. (1978). 'Effects of Turbulent Structure and Local Concentrations on Soot Formation and Combustion in C_2H_2 Diffusion Flames', Seventeenth Symposium (International) on Combustion, The Combustion Institute,p. 1383.

McGarvey, R.G. (1983). Formulation and Numerical Solution of the Equations of Mition for a 2D Suspension Flows, PhD Thesis, UCD.

Migdal, D. and Agosta,V.D. (1967). 'A Source Flow Model for Continuum Gas-Particle Flow,' Transactions of the ASME, Journal of Applied Mechanics, p. 860.

Nee, V.W. and Kovasznay, L.S.E. (1969). 'The Calculation Boundary Layers by a Simple Theory', Physics in Fluids, 12, p 473.

Neilson, J.H. and Gilchrist, A. (1968). 'An Analytical and Experimental Investigation of the Velocities of Particles Entrained by the Gas Flow in Nozzles', J. Fluid Mechs., Vol 33, p 131.

Papadopoulos, C. (1989). The prediction of Two Phase Flows, PhD Thesis, University of London.

Patankar, S.V. and Spalding, D.B. (1970). Heat and Mass Transfer in Boundary Layers, Intertext Books, London.

Patankar, S.V. and Spalding, D.B. (1972). 'A Calculation Procedure for Heat, Mass and Momentum Transfer in Three - Dimensional Parabolic Flows', International Journal for Heat and Mass Transfer, Vol. 15, p 1787.

Patankar, S.V. (1980). Numerical Heat Transfer and Fluid Flow, Hemisphere P.C.

Patel, V.C. (1965). 'Calibration of the Preston Tube and Limitationsof its Use in Pressure Gradients', Journal of Fluid Mechanics, Vol. 23, p. 185.

Pope, S.B. (1990). 'Computations of Turbulent Combustion : Profress and Challenges', Twenty - Third Symposium (International) on Combustion, The Combustion Institute, pp. 591 - 612.

Pourahmadi, F. and Humphrey, J.A.C. (1983). 'Modelling Solid - Fluid Turbulent Flows with Application to Predicting Erosive Wear', PhysicoChemical Hydrodynamics, Vol.4, No 3, p.191.

Prandtl, L. (1925). 'Bericht uber Untersuchungen zur ausgebildeten Turbulenz, ZAMM,5,p.136

Prandtl, L. (1945). 'Uber ein neues Formelsystem fur die ausgebildete Turbulenz, Nachirchten von der Akad. der Wissenschaft in Gottigen.

Pun, W.M. and Spalding, D.B. (1967). 'A Procedure for Predicting the Velocity and Temperature Distribution in a Confined, Steady, Turbulent Gaseous Diffusion Flame', Proceedings International Astronautical Federation Meeting, Belgrade.

Raithby, G.D. and Torrance, K.E. (1974). 'Upstream - Weighted Differencing Schemes and their Application to Elliptic Problems Involving Fluid Flow', Computer and Fluids, Vol. 2, pp. 191 - 206.

Rizvi, S.M.A. (1985). 'Prediction of Flow,Combustion and Heat Transfer in Pulverised Coal Flames', PhD Thesis, University of London.

Roache, P.J. (1982). Computational Fluid Dynamics, Hermosa Publishers, Alburquerque.

Robinson, G.F. (1985). 'A Three - Dimensional Analytical Model of a Large Tangentially Fired Furnace', Journal of the Institute of Energy, pp. 116 - 149.

Rodi, W. (1970). "Basic equations for turbulent flow in Cartesian and cylindrical co-ordinates," Imperial College, Mechanical Engineering Department, Report No.BL/TN/A/36.

Rodi,W.(1980), 'Turbulence models and their application in Hydraulics' , IAHR, State of the Art paper, Presented by IAHR-Section on Fundamentals of Division II : Experimental and Mathematical Fluid Dynamics

Shah, N.G. (1979). Computation of Radiation Heat Transfer, PhD Thesis, University of London.

Sirignano, W.A. (1983), 'Fuel droplet Vaporisation and Spray Combustion Theory', Progress in Energy and Combustion Science, Vol. 9, p. 291.

Smith,P.J., and Fletcher, T.H. 'A Study of Two Chemical Reaction Models in Turbulent Coal Combustion', Combustion Science and Technology, Vol. 58, pp.59-76.

Smoot, L.D., and Pratt, D.T. (1979). Pulverised Coal Combustion and Gasification, Plenum Press, New York.

Spalding, D.B. and Jayatillaka, C.L.V. (1966). 'A survey of the Theoretical and Experimental Information on the Resistance of the Laminar Sub - Layer to Heat and Mass Transfer', Proc. 2nd All Soviet Union Conf. on Heat and Mass Transfer, Minsk, USSR, 1964, Vol. 2, pp. 234 - 264 (In Russian); English Translation , Ed. by C.Gayley, J.P. Harnett and E.R.G. Eckert, Rand. Corp., California.

Spalding,D.B.(1969), 'The prediction of two-dimensional, steady turbulent flows', Imperial College, Heat Transfer section, Rep EF/TN/A/16

Spalding, D.B.(1972), 'A Novel Finite Difference Formulation for Differential Expressions Involving both First and Second Derivatives', Int. J. Num. Meth. Engrg. Vol.4, pp. 551-559.

Spalding, D.B. (1979). Combustion and Mass Transfer, Pergamon Press

Stewart, F.P. and Cannon, P. (1971). 'The Calulation of Radiative Heat Flux in a Cylindrical Furnace Using Monte Carlo Method', International Journal of Heat and Mass Transfer, Vol. 4, p. 249.

Swithenbank, J., Poll, I., Vincent, M.W. and Wright, D.D. (1973). 'CombustionDesign Fundamentals', Fourteenth Symposium (International) on Combustion, The Combustion Institute.

Tennekes, H. and Lumley, J.L. (1972). A First cource in Turbulence, The MIT Press.

Tesner, P.A., Snegiriova, T.D. and Knorre, V.G. (1971). 'Kinetics of Dispersed Carbon Formation', Combustion and Flame, Vol. 17, p 253.

Tribus, M. (1961). Thermostatics and Termodynamics, Van Nostrand, London.

Truelove, J.S. (1976). 'A MixedGrey Gas Model for Flame Radiation', AERE Harwell, Report No HL 76/3448.

Truelove, J.S. and Holcombe, D. (1990). 'Measurement and Modelling of Coal Flame Stability in a Pilot - Scale Combustor', Twenty - Third Symposium (International) on Combustion, The Combustion Institute, pp. 963 - 971.

Truelove, J.S. and Williams, R.G. (1988). 'The Modelling of Ignition and Combustion in Swirl Burners for Pulverised Coal', National Energy Research, Development and Demonstration Program, Australia.

Van Niekerk, J.E. (1992). "Modelling of Carbon Black Formation', Internal Report, Imperial College, London.

Visser, B.M., Smart, J.P., Van De Kamp, W.L. and Weber, R. (1990) 'Measurements and Predictions of Quarl Zone Properties of Swirling Pulverised Coal Flames', Twenty - Third Symposium (International) on Combustion, The Combustion Institute, pp 949 - 955.

Wagner, H.G.G. (1979). 'Soot Formation in Combustion', Seventeenth Symposium (International) on Combustion, The Combustion Institute, p.3.

Wallis, G.B. (1969). One Dimensional Two - Phase Flow', McGraw Hill Company.

Weidman, G., H. and Utterback, P., M. (1976). 'Liquid Fuel Analysis - Their Effect on Combustion and Emissions', PGTP 76-45, Combustion Intitute's Central States Section Spring Meeting, Colombus, Ohio, April 5-6.

Yuen, M . C . and Chen, L . W . (1976). 'On drag of evaporating liquid droplets', Combustion Science and Technology, Vol. 14, p. 147.

Yuen, M . C . and Chen, L . W . (1978). 'Heat transfer measurements of evaporating liquid droplets', International Journal of Heat and Mass Transfer, Vol. 21,p. 537.

Zubar, N. (1964). 'On the Dispersal Two - Phase Flow in the Laminar Flow Refion', Chemical Engineering Science, Vol. 19, p.897.

APPENDIX A

The combustion model adopted in the present study assumes a global, one-step, infinetely fast chemical reaction between fuel and oxidant. It also assumes that the effective exchange coefficient $\Gamma eff \equiv \frac{\mu_{eff}}{\sigma}$, are equal for all the species. As a consequence, the thermodynamic state of the flow can be related to a single strictly conserved scalar variable for which a transport equation may be derived.

The time-averaged transport equations of the mass fraction of the fuel and oxidant are given by:

$$\frac{\partial}{\partial x_i}(\rho u_i \overline{m_{fu}}) - \frac{\partial}{\partial x_i}[\Gamma_{eff} \frac{\partial \overline{m_{fu}}}{\partial x_i}] = R_{fu} + S_{d,m} \qquad (A.1)$$

and

$$\frac{\partial}{\partial x_i}(\rho u_i \overline{m_{ox}}) - \frac{\partial}{\partial x_i}[\Gamma_{eff} \frac{\partial \overline{m_{ox}}}{\partial x_i}] = R_{ox} \qquad (A.2)$$

and introducing the convection/diffusion operand, $L(\,) \equiv \frac{\partial}{\partial x_i}(\rho \overline{u_i}) - \frac{\partial}{\partial x_i}[\Gamma_{eff} \frac{\partial}{\partial x_i}]$, on the left hand side equations (A.1 and 2) may be written :

$$L(\overline{m_{fu}}) = S_{fu} + S_{d,m} \qquad (A.3)$$

$$L(\overline{m_{ox}}) + S_{ox} \qquad (A.4)$$

where $S_{d,m}$ is the source of mass due to droplet evaporation and R_{fu} and S_{ox} are the reaction rates of fuel and oxidant respectively. Multiplying Eq (A.3) by the stoichiometric factor, s, and substracting from it Eq. (A.4) gives:

$$L(\overline{\phi}) = (s R_{fu} - R_{ox}) + S_{d,m} \qquad (A.5)$$

where is a scalar quantity defined as:

$$\phi \equiv s \overline{m_{fu}} - \overline{m_{ox}} \qquad (A.6)$$

As the combustion model assumes instantaneous one-step reaction between the fuel and the oxidant, the two reaction rates will be equal. Eq (A.6) may be rewritten as :

$$L(\overline{\phi}) = S_{d,m} \tag{A.7}$$

The time-averaged value of the mixture fraction is defined as:

$$\overline{f} = \frac{\overline{\phi} - \phi_0}{\phi_1 - \phi_0} \tag{A.8}$$

where the subscripts 1 and0 designate the fuel and oxidant bearing streams. Substituting the mixture fraction f as a function of ϕ the final form of the transport equation of the mixture fraction became:

$$L(\overline{f}) = S_{p,f} \tag{A.7}$$

where Sp,f is the gas-droplet intraction source term which is given by:

$$S_{p,f} = S_{p,m}\left(\frac{1 - \phi_0}{\phi_1 - \phi_0}\right) \tag{A.9}$$

BIBL. LONDIN. UNIV.